Understanding the Interplay Between Iron Adsorption, Surface Reconstruction, and Electrocatalytic Oxygen Evolution by Transition Metal (Hydr)oxides

by

Liam P. Twight

A dissertation accepted and approved in partial fulfillment of the
requirements for the degree of
Doctor of Philosophy
In Chemistry

Dissertation Committee:
Carl Brozek, Chair
Shannon Boettcher, Advisor
Ramesh Jasti, Core Member
Erin Moore, Institutional Representative

University of Oregon

Fall 2024

DISSERTATION ABSTRACT

Liam P. Twight

Doctor of Philosophy in Chemistry

Title: Understanding the Interplay Between Iron Adsorption, Surface Reconstruction, and Electrocatalytic Oxygen Evolution by Transition Metal (Hydr)oxide Electrocatalysts

Renewable electricity-driven alkaline water electrolysis is poised to be a key technology for reducing the CO_2 emissions from combustion of fossil fuels in industrial sectors like aviation and fertilizer manufacturing. One of the largest costs of operating water electrolyzers is that of the electricity needed to drive the liberation of hydrogen and oxygen gases. Therefore, improving electrolyzer efficiency – lowering the electrical power needed per kilogram of H_2 generated – is essential to their widespread deployment. The anodic oxygen evolution reaction (OER) is a process with intrinsically slow kinetics that makes large contributions to electrolyzer inefficiency. The kinetics of OER can be hastened with the proper choice of catalyst the best of which are based on Ni and Co oxides or hydroxides with a minority component of incorporated Fe. Decades of research involving Ni/Co/Fe OER catalysts have been done, but there is still debate about the nature of the active sites in these materials. The complexity of these systems is to blame; the formation and maintenance of high OER activity sites depends on highly dynamic processes involving surface iron site dissolution-redeposition and catalyst structural change both of which are likely functions of the electrolyte pH, iron concentration in electrolyte, applied electrical bias, and catalyst chemical composition.

This dissertation advances understanding of the nature of extremely high activity Fe active sites which form *in-situ* on nickel and cobalt hydroxide and lanthanum nickel oxide, three technologically promising catalysts. In Chapter I, I describe from a broad perspective the areas where high efficiency alkaline electrolyzers could serve to eliminate CO_2 emissions and the role that OER catalysts will play in accomplishing this goal. In Chapter II, I report the results of fundamental investigations which reveal that Fe active sites are not of one, but two kinds: one that forms by surface adsorption of electrolyte Fe and another that substitutes for host metal atoms. In Chapter II, I describe the results of a deeper mechanistic investigation into the thermodynamic parameters that govern the

activity of these surface Fe sites. Chapter III extends the methods used to understand Fe-sites on nickel hydroxides to an understudied perovskite oxide, lanthanum nickelate ($LaNiO_3$). Together, these studies deepen our understanding of why Fe is a ubiquitous activator of OER catalysts and broaden the family of catalysts for which Fe activation is integral. As a result, new design principles for high performance alkaline electrolyzer anodes become evident. Catalysts should have a high density of sites for cooperative surface Fe site adsorption such that the activation energy and pre-exponential factors are optimized. Surface restructuring should be purposefully induced for those that need it for high OER activity to maximize active site formation. Where restructuring is required for high activity, surface chemical descriptors should be developed and utilized instead of bulk ones which may not directly connect to the relevant physical picture of catalysis. This dissertation contains previously published and un-published co-authored materials.

CURRICULUM VITAE

NAME OF AUTHOR: Liam P. Twight

GRADUATE AND UNDERGRADUATE SCHOOLS ATTENDED

University of Oregon, Eugene, OR

California State University, Long Beach, Long Beach CA

DEGREES AWARDED

Doctor of Philosophy, Chemistry, University of Oregon

Master of Science, Chemistry, University of Oregon

Bachelor of Science, Chemistry, California State University, Long Beach

AREAS OF SPECIAL INTEREST

Electrochemistry: electrocatalysis; water oxidation; electrolyzer devices

Materials science: characterization; surface chemistry; quantitative analysis

PROFESSIONAL EXPERIENCE

Graduate research associate, 2019 - 2024

UO Inductively-coupled plasma mass spectrometry manager, 2020 - 2024

General chemistry lab instructor 2019 - 2020

GRANTS, AWARDS, AND HONORS

University of Oregon

Renewable Energy Foundation: Sir Fraser Stoddart Scholarship, 2021

NSF Graduate Research Fellowship Program: Honorable Mention, 2020

UO Doctoral First Year Merit Award, 2019

California State University, Long Beach

Undergraduate Award for Outstanding Research, 2018

James L. Jensen Undergraduate Research Fellowship, 2018

Women in Philanthropy Undergraduate Research Scholarship, 2018

American Chemical Society Award in Physical Chemistry, 2018

CSULB Presidential Scholarship, 2015

PUBLICATIONS

*denotes equal contributions

1. Reactive surface Fe sites on nickel oxyhydroxide OER catalysts: coverage evolution, activity, and enthalpy-entropy compensation from temperature-dependent kinetics. **Twight, L.** Boetcher, S. W. *in preparation for submission to J. Am. Chem. Soc.* 2024.

2. Trace Fe activates perovskite nickelate OER catalysts in alkaline media via redox-active surface Ni species formed during electrocatalysis. **Twight, L.,** Boettcher, S. W. *et al. J. Catalysis* 432, 2024.

3. Cooperative Fe sites on transition metal (oxy)hydroxides drive high oxygen evolution activity in base. **Twight, L.*,** Ou, Y.*, Boettcher, S. W. *et al. Nat. Comm.* 14, 7688, 2023.

4. Purification of residual Ni and Co hydroxides from Fe-free alkaline electrolyte for electrocatalysis studies. **Twight***, **L.,** Liu, L.*, Fehrs, J., Ou, Y., Sun, D., Boettcher., S. W. *ChemElectroChem.* 9, 2022.

5. Anode catalysts in anion-exchange-membrane electrolysis without supporting electrolyte: Conductivity, dynamics, and ionomer degradation. Krivina, R., Lindquist, G., Beaudoin, S., Stovall, N., Thompson, W. **Twight**, **L.,** Marsh, D., Grzyb, J., Fabrizio, K., Hutchison, J., Boettcher. S. W. *Adv. Mater.* 34, 2022.

6. Size-dependent properties of solution-processable conductive MOF nanocrystals. C. Marshall, J. Dvorak, **L. Twight**, L. Chen, K. Kadota, A. Andreeva, A. Overland, T. Ericson, A. F. Cozzolino, C. Brozek. *J. Am. Chem. Soc. (144)* 2022.

7. Hydrogen-evolution-reaction kinetics pH dependence: Is it covered? J. Mitchell, M. Shen, **L. Twight**, S. Boettcher. *Chem. Catal. (2)* 2022.

8. Tunable band gaps in MUV-10(M): A family of photoredox-active MOFs with earth-abundant open metal sites. K.

9. Fabrizio, K. Lazarou, L. Payne, **L. Twight**, S. Golledge, C. Hendon, C. Brozek. *J. Am. Chem. Soc. (143)* 2021.

10. Oxygen electrocatalysis on mixed-metal oxides/oxyhydroxides: From fundamentals to membrane electrolyzer technology. R. Krivina, Y. Ou, Q. Xu, **L. Twight**, N. Stovall, S. Boettcher. *Acc. Mater. Res.* (*2)* 2021.

11. Improved Water Transport via Cationic Thin-Layers Enables High-Current Density Bipolar Membrane Electrolyzers. Sebastian Z. Oener, **Liam P. Twight**, Grace A. Lindquist, Shannon W. Boettcher. ACS Energy Lett. 6, 2020.

12. Phase dependent encapsulation and release profile of ZIF-based biocomposites. F. Carraro, M. de J. Velásquez-Hernández, E. Astria, W. Liang, **L. Twight**, C. Parise, M. Ge, Z. Huang , R. Ricco, X. Zou, L. Villanova, C. O. Kappe, C. Doonan and P. Falcaro. *Chem. Sci.,* (*11*) 2020

13. Gamma radiolysis of hydrophilic diglycolamide ligands in concentrated aqueous nitrate solution. G. P. Horne, A.Wilden, S. P. Mezyk**, L. Twight**, M. Hupert, A. Stärk, W. Verboom, B. J. Mincher, G. Modolo. *Dalton Trans. (48)* 2019.

14. Radiolytic and hydrolytic degradation of the hydrophilic diglycolamides. A. Wilden, B. J. Mincher, S. P. Mezyk, **L. Twight**, K. M. Rosciolo-Johnson, C. A. Zarzana, M. E. Case, M. Hupert, A. Stärk, & G. Modolo. *Solvent. Extr. Ion Exc.,* (36) *2018*

ACKNOWLEDGEMENTS

The work in Chapters II and IV was supported by the National Science Foundation Chemical Catalysis Program, Award #1955106. The ICP-MS instrument was funded by an NSF MRI Award #2117614. The work in Chapter III was supported by the National Science Foundation Chemical Catalysis Program, Award #2400195. The work in this dissertation benefited from contributions from many excellent collaborators. XAS measurements in collaboration with the Helmholtz-Zentrum Berlin für Materialien und Energie would not have happened without Marcel Risch and his team: Javier Villalobos, Joaquín Morales-Santelices, and Denis Antipin, whom I gratefully acknowledge. The computational aspects of Chapter II were performed by Bipasa Samanta and Santu Biswas under direction of Maytal Caspary Toroker at Technion-Israel Institute of Technology. The extension of the perovskite study in Chapter IV would not have been possible without the preparation of key materials by Kunal Velinkar and Samji Samira of Eranda Nikolla's group at University of Michigan. Much of the characterization was enabled only through the expert training and advice provided by members of the UO CAMCOR staff, Steve Golledge, Kurt Langworthy, Josh Razink, and Valerie Brogden.

It is a simple fact that it takes a community to mint a new PhD student. I extend my sincere thanks to the leader of that community at UO, my advisor, Shannon Boettcher, who gave me the crucial opportunity to grow as an electrochemist in his lab, taught me how to think carefully and rigorously in the design and execution of basic research, and has been ever supportive of my intellectual goals. I thank all my lab colleagues and friends, who with their experience and unwavering willingness to help, were essential for me to make it to this finish line. Thank you especially Grace Lindquist, Jess Fehrs, Raina Krivina, Nicole Sagui, Nick D'antona, Aaron Kaufmann, Haokun Chen, Ana Konovalova, Minkyoung Kwak, and Olivia Traenkle for forming a wonderful lab community and the many memories we all made together that I will look back on fondly. Thank you also to my cohort members and friends with whom I have shared many needed moments of commiseration about the challenges of grad school and pleasant get-togethers filled with laughter, food, drinks, games, movies, and music.

Before the UO community there was a CSU Long Beach community. Stephen Mezyk, my undergraduate advisor deserves my special gratitude as the first person to see my potential as a scientist without whom I may not have decided to reach beyond the baccalaureate level. Thank you Mezyk lab members at the time, Brittany, Kylie, Jamie, Amir, Michael, Christian, and Landon for your friendship and mentorship. Thank you to the CSULB Presidential Scholarship Program who noticed the hard work I put into my academics in high school and gave me a scholarship that launched my entire endeavor in scholarship as it does for so many other deserving students.

Finally, thank you to the most important people in my life: my parents, sister, and partner. To my parents for giving me a start in life that required enormous effort on their part to provide, but is absolutely needed for a child to develop and tackle ambitious goals later in life. To my sister, for understanding me as only a sibling does. To Audrey, my partner, whose laughter, kindness, and love has changed my life.

TABLE OF CONTENTS

LIST OF FIGURES

LIST OF TABLES

I. THE ROLE OF OXYGEN EVOLUTION IN GREEN ELECTROLYSIS TECHNOLOGIES

It is broadly and unequivocally recognized among the scientific community that the rising emission of CO_2 from fossil fuel combustion[1] has increased average global land and sea temperatures[2] via the greenhouse effect, a mechanism rooted in over a century of physics and chemistry research[3-16]. The 6th Assessment Review of the Intergovernmental Panel on Climate change (IPCC), authored by 743 international climate experts of its member nations, reports that this warming was ~1.1 $^{\circ}$C compared to the period 1850-1900 based on decades of collecting climatic observations and modeling. Far from benign, this global warming has, to a high degree of confidence, decreased food and water security, increased chance of extreme weather events, accelerated sea level rise and ocean acidification, and damaged substantially (in some cases irreversibly) terrestrial, aquatic, marine, and cryospheric habitats. The magnitude of these processes and the risk of low-probability, irreversible, catastrophic turning points increases with every future increment of warming. Only "deep, rapid, and sustained" and in many cases "immediate" reduction of greenhouse gas emissions is required to keep global temperature rise below international targets of 1.5°C and 2°C thereby mitigating the worst climatic effects. The IPCC estimates that humanity has a carbon budget of about 1000 gigatons of CO_2 remaining for 2024 onward before warming of 2°C is reached (67% probability). For scale, this is equivalent to the amount emitted between the 30 year period between 1990 and 2019[17].

To eliminate CO_2 emissions, a rapid transition must be made toward a net-zero CO_2 energy portfolio based on renewable sources. Currently, only 14% of global energy is supplied by renewables (solar, wind, biofuels, or hydropower), the large majority of which is from hydropower[18]. Thus a large gap exists between clean energy goals and clean energy deployment. There are many possible paths to overcome that gap[19-21], any of which will be determined by current and future regulatory and technoeconomic conditions. In 2021, The International Energy Agency (IEA) published *Net Zero by 2050*, the first global timeline of targets by which the world might achieve a net-zero CO_2 emission (NZE) reality. In the IEA model, annual global emissions fall in concert with increased integration of renewables from 37GtCO_2 in 2023 to 21 GtCO_2 by 2030 and then 0 GtCO_2 by 2050. The

total energy consumption in 2050 consists of only 20% fossil fuels, these having been largely replaced with renewables and nuclear. The key mechanisms by which the NZE is attained are swift deployment of renewable energy technology, broad end-use electrification, increased energy efficiency, use of hydrogen and hydrogen based fuels, behavioral change by citizens, and policy instruments like CO_2 pricing and termination of fossil fuel subsidies all of which would need to occur globally through international cooperation[20]. Tesla has also weighed in on the matter, publishing an influential 2023 analysis of what a transition to a sustainable economy might look like. In its *Master Plan: Part 3,* the Tesla team prescribed 6 actions that should be taken, among these were repowering the existing grid with renewables, switching to higher efficiency electric vehicles and heat pumps, and sustainable synthesis of aviation and shipping fuel. Taken together and assuming accurate forecasting of material costs and future electricity demand, this transition could occur with 30 TW installed renewable power capacity (~10x the 2023 total capacity)[22], 10% of 2022 World GDP, $10 trillion dollars manufacturing investment (~36% of 2024 U.S. GDP and $4 trillion less than the fossil fuel only scenario)[23], and 0.21% land area required[21]. Unlike that of the IEA, the Tesla decarbonization path does not break down this target into a series of intermediate targets. Proposed pathways for U.S-specific decarbonization echo the content of these global plans[24].

While direct electrification of CO_2 emitting end uses is a prominent strategy for decarbonization, this is not a feasible strategy for every area of the economy. Parts of the industrial and transportation sectors[20] will require a fuel source with energy density akin to that of fossil fuels. These are typically classified as “hard-to-abate” industries and include – with the percentage of global CO_2 emissions given in parentheses – long-haul shipping[25] (2%)[26], aviation[27, 28] (3%)[29], steel refining (7%)[30], ammonia-based fertilizer (1.3%)[31], cement (7%)[32], and glass[33] production (~0.2%)[34]. Taken together, the emissions from these industries constitute ~20% of the global total, a significant portion.

Most decarbonization plans recommend hydrogen as a chemical fuel suitable for abating emissions from these industries because hydrogen can be produced without CO_2 as a byproduct via direct electrolysis of water using renewable electricity[20, 35]. This “green” hydrogen can directly substitute unabated hydrogen in traditional applications in industry

and refining such as the Haber-Bosch process in which H_2 is used to reduce N_2 to ammonia[36] and direct iron reduction[37]. In addition to direct substitution of fossil fuel-derived hydrogen, green hydrogen can do so indirectly. For example, it has been used to reduce CO_2 via the Fischer-Tropsch process to make CO, a molecule which can be electrochemically transformed to higher molecular weight organic products suitable for use as jet fuel[27]. Hydrogen could also serve to smooth the problematically intermittent supply profile of renewable electricity by diverting excess solar and wind electricity to an electrolyzer plant. The stored hydrogen from electrolysis could then be tapped when renewable electricity is relatively scarce by feeding it to a fuel cell plant, generating needed electricity with high efficiency[38]. Despite the proposed benefits of using green hydrogen for energy storage and distribution, they have not been realized at scale and are expected to have a minor impact in relation to applications in traditional industry and refining[35].

Meeting the demands of traditional industry with green hydrogen is a formidable challenge. In 2022, 95 Mt of hydrogen were consumed globally the overwhelming majority of which was used for heavy industry (53 Mt) and refining (41 Mt). Less than 0.1% of this hydrogen was produced by water electrolysis. Replacing 2022 levels of dedicated hydrogen production with green hydrogen is estimated to require 730-940 GW of installed electrolyzer plant capacity. Given only 700 MW of installed electrolysis capacity in 2022, a 1,040 – 1340-fold increase is needed to meet global hydrogen demand. The IEA estimates that capacity of 175 GW could be accomplished by 2030 based on announced projects and 430 GW if early stage, unannounced projects are taken into account[35]. There are several obstacles to rapid deployment of electrolyzer capacity at hundreds of GW scale. Two notable ones are uncertainty about regulation and certification, and dearth of hydrogen distribution infrastructure, but chief among these is a high levelized cost of hydrogen (LCOH), the price per kg of hydrogen taking into account lifetime costs of a plant. LCOH is \$3.4 -12.0/kg H_2 when produced by water electrolysis versus only \$1-3 kg H_2 from methods using unabated fossil fuels.[35, 39] LCOH is influence by multiple factors, but cost of electricity is the main driver for hydrogen produced using electrolyzers[40] with additional variability attributed to choice of technology: proton exchange membrane (PEM), alkaline exchange membrane (AEM), or liquid alkaline (LA) electrolysis[41]. Decreasing the contribution of electricity cost to LCOH can be approached from two directions: decrease

the cost of electricity for renewables and/or increase the efficiency of electrolyzer electricity use. Accomplishing the former will require thoughtful efforts by policy makers to stimulate the build-out of transmission and generation infrastructure. The latter challenge motivates this dissertation as it can be addressed from a basic science and engineering standpoint.

This thesis details fundamental electrochemical and material science investigations that may help lower the LCOH for liquid alkaline electrolyzers by improving electrolyzer efficiency. As of 2022 alkaline electrolyzers made up 60% of installed electrolysis capacity[35], and are therefore likely to significantly contribute to hydrogen production in the future. A simple model of a typical liquid alkaline electrolyzer is depicted in Figure 1.

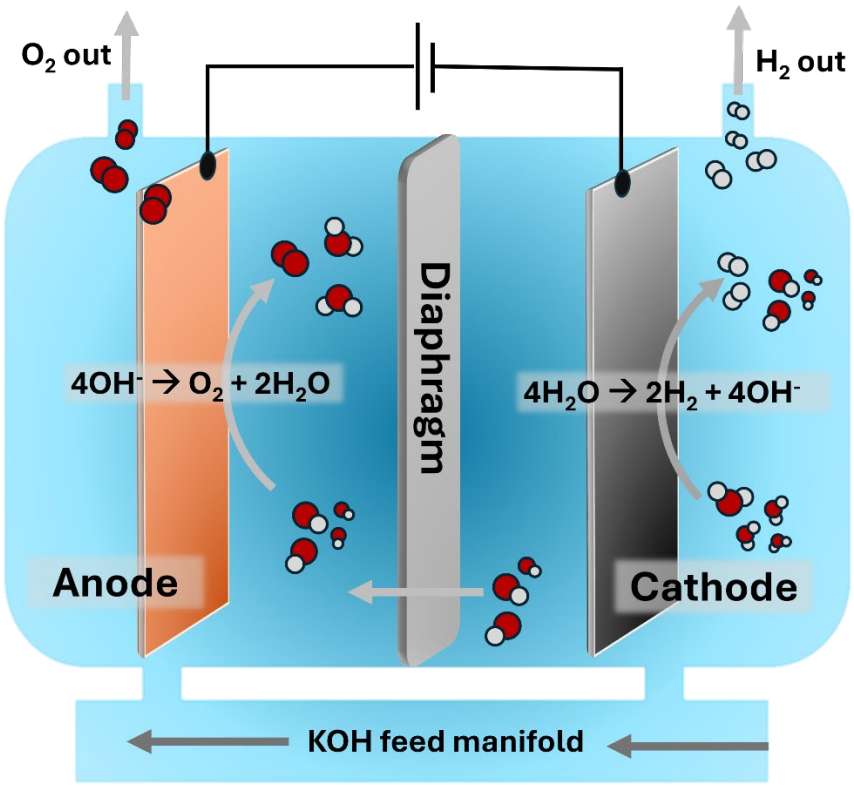

Figure 1. Generalized liquid alkaline electrolysis cell.
An applied voltage oxidizes hydroxide to oxygen gas at the anode and hydrogen evolution from water reduction at the cathode in a cell flooded with alkaline electrolyte, usually KOH.

It consists of two electrodes, cathode and anode, in an alkaline electrolyte separated by a diaphragm to prevent electrode shorting and mitigate gas crossover. The electrochemical

half-reactions are the cathodic hydrogen evolution reaction (HER) and anodic oxygen evolution reaction (OER) given in the figure. Note the sum of these half-reactions sum to the total water splitting reaction. The half-reactions are driven by an applied voltage leading to a net current in the external circuit that is related to the stoichiometry of the chemical reaction. Using the Gibb's free energies of formation for reactants and products for the water splitting reaction one finds that the total thermodynamic voltage required to drive these half-reactions is 1.23 V.[42] In practice, the total voltage needed to drive an appreciable current density is higher because of additional contributions to the thermodynamic minimum from kinetic, ohmic, and mass transport phenomena.

Kinetics contribute a significant overpotential to water electrolysis in an electrolyzer. The anodic oxygen evolution reaction (OER) is a 4-electron reaction while that of the cathodic hydrogen evolution reaction (HER) is a 2-electron reaction. The greater number of electrochemical steps in OER leads to kinetic sluggishness relative to HER, limiting the overall rate of reaction and contributing hundreds of millivolts of overpotential to the thermodynamic minimum for water electrolysis. Decades of electrochemical research[43, 44] have been performed to improve OER kinetics with appropriate electrocatalysts that reduce the energetic barriers of rate-limiting intermediate steps associated with the reaction. Even so, losses in efficiency from slow OER kinetics are sizeable across electrolysis applications. This has been particularly well-illustrated by measurements using integrated reference electrodes which quantify the (often large) contribution of OER to the total cell potentials of alkaline exchange membrane[45], proton exchange membrane[46], and CO_2 reduction electrolyzers[47].

A wide variety of materials have been tested as alkaline OER electrocatalysts including precious metal oxides, transition metal alloys, perovskite oxides, spinels and hydroxides, metal chalcogenides and metal pnictides.[48] Using thin-film model systems where every deposited metal site participates in charge transfer, it has been found that materials with the highest alkaline OER activity are based on nickel and cobalt hydroxides and their derivatives.[49] Developing a comprehensive, molecular-level understanding of why these materials are the best alkaline OER catalysts is ongoing and a source of debate in the literature. One influential idea is based on the Sabatier principle – that the rate of

OER is fastest on those materials which bind reactants just strongly enough to allow the reaction to proceed, but not so strongly that the products cannot desorb and poison the catalytic site[50]. Since the binding of reaction intermediates occurs by bonding between intermediate and surface atom orbitals, it follows that the rate of OER should have a "volcano"-shaped dependency on periodic trends in electronic structure descriptors that characterize chemical bonding *i.e.* the reaction rate would be expected to maximize at descriptor values in the intermediate range[51]. For example, Trasatti obtained a volcano shape plot of OER overpotential versus enthalpy of lower to higher oxide transition (*e.g.* $Ru_2O_3 \rightarrow RuO_2$), a proxy for the heat of adsorption of oxygenated intermediates of the lower oxide during OER.[52] Shao-Horn and coworkers reported a volcano shaped relationship between OER potential at 50 μA cm^{-2}_{oxide} (area normalized to the oxide surface area obtained form gas sorption measurements) and the occupancy of the antibonding e_g orbital of the B-site transition metal site in a series of perovskite oxides[53]. A more detailed exposition of descriptors in OER catalysis can be found in Chapter IV.

These studies share a key feature: extraction of an electronic descriptor from DFT calculations, literature data, or measurement using the pristine, as-synthesized material structure as a model. The volcano plot is then formed using this descriptor as the independent variable. This approach requires the tacit assumption that the pristine catalyst structure accurately represents the surface structure. There is strong evidence that this is a poor assumption. At least two key phenomena complicate the conventional conclusions about OER activity trends obtained using bulk electronic descriptors:

1) **Iron impurity incorporation.** Catalysts with activity in the highest percentiles almost always have incorporated iron either from impurities in the electrolyte or intentional inclusion during synthesis[54]
2) **Surface reconstruction.** Across OER literature and material classes, *in-situ* reconstruction of as-prepared materials leads to formation of new surface structures the OER mechanism and activity of which is responsible for the observed reaction rate[55]

It is not trivial to understand how each of these processes affects the electrochemical characteristics of a given catalyst. Iron, for example, is a common impurity in

commercially available KOH[56]. If steps are not taken to remove this impurity[57], the iron can adsorb to the catalyst under study and increase the OER activity[58], unbeknownst to the well-meaning experimentalist. Adventitious nickel impurities also present problems to unambiguous assignment of catalytic activity[57, 59]. When reconstruction occurs it can lead to very thin layers, as small as a few unit cells thick, or involve species that are heterogeneously distributed, which appear and disappear reversibly[60-65]. Identification of this kind of surface species may require exotic *operando* experimental methods not routinely available to most electrochemists. Adsorption of impurities or unidentified reconstruction during a study in which electronic descriptors are the focus could lead to unwitting rationalization of OER activity with catalyst features that are not relevant to the actual mechanism of catalysis. Conversely, if direct connection between OER activity and bulk electronic descriptors is obscured by impurities and reconstruction then in-depth study of the catalytic activity of sites formed *by those very impurities and reconstruction* is necessary to develop a physical model of catalysis by the highest activity materials.

This dissertation addresses the connection between high OER activity of nickel and cobalt oxides, surface reconstruction, and impurity Fe species. In chapter II, introduction of Fe into an electrochemical cell during polarization of the electrode at OER potentials is used to prepare surface Fe sites which are distinct from bulk Fe sites prepared by co-electrodeposition. This permitted measurement for the first time of the turnover frequency of surface and bulk Fe sites. It is shown that surface Fe sites are undercoordinated and have a more elongated nearest-neighbor environment than their bulk counterparts. They also exhibit cooperativity - the intrinsic activity per Fe site increased with Fe site loading. Density-functional theory calculations suggest this cooperativity functions via delocalization of oxidative charge among multiple Fe centers. This work was published in *Nature Communications* by myself as co-first author with Yinqing Ou and Bipasa Samanta. Contributing authors to the published version of this work are: Lu Liu, Santu Biswas, Jessica L. Fehrs, Nicole A. Sagui, Javier Villalobos, Joaquín Morales-Santelices, Denis Antipin, and. Marcel Risch. Corresponding authors were Maytal Caspary Toroker and Shannon W. Boettcher.

The ability to control Fe-site conformation enabled surface-Fe-specific temperature-dependent kinetic studies. The results were analyzed using Butler-Volmer, Arrhenius, and absolute rate theory to provide mechanistic insight. Contrary to expectations based on the Butler-Volmer theory approach to analysis of these data, the Tafel slope is constant at temperatures from -5 to 70°C indicating an unexpected temperature-dependence of the transfer coefficient. Further, a compensation between the enthalpy and entropy of activation at various overpotentials was revealed. It is proposed this behavior is consistent with concepts relevant to inner sphere rather than outer sphere electron transfer such as the change of intermediate coverage and solvent structure with potential. This work was completed by myself and is unpublished as of the writing of this dissertation.

Chapter IV provides new evidence that Fe-site driven OER is not restricted to oxyhydroxides and is likely a universal feature of catalysis by perovskite oxide nickelates, contrary to most literature on the subject. Observations were made of surface reconstruction-mediated Fe site formation on perovskite oxide $LaNiO_3$ and Ruddlesden-Popper oxide La_2NiO_4 by combining electrochemical and materials characterization methods. The amount of surface reconstruction is compared between these two seemingly disparate compounds and normalization of their OER activity to the quantity of reconstructed nickel suggests that the intrinsic activity of the reconstructed phase is similar if not identical, suggesting a convergence toward a thermodynamic minimum energy structure. An experimentally accessible surface chemical descriptor is proposed as an alternative to bulk electronic descriptors of OER activity. These results were published in *Journal of Catalysis* by myself as sole first author along with contributions from Ally Tonsberg, Samji Samira, Kunal Velinkar, Kora Dumpert, Yingqing Ou, Le Wang, and Eranda Nikolla. Shannon Boettcher served as corresponding author on the published version of this work

II. COOPERATIVE FE SITES ON TRANSITION METAL (OXY)HYDROXIDES FOR HIGH OXYGEN EVOLUTION ACTIVITY

Yingqing Ou[1,2‡], **Liam P. Twight[1‡]**, Bipasa Samanta[3‡], Lu Liu[2,5], Santu Biswas,[3] Jessica L. Fehrs[1], Nicole A. Sagui[1], Javier Villalobos[6], Joaquín Morales-Santelices[6], Denis Antipin[6], Marcel Risch[6], Maytal Caspary Toroker[3,4]*, and Shannon W. Boettcher[1]*

‡ These authors contributed equally to the manuscript

This chapter contains co-authored work published in *Nature Communications* in 2023. Reproduced with permission from [*Nat. Comm.* **2023,** 14, 7688][66] The study was conceived and designed by Y.O., S.W.B, J.L.F, and **L.P.T**. S.W.B. directed the research project. Y.O. collected most of the electrochemical and ICP-MS experimental data. L.P.T. performed the materials characterization of the catalysts using electron microscopy and X-ray absorption spectroscopy and additional electrochemical stability and activity tests.; B.S. and S.B. completed the computational studies, directed by M.C.T.; Y.O., **L.P.T**., B.S., M.C.T. and S.W.B. analyzed the data and wrote the manuscript. **L.P.T**., N.S., J.V., J.M.S., D.A., and M.R. designed the *in-situ* XAS study, collected, and analyzed the XAS data.

Introduction

The electrolysis of water ($2H_2O \rightarrow 2H_2 + O_2$) to produce hydrogen fuel is critical for renewable-energy infrastructure[67, 68]. Even in optimized electrolyzers, the efficiency is reduced by the slow kinetics of the oxygen evolution reaction (OER, $4OH^- \rightarrow 2H_2O + 4e^- + O_2$ in alkaline media)[69, 70]. Among the many OER catalysts studied over decades, Fe is

broadly pivotal in promoting the catalytic activity in alkaline media[71-73]. In particular, Ni and Co (oxy)hydroxides require Fe to achieve high activity, regardless of whether it is introduced intentionally or incidentally[74, 75]. Sustaining the high activity of these Fe-containing (oxy)hydroxides requires soluble Fe species in the electrolyte due to the dynamic Fe exchange at the catalyst/electrolyte interface[76-79]. High-activity perovskite oxides also involve active Fe sites[80]. $La_{1-x}Sr_xCoO_3$ perovskites form CoO_xH_y layers in alkaline electrolyte with enhanced activity in the presence of trace-level Fe electrolyte species[81]. $Ba_{0.5}Sr_{0.5}Co_{0.8}Fe_{0.2}O_3$ undergoes surface reconstruction and transforms to OER-active Co/Fe oxyhydroxides[82]. In fact, Fe-containing (oxy)hydroxides are ubiquitous for OER-active materials including transition-metal oxides, sulfides, selenides, and phosphides[83-85].

Typically Ni-Fe and Co-Fe hydroxides adopt structures analogous to α-phase $Ni(OH)_2$ and $Co(OH)_2$, which consist of layers of $[M(OH)_6]$ octahedra with rotational disorder and water/ions intercalated into the interlayer space[86-89]. The Fe^{3+} is thought to substitute for the M^{2+} sites with the extra charge balanced by intercalated anions[90]. Prior to OER, Fe-doped α-$M(OH)_2$ is oxidized to (nominally) γ-MOOH, accompanied by a contraction of the M-O bond length and interlayer distance, consistent with stronger M-O bonds upon formal cation oxidation[91]. Fe substitution induces a positive shift of the apparent M^{2+}/M^{3+} redox potential, indicative of electronic interactions between Fe and host Ni or Co cations. The oxidation state of Fe during OER at the active site remains a point of discussion. Both Fe^{3+} and Fe^{4+} were found under OER conditions for co-deposited Ni-Fe or Co-Fe (oxy)hydroxides, while in non-aqueous electrolyte Fe^{6+} was identified and invoked as the active intermediate[92-95]. *Operando* Mössbauer spectra show the oxidation of Fe^{3+} in Ni-Fe (oxy)hydroxide to Fe^{4+} during OER and that these Fe^{4+} species largely persist after the potential was decreased into a non-OER region[96]. Such Fe^{4+} species were hypothesized to arise from fully coordinated internal sites within the NiOOH that were too kinetically slow to catalyze OER. In contrast, the detected Fe^{4+} population in a $CoFeO_x$ film from a separate Mössbauer study correlated with OER activity, suggesting a central role of Fe^{4+} in catalysis[97]. One hypothesis to explain this discrepancy would be the presence of different populations of Fe cations, for example in the interior regions of the (oxy)hydroxide sheets versus under-coordinated surface or edge Fe species.

We previously found evidence for different Fe local environments within the host (oxy)hydroxides affecting OER activity[77, 98]. When cycled, both NiO_xH_y and CoO_xH_y adsorb Fe^{3+} (intentionally added to the electrolyte) onto sites that were hypothesized to be easily accessible, i.e. at edges, corners, or defects in the two-dimensional (oxy)hydroxide structure. The Fe incorporated during the first voltammetry cycle dramatically enhanced the OER activity but had negligible influence on the host NiO_xH_y redox-peak position or size, indicating weak electronic interaction between these "surface" Fe and the majority of the Ni cations. Repeated voltammetric cycling increased the amount of Fe incorporated, up to a Fe:Ni ratio of ~ 0.25, and the Ni redox wave shifted positive indicating strong coupling between the additionally added Fe and the Ni cations. Yet this additional Fe caused only a small increase in OER activity. These data led to the hypothesis that at least two general types of Fe sites exist in the (oxy)hydroxides, *i*) OER-active surface sites from electrolyte Fe adsorption and *ii*) interior sites where Fe sits fully coordinated with bridging O(H) to neighboring M sites. Supporting this idea, $NiFeO_xH_y$ with proposed surface-attached FeOOH nanoclusters has been reported to be more OER-active than benchmark Ni-Fe catalysts[99, 100]. The above findings illustrate that structural information or activity measurements for Fe-based sites collected from co-deposited (oxy)hydroxides are the weighted average of the multiple Fe environments which have very different properties. The precise intrinsic activity on the most-active "surface" Fe, and the associated key OER mechanism, remains unknown.

Here we show how to confine the absorption of Fe to nominally surface sites where they have exceptionally high per-Fe activity yielding the catalysts Fe:NiO_xH_y and Fe:CoO_xH_y. We study how the intrinsic structural features and dynamics of NiO_xH_y and CoO_xH_y affect the incorporation. Fe added into the electrolyte during chronoamperometry under OER conditions (positive of the $Ni^{2/3+}$ redox wave) yields electrolyte-adsorbed Fe species primarily on the surface (presumably at edge/defect sites) of Ni and Co (oxy)hydroxides. In contrast, potential cycling pure NiO_xH_y in the presence of Fe^{3+}(aq.) or Co^{2+}(aq.), yields more-homogeneous Ni(Fe)O_xH_y or Ni(Co)O_xH_y phases, respectively. Similarly, we find that it is more difficult to incorporate Fe^{3+} into the interior sites of CoO_xH_y compared to NiO_xH_y, consistent with the larger Co^{2+}-O(H) bond strength compared to Ni^{2+}-O(H)[101] and higher sheet-morphology stability of CoO_xH_y[102]. With this

platform to control the location of the Fe-based active sites, we measure the intrinsic OER activity of surface Fe sites on Fe:NiO_xH_y and Fe:CoO_xH_y and compare these to activities with Fe at interior sites in NiO_xH_y. The turn-over frequency for OER, normalized to the number of Fe sites (TOF_{Fe}), increased linearly with the amount of absorbed surface added until a saturation limit, suggesting possible cooperativity of active sites, in sharp contrast to previous studies where the location of the Fe sites was uncontrolled[79]. We find an intrinsic TOF_{Fe} of ~40 s^{-1} at 350 mV for Fe:NiO_xH_y which is at least five times higher than for benchmark co-deposited phases[73]. This finding illustrates a cooperative effect between multiple Fe sites on the surface of NiO_xH_y and CoO_xH_y. Density-functional-theory (DFT) calculations suggest that this effect is derived from the ability of neighboring Fe atoms in a Fe-O-Fe cluster to share and stabilize positive charge during the oxidation of key intermediates, compared to a single FeO_x supported on NiO_xH_y. These findings are important to understand and control structure in the design of higher-performance OER catalysts from earth-abundant metals for use in advanced electrolyzers[69, 103] and photoelectrochemical systems.

Methods

Solution Preparation. Stock solutions of 0.1 M $Ni(NO_3)_2 \cdot 6H_2O$ (Sigma Aldrich, 99.999% trace metal basis) and 0.1 M $Co(NO_3)_2 \cdot 6H_2O$ (BeanTown Chemical, ≥ 99.999% trace metal basis) were separately prepared in 18.2 MΩ·cm water for the electrodeposition of NiO_xH_y and CoO_xH_y films. For the co-deposition of Ni(Fe)O_xH_y and Co(Fe)O_xH_y, $FeCl_2 \cdot 4H_2O$ (ACROS Organics, 99+%) was freshly dissolved in N_2-purged 18.2 MΩ·cm water to 0.1 M. Then 0.1 M $Ni(NO_3)_2 \cdot 6H_2O$ or $Co(NO_3)_2 \cdot 6H_2O$ was purged with N_2 for ~20 min prior to the addition of 0.1 M aq. $FeCl_2 \cdot 4H_2O$. Stock solutions of semiconductor grade 1.0 M KOH (Sigma Aldrich, 99.99% trace metal basis) and further-purified "Fe-free" 1.0 M KOH were used for electrochemical measurements. The electrolyte purification was conducted as reported previously[74]. Briefly, about 2 g of $Ni(NO_3) \cdot 6H_2O$ was dissolved in ~4 mL of 18.2 MΩ·cm water in a 50 mL centrifuge tube and high purity $Ni(OH)_2$ precipitated by rapid addition of ~20 mL of 1 M semiconductor grade KOH. The green $Ni(OH)_2$ precipitate was washed by 2 rounds of addition of a 20 mL of water/ 2 mL of 1 M KOH solution. After the final wash, the supernatant was removed by centrifugation and the tube was filled with

semiconductor grade 1 M KOH. The tube was shaken vigorously to redisperse the precipitate and allowed to sit overnight during which time the $Ni(OH)_2$ absorbs Fe impurities. All electrolyte used was pH 13.88 ± 0.06. The Fe-free KOH was recovered by centrifuging and then filtered using a 0.1 μm polyethylene sulfone (PES) syringe filter to remove residual $Ni(OH)_2$ particulates. Stock solutions of 0.1 mM $Fe(NO_3)_3 \cdot 9H_2O$ (Sigma Aldrich, ≥ 99.999% trace metal basis), 0.1 mM $Ni(NO_3)_2 \cdot 6H_2O$ (Sigma Aldrich, 99.999% trace metal basis), and 0.1 mM $Co(NO_3)_2 \cdot 6H_2O$ (BeanTown Chemical, ≥ 99.999% trace-metal basis) were separately prepared for foreign-ion "spiking" experiments. To prevent the precipitation of Fe^{3+}, the pH of the 0.1 mM aq. $Fe(NO_3)_3 \cdot 9H_2O$ solution was adjusted to ~2 with HNO_3.

Film preparation. All electrodepositions were performed with a two-electrode configuration using pre-cleaned carbon cloth as the counter electrode. Prior to deposition, a bare substrate was cycled five times in Fe-free 1.0 M KOH to verify its cleanliness and induce hydrophilicity. $Ni(Fe)O_xH_y$ was cathodically electrodeposited at -0.1 $mA \cdot cm^{-2}$ for 120 s. $Co(Fe)O_xH_y$ was electrodeposited at -2 $mA \cdot cm^{-2}$ for 8 s. The total metal-ion concentration in the electrodeposition bath was 0.1 M. For co-electrodeposited films, the Fe/Ni and Fe/Co ratios were adjusted by the Fe content in the deposition solution. Pt/Ti (50/10 nm) on glass slides, or Pt/Ti-coated quartz crystal microbalance (QCM) crystals (5 MHz, Stanford Research Systems QCM 200), were used as the substrates for electrodeposition. The deposited composition and molar amount were determined by elemental analysis (see below). The mass loading of Ni in the NiO_xH_y film was ~ 2.7 $\mu g \cdot cm^{-2}$. The mass of Co in the film of CoO_xH_y was ~5.0 $\mu g \cdot cm^{-2}$. The film mass loading and change during electrochemistry were determined by the frequency change of the QCM electrode using the Sauebrey equation ($\Delta f = -C_f \cdot \Delta m$, where Δf is the measured frequency change of quartz crystal, C_f is the sensitivity factor with a value of 56.6 Hz $cm^2 \cdot \mu g^{-1}$, and Δm is the mass change per unit area, $\mu g \cdot cm^{-2}$).

Electrochemical Characterization. Electrochemical measurements were made with a potentiostat (Bio-Logic SP300 or SP200) using a typical three-electrode setup. Different Hg/HgO reference electrodes (CH Instruments) were used for Fe-free and Fe-containing measurements. The standard electrode potential of the 1 M KOH Hg/HgO reference ($E^0_{Hg/HgO}$) was calibrated to be 0.094-0.099 V vs. NHE[104]. All recorded potentials were converted to the reversible hydrogen electrode (RHE)

scale by $E_{RHE} = E_{Hg/HgO} + E^{0}_{Hg/HgO} + 0.059 \cdot pH$, where $E_{Hg/HgO}$ is the recorded electrode potential vs. Hg/HgO. A Pt coil was used as the counter electrode and pre-cleaned by aqua regia and 18.2 MΩ·cm water. Because alkaline media etches glass leaching Fe into the electrolyte, all measurements were made using inexpensive plastic (polymethylpentene) cells. The glass section of the substrate was covered by epoxy (Loctite, EA 9460) and hot glue (a commonly available hot-melt polymer adhesive). The overpotential (η) was calculated by the equation: $\eta = E_{RHE}$ - 1.23 V - iR_u, where R_u is uncompensated series resistance. R_u was determined by equating R_u to the minimum impedance between 10 kHz and 1 MHz, where the phase angle was closest to zero[104]. The double-layer capacitance (C_{DL}) of the metal-oxyhydroxide films was determined by fitting the results of potentio-electrochemical impedance spectroscopy (PEIS) measurements in a potential region where the electrocatalyst films are conductive[105] over the frequency range of 0.1 Hz to 1 MHz. Experimental details for the XAS measurements are provided in the Supplementary Information.

Metal-ion-spiking. In CA tests, catalyst films were first polarized in purified Fe-free semiconductor-grade 1.0 M KOH electrolyte for 3-5 min. Then 715 µL of 0.1 mM metal ion aq. solution was added dropwise into the 40 mL of KOH electrolyte to reach a concentration of added metal of 0.1 ppm (wt. Fe / wt. H_2O). The low concentration of 0.1 ppm was chosen to mitigate effects of insoluble $Fe(OH)_3$ colloids or particles that form at higher Fe concentrations and obfuscate effects of the absorbed Fe species. We estimate from solubility constants[106] that the solubility of Fe^{3+} is about 35 ppb in 1 M KOH and have historically used 0.1 ppm spiking amounts with no observation of precipitation. In voltammetry studies, the catalyst films were first measured in purified Fe-free or semiconductor grade 1.0 M KOH electrolyte for 2-4 cycles to get a stable electrochemical response. Then 715 µL of 0.1 mM metal-ion solution was added dropwise into the 40 mL KOH electrolyte. Magnetic stirring was used throughout the measurement to promote transport of the added metal ions and prevent bubble accumulation. After measurements, the electrode was removed and rinsed in 18.2 MΩ·cm water.

Loading analysis and turnover frequency (TOF) calculation. Film mass loading of each element were determined by ICP-MS (iCAP-RQ Qnova Series, Thermo Fisher Scientific).

Calibration curves were prepared from third-party-certified reference solutions of the analyte of interest. Electrodes were immersed in 2 mL of 10 v/v% HNO_3 for at least 24 h to dissolve the catalyst films. The HNO_3 solution was then diluted with 2 mL 18.2 MΩ·cm water for ICP-MS analysis. To verify the full dissolution of catalysts into HNO_3 solution, the substrates were rinsed by 18.2 MΩ·cm water and cycled in Fe-free KOH. The lack of Ni or Co redox peaks and similar OER activity to bare Pt/Ti substrate indicated the full dissolution of catalyst films[104]. To compare the intrinsic activity of Fe sites in different matrices, the TOF_{Fe} based on the total mass of Fe in the film was calculated at a constant overpotential[104]:

$$\mathrm{TOF}_{Fe} = \frac{\text{current} / 4F}{(\text{mol of Fe sites})} \qquad (1)$$

where F is faraday's constant. The number of Fe sites was determined by ICP-MS. The OER current was recorded from real-time iR_u compensated chronoamperometry tests.

DFT calculations. Vienna *ab initio* Simulation Package (VASP)[107-109] was used to perform the spin-polarized density functional theory (DFT) calculations with the DFT+U formalism of Duradev et. al[107, 108, 110]. For the effective modelling of DFT+U, U-J terms of 5.5 and 4 for Ni[111-114] and Fe[115, 116] were used, respectively. All calculations were performed using the Perdew−Burke−Ernzerhof (PBE)[117] exchange-correlation functional of the generalized gradient approximation (GGA). The projected augmented wave (PAW) potentials[109, 118] include the contribution of core electrons of each atom. An energy cut-off of 600 eV with k-point mesh of 1×1×1 was used for the entire calculation in accordance with the values reported in previous work (65,66). The structures were minimized with energy and force convergence criteria of 10^{-4} eV and -0.03 eV·Å^{-1}, respectively. Gaussian smearing[119] was used with symmetry imposition for all calculations. The geometries were relaxed with a conjugate gradient algorithm.[120]

The overpotential (η) of each reaction pathway is defined as the minimum potential required to make all reaction steps exothermic. Based on the calculations of the Gibbs free energy of each reaction step, the theoretical overpotential was calculated as follows[121]:

$$\eta = \max(\Delta G_1, \Delta G_2, \Delta G_3, \Delta G_4, \Delta G_5) - V_{OER} \qquad (2)$$

where ΔG_i is reaction energies of each step and V_{OER} is the equilibrium potential of water oxidation and its reported value is 1.23 eV. The potential energies obtained from the density functional theory calculations are converted to Gibbs free energies as detailed in the Supplementary Information. The overpotential changes were analyzed in terms of changes in the atomic oxidation states of Fe and Ni of each of the reaction intermediate. The oxidation state of Ni and Fe was inferred from the atomic magnetization observed in the output file. For Ni +2, +3 and +4 oxidation states are related to two, one and no singly occupied orbitals, respectively. For Fe +2, +3, +4 and +5 oxidation states are related to four, five, four and three singly occupied orbitals, respectively. The reduction in magnetization values observed results in increase of formal oxidation state. The Gibbs free energy reported here includes the zero-point energy correction.

Results and Discussion

Mechanisms of foreign-cation incorporation into NiO_xH_y and CoO_xH_y. We define two classes of sites where foreign ions can incorporate that contribute differently to the OER activity and electrochemical response. First, there are interior "bulk" sites where the cation is substituting either Ni or Co cations. These modify the electronic energies of the redox-active host metal atoms (Ni or Co) and thus influence the peak position of the Ni or Co redox waves during voltammetry[8, 122, 123]. Second, surface sites where the cations are adsorbed onto, rather than substituted into, the host NiO_xH_y and CoO_xH_y porous structures (Figure 20) where the coordination by water and terminal hydroxyls makes them likely OER active sites[77, 98]. These seem to have little effect on redo- wave position, but generate most of the catalytic enhancement. To study these different sites, hydrated, electrolyte-permeable NiO_xH_y and CoO_xH_y films were cathodically electrodeposited on Pt/Ti/glass substrates. Pt was used because it is OER inactive and has limited electronic interaction with any *in-situ* formed FeO_xH_y when Fe species are present in the electrolyte[124]. The porosity and thinness of the films ensured that almost all metal cations in the film are

electrochemically active as confirmed by electrochemical microbalance studies[73, 104]. SEM images of a representative NiO_xH_y film (Figure 32) illustrate the porosity and roughness of the film and cross sections (Figure 33) suggest a thickness between 5-20 nm.

We use the redox response of Ni and Co cations to gain insight into the incorporation of foreign metal species from the electrolyte. Directly tracking the different Fe sites using electrochemistry is not possible as they do not provide a useful redox signature[125]; Fe^{3+} oxidation occurs at potentials within the OER regime and Fe^{3+} reduction occurs at potentials where the NiO_xH_y and CoO_xH_y host are electrically insulating. We expect that when foreign cations adsorb on the host they should provide a distinct wave separate from that of the host (if they are redox active), while when incorporated substitutionally in interior sites they will exert an electronic affect manifesting as a shift of the host redox-wave potential.

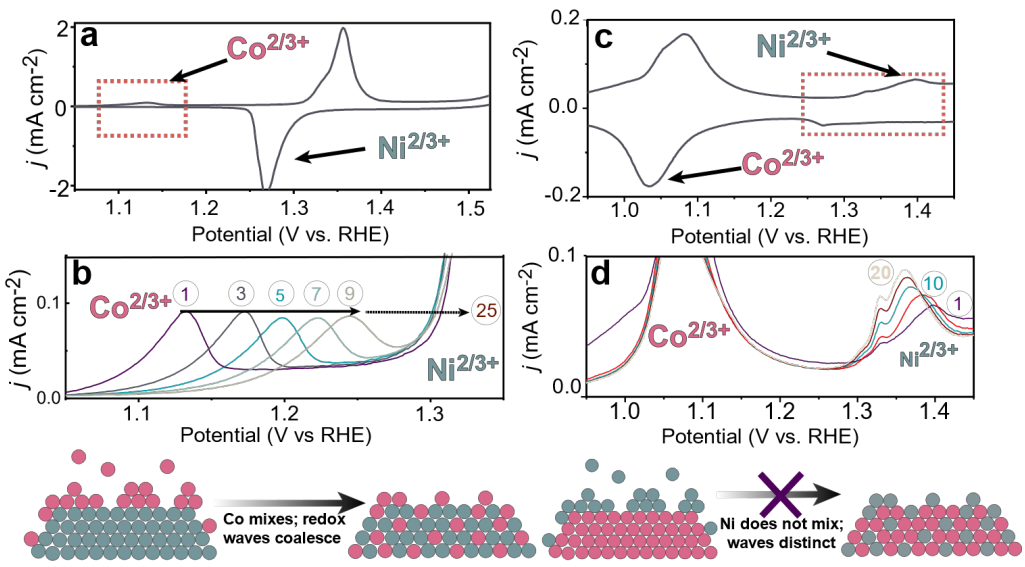

Figure 2. Foreign cations interaction with oxyhydroxides via redox signatures.

Cyclic voltammetry of Co-spiked NiO_xH_y **(a,b)** and of Ni-spiked CoO_xH_y **(c,d)** showing the evolution of redox features of the host metal hydroxide and phase formed by spiked ions. Inset numbers in **(b)** and **(d)** correspond to the cycle number, while the bottom cartoon illustrates schematically the process intentionally without atomic detail that is yet unknown. The data above was not iR_u-compensated.

When 0.1 ppm Co^{2+} is added into the electrolyte during constant-potential polarization of NiO_xH_y we observed a new redox feature centered at 1.13 V vs. RHE (Figure 2a), ~50 mV positive of the same wave for as-deposited CoO_xH_y on Pt, which is thus assigned to $Co(OH)_2$/CoOOH. During the CA, the OER current increased by a factor of five after Co^{2+} was added (Figure 24a), consisting with CoO_xH_y, which is more OER active[122], absorbing on the NiO_xH_y.

With subsequent voltammetry cycles (Figure 2b), the CoO_xH_y wave shifts to higher potential, and the host NiO_xH_y wave broadened (Figure 24). After 10 cycles the $Ni(OH)_2$/NiOOH redox peaks also shifted negative by 11 mV (Figure 27a). By 25 cycles, the characteristic CoO_xH_y redox peaks have moved positive in potential and coalesced (Figure 2b) with that of NiO_xH_y. The loss of the independent CoO_xH_y redox peaks and the negative shift of the NiO_xH_y is consistent with the Co cations which were initially adsorbed in a phase separate from the host NiO_xH_y to disperse into the NiO_xH_y. The negative shift of the Ni redox wave with Co^{2+} incorporation is similar to that observed for co-deposited $Ni(Co)O_xH_y$ films and indicates strong electronic coupling between dopant Co and host Ni sites[126, 127]. By analogy, similar processes are proposed when NiO_xH_y is cycled in the presence of solution Fe cations that have no apparent redox signature.

In contrast to NiO_xH_y, cycling CoO_xH_y in Ni^{2+}-spiked KOH yields a wave centered at ~1.32 V vs. RHE (Figure 2c), typical for the $Ni(OH)_2$/NiOOH couple. The OER current during CA for CoO_xH_y is unaffected by spiking Ni^{2+} into the electrolyte (Figure 26a), consistent with NiO_xH_y being less OER-active than CoO_xH_y[122]. The new $Ni(OH)_2$/NiOOH wave that appears persists after cycling with only a slight negative shift of the peak potential (Figure 2d), while the $Co(OH)_2$/CoOOH wave position is unaffected (Figure 27b). The lack of electronic interaction between foreign Ni cations on the CoO_xH_y host redox is consistent with Ni cations that persistently reside on the surface of CoO_xH_y as a separate NiO_xH_y phase despite cycling. The inability of CoO_xH_y to easily incorporate foreign cations, relative to NiO_xH_y, is consistent with its greater structural stability[128] and its stronger Co-O(H) bonds relative to Ni-O(H)[129, 130]. Because the procedures used in these Co- and Ni-spiking experiments are identical to those used for Fe spiking in activity measurements below, we propose that Fe^{3+}(aq.) adsorbs in a phase distinct from CoO_xH_y

and remains as such after cycling, but that Fe^{3+} incorporates into the internal sites when the host NiO_xH_y is electrochemically cycled. Evidence for separate phase formation by adsorbed electrolyte ions using this method has not before been previously demonstrated and is critical to understanding the origin of exceptional TOF_{Fe} described below.

The different locations of the foreign cations, in or on, NiO_xH_y and CoO_xH_y films appear driven by structural changes during voltammetry. Using an electrochemical quartz crystal microbalance (EQCM), the mass change of NiO_xH_y and CoO_xH_y films upon cycling was monitored during voltammetry (Figure 21). During the positive oxidative scan of NiO_xH_y, the film mass increases at the potential where $Ni(OH)_2$ oxidation is measured and continues into the OER region. The mass increase in the forward scan is ~ 0.33 μg $\cdot cm^{-2,}$ accounting for ~4.5% of total film mass (4.2 ± 0.2 g per mole e^- passed). Mass loss is observed in the backward scan, particularly with the reduction of Ni species (~0.33 V vs. Hg/HgO). At the end of the cycle, the film mass returns to its initial value. For CoO_xH_y, a slight and irreversible mass gain (~0.2% of total film mass) is observed after the second voltammetry cycle, but no detectable mass change accompanies the oxidation of $Co(OH)_2$.

The mass gain with oxidation of Ni^{2+} is thought to originate from K^+ and OH^- intercalation along with release of H_2O in the interlayer space of NiO_xH_y[131-133]. Oxidation also causes contraction of the Ni-O bond and interlayer spacing, which introduces mechanical stress[91, 133]. Restructuring of $Ni(OH)_2$ single-layer nanosheets into small nanoparticles was found by electrochemical atomic force microscopy (EC-AFM) suggesting that $Ni(OH)_2$ undergoes a dissolution-redeposition process during cycling[128, 134]. When Fe or other cations exist in the electrolyte, these cations can exchange for Ni leading to atomic-level mixing with the host Ni. In contrast, the voltammetry of CoO_xH_y does not involve obvious molecule/ion exchange based on EQCM and EC-AFM measurements and shows structural stability compared to NiO_xH_y[128], apparently making it difficult to incorporate foreign cations from the electrolyte into the structure interior.

Confining Fe cations on the surface of NiO_xH_y and CoO_xH_y. Using the insights from the Ni- and Co-spiking experiments, we add Fe^{3+} during chronoamperometry to prepare Fe:NiO_xH_y and Fe:CoO_xH_y OER catalyst where Fe is surface-adsorbed. First, we applied ~1.55 V vs. RHE to NiO_xH_y (nominally NiOOH at this potential) in Fe-free 1.0 M

KOH for 3-5 min and recorded the (low) baseline OER activity. Then Fe^{3+} was added to a reach a concentration of 0.1 ppm (this low amount of Fe was selected to prevent bulk electrodeposition of nominally FeOOH we observed previously by electrochemical AFM at > 1 ppm[51]). A dramatic increase in OER current was immediately observed reaching a maximum after ~15 min, suggesting the fast adsorption of Fe species on NiOOH, likely limited by mass transport of Fe species to the electrode. The incorporation of foreign cations at *fixed* potentials in the OER regime, and positive of the nominal $Ni^{2+/3+}$ redox wave, is important to limit the amount of host restructuring and associated intermixing that is driven by the redox transitions[128, 134].

After ~15 min the OER current reaches a stable maximum ~90× that of Fe-free NiOOH (without *iR* compensation) and ICP-MS analysis of the catalyst film shows ~5 at. % Fe (relative to Ni). The same measurements were performed with CoO_xH_y and the OER activity in Fe-free KOH was higher than NiO_xH_y, consistent with our previous reports[122]. Adding 0.1 ppm Fe^{3+} in the electrolyte resulted in a ~7-fold increase in OER current (Figure 3c), a much smaller enhancement than for Fe:NiO_xH_y. The observed activity difference between Fe:NiO_xH_y and Fe:CoO_xH_y likely derives from different intrinsic activities of surface Fe on the two chemically different hosts (see below).

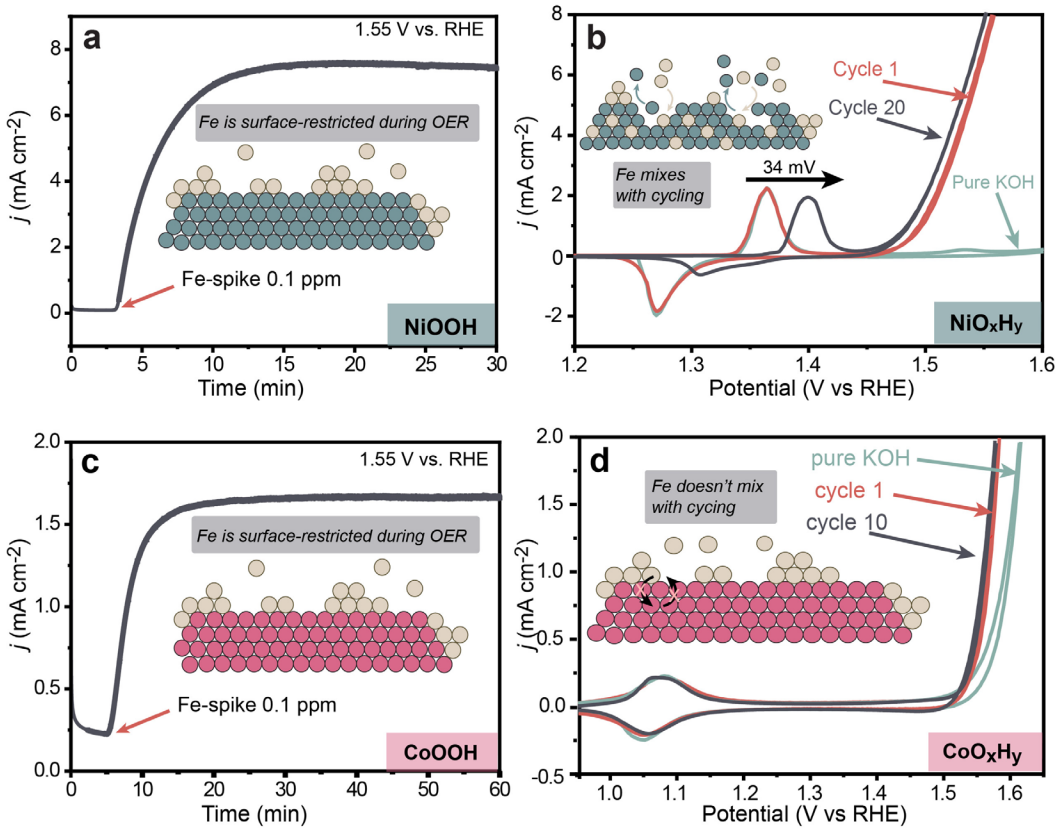

Figure 3. Surface-confined Fe sites via chronoamperometric (CA) metal-ion-spiking.
CA measurements of (**a**) NiOOH and (**c**) CoOOH at 1.55 V vs. RHE. After starting the measurement in purified Fe-free 1.0 M KOH electrolyte, aqueous $Fe(NO_3)_3$ was added to a concentration of 0.1 ppm. The first voltammetry cycle (red, 10 mV/s) after Fe-spiking CA measurements shows the dramatic effect of Fe incorporation on the OER activities of NiO_xH_y (**b**) and CoO_xH_y (**d**), but a minimal effect on the redox wave compared to the light green lines that show the initial voltammetry (cycle two) recorded in purified Fe-free 1.0 M KOH. The grey curves illustrate the large effect on the redox wave position for NiO_xH_y but not for CoO_xH_y after cycling, but that the OER activity doesn't further change much. The data is not iR_u compensated. The cartoons illustrate schematically the process intentionally without atomic detail that is yet unknown.

The first voltammetry cycle of Fe:NiO_xH_y after chronoamperometric (CA) Fe incorporation shows nearly identical redox response as Fe-free NiO_xH_y (Figure 3b), despite having dramatically enhanced OER activity. This implies that the Fe incorporated during CA is not yet electronically interacting with the majority of the host Ni metals. The Fe:NiO_xH_y was then cycled 20 times in the Fe-spiked KOH (Figure 3b, blue). The Ni wave shifts positively by 34 mV and the integrated peak area shrinks as the Fe incorporates into the oxyhydroxide structure to form Ni(Fe)O_xH_y (that also contains surface-absorbed Fe) with no change in OER activity. The positive shift of the NiO_xH_y wave is known to occur

upon mixing with Fe by co-deposition[74]. This data implies an intrinsic activity difference for surface and internal Fe-based sites. Similarly, the first CV cycle of Fe:CoO_xH_y after CA-spiking test shows almost the same redox peak position and area compared to CoO_xH_y, despite the enhanced OER activity (Figure 3d). Subsequent voltammetry on Fe:CoO_xH_y only slightly decreases the OER overpotential, with the redox waves almost unchanged. Bare Pt and Au substrates also absorb Fe increasing OER activity[124], but the Fe-spiked electrolyte barely affected the activity of control Pt electrodes under CA conditions here (Figure 23). Thus the enhanced activity observed for NiO_xH_y or CoO_xH_y loaded on Pt is derived from Ni(Fe)O_xH_y or Co(Fe)O_xH_y, with the Fe-based active sites proposed to be all absorbed on the "surface" of the host oxyhydroxide.

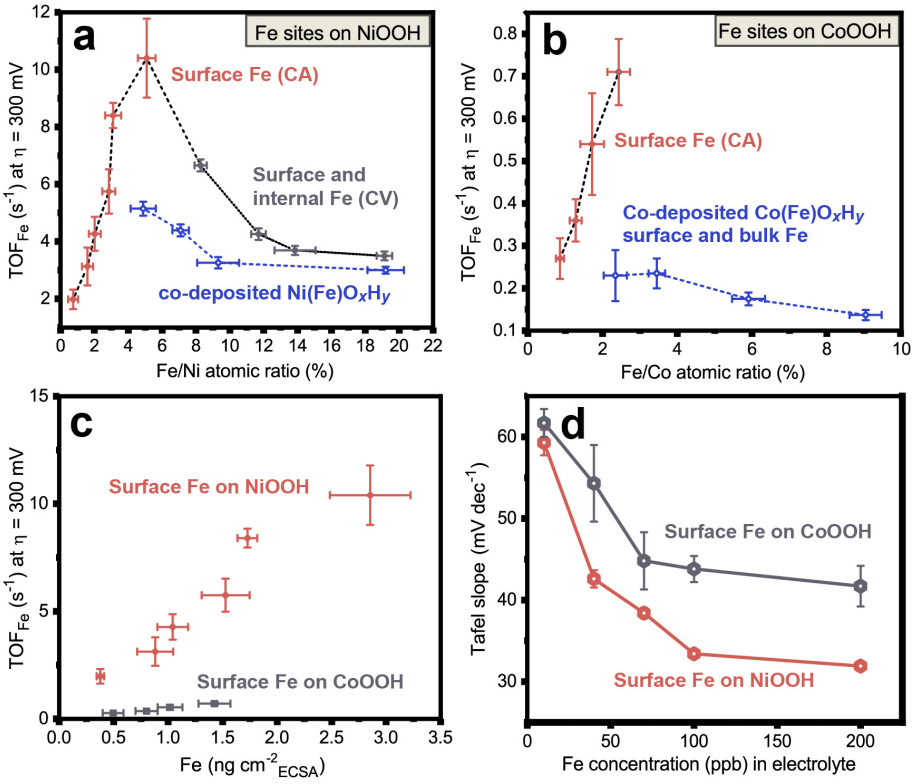

Figure 4. Intrinsic OER activity measured by turnover frequency (TOF_{Fe}) at η = 300 mV.
The TOF_{Fe} is calculated based on the mass of all Fe sites determined by ICP-MS of each dissolved film. (**a**) Correlation between TOF_{Fe} and Fe/Ni atomic ratio for surface-confined Fe generated by CA, as well as mixed systems from cycling or co-deposition. (**b**) Correlation between TOF_{Fe} and Fe/Co atomic ratio. (**c**) Correlation between the TOF_{Fe} of surface-Fe sites on NiOOH (red) and CoOOH (grey) and the adsorbed Fe mass loading normalized by the electrochemical surface area of host oxyhydroxide. (**d**) Tafel slopes of Fe:NiO_xH_y (red) and Fe:CoO_xH_y (grey) as a function of Fe concentration (10, 40, 70, 100, and 200 ppb) in 1.0 M KOH electrolyte. Tafel analysis was performed using constant current steps from 0.18 to 3.2 mA·cm^{-2}, with each step held for 3 min. The steps were then repeated in reverse order. Before Tafel analysis, constant potential OER in Fe-spiked electrolyte was performed until the maximum OER current was reached. All current values

used for TOF_{Fe} concentrations were iR_u-compensated where R_u was in the range 15.1 ± 0.5 Ohms. Error bars represent one standard deviation from the average of triplicate measurements

Intrinsic activity of Fe sites on metal (oxy)hydroxides. The OER turnover frequency (TOF) is defined as the total number of O_2 molecules generated per active site, per unit time[104]. One important fundamental challenge is the identification and quantification of the true active sites to enable catalyst design. TOF for OER for these systems can be calculated in several ways[104]. The simplest is to use the total number of cations in the film (regardless of their location and chemistry, including Ni, Fe, Co, etc.) to calculate TOF_{tm} which thus provides the average activity at all metal sites, simplifying the reality of many sites with a range of activities.

We calculate a TOF based on the total number of Fe cations (TOF_{Fe}), including both the interior and surface sites discussed here, as Fe is essential at the active site[135-137]. Our results show that Fe incorporates at surface sites at constant OER potentials and mixes into the interior only after cycling. The number of surface-adsorbed Fe sites can be controlled by stopping the CA experiment at different times while Fe is accumulating on the NiO_xH_y or CoO_xH_y, thus providing the first known route to create and study specific types of Fe sites in these important materials.

Figure 4a shows the TOF_{Fe} values at η = 300 mV (iR_u corrected) for Fe:NiOOH and Ni(Fe)OOH. For Fe:NiOOH, TOF_{Fe} increases nearly linearly with the amount of Fe absorbed. Initially the sample is ~0.7 at.% Fe on NiO_xH_y and the TOF_{Fe} is 2.0 ± 0.3 s^{-1}. The TOF_{Fe} increases until maximum Fe adsorption and OER current at 5.1 at.% Fe on NiO_xH_y and the incredibly high TOF_{Fe} of 10.4 ± 1.4 s^{-1} at η = 300 mV. This data shows that each Fe-based-site becomes more OER active as surface-absorbed Fe sites accumulate.

After reaching a maximum OER current at constant potential in Fe-spiked KOH, the resulting Fe:NiO_xH_y was cycled (Figure 28) resulting in the absorption of additional Fe, including at internal sites, and thus a large decrease in TOF_{Fe} as Fe increases to ~ 20 at. % (Figure 4a). These data are consistent with the hypothesis that the absorbed Fe at surface sites drives OER, while internal Fe sites are comparatively inactive. We also prepared mixed Ni(Fe)O_xH_y via co-electrodeposition, for which Fe is homogeneously substituted for Ni. TOF_{Fe} values for these co-deposited samples decrease with Fe content

and are substantially smaller than those obtained from Fe spiking, consistent with an activity difference between surface and internal Fe sites. TOF_{Fe} at η = 350 mV shows similar trends (Figure 38). The highest TOF_{Fe} of ca. 40 ± 2 s^{-1} at η = 350 mV is obtained at the maximum surface adsorption. Previous studies show that the co-deposited optimal $Ni_{0.75}Fe_{0.25}O_xH_y$ has a TOF_{Fe} of ca. 9 s^{-1} at η = 350 mV[122]. On a TOF_{Fe} basis, the Fe:NiO_xH_y reported here has the highest activity among all alkaline OER catalysts[138].

The surface Fe sites also become more OER active with increasing number on the surface of CoO_xH_y (Figure 4b). At maximum adsorption, ~2.4% Fe is adsorbed on CoO_xH_y and the highest TOF_{Fe} at η = 300 mV is 0.71 ± 0.08 s^{-1}. This value is smaller than the TOF_{Fe} in Fe:NiO_xH_y with similar absorbed surface Fe amount (~5 s^{-1} at η = 300 mV with ~2.5% Fe) showing a large intrinsic activity difference between Fe sites on CoO_xH_y versus NiO_xH_y. The TOF_{Fe} of co-electrodeposited Co(Fe)O_xH_y is, like the Ni system, also smaller than that of the surface Fe sites on CoO_xH_y and decreases with Fe content (due to a larger fraction of less-active internal Fe sites). Because NiO_xH_y and CoO_xH_y films have different mass loading and electrochemically active surface area (ECSA), the TOF_{Fe} values are shown as a function mass of adsorbed Fe (from ICPMS) normalized to geometric surface area and ECSA (Figure 38 c-d).

In contrast to our results, Chung and Markovic et al. observed a linear relationship between OER activity and the amount of absorbed Fe on several transition-metal (oxy)hydroxides including NiO_xH_y, CoO_xH_y, Ni(Cu)O_xH_y, and Ni(Mn)O_xH_y by incorporation of Fe from electrolyte. This data was used to argue that each Fe site has similar activity and thus the improvement of OER catalysis mainly relies on increasing the number of Fe sites by increasing the absorption energy of the Fe on the host[79]. The difference between our work and this study is that the nature of the Fe sites was not previously controlled. The higher Fe at. % of > 18% from their experiments indicate that Fe was not restricted to edge and defect sites and thus the number of active surface sites, versus fully coordinated interior ones, was unknown and uncontrolled and so the intrinsic activity of the two could not be separated nor cooperative effects between Fe sites discovered.

The above TOF_{Fe} calculations demonstrate that the intrinsic OER activity of Fe sites is dependent on the local configuration: *i*) surface Fe sites have much higher OER activity than bulk sites, *ii*) the intrinsic activity of surface Fe sites is affected by the interface with the host material, as exemplified by the difference in TOF_{Fe} on NiO_xH_y and CoO_xH_y at a fixed Fe loading, and *iii*) the surface Fe sites show increasing activity on a per-site basis with the extent of surface Fe accumulation.

The emergence of surface-absorbed-Fe-site cooperativity can be explained simply. As more Fe is adsorbed, for example, the likelihood of two or more Fe sites being located adjacent to each other increases. This may create overall a catalytic site with favorable electronics for adsorbate formation and evolution (i.e. to be neither too strong nor too weak via the Sabatier Principle). There is precedent in the literature for clusters of different sizes to display different catalytic activity. For example, smaller clusters of CoO_x were found to be more active for OER per Co site[139] and size-dependent catalysis by metal clusters is a well-known phenomenon which, in general, arises from optimal electronic structure, and hence absorption energies, at a particular size.[140, 141] This, however, is but one possible explanation for the data, and other mechanisms invoking interfacial Ni-FeO_x cooperation[142] could also be at play, especially considering that the intrinsic activity of Fe:NiO_xH_y is greater than that of Fe:CoO_xH_y at a comparable Fe loading. Related catalyst/support-type interactions of this kind are known for FeO_xH_y thin films on Au substrates whose activity is much higher than when they are deposited on Pt[125].

Electrokinetic analysis of cooperative Fe sites. The Tafel slopes of Fe:NiO_xH_y and Fe:CoO_xH_y decrease with increased Fe concentration in the electrolyte (Figure 4d), which suggests Fe-absorption process that modulates OER mechanism and not just number of active sites[76, 79]. At low Fe concentration of 10 ppb, surface-Fe Fe:NiO_xH_y and Fe:CoO_xH_y have Tafel slopes of ~59 and ~62 mV dec^{-1} respectively, suggesting a similar OER mechanism when small amounts of Fe are adsorbed, perhaps as isolated sites. Tafel slopes of ~33 and 32 mV dec^{-1} are obtained with 100 and 200 ppb Fe^{3+} in the electrolyte (after the CA experiment until the maximum OER current results), like co-deposited $Ni_{0.75}Fe_{0.25}O_xH_y$. This result suggests that a similar mechanism is operative, likely due to the presence of cooperative surface Fe as the competent catalyst species in both. In

comparison, (surface-Fe) Fe:CoO_xH_y has Tafel slopes of ~44 and 42 mV dec^{-1} with 100 and 200 ppb Fe^{3+} in the electrolyte, slightly higher than those for co-electrodeposited $Co_{1-x}Fe_xO_xH_y$ (x = 0.33~0.79 and Tafel slopes of 26~39 mV dec^{-1}) films[73]. In both Fe-free and 100-ppb-Fe electrolyte, Tafel slopes of Fe:NiOOH increase as a function of cycling (Figure 49) with the increase faster for the Fe-free electrolyte, consistent with both the desorption of surface Fe into the electrolyte for the Fe-free case, and scrambling of the surface Fe with internal sites in the Fe-spiked electrolyte upon potential cycling. Further detailed electrokinetic analysis on a broader set of materials derived from these methods would be useful to understand how the proposed Fe-based local structures control apparent reaction pathways[143].

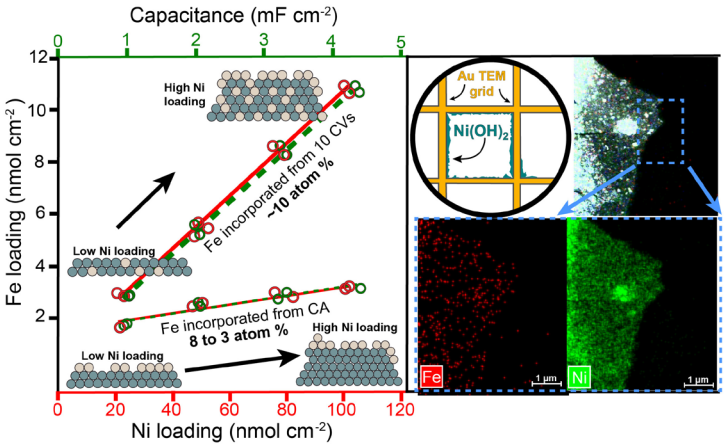

Figure 5. Fe versus Ni loading and TEM of Fe sites.
Plot (left panel) of the change in Fe loading by incorporation during CA and with CA plus 10 subsequent CV cycles versus the total Ni mass loading and film capacitance. All elemental data was obtained with ICP-MS measurement of the dissolved films. The inset depicts how the mol or at % changed for each Fe incorporation technique from the lowest to highest Ni loading. While Fe incorporates at roughly constant mol % when the Ni and Fe species are allowed to mix by CV, the mol % of Fe incorporated by CA decreases substantially as the Ni loading is increased. The right panel TEM-EDX images of NiO_xH_y electrodeposited directly onto a gold TEM grid after Fe was adsorbed during chronoamperometry at 1.55 V vs RHE. While we observe localized Fe signal, it is not possible with this technique to distinguish between the surface absorbed and internal/bulk sites nor to quantify accurately the size of the Fe clusters.

Structural characterization. TEM with EDX mapping reveals the proposed Fe-oxo clusters must be small (Figure 5 and 34), likely of molecular dimensions, and consistent with electrochemical and ICP-MS data. Still, EDX is limited when low concentrations are being measured. We thus also quantified the amount of Fe incorporated in NiO_xH_y during CA in 0.1 ppm Fe as a function of NiO_xH_y mass loading (Figure 4) using ICP-MS to understand how Fe is incorporated. Both the integrated charge in the Ni redox

wave and the double-layer capacitance (C_{DL}, measured in the oxidized state) of the films increased linearly with mass, showing the films are electrolyte-permeable and fully electron-accessible. The amount of Fe, ~10 at. %, incorporated by 10 voltammetry cycles was constant with mass loading up to the maximum loading studied of ~100 nmol·cm^{-2} Ni, consistent with cycling incorporating Fe throughout the NiO_xH_y. In contrast, the amount of incorporated Fe from constant-potential CA decreases from ~ 8 at. % to 3 at. % as the Ni loading is increased from 20 to 100 nmol·cm^{-2}. This is consistent with FeO_x primarily absorbing on edge or defect sites. As NiO_xH_y loading is increased, both new nanosheets form and existing nanosheets grow, thus decreasing the amount of edge-site-area per mass. Pair-distribution-analysis (PDF) also shows the size of coherent-scattering $Ni(Fe)O_xH_y$ domains increases with mass loading[144]. From the previous PDF data, we estimate that if all the edges of each coherently scattering domain, containing roughly 100-200 Ni cations, were decorated with single row of absorbed FeO_x, this would correspond roughly 20 at. % Fe. The 3-8 at. % observed here indicates that absorption of Fe is not uniform along all edges and that all the edges are not covered.

We next investigated the local structure of Fe adsorbed during CA on NiO_xH_y using *operando* XAS. The Fe^{3+} spiking experiments and EDX analysis suggest Fe species adsorbed during CA are at surface sites as low-nuclearity clusters of FeO_xH_y, which grow with time under positive polarization in the Fe-spiked solution. If so, we expect the Fe-O bond lengths of these species to more-resemble Fe oxyhydroxide and that subsequent cyclic voltammetry would lead to a contraction of the Fe-O bond due to incorporation into the NiOOH host (which has a shorter M-O bond length). This reasoning is based on the XAS measurements on co-deposited $NiFeO_xH_y$ by Bell and coworkers[91] where the Fe-O bond length measured under OER conditions had values that increased with the amount of Fe in the $NiFeO_xH_y$ with the pure FeO_xH_y having the longest bonds. XAS measurements at the Fe K-edge were performed during polarization at 0.68 V vs Hg/HgO immediately after spiking with CA and again after cycling (Figure 44). The current increased immediately after Fe spiking and again after cycling (Figure 43) though these could not be normalized to the amount of Fe incorporated in this experiment. The similarity of the shape and position of the XANES edges of our sample and Fe_2O_3 corroborates that Fe is predominantly in a 3+ oxidation state (Figure 45); minor differences in shape may arise

from difference in crystal structure. From the EXAFS data fitting (Figure 46 and Table 1), we find that before cycling the Fe-O bond length was 1.953 ± 0.004 Å and after cycling it contracted to 1.939 ± 0.011 Å; consistent with the hypothesis of Fe moving from Fe-rich surface absorbed structures to internal sites. The determined coordination numbers (CN) of the first and second shell of near 5 for later stages of Fe adsorption are consistent with an Fe-oxo cluster of a molecular dimensions larger than a dimer adsorbed on the surface (CN 3) but smaller than an extended crystal (CN 6), for which also further Fe-M shells should have been resolved. The error bounds on the EXAFS data, however, precludes a definitive conclusion from this XAS data alone, and further study with XAS and complementary *operando* techniques is needed to elucidate in detail the nature of the cooperative Fe sites formed by adsorption under OER conditions.

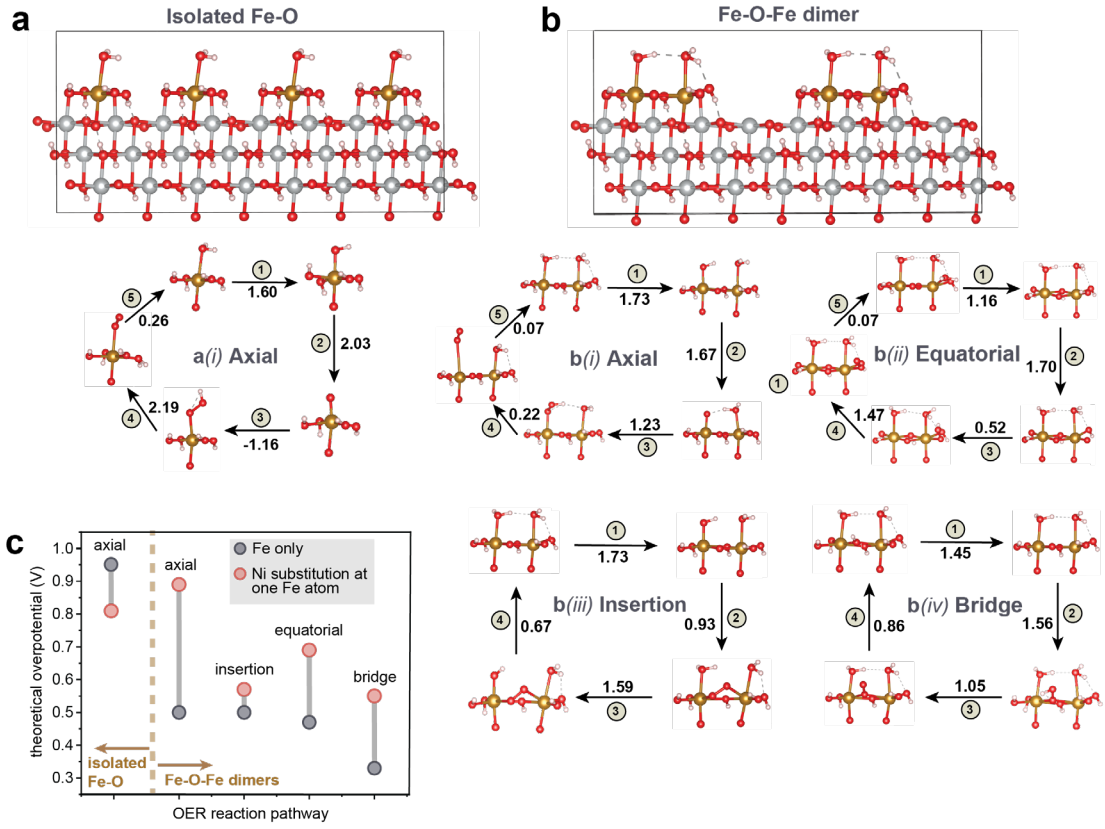

Figure 6. Computational models and OER mechanisms for Fe sites on NiOOH.
(a,b) Schematic of adsorbed active sites on the NiOOH ($0\bar{1}5$) surface: **(a)** the isolated "Fe-O" case and **(b)** dimer "Fe-O-Fe" case, along with the mechanisms chosen for investigation. Values along the reaction pathways are the theoretical overpotential in units of eV for each step. **(c)** Summary of the total theoretical overpotentials for each depicted pathway including the effect on the overpotential of a single Ni substitution

at an Fe in the isolated Fe-O monomer or Fe-O-Fe dimer. Models are shown at larger scale in Supplementary Figure 52.

Understanding OER Mechanisms via DFT calculations. To test how Fe cooperative interactions affect the OER mechanism and overpotential we built two model systems: *i*) Fe cations separated and each coordinated by four hydroxides, one water, and one oxo bonded to the surface Ni denoted as "isolated Fe-O" species (Fig. 6a, top, note there are no Fe-O-Fe linkages), and *ii*) two adsorbed Fe cations directly bonded by a bridge oxygen ligand as a "Fe-O-Fe dimer" (Fig. 6b, top). These two models simulate cooperation of neighboring surface-absorbed Fe-O species as a model active site, which may also be found on larger clusters. The structure of the adsorbed clusters at different view angles are shown in Figure 51. To build the surface, the bulk NiOOH structure was cleaved at the $0\bar{1}5$ plane due to its known activity[145-149]. The $0\bar{1}5$-oriented unit cell is then multiplied in 2×1×1 direction to have Fe concentration of 9%, similar to the experimental values for maximum TOF_{Fe}. The bottom part of Figure 6 shows elementary reactions steps and energy changes (eV) in the various mechanisms considered for the Fe-O and Fe-O-Fe modified surfaces. The theoretical overpotential (η_{th}) is defined as the voltage needed for all the reactions steps to have negative Gibbs free energies and are summarized in Figure 6c and Supplementary Table 3.

Water oxidation at the axially coordinated water (*axial* pathway) is the common mechanism for both Fe-O-Fe dimers and isolated Fe-O species. Based on the calculated ΔG for each step in the *axial* mechanism (Table 7), the Fe-O-Fe dimer has a η_{th} of 0.50 V, while for isolated Fe-O it is 0.96 V. Critically, both the Fe cations in the Fe-O-Fe dimer change their oxidation state from 3 to 4 during the step with the largest ΔG (Table 6), while for the isolated Fe-O only the Fe cation at the active site changes its oxidation state. To test whether the lower overpotential requires specifically two adjacent absorbed Fe cations, one of the Fe was replaced with Ni. In the Fe-O-Ni dimer, Fe changes its formal oxidation state from 4 to 5 while the Ni oxidation state is unchanged, yielding η_{th} = 0.89 V. For the isolated Fe-O species, Ni substitution at one of the Fe atoms reduces η_{th} only from 0.96 V to 0.80 V. To check whether the lowered overpotential upon Fe dimerization is facet

specific, the (001) surface of NiOOH (0Figure 50) was also modeled[150]. Like the $(0\bar{1}5)$ surface, the Fe-O-Fe dimer on the (001) surface has roughly half the η_{th} compared to the isolated Fe-O. The oxidation-state changes are similar as well with both Fe^{3+} cations in the Fe-O-Fe dimer oxidized to Fe^{4+} during the potential-determining step. In general, the investigation of the *axial* pathway for both types of surfaces showed that isolated monomers tend to have higher OER overpotentials than dimers (when all surface-attached group atoms are Fe), in agreement with experimental TOF_{Fe} trends. Beyond dimers, larger surface Fe-oxo clusters, as compatible with EXAFS analysis, may further stabilize the potential-determining intermediate by spreading oxidative charge over multiple Fe sites. We note that the actual experimental system likely includes various more-complex surface geometries with more absorbed Fe cations than the simple dimer considered in the calculation.

For the Fe-O-Fe dimer on the $0\bar{1}5$ surface other possible mechanisms were also investigated (Figure 6b). The *axial* and *equatorial* pathways proceed through the same intermediates except that they take place at two different positions; both have similar η_{th} of 0.50 and 0.47 V and in both cases the Fe oxidation state changes from 3 to 4. The *equatorial* pathway on the isolated Fe-O was also assessed and found impractical due to the instability of the water-coordinated structure. The *insertion* pathway shares the same first step that has the largest free-energy change with the *axial* pathway and thus both mechanisms have similar η_{th}. The key feature of the *bridge* mechanism that sets it apart from the others is that the bridge oxo group attached to two Fe and one Ni. When the bridging oxo group is deprotonated, all of these surrounding metal atoms are oxidized; the two Fe and one Ni increase their oxidation state from +3 to +4 (Table 7). Consequently, the *bridge* mechanism exhibits the lowest overpotential of all mechanisms studied for the Fe-O-Fe dimers with η_{th} of 0.33 eV.

Conclusion

We studied the incorporation and OER-activation by foreign electrolyte ions into electrodeposited NiO_xH_y and CoO_xH_y films and discovered that under controlled oxidative conditions the incorporation can be limited to surface sites. In the case of Fe on NiO_xH_y,

we used this approach to demonstrate both record intrinsic OER activity (at optimal surface-Fe loading), and a fundamental picture emphasizing cooperative effects between multiple Fe sites that share oxidative charge. The computational calculations show that new low overpotential pathways for OER are possible through synergistic interaction of Fe multiple Fe species and host metal atoms whereby oxidative charge can be favorably delocalized and stabilized. The substitution of one Fe by Ni in a model dimer increases the overpotential from 0.33 to 0.55 eV, likely because only one of the three atoms changes its oxidation state, implying that Fe-O-Fe motifs play a key role in charge delocalization. A similar investigation, but for a cobalt host could explain the discrepancy between TOF_{Fe} of Fe:NiO_xH_y and Fe:CoO_xH_y at fixed Fe loading, namely, Co may not be as effective at sharing oxidative charge with surface Fe-O-Fe. This insight was accomplished through careful electrochemical and analytical techniques—in large part the tools of material characterization (SEM/TEM/XAS) fail to provide these insights because of the disordered nature of the NiO_xH_y support and low Fe loadings associated with the record-TOF_{Fe} surface FeO_x species.

This work thus provides insight into the exceptional OER activity of Fe-based mixed-metal oxyhydroxide catalysts from which design principles emerge that are important for advanced alkaline water electrolyzers (operating in hot concentrated basic electrolyte), alkaline membrane electrolyzers (that use a solid-ionomer electrolyte and pure water or dilute soluble electrolyte salts), and for broad classes of photoelectrochemical systems. Maximal OER activity is not only a function of the Fe content in NiO_xH_y and CoO_xH_y[79], but also exactly where that Fe is located and how it interacts. Because the Fe sites are dynamic, depositing from electrolyte but also simultaneously dissolving[76-79], advanced electrolyzers should engineer the electrolyte "impurity" levels and/or the local dissolution/re-deposition environment such that the highest-activity cooperative Fe sites can be continually maintained during operation. These sites should be optimally supported on NiO_xH_y-based oxyhydroxides surfaces that provide electrical interconnection and nanostructure, but for operational stability and during, e.g., potential changes with on/off cycles, structurally more-robust CoO_xH_y (or other oxides) can be alloyed[151] with the host NiO_xH_y and supported on stable porous-transport layers.

In the next chapter, the method of CA Fe-spiking to selectively make surface Fe sites is leveraged for temperature-dependent kinetic measurements yielding parameters which describe the activation barriers for the rate-determining step in the OER mechanism on this high activity sites.

III. TEMPERATURE-DEPENDENT KINETICS OF REACTIVE SURFACE FE SITES ON NICKEL OXYHYDROXIDE

Liam P. Twight, Shannon W. Boettcher

This chapter contains unpublished work which has been prepared for submission to *Journal of the American Chemical Society* in 2024. The study was conceived and designed by **L.P.T** and S.W.B. S.W.B oversaw the project. All experimental design, measurement, and data analysis was performed by **L.P.T.** The manuscript was written by **L.P.T** with editorial assistance from S.W.B.

Introduction

Nickel-iron hydroxides ($Ni_zFe_{1-z}O_xH_y$) are the highest intrinsically active alkaline OER catalysts identified by three-electrode measurements[49, 152]. Comparison between the OER activity of NiO_xH_y in electrolyte rigorously purified of iron and in electrolyte with intentionally added Fe (100 ppb) have shown that iron incorporation into the oxyhydroxide host is essential and without which the record-low reductions in the OER kinetic overpotential of OER are not observed[58]. Yet, understanding the mechanistic details which enable this high activity is far from trivial because Fe sites are dynamic - they actively dissolve and redeposit during OER[79], the nickel hydroxide host exhibits potential-dependent structures[133, 153] that change the local chemical environment of adsorbed Fe

sites[66], and $Ni_zFe_{1-z}O_xH_y$ appears to form ubiquitously *in-situ* on the surface of crystalline solids like NiO[152], $LaNiO_3$ and La_2NiO_4,[154] $BaNiO_3$,[155] and metal chalcogenides[156] where the surviving pre-catalyst could affect the Fe active sites by electronic[125] or epitaxy effects[157].

Temperature-dependent measurements can be used to characterize the evolution of kinetic barriers with site structure. An Arrhenius plot of the rate versus inverse temperature allows extraction of the activation energy of the reaction from the slope and of the pre-exponential factor from the intercept which should be characteristic for a given site type[158]. Absolute rate theory can then be applied to decompose these parameters into one which contain the enthalpy and entropy of activation describing equilibrium between reactants and the activated complex. Further, if the temperature-dependent data is collected at different voltages, one gains insight into how this activation equilibrium changes with the potential energy surface of the reaction, a surface which is a function interfacial environment dictated by the electrochemical driving force. Thus they could serve as quantitative handles for differentiating the effects of Fe site configuration and host structure on reaction rates.

However, temperature-dependent data sets are scarce in the electrocatalysis literature[159] and there are none related to surface Fe sites. Swierk *et al.* measured the activation energy for OER of co-electrodeposited $Ni_{1-z}Fe_zO_xH_y$ films (z = 0 - 100) in 1 M KOH purified of iron imputies. They found a U-shaped dependence on the percent Fe in the film with the lowest activation energy of ~25 kJ mol^{-1} observed for an Fe percentage of ~20-25%.[160] Chen *et al.* measured the temperature-dependent I-V curves for water dissociation by TiO_2 in a bipolar membrane electrolyzer and found the activation energy was constant at different overpotentials, but the pre-exponential factor linearly increased with overpotential. This led to proposal of a new model for water dissociation in which an areal proton conductance described the pre-exponential factor change with driving force.[161] Temperature-controlled kinetics also allow one to access OER reaction rates for Fe sites at the elevated temperatures relevant to their application in industrial liquid alkaline electrolyzers[162].

Here are reported the Tafel slopes, exchange current densities, activation energies, and Arrhenius pre-factors as a function of temperature for surface-adsorbed iron sites on nickel oxyhydroxide. These surface iron sites are expected to be of the same "cooperative" kind our group prepared and distinguished from bulk iron sites in the nickel oxyhydroxide lattice in prior work[66]. First, the change in surface Fe site density as a function of temperature is measured, revealing a decrease in the average loading from ~2.7 % at temperatures between -5 to 21 °C to ~1.5 % at 70 °C. Coupling these iron loadings to the measured OER current at different temperatures allowed the extraction of the activation energy and Arrhenius pre-factor, both of which decreased over the range studied. Additionally, we found, contrary to expectations from conventional Butler-Volmer formalism[163], that the Tafel slope is insensitive to temperature (~40 mV dec^{-1}), requiring a temperature-dependent value of the transfer coefficient. Possible origins for this behavior are considered in view of the physical parameters which differentiate outer and inner sphere electron transfer reactions as well as similar experimental observations by Conway[164-166] for the hydrogen evolution reaction on metal electrodes.

Methods and Materials.

Preparation of NiO_xH_y catalyst films

A Pt gauze working electrode (BASi; EF-1355) was used for all measurements unless otherwise specified. The Pt was immersed in fresh aqua regia for 15-20 seconds and rinsed with DI water prior to deposition of the film. Deposition was performed by cathodic chronopotentiometry in high purity aqueous 0.1 M nickel (II) nitrate at -30 uA (~ -40 uA cm^2) for 6 minutes providing films which showed between 2-5 mC total charge upon integration of the Ni redox peak after deposition.

Electrochemical measurements

All measurements were performed in semiconductor grade KOH after purification of Fe by suspension of precipitated $Ni(OH)_2$ in the KOH and removal of Ni residuals from this Fe removal step using 0.1 μm pore-size PES syringe filtration as detailed in our previous work[57]. Temperature dependent measurements were performed inside a custom-made

plastic cell fashioned from a 15 mL centrifuge tube. The end of the tube was cut off and plastic film was secured to the bottom by first stretching the film over the hole at the cut end of the tube and pushing 3 O-rings over the film and around the outside of the tube. The O-rings hold the film taught over the cut end of the tube leading to a good seal against electrolyte leakage and thermal bath fluid intrusion. Further the use of the plastic film provided a thin membrane at the bottom of this custom cell to permit rapid heat exchange with the electrolyte such that the cell equilibrated <5 min after the recirculating chiller equilibrated. Next we added ~5 mL of 50/50 ethylene glycol/water into a three-neck borosilicate glass electrochemical jacket cell (PROGLASS, 25 mL). The custom cell was filled with 3 mL of purified electrolyte and placed into the jacket cell. The 5 mL of EG/water mixture provided the necessary thermal transfer from the interior walls of the jacket cell to the exterior of the inserted plastic cell. A Hg/HgO reference (CH Instruments; part # CHI152) filled with purified 1 M KOH was bundled together with the working electrode and a Pt coil counter electrode cleaned in fresh aqua regia for 15-20 seconds. This electrode assembly was inserted into the plastic cell holding 3 mL of electrolyte for subsequent voltammetry. Temperature-control was enabled via a recirculating bath chiller (Julabo DD-200F) connected to the jacket cell.

We verified that the Hg/HgO potential was invariant with temperature by measuring its open-circuit potential versus an integrated RHE (Gaskatel HydroFlex; SKU: 81010) while varying the temperature according to the experimental procedure. The potential was found to vary by less than 3 mV. Although the Nernst equation suggests that the Hg|HgO potential should be temperature dependent, we think the observed invariance arises because the actual HgO solid and filling solution is housed in Teflon which is highly thermally insulating. Thus the interior of the reference electrode does not change temperature to a degree noticeable over the timescale of the experiments.

Inductively-coupled plasma mass spectrometry (ICP-MS) measurements

ICP-MS measurements were performed using an iCAP-RQ (Thermofisher Scientific) operated in kinetic energy discrimination mode. All standards were prepared from ICP-MS grade stock solutions. Internal standardization was ensured for each sample utilizing Sc and Y sample spiking. Fe:NiO_xH_y films were digested in TraceMetal grade nitric acid (68

-70 m/m%; Fisher Scientific) for 10 minutes with 1 minute of sonication. Complete film dissolution was confirmed by collecting an additional cyclic voltammogram in 1 M KOH and noting the absence of the characteristic $Ni^{2/3+}$ wave. Levels of Fe in typical sample measurements were at least 10x higher than adventitious Fe from the environment as determined by replicate method blank preparation (Figure 54). This is a critical step because the amount of surface Fe sites formed is very small and Fe is a relatively abundant contaminant in the laboratory.

Results and Discussion.

To correlate kinetic parameters with surface Fe site loading, we first had to optimize the choice of substrate used for NiO_xH_y deposition to ensure a high enough Fe loading that our typical Fe-spiking procedure yielded concentrations of Fe in ICP-MS samples 10x higher than replicate method blanks. This is not trivial as Fe is a relatively abundant contaminant and we wished to keep our films as thin as possible to prevent artefacts related to large electron transport distances. Figure 54 shows the results of optimizing for Pt substrate geometry and film thickness. To enhance the surface Fe loading, a substrate with higher geometric surface area than planar substrates, a Pt gauze, was found to meet the necessary detection criteria when depositions yielded > 1.5 mC total anodic charge in the post-deposition CVs.

Optimization of the Pt wire substrate afforded an opportunity to test a hypothesis related to surface Fe site formation. When Fe is introduced into the electrolyte during fixed-potential chronoamperometry, the current density gradually increases to a plateau. Despite the fact that introduction of Fe into the electrolyte takes only ~10 seconds, this growth and plateau in the current density occurs over the course of tens of minutes[66]. This could be because the adsorbed Fe is not merely on the "topmost" sites most easily accessible to ions in electrolyte. Rather Fe might diffuse through the hydrated, turbostratically-disordered, gas evolving α-$Ni(OH)_2$ sheet structure[167] and adsorb at relatively buried sites, a process that would likely not be instantaneous especially during active oxygen bubble evolution. To test the idea that Fe adsorbs at "internal" adsorption sites we examined the CA Fe spike activation behavior of films of varying thickness by deposition on a Pt wire of ~0.026 cm^2

as determined by the length and gauge of the wire. If the model of Fe site formation above is accurate, one would expect a slower time to the activation plateau for thick films. Figure 7 shows the effect of varying the film loading on the working electrode over about 2 orders of magnitude and appears consistent with our hypothesis that some "surface" sites form within the hydrated internal sheets of the deposited film.

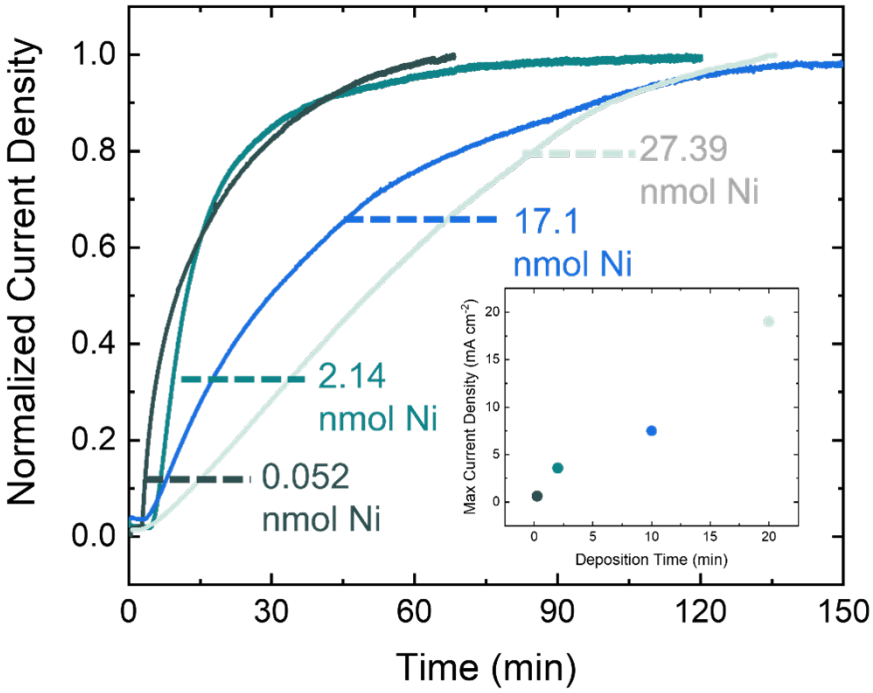

Figure 7. Time to surface Fe-induced activation as a function of NiO_xH_y film thickness.

With an optimized Pt substrate and deposition time in hand we proceeded to the collection of temperature-dependent OER rates beginning with the question of whether the molar percent of surface Fe sites relative to the amount of total Ni in the films changed with temperature. Surface Fe sites appear to participate in an OER-induced dissolution-redeposition cycle[66, 79]. We hypothesize that this dissolution occurs by formation of soluble FeO_4^{2-}, a process that is thermodynamically favorable at high pH and very low concentration of dissolved FeO_4^{2-} in solution[168]. Redeposition may occur by turnover of the site and precipitation from the alkaline electrolyte. The solubility of Fe^{3+} also increases with temperature[169], thus it is possible that an increase in temperature could drive the dissolution-redeposition equilibria towards dissolution. Quantifying such an effect of

temperature on surface Fe site formation would be important for Fe site management in electrolyzers which operate at these elevated temperatures.[170] We prepared NiO_xH_y films by cathodic electrodeposition at -0.03 mA such that the integrated redox waves of the films were between 2-5 mC total charge. This was found to be an optimized balance between film thickness and total surface Fe loading as described above. Working electrodes were placed into a custom plastic cell housed in glass flow cell capable of temperature control via a recirculating chiller. The plastic insert was necessary to prevent leaching of iron that occurs when alkaline electrolyte etches glass. The film was then polarized at 300 mV overpotential and 100 ppb Fe^{3+} was introduced via dropwise addition. The current rose as expected from the formation of high activity surface Fe sites as observed in our previous study.[66] After the current reached a new steady-state, the electrolyte temperature was changed to the desired temperature via the recirculating chiller and allowed to equilibrate. The new steady-state current was recorded and the film was removed and digested for ICP-MS analysis.

Figure 8a shows the change in surface Fe sites as a function of electrolyte temperature as the fraction of adsorbed Fe relative to the total amount of Ni in the deposited film measured with ICP-MS. There is a small decrease in the amount of Fe sites formed from 2.7 ± 0.5 % at temperatures between -5 – 21 °C to 1.5 ± 0.5 % at 68.1 °C. Despite this small decrease in total number of surface Fe sites the total current increases for near-identical electrodes because the intrinsic activity per site increases. The fraction of Fe sites at room temperature is lower than observed in our previous work of about 5%.[66] We expect this is because the films here are thicker and thus there is larger contribution to the calculated Fe fraction from bulk Ni that does not support adsorption sites hinting that Fe adsorption sites may not scale linearly with Ni loading. Figure 8b shows the turnover frequency (mol O_2 per mol Fe per second) at -5.2, 1.5, 21, 39.6, 49.8 and 69.1 °C. An exponential relationship is observed consistent with classical temperature-activated catalysis. At ~70 °C the intrinsic activity of surface Fe sites are about an order of magnitude higher at 300 mV overpotential (35.7 ± 4.5 s^{-1}) than at room temperature (4.6 ± 1.3 s^{-1}). We note that the room temperature TOF_{Fe} measured in this study for ~2.7 mol% Fe samples compares favorably with data from our prior study of cooperative surface Fe sites[66] where NiO_xH_y films with 2.9 ± 0.4 Fe mol% were found to have a TOF_{Fe} of 5.8 ± 0.8 s^{-1}.

The temperature-dependent data were then used to extract the activation energy and Arrhenius pre-factor by noticing that the turnover frequency is a site-normalized current density, which permits plotting its natural logarithm versus T^{-1} according to linearization of the phenomenological Arrhenius equation[159] (1)

$$TOF_{Fe} = Ae^{-E_a/RT} \quad (1)$$

Figure 8c shows the linear relationship between $\ln(TOF_{Fe})$ and T^{-1} and the fit results yielding an activation energy of ~39 kJ mol^{-1} and pre-exponential factor of 5 x 10^7 s^{-1}. The activation energy measured here is comparable to the only other literature report of Arrhenius parameters for a nickel-iron hydroxide OER catalyst of which we are aware. Swierk *et al.* reported activation energies between 25 and 40 kJ mol^{-1} for $Ni_{1-z}Fe_zO_xH_y$ films for z between 10 and 40 by plotting the log of the exchange current versus T^{-1}. The films in that study likely had bulk and surface iron sites while our study is particular to the surface Fe and it was not clear to what overpotential those data corresponded. A higher total amount of Fe active sites or overpotential may be responsible for the lower activation energy in Swierk. No pre-exponential factor was reported[160] and thus we cannot make a comparison with our value. Pre-exponential factors and activation energies have also been measured in the context of water dissociation. Chen *et al.* measured these parameters for nanoparticle TiO_2-P25 water-dissociation catalysts and found an activation energy of 25-30 kJ mol^{-1} independent of potential and pre-exponential factors on the order of 10^7-10^8.[161] Direct comparison of magnitudes with that work is very limited because water-dissociation is a process mediated by nanoparticle oxides in an electric field established by depletion of ions at the interface between two ion exchange membranes, not one that occurs at a polarized electrode surface.

In liquid alkaline electrolysis, Fe loading must be optimized; enough electrolyte Fe^{3+} must be present to sustain the dynamic Fe site equilibrium[79] for fast OER kinetics, but not so much that excess Fe can plate on and poison the cathode.[171] Applying this qualitative design target *quantitatively* can be done using the TOF_{Fe} values in Figure 8b. We used the TOF_{Fe} of 35.7 s^{-1} at 70°C to calculate theoretical surface Fe site loading needed to pass various current densities on a 10 cm^2 electrode. We assume an electrolyte concentration of 1 M KOH and an electrode roughness factor of 1000, an underestimate

considering that nickel nanowire meshes have an internal surface area on the order of 10^5 cm^2 cm^{-3}.[172] Assuming monolayer coverage of β-$Ni(OH)_2$, and a 300 mV kinetic

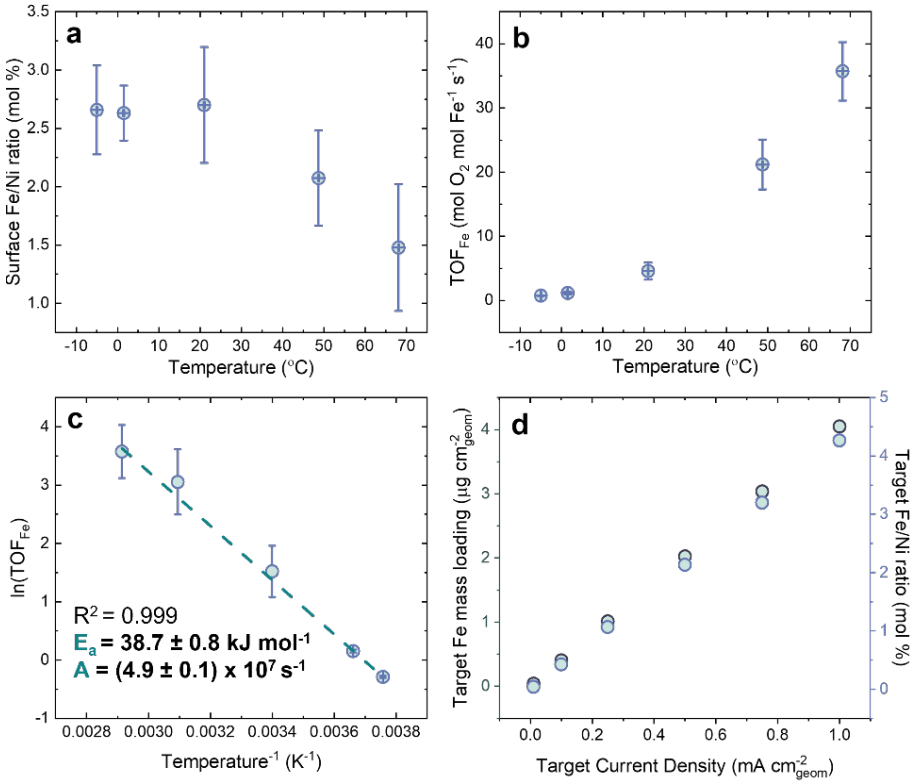

Figure 8. Surface Fe loading and Arrhenius data at 300 mV overpotential
(a) Surface Fe loading versus temperature as determined by temperature-controlled chronoamperometry followed by ICP-MS analysis of the films. Data was collected in duplicate or triplicate. (b) Turnover frequency per surface Fe site as a function of electrolyte temperature. (c) Arrhenius plot with linear fit shown allowing extraction of activation energy and pre-factor at 300 mV. (d) Calculated iron loading needed for various target current densities for a theoretical electrolyzer anode coated with 1 MLE of nickel hydroxide.

overpotential we find the target loading of iron in Figure 8d. The calculations suggest that a very small amount of iron, ~1-4 µg cm^{-2} geometric area is required to sustain high current densities even up to 1 A cm^{-2}. Of course, these calculations should be tested against measurements in future work, but they demonstrate that electrolyzer anode design may require management of a very low loading of iron sites.

To measure the OER current from surface Fe sites at different temperatures, working electrodes were introduced into the modified jacketed 3-neck electrochemical cell with temperature control via a recirculating chiller.

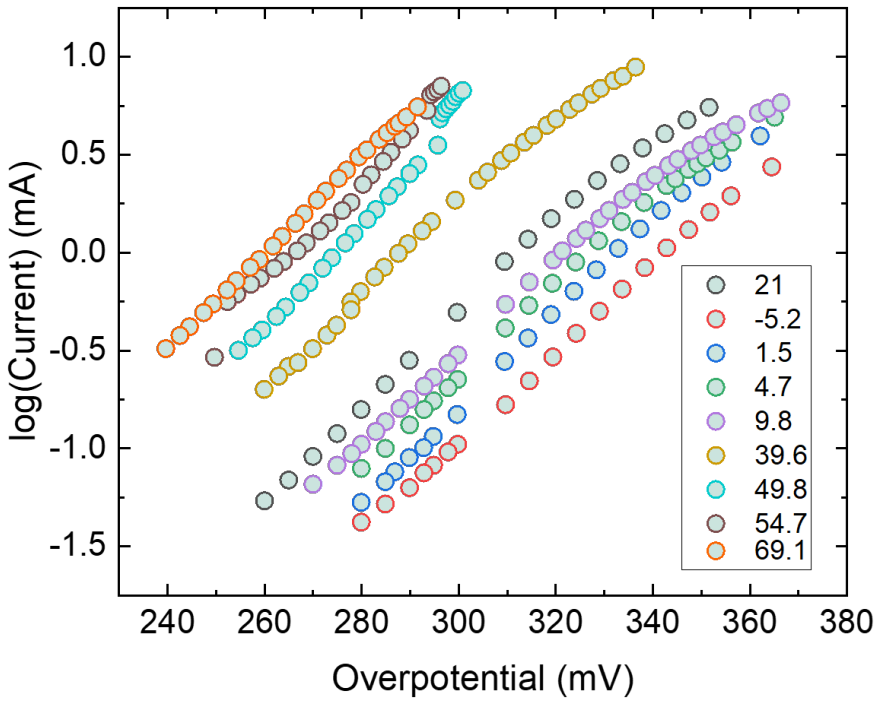

Figure 9. Temperature-dependent Tafel plots for Fe:NiO_xH_y.
The slopes of these lines yields the reciprocal Tafel slope and the y-intercept, the natural logarithm of the exchange current.

Surface Fe sites were freshly prepared at room temperature (21 °C) by spiking Fe into the electrolyte at 100 ppb while the working electrode was polarized at 300 mV overpotential. The NiO_xH_y catalyst OER current was allowed to rise and plateau. We will refer to surface Fe-site decorated NiO_xH_y as Fe:NiO_xH_y in the remainder of the discussion. To collect the Tafel data, the potential was then stepped below 300 mV overpotential to ~250 mV and then up to ~350 mV while never depolarizing the electrode below OER potentials until all the Tafel data were collected. This ensured that surface Fe-sites were not mixed into the Ni^{3+} positions where they are much less active[66, 173]. This procedure was repeated after setting the next desired temperature and waiting for subsequent equilibration until Tafel data at all temperatures was collected.

Figures 55 shows the raw chronamperometric data acquired with the above method. Figure 56 shows the current-potential curves formed by extraction of the average current at each potential step in the raw data. They show the expected exponential (Tafel) relationship between current and potential between current and temperature where higher temperatures promoted a higher absolute rate of reaction for the same electrode. Figure 9

shows the Tafel plots which permitted calculation of the Tafel slope and exchange current densities upon fitting (Figure 57). The parameters are plotted as a function of temperature in Figures 10a and 10b. The Tafel slope was roughly constant at ~ 40 mV dec^{-1} with respect to temperature implying a temperature-dependence of the transfer coefficient, α. Calculated values of α are given in Fig 10c and show they are > 1 and increase with temperature from ~1.3 to 1.7.

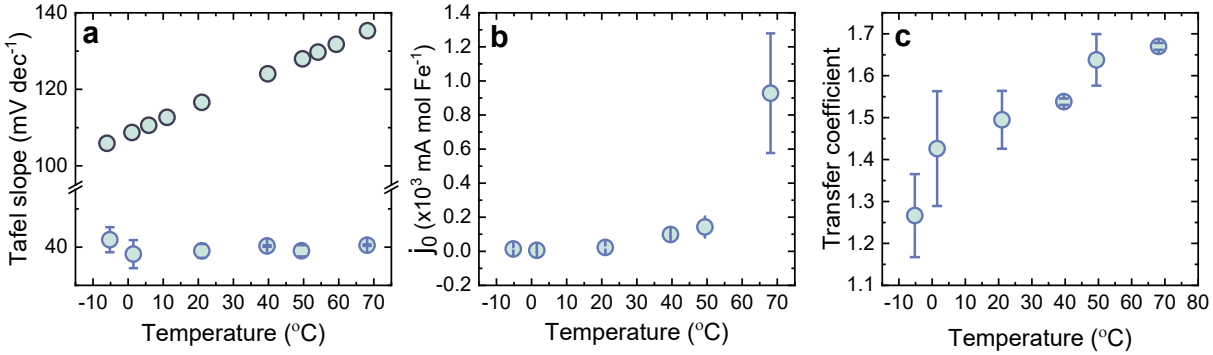

Figure 10. Tafel parameters versus temperature for Fe:NiO_xH_y.
(a) Measured Tafel slopes at various temperatures (blue) compared to Tafel slopes obtained with conventionally taken values of the transfer coefficient $\boldsymbol{\alpha}$ = 0.5 (navy). (b) Exchange current per Fe site at various temperatures. (c) Value of the transfer coefficient calculated using $\boldsymbol{\alpha}$ = 2.3RT/bF where b is the value of the Tafel slope at the temperature of choice in Figure 9.

The transfer coefficient is a phenomenological parameter. It characterizes the exponential rise in the current as overpotential is increased. Ascribing deeper, *accurate* meaning to this purely empirical parameter requires precise knowledge about the potential energy surfaces on which reactant, activated complexes, and products exist at a given value of the overpotential. Near an electrified interface, this potential energy surface is not just a function of molecular vibrations, rotations, and electronics of the relevant species, but also of the electrochemical double-layer structure. As a result, it is not a simple task to understand what the transfer coefficient represents. Interpretation should be made cautiously.

There are two interesting features to note in our data: the value of $\alpha > 1$ and increases with temperature. For an outer-sphere reaction, $\alpha > 1$ could be interpreted in relation to *n'* number of electrons passed prior to the rate-determining step (RDS) and of

an α for the RDS between 0 and 1.[42, 174] This approach is not generally valid for a multi-step inner-sphere mechanism where the rate-determining step may involve potential-dependent processes not accounted for in an outer-sphere model such as adsorption, ion-transfer, or chemical bond formation/rupture[175]. Therefore there is no reason *a priori* to think that the transfer coefficient should be between 0 - 1. We illustrate this point below with a simple accounting of surface coverage in the rate expression inspired by a similar approach in absolute reaction rate theory[176]. For an electrochemical reaction involving the 1 e^- oxidation of a surface-adsorbed species, O^*, to its product, R^*, of the form:

$$O^* \rightarrow R^* + e^- \tag{1}$$

The rate is expected to display an exponential relationship not unlike that proposed for other OER catalysts[175]:

$$i = FAi_0(\theta_{O^*} e^{\alpha f \eta}) \tag{2}$$

where θ is the fractional coverage - the amount of adsorbed O^* relative to that in a single monolayer (*e.g.* 50% surface coverage corresponds to θ = 0.5). In Tafel analysis of an outer-sphere reaction the ratio of surface reactant to that in bulk solution appears in place of θ and is assumed to be 1 under conditions of good mass transport. This is not necessarily valid for reactants which are bound to the electrode surface. Coverage of surface species is instead determined by its adsorption isotherm. We choose the simplest - a Langmuir isotherm - which neglects the effect of interactions between adsorbed species. The conclusions which may be drawn using the Langmuir model hold for cases where more complicated isotherms are applicable. We find then that:

$$\theta_{O^*} = a_i^b e^{-\frac{\Delta \bar{G}_{ads}}{RT}} \tag{3}$$

Here a_i^b is the activity of the adsorbed species in bulk solution and $\Delta \bar{G}_{ads}$ is the electrochemical free energy of adsorption which by definition is a function of the electrode potential.[42, 163] If we suppose $\Delta \bar{G}_{ads}$ depends on the potential by a factor $\pm \alpha_{ads} f \eta$ where α_{ads} might be called an "adsorption" coefficient, substitution into the current-potential relationship and linearization yields an apparent transfer coefficient, α_{app}:

$$\alpha_{app} = \alpha_{ads} + \alpha \tag{4}$$

In a case where reaction (1) is rate-limiting then we find the apparent transfer coefficient has two contributions: one from the effect of the potential on the free energy of adsorption, α_{ads}, and another on the free energy of activation, α. If both lie between 0 and 1 then an apparent transfer coefficient between 1 and 2 is reasonable without any misapplication of expressions used for outer-sphere reactions. This is but one scenario assuming a particular rate-determining step and we do not claim such a mechanism is necessarily operative. Rather, this is a simple demonstration of how consideration of factors expected to be important in an inner-sphere reaction can qualitatively account for measured Tafel parameters.

Other relations having a similar form to (2) have been suggested. Moss *et al.* used spectroelectrochemistry to measure a Frumkin-like potential dependence of the coverage of the OER intermediates responsible for catalytic turnover. Positing two Brønsted-Evans-Polanyi (BEP) scaling relationships, one between the activation energy and the binding energy of intermediates and the second between this binding energy and the potential-dependent coverage, the authors write an expression with an exponential *and* pre-exponential factor which contains a dependence on the applied potential. This model fit their measured Tafel slopes well. It is not clear what terms could be compared to our transfer coefficient so we will not do so, but the work illustrated that consideration of potential-dependent coverage of species displaying Frumkin behavior can lead to models with coefficients whose values can vary depending on the choice of model.[177].

In addition to a transfer-coefficient > 1 we find its value is temperature-dependent, a consequence of the near-constant Tafel slope in Figure 10a. The transfer-coefficient increased with temperature in an approximately linear fashion with a slope of (4.6 ± 0.3) x 10^{-3} units per Kelvin with an intercept near zero. To our knowledge this is the first measurement of this kind for OER on surface Fe-sites. The earliest systematic measurements and explanation of similar data was undertaken by Conway[178]. In a seminal paper[164] temperature-dependent transfer coefficients were observed in a study of the hydrogen evolution reaction on Ni, Pb, Pt, Cd, and Hg metals in methanolic/ethanolic hydrochloric acid solutions and bromine evolution at graphite. Conway suggested this temperature-dependence could be consistent with several explanations. The first involved

specific ion adsorption expanding on Parsons' [179] approach showing a relationship between the activity coefficient of the activated complex in absolute reaction-rate theory[180] and the properties of specifically adsorbed ions. A temperature-dependence of the transfer coefficient could be derived from this model. In the absence of specific adsorption effects, the potential dependence of the standard electrochemical entropy of activation ($\Delta\bar{S}_0^{\ddagger}$) was proposed as an explanation and theoretically supported (Supplementary Calculation 2). He suggested that the value of the transfer coefficient is one instance of a general rule expressed in two parts: a component related to the standard electrochemical enthalpy of activation ($\Delta\bar{H}_0^{\ddagger}$), α_H, and one related to $\Delta\bar{S}_0^{\ddagger}$, α_S:

$$\alpha = \alpha_H + \alpha_S T \tag{5}$$

This concept was applied in subsequent work in which α_S values similar to ours were observed for the HER on Hg of ~6 x10^{-4} K^{-1} in 0.1 M HCL and of ~ 1 x10^{-3} K^{-1} in 1 M CF_3SO_3H and 1M HCL (in methanol).[165] A physical interpretation of α_S was offered and based in the likely scenario that the structure of near-surface solvent layers are strongly influenced by the electrode potential. This interfacial solvent environment was expected to affect on activated complex formation. Indeed, this connection between solvent orientation and entropy of activation in electrochemical reactions has been more recently explored in the context of water-dissociation with the interfacial stored charge as a corollary[181, 182]. Borrowing from Conway's approach, we might conclude that OER on surface Fe-sites is more strongly influenced by changes to the electrochemical entropy of activation than the few other examples available in the literature. This could originate in a relatively larger volume or more weakly bound condition of the activated complex involving these sites. This is speculative, and further research using carefully chosen catalytic systems for comparison with the aid of computational modelling would be needed to test this hypothesis rigorously. An obvious extension of this work would be measurement and comparison of α_S for bulk Fe sites which we found have a different local chemical environment from surface sites with *in-situ* XAS in Chapter II.

The connection developed between $\Delta\bar{S}_0^{\ddagger}$ and α could be argued to be somewhat problematic as proposed[164] because $\Delta\bar{S}_0^{\ddagger}$ corresponds to a defined set of reference conditions - standard conditions - hence k_0 is a constant in the Butler-Volmer formulation of i_0.[42] It is unclear then what is meant by the proposition that a quantity defined only at standard conditions is potential dependent. This may be a symptom of the poor ability of the Butler-Volmer theory to explain inner sphere reactions. One alternative route to recovering the empirical temperature dependence of α might be relaxation of the assumption of Butler-Volmer theory that the pre-exponential factor, A, in the expression for k_0 is potential independent. Then one could in principle write an expression for A as a function of η where some coefficient α' modulates the functional relationship. Insights into the nature of physical processes described by A - collisional frequencies between reactants and the sterics of those collisions, to name two possibilities - would be required to develop appropriate formulations.

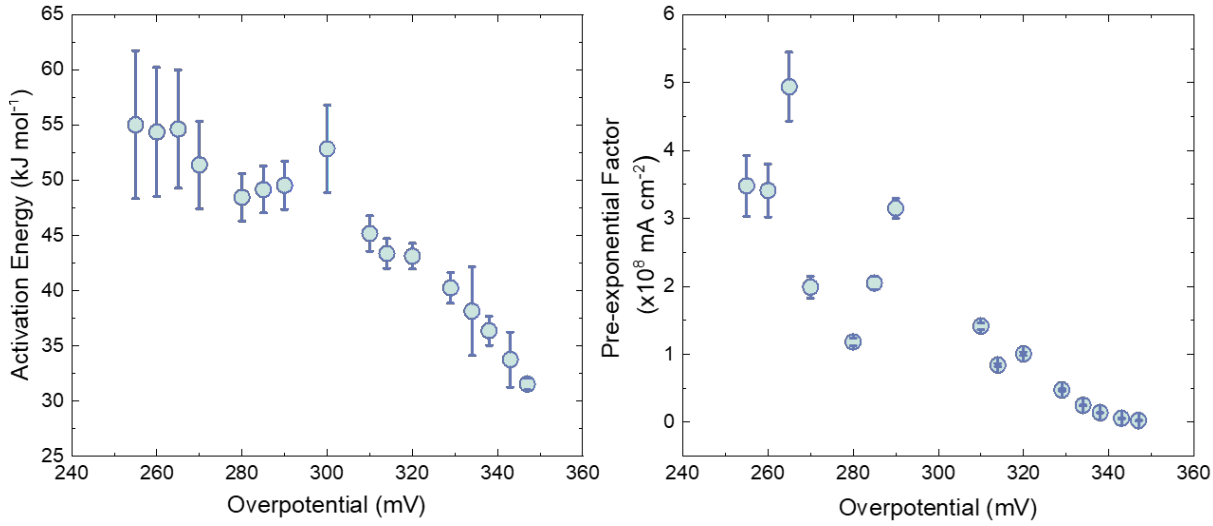

Figure 11. Activation energy and pre-exponential factor as a function of overpotential
Activation energy (left) and Arrhenius pre-factor (right) as a function of overpotential for surface Fe sites extracted from plots of current density versus 1/T (K^{-1}) (Figure 59 shows how use of TOF_{Fe} affects the anlaysis). Error bars correspond to 1 standard error of the fit to each Arrhenius plot.

We used the temperature-dependent Tafel data in Figure 9 to extract Arrhenius plots for various fixed values of the overpotential in the manner of Chen *et al.*[161] Fits to the data (Figure 58) yielded the activation energies and Arrhenius pre-exponential factor as a function of driving force as shown in Figure 11. The activation energy and pre-exponential

factor decreased in the range η = 255 - 350 mV. We note that because the curvature of the Tafel plots start to become evident for data collected above 320 mV overpotential, the activation energies in that potential regime may be underestimated. If so, a more modest reduction of the activation energy from applied potential than that shown would be observed.

Recalling the Eyring equation[180], the activation energy is proportional to the enthalpy of activation ($\Delta H^{\ddagger}$) and the pre-exponential factor to the entropy of activation ($\Delta S^{\ddagger}$). For OER on Fe:NiO_xH_y, $\Delta H^{\ddagger}$ and $\Delta S^{\ddagger}$ both decrease with electrochemical driving force, η. The decrease of the activation energy with increased potential has been previously explained in terms of a BEP relationship between E_a and ΔH_{rxn} (the enthalpic difference between reactant and product states) for a study of IrO_x in acid. The activation energy was thought to decrease because of increasing oxidation of the catalyst via Ir and O redox driven by increasing potential. Extent of oxidation was quantified in terms of the surface hole coverage which was used to write an Eyring-like equation for the rate that reproduced the observed current-potential data. Thus the authors concluded that E_a decreases with potential because surface hole coverage decreases ΔH_{rxn}. The entropy of activation was not directly probed though the authors note that the linear relationship between E_a and ΔH_{rxn} was largely unchanged by the presence of two solvent layers in their accompanying computational modelling.[175] Nickel hydroxide can also store oxidative equivalents by redox of the Ni sites (and probably of Fe at higher potentials) as can be seen in the voltammetry and time-resolved XAS[183] so a similar mechanism could be operative here.

The OER involves electron *and* proton transfer. In an inner sphere reaction, transference of a proton to reacting species will be strongly affected by solvent structure near the electrode. In water, proton transfer is driven by collective fluctuation and rupture in the hydrogen-bonding network[184, 185] around a Zundel-type (a proton flanked by two waters) solvated proton complex[186]. Carpenter performed infrared transient absorption anisotropy decay experiments to measure the timescale of relaxation of bending modes in the Zundel excess proton complex. Larger timescales for the anisotropy decay corresponded to slower kinetics of proton transfer. It was observed that the timescale of relaxation was sensitive to the identity and concentration of anions in solution as well as

its viscosity. Relaxation followed an Arrhenius relation permitting the extraction of activation energies and pre-exponential factors. Higher concentrations of HCl for example led to a relatively slower rate of relaxation despite a *lower activation energy*. The pre-exponential factor however also decreased with increasing concentration of anions. Again, utilizing the Eyring equation as a framework for understanding these trends, Carpenter proposed that high anion concentration solutions have a lower entropy of activation for proton transfer because the anions reduce the number of possible configurations for collective H-bond network fluctuations that result in proton transfer and increase the solution rigidity (interpreted as resistance to dynamical fluctuation) by increasing the viscosity[187].

Here, we investigated a reaction in basic conditions, but there is evidence that the same concepts evident in the field of aqueous proton transfer can be leveraged, especially the effect of solution "rigidity" on the entropy of activation. Koper and coworkers have argued that the barrier to solvent reorganization during charge transfer is a descriptor for the pH-dependence of HER rate on Ni-decorated Pt electrodes. Far from the point of zero charge (pzc; where excess charge on the metal surface is zero) the solvent is highly-ordered and thus is difficult to reorganize to accommodate charge transfer, resulting in a kinetic penalty. This effect was identified as enthalpic, however, and was differentiated from computational work predicting reaction rate pH-dependencies originating from surface configurational entropy barriers for proton transfer. Entropic effects of solvent structure on HER kinetics were considered in a related study where phase sensitive second-harmonic generation optical spectroscopy measurements on Pt and Ni-decorated Pt permitted experimental determination of the pzc for both catalytic systems. Ni-decoration lowered the pzc cathodically by 360 mV which provided a more "relaxed" solvent environment and faster HER kinetics. This relaxation effect was not explicitly connected to either enthalpy or entropy barriers.[188] Assuming in this study that we are polarizing in a direction away from the pzc of NiOOH we can reasonably borrow from the aqueous proton transfer literature and the above cited studies; the decrease in entropic contribution to the activation energy observed here could be related to restrictions on ion transfer through a tightly-organized solvent that is a function of potential[189].

In heterogeneous catalysis, many systems display what has been coined "compensation" of the activation energy by changes in the natural logarithm of the frequency factor. For such systems an apparent linear relationship, between these quantities can be shown:

$$\ln(A) = mE_a + b \tag{6}$$

The proportionality constant, *m,* characterizes the magnitude of the compensation. Very often, it is a positive value - the frequency factor increases as the energy of activation increases.[190, 191] We observe compensation of the Arrhenius parameters in this work evident in Figure 12. Physical explanations of this effect vary. Bligaard investigated compensation computationally using the dissociation of a diatomic gas on free sites of a catalyst as a model rate-limiting step in a kinetic scheme. Positing a linear relationship between activation energy and binding energy of the adsorbate gas and substitution into their rate equation showed that the ln(A) and E_a varied in the same region of catalyst binding energies as did the availability of free sites (1 - coverage).[191] Teschner also suggested that compensation exists for HCl oxidation over RuO_2 because the E_a and ln(A) both share a dependence on the coverage of oxygen as determined with temporal analysis measurements of the amount of Cl_2 produced after pulses of oxygen of different durations. They suggest that the critical high activation energy step of re-oxidation of a Cl-crowded catalyst surface is compensated by increased surface configurational entropy, a parameter that scales with the number of free sites. A compensation slope of 0.22 mol kJ^{-1} was measured for HCl oxidation[192].

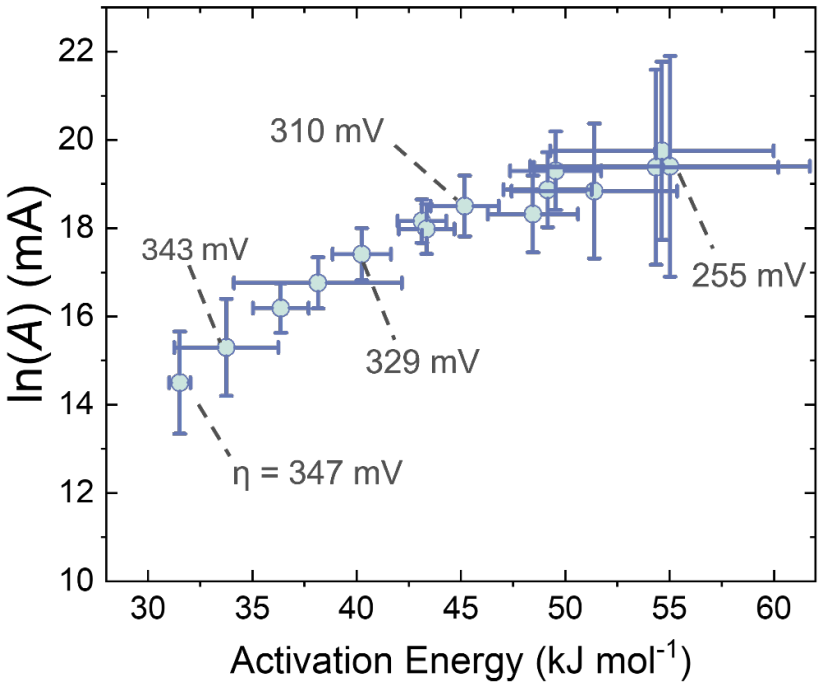

Figure 12. Plot of Arrhenius activation energy and ln(*A*)
Compensation effect plot showing the variation of the Arrhenius plot y-intercepts versus the activation energies in Figure 11. A linear fit to the data yields the slope given as an inset (R^2 = 0.914).

Rodellar reported compensation effects in the kinetic analysis of water dissociation by metal oxide catalysts and catalyst-free bipolar membranes. Slopes of 0.11 and 0.25 mol kJ^{-1} were reported for metal oxide catalyzed and uncatalyzed water dissociation, respectively. Citing Teschner, the increase of E_a with ln(*A*) was suggested to arise from changes in the surface configurational entropy and was thought to vary in tandem with the difference between a metal oxide's point-of-zero charge and the local pH established in the catalyst-membrane junction.[181] A similar study by the same group was performed for HER, ammonia oxidation, and oxygen reduction on polycrystalline Pt in 0.1 M KOH, but in this case E_a and ln(*A*) increased at higher overpotentials contrary to the compensation observed in our study of OER.[182] We hypothesize that at higher overpotentials the surface of Fe:NiO_xH_y is highly crowded with reactive intermediates. This crowding works to lower the activation energy because of inter-site interaction and destabilization in the manner described by Moss for CoOOH.[177]While the lower E_a acts to

increase the rate, higher occupation of surface sites decreases the entropy of the relative steps because there is little surface configurational entropy to be gained in such a scenario. This hypothesis is almost certainly too simple - for example it neglects changes to entropy which may arise from interfacial solvent[182]. Likely one would need *in-situ* characterization of coverage and interfacial solvent structures for a series of OER catalysts which display different levels of compensation. This might be possible with carefully deconvoluted capacitance measurements[181] coupled with sum frequency generation vibrational spectroscopy[193].

Conclusion

In this study, temperature-dependent OER rates and surface Fe-site quantity were measured for Fe:NiO_xH_y. A moderate decrease in the percentage of surface Fe sites relative to the Ni in the host film was observed when the cell was heated to > 50 °C. The intrinsic activity (TOF_{Fe}) increased with temperature as expected up to ~36 s^{-1} at the highest temperature of 70 °C. Tafel plots at varying temperatures were prepared and the slopes were insensitive to temperature necessitating a temperature-dependence of the transfer coefficient. This may be related to temperature-dependent entropic or coverage effects pending further research. Finally, Arrhenius parameters were measured for surface Fe sites for the first time on nickel oxyhydroxide. An apparent compensation of the activation energy by the pre-exponential factor with increasing overpotential was observed. Attributing molecular details to the value and temperature-sensitivity of the transfer coefficient and the compensation between Arrhenius parameters should be the subject of follow-up studies. Given that potential and temperature-dependence of adsorbate coverage appears to be, if not determinative, consequential for understanding the inner sphere OER reaction, studies that can directly measure such coverage and relate it to the potential energy surface of rate-determining steps with advanced theory could be particularly impactful.

In Chapter IV I will show that our understanding of Fe sites can be applied to other technologically relevant oxides and that the conclusions of Chapters II and III have a wider scope than research on oxyhydroxides.

IV. TRACE FE ACTIVATES PEROVSKITE NICKELATE OER CATALYSTS IN ALKALINE MEDIA VIA REDOX-ACTIVE SURFACE NI SPECIES FORMED DURING ELECTROCATALYSIS

Liam P. Twight, Ally Tonsberg, Samji Samira, Kunal Velinkar, Kora Dumpert, Yingqing Ou, Le Wang, Eranda Nikolla, and Shannon W. Boettcher

L. P. T. and S.B. conceived of the research with assistance from Y.O. S.W.B. directed the research project. **L. P. T.** collected most of the experimental data, with assistance from A.T. and K.D.; K.V. and S.S. directed by E.N. synthesized and characterized the R-P 214-LNO materials as well as advised on their properties. L. W. prepared the epitaxial $LaNiO_3$ films. **L. P. T**. and S.W.B. analyzed the data and **L.P.T**. wrote the manuscript with contributions from S.B., E.N., K.V, S.S, and L.W

Introduction

Perovskite oxides have been studied as oxygen evolution reaction (OER) electrocatalysts for decades due to their apparent high activity and use of relatively abundant transition metals [194]. Early efforts to rationalize the activity of these catalysts made use of activity correlations with bulk thermodynamic concepts such as lower-to-higher enthalpy of oxidation and *d*-electron count on the B-site metal cation [195]. More recently, descriptors such as the extent of transition-metal-oxygen hybridization (covalency) [196], O-2*p* band position band position relative to the Fermi energy [197], and e_g electron count of the transition metal cation [53] have been used to connect the activity of perovskite oxides to their electronic structures.

Bulk electronic structure descriptors can be useful for developing a physical and possibly predictive model for perovskite OER activity, as has been presented for the hydrogen-evolution reaction (HER) on metal surfaces [198-200]. However, the predictive power of these descriptors can be limited by dynamic processes that occur on the surface of perovskite oxides, causing large deviations of surface chemistry and composition from that of the bulk structure used to perform electronic-structure calculations [201]. In such a case, electronic descriptors might fail to accurately capture the relevant mechanistic

parameters of the active surface. The most-dramatic and well-characterized examples of dynamic surface phenomena among perovskite oxides involve cobalt-based materials with partial substitution of alkaline-soluble species, like Sr^{2+}, at the A-site. $Ba_{0.5}Sr_{0.5}Co_{0.8}Fe_{0.2}O_3$ (BSCF), was proposed to be active based on its optimal e_g electron count of around unity [53], but was later found to be unstable during OER [202]. Large proportions of the surface and eventually parts of the bulk "amorphized" via Sr-leaching and oxygen-vacancy formation forming an OER active $Co(Fe)O_xH_y$ surface phase[202], similar to that made by other methods such as electrodeposition [203]. In a related study, a surface Co/Fe spinel oxide minority species on the underlying BSCF perovskite was determined to be responsible for dynamic, reversible conversion to an oxyhydroxide[204]. Sr-segregation and leaching, oxygen-vacancy formation, and subsequent surface reconstruction has also been clearly shown for the $La_{1-x}Sr_x CoO_3$ (LSCO) family of perovskites [205-207]. The implication of these studies is that rationalization of activity based on bulk electronics of the pristine BSCF and LSCO alone would fail to capture the real properties of the OER-active surface phase which has different oxidation states, composition, protonation state, and local structure. The active surface phase was, and likely is in many others, a completely different material. The intrinsic activity of the parent perovskite oxide with the pristine surface termination remains an open question. We hypothesize that, in fact, the presence of disordered conformationally dynamic surface phases with low activation barriers to rearrangement during the water-oxidation process is key to driving water oxidation at any reasonable overpotential.

The formation of nominally amorphous Co hydroxides has been observed on certain perovskites after OER and are active catalysts [61], especially in the presence of Fe impurities [208]. Whether formation of amorphous Ni hydroxides occur widely on nickelate perovskites is less clear. Inducing large structural changes by Sr-doping, as has been done with cobaltates, is not as accessible for nickelates because of the formation of impurities at low doping levels [209, 210]. Most of the insights so far have been from studies using epitaxial $LaNiO_3$ model systems[211]. Redox waves and thin ~2 unit cell-thick amorphous layers were observed by Bauemer et. al. and attributed to a NiO_xH_y-like species based on accompanying spectroelectrochemical data [62]. This work was recently extended, showing that redox-wave formation is also facet dependent with the highest stability and activity arising from the

[111] facet. X-ray absorption fine structure analysis (XAFS) showed a new peak assigned to edge-sharing NiO_6 octahedra after 16 h chronoamperometry (2.5 V vs RHE), as had been observed for Sr-doped $LaCoO_3$ [212].

Localized amorphization on $LaNiO_3$ epitaxial films has been observed with TEM in a different study [213], but the role of these regions in OER was not discussed. Substitution of Sr^{2+} and Nd^{3+} at the A-site of such films improved the OER activity [214, 215], which was attributed to improvements in Ni-O hybridization from an upward shift in the O-2*p* band energy relative to the Fermi level and to optimal occupation of the B-site e_g antibonding orbital, respectively. Notably, the films with the best OER activity in these two studies also appear to have the largest redox-active Ni wave present in the cyclic voltammograms. Adiga and coworkers showed that Sr-leaching, Ni redox-wave formation, and surface amorphization occurs during cycling of $La_{0.5}Sr_{0.5}Ni_{1-x}Fe_xO_{3-\delta}$; evidence strongly suggestive of surface reconstruction[216]. Similar redox waves were observed without Sr-doping in $LaNi_{1-x}Fe_xO_3$ (x = 0 – 0.5) with the largest being observed for $x = 0.375$ [217]. Bak *et al.* report a favorable "perturbation" (not amorphization) of oxygen octahedra in the near-surface layer of epitaxial perovskite nickelates after pre-reduction and pre-oxidation of the surface followed by exchange of Fe in the electrolyte. A related family of materials with high OER activity are the Ruddlesden-Popper oxides with formula $(AO)(ABO_{3\pm\delta})_n$. Forslund and coworkers examined the family of compounds $La_{0.5}Sr_{1.5}Ni_{1-x}Fe_xO_{4\pm\delta}$ (x = 0-1) for trends in OER activity. They found that redox waves were present for all samples and the size, shape, and peak position differed as a function of Fe-content. Catalyst activity increased with Fe content up to $x = 0.3$ (interestingly near the solubility limit of Fe in NiO_xH_y) [91], then decreased as x increased to 1. This was attributed to Fe inducing a "cross-gap hybridization" that allowed optimal charge transfer through Fe-O-Ni bridges. Although surface amorphization was ruled out by pH-dependent measurements, no post-mortem TEM or other microscopy was reported [80].

If perovskite nickelates are reconstructing at the surface to the thermodynamically stable nickel (oxy)hydroxide, understanding the interaction of the surface with Fe impurities is imperative, yet is rarely explicitly probed. This is especially important to understand because NiO_xH_y is much more strongly activated by Fe than is CoO_xH_y [49]. Here

we identify and analyze the emergence of redox-wave during/after OER catalysis on particulate and epitaxial $LaNiO_3$ samples and surface Ni-rich La_2NiO_4 nanorods which do not have any A-site or B-site doping. The size of the redox waves scale with the length of time of electrochemical treatment and their peak positions resemble that observed for NiO_xH_y. Upon introduction of Fe^{3+} into the Fe-free alkaline electrolyte, dramatic enhancement of the OER activity occurs along with an anodic peak shift of the redox waves for each sample. Normalization of the catalysts' OER currents to the integrated area of their redox waves suggests their activity in Fe-containing electrolyte is equivalent across the materials and in fact governed by the surface redox-active $Ni(Fe)O_xH_y$ or similar phases. Characterization with electrochemical impedance spectroscopy (EIS), atomic force microscopy (AFM), and X-ray photoelectron spectroscopy (XPS) suggest surface reconstruction occurs on these materials, although direct imaging by transmission electron microscopy was unsuccessful; likely because the reconstructed layers are very thin and/or heterogeneously distributed. These insights are consistent with the formation of a $Ni(Fe)O_xH_y$-like surface phase. We argue that in any electrolyte not rigorously cleaned of Fe impurities, the intrinsic ability for a perovskite to generate surface redox-active Ni (as-determined from the integrated area of redox waves) should be considered as the primary descriptor for its OER activity.

Results and Discussion

Redox-active Ni is apparent from cycling and grows with cycle number. To investigate the structural stability of $LaNiO_3$ (LNO) and La_2NiO_4 (214-LNO) during OER, the catalysts were cycled between 50 - 100 times between 0 and 0.8 V vs. Hg|HgO (0.9 – 1.7 V vs RHE) in 1.0 M KOH at a scan rate of 20 mV s^{-1}. Measurements were conducted in Fe-free and Ni-free 1 M KOH purified by methods detailed elsewhere [57, 58]. Catalyst films were made by spin-coating 80 µL of a 26.2 µg/µL ink which has a 5:1:1 mass ratio catalyst, acetylene carbon black, and Nafion (neutralized), respectively. Phase purity, powder morphology, and elemental composition of the LNO catalysts were confirmed by powder X-ray diffraction (PXRD), electron dispersive spectroscopy (EDX), scanning electron microscopy (SEM), and inductively coupled plasma mass spectroscopy (ICP-MS) given in Figures 60, 61 and 62. The rod-shaped geometry and composition of 214-LNO as

well as its tetragonal structure corresponding to the I4/*mmm* space group was confirmed using TEM imaging and X-ray diffraction (XRD) studies, respectively (Figure 63 and 64). The Brunauer-Emmett-Teller surface areas were acquired from their nitrogen adsorption isotherms (Figure 65). Epitaxial LNO was grown on $LaAlO_3$ substrates identically to those in Wang *et al.*[217], but without any aliovalent substitution. They were (001)-oriented and expected to have La-O termination based on the annealing temperature of 700°C used during synthesis [62], although the specific termination was not explicitly investigated in this study.

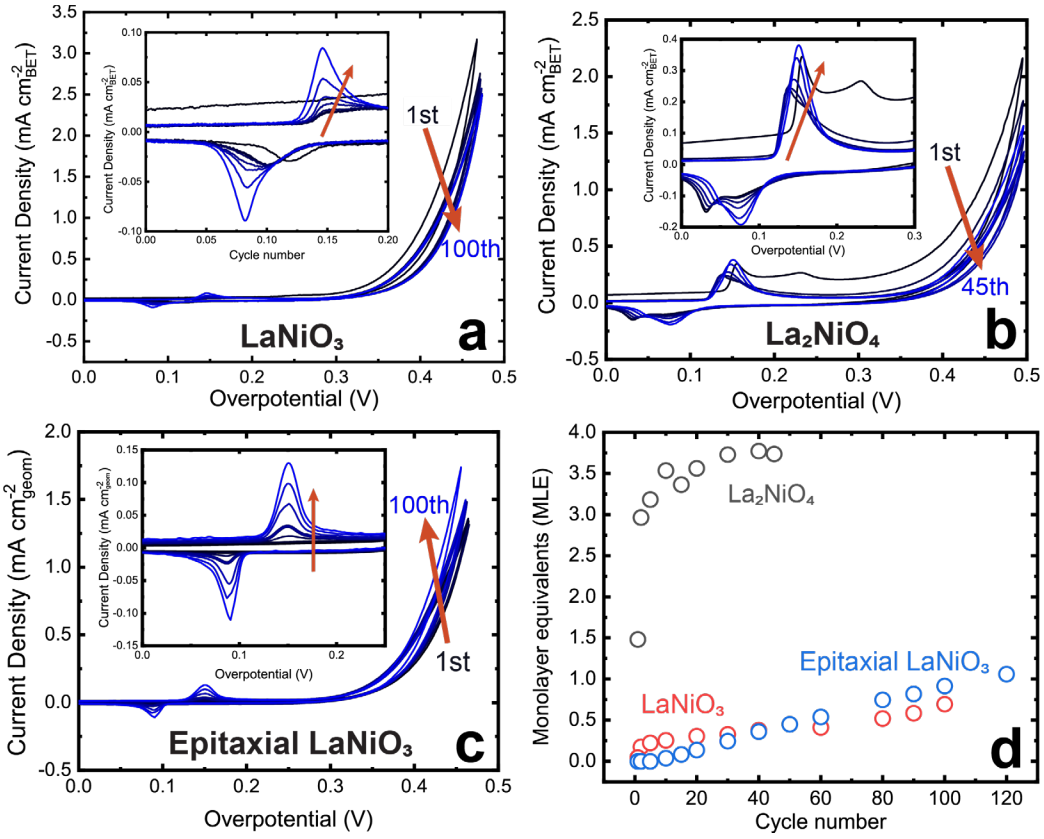

Figure 13. Extended cycling of $LaNiO_3$ in Fe-free KOH
Extended cycling in Fe-free 1 M KOH of **(a)** particulate LNO **(b)** 214-LNO and **(c)** epitaxial LNO. Inset red arrows indicate the progression from first to last cycle. **(d)** the number of monolayer equivalents (MLE) of hydroxide calculated from the integrated charge of the peaks in **(a-c)** and BET surface area of the catalyst film.

We hypothesized that if LNO is thermodynamically unstable during OER, as has been posited as a universal feature of oxides [218], restructuring to the stable NiO_xH_y phase would occur at the catalyst surface on a timescale dictated by the oxide material transformation kinetics. If the instability generated such a species, a minimum consequence

would be observable Ni redox peaks. This follows from the observation that peak-like redox behaviour is not observed for a double-layer charging process where the electronic charge is in a band state and the ionic charge is in the double layer (unreconstructed nickelate), but it is observed when redox-active species are coupled to conducting surfaces and reside within the electrochemical double layer[219, 220], as would be the case for surface phases of Co or Ni (oxy)hydroxide species formed from surface reconstruction. Such a structural change may also be evident in observable loss of crystalline phase purity, change in surface or bulk composition, and/or an increased nominal double-layer capacitance, depending on rate and extent. Figure 13 a-c shows the evolution of current response within the cyclic voltammograms of LNO, 214-LNO, and epitaxial LNO.

For all the nickelates shown in Figure 13, small but distinct pre-catalytic redox waves emerged and grew with continued cycling with comparable average peak positions of ~0.41 V vs Hg|HgO or 1.34 V vs RHE. There is also no clear plateau observed for this cycling protocol, suggesting further growth of the wave is possible. Future studies might investigate whether these waves plateau at a certain redox Ni coverage and/or amount of OER charge passed. The redox-peak positions agree with the known Ni^{2+}/Ni^{3+} redox process of nominally amorphous nickel (oxy)hydroxides [58, 152, 221] but seem to be closer to those observed in ordered β-$Ni(OH)_2$ than in disordered α-$Ni(OH)_2$. This could stem from the influence of the crystalline LNO substrate on the *in-situ* grown Ni surface phase, leading to higher structural order. Such influence of the substrate structure on a grown overlayer is reminiscent of strain-induced electronic structure changes in epitaxial $LaNiO_3$ films [222]. The elemental composition of the films using ICP-MS are given in Table 10, and in general did not change substantially from pristine stoichiometry after cycling.

For LNO, redox waves were initially small and could be easily missed in a study which was not explicitly looking for them. The epitaxial samples required ~ 20 cycles for the redox waves to become clearly observable. Baeumer *et al.* also observed distinct redox features in the pre-OER region when cycling single-crystal epitaxial $LaNiO_3$ films. The redox waves were immediately formed by the Ni-terminated films and their size decreased monotonically with increasing surface La termination. Redox-wave formation in that study was associated with the formation of amorphous 2 unit cell-thick NiO_xH_y [62]. That we see

redox waves in this study shows that extended cycling may be crucial to reveal possible reconstruction when La termination is present. Using the geometric area of the epitaxial film, pseudo-cubic lattice parameters of 3.81 Å (from Wang *et al.*[217]), and the integrated charge from the 100th cycle we find that ~1.4 layers or 4.6% of the total Ni in the LNO epitaxial layer implicated in the redox. This increases to ~2 unit-cell thickness (6% of the total Ni) after 145 cycles. Also notable is that the CVs of 214-LNO show two peaks during early cycles which merge into one in later cycles. This may occur by homogenization of two distinct redox Ni species by a dynamic surface process and cation mobility during cycling. Although we do not have direct evidence of this, the behavior resembles the process proposed to cause incorporation of "surface" Fe sites into the bulk/interior sites of NiO_xH_y [66].

These waves were confirmed not to be from Ni residues from the Fe-purification process. Ni amounts were routinely below the limit of ICP-MS detection of 0.57 ppb. Even if the maximum undetectable amount (~0.5 ppb) were present in a 10 mL volume electrolyte used in these experiments, the total amount of available Ni in the cell would only account for ~10% of the size of the largest redox waves. Further, we observe redox waves in $Co(OH)_2$-cleaned KOH (Figure 66) and see no observable redox peaks when $LaCoO_3$ (Figure 67) or a high-surface-area Pt coil (Figure 68) is cycled. These control experiments show the source of the Ni redox waves as being the surface of the given catalyst. The OER activity also decreases over time in Fe-free conditions. Although this could be due to formation of a less-active surface species, in part this is also likely due to small O_2 bubbles that build-up on the surface of the electrode even under vigorous stirring, which we show in Supplementary Figure 10 likely decreases the active area by ~10%.

To understand if the redox-active changes in the Ni surface structure only stem from a cyclic application of voltage, we also performed chronoamperometric studies. It was found that redox-active Ni growth was not dependent on the cyclical application of voltage. Chronoamperometry (CA) at 0.8 V vs Hg/HgO of a spin-coated film of LNO was performed for 1 h with diagnostic CVs scanned at a rate of 20 mV s^{-1} taken before the experiment and at 5-min intervals (Supplementary Figure 11). Integration of redox waves show that the amount of NiO_xH_y increases as a result of steady-state polarization.

Immersion of a pristine electrode in 1.0 M KOH was performed to test if this increase could occur from electrolyte soaking alone. No change in the redox wave size occurred (Figure 71). Application of anodic voltage was *required* for this Ni redox feature to increase in size.

If it is assumed the observed Ni-based redox features in Figure 13 originate from a (oxy)hydroxide-like structure, their integrated charge and catalyst BET surface area can be used to calculate a monolayer equivalent (MLE) of (oxy)hydroxide on the surface (Supplemental Calculation 2). This assumption is made based on the analogous behavior of the perovskite in the presence of Fe impurities to that of nickel (oxy)hydroxide and because we do not know the exact dimensions of the unit cells comprising the possibly reconstructed surface. The MLE value is the number of times the perovskite catalyst surface could be entirely covered by the redox-active Ni phase if it had the lattice parameters of β-$Ni(OH)_2$. Such an analysis would be particularly useful for characterizing these catalysts if it is confirmed that the redox species can be modeled as NiO_xH_y formed by dissolution-redeposition of Ni cations and if this new phase dominates the OER activity. We note that after surface reconstruction it may be that either $La_zNi_{1-z}O_xH_y$, for example as directly accessed from mixed precursors, or separate LaO_xH_y and NiO_xH_y phases[123, 223], as reported from decomposition of $La_{0.6}Sr_{0.4}CoO_{3-\delta}$, might be formed [224].

Using 1.7 nmol Ni cm^{-2} for a single MLE based on the unit cell parameters for brucite β-$Ni(OH)_2$ (International Crystal Structure Database structure code: 169978), as discussed by Batchellor *et al.*[225], we find that the 214-LNO has 3.1 ± 0.5 MLE and LNO has 0.3 ± 0.1 MLE of nominally β-$Ni(OH)_2$ after 30 cycles. Because the MLE parameter is proportional to the amount of redox-active Ni per cm^2 on the surface, it captures the intrinsic ability of a given catalyst to produce these species. Figure 1d summarizes the evolution of this intrinsic capacity for redox with cycle number. Particulate LNO and epitaxial LNO show the same rate of MLE growth indicating they likely have similar surface chemistry. By contrast, 214-LNO rapidly formed ~ 3 MLE before the growth slows in later cycles. If the entire catalytic surface reconstructs homogeneously (that is, it does not form isolated pockets), and the surface species resembles NiO_xH_y, then given long duration electrolysis one could expect multiple monolayers of reconstructed surface on

these nickelates.

The difference in observed intrinsic redox-active Ni can be explained by differences in surface termination and morphology between LNO and 214-LNO. Previous TEM and selected-area electron-diffraction (SAED) experiments show that the nanorods are primarily terminated by (001) facets along their longitudinal axis[226]. Previous work using depth-profiling low-energy ion-scattering spectroscopy (LEIS), atomic-resolution high-angle annular dark-field (HAADF) imaging, and electron energy loss spectroscopy (EELS) performed in aberration-corrected scanning TEM (STEM) mode revealed that these (001) facets were primarily Ni-O terminated rather than La-O terminated[227, 228]. By contrast we expect the epitaxial and LNO particulates to be primarily La-terminated because they were annealed at temperatures above that expected to promote Ni-termination [62]. Thus we attribute the difference in MLE quantity and initial restructuring rate to the pathways provided by the relatively Ni rich (001) surfaces of the nanorod bodies compared to LNO. The high proportion of Ni-terminated surface in the 214-LNO material could explain the faster rate of reconstruction of the first monolayer surface, but the apparent ease with which subsurface monolayers of NiO_xH_y form on 214-LNO suggest that the *sub*surface chemistry may also play a role. We hypothesize that oxygen non-stoichiometry and transport play roles in accessing the subsurface, especially considering that the electrochemical dissolution typically involves the formation of oxygen vacancies [205, 218] and oxygen is labile in the Ruddlesden-Popper oxides [229]. Further study is needed to understand how the concentration and formation energy of oxygen vacancies at the surface and bulk of these materials influences the restructuring process, if at all.

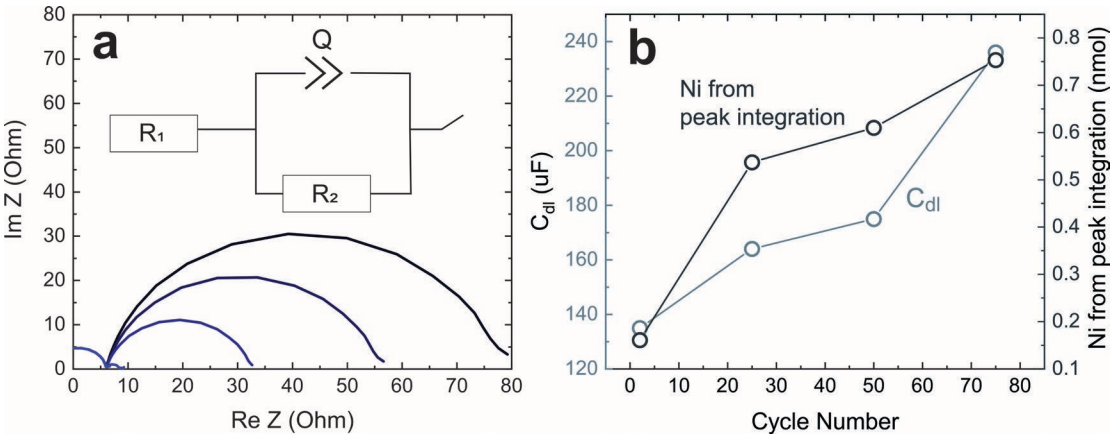

Figure 14. EIS of LNO at 1.7 V vs RHE

a) EIS of LNO at ~1.7 V vs RHE after 0, 25, 50, and 75 cycles in 1.0 M semiconductor grade KOH (not rigorously Fe-free) showing decreasing R_{CT} as a function of cycle number. The inset shows the equivalent circuit used to fit the data: solution and cell resistance, R_1, in series with a Randles cell element with constant phase element Q parallel with faradaic impedance, R_2. b) Double-layer capacitance (C_{dl}) and Ni from redox peak integrated area as a function of cycle number.

Surface reconstruction may also change the electrochemically active surface area. This can be probed from the double-layer capacitance (C_{dl}) obtained via electrochemical impedance spectroscopy (EIS) [225]. Impedance scans were taken every 25 cycles up to 75 cycles of LNO in unpurified semiconductor grade KOH and are shown in Figure 14. Note that EIS was measured with the DC potential in the OER region (~1.7 V vs RHE; 0.8 V vs Hg|HgO) rather than at open circuit because NiO_xH_y is only electronically conductive at potentials positive of the nominal $Ni^{2+/3+}$ reduction potential [225]. The C_{dl} measured in the non-faradaic open-circuit potential region is representative only of the conductive support, not the active surface phase. The vertically compressed nature of the EIS semicircles led to us model the capacitive element as a constant phase element given in the inset of Figure 2a. Representative fit to the data is given in Figure 72. The values of C_{dl} increased with prolonged cycling and the data directly mirror the increasing redox-active Ni from integrating the pre-OER redox wave. This result is consistent with the observed increase in surface area being due to the changing amount of Ni redox species at the LNO surface.

Assuming that the change in C_{dl} every 25 cycles is due to the formation of redox-active Ni phase, we can calculate the amount of Ni contributing to that change using the apparent capacitance per "monolayer equivalent" of NiOOH established from previous work [225]. Comparing this value to the change in redox-peak area, we find the two values are in good agreement (Figure 73). Consistency between the amount of Ni from the redox wave and that predicted from EIS using NiOOH as a model [225] further suggests that the Ni redox from LNO can be assigned to a (oxy)hydroxide-like phase. The observed decreasing charge-transfer resistance is likely from the incorporation of trace Fe from semiconductor grade KOH in this experiment, which would also explain the slight improvement of activity during cycling compared to the slight decrease observed in the data in Figure 13. We note that Fe was not measured explicitly here, and the role in activation by Fe impurities is discussed below.

$LaNiO_3$, La_2NiO_4, and epitaxial $LaNiO_3$ thin films are all activated by electrolyte Fe impurities. After cycling, if the surface phase on LNO is nominally NiO_xH_y, the introduction of trace Fe impurities into rigorously Fe-free KOH electrolyte should increase OER activity via the formation of $NiFeO_xH_y$ [173]. Following the extended cycling shown in Figure 13a-c, we spiked the electrolyte with 100 ppb Fe^{3+}. As shown in Figures 15a-c, dramatic enhancement of the OER activity was observed for all samples. In general, the largest rate of activity increase per cycle is observed in the first 1-4 cycles after spiking, which slows to a near-constant rate after this primary activation event. The different rate of activity enhancement in earlier cycles compared to later ones can be explained by initial rapid Fe adsorption to redox-active NiO_xH_y formed before the spike, making high-activity $Ni(Fe)O_xH_y$. In subsequent cycles, the current increases more slowly perhaps because all sites for Fe adsorption have been filled and formation of more high activity Fe sites is bottlenecked by the incremental increase in reconstructed Ni every cycle. Figure 74 shows this constant incremental increase in later cycles in the full Fe spiked profile of an epitaxial LNO sample. Further, the magnitude of the enhancement observed in the first cycle immediately after Fe-spiking was variable, implying that the Fe-activation process is controlled by a mix of factors such as mass transport and accessibility of adsorption sites. Extended cycling (>100 CVs) is not necessary to observe an increase of activity after Fe spiking. Fe-based activity enhancement reproducibly occurs in as few as 8 cycles and with only 30 ppb of Fe^{3+} in the electrolyte, an amount below the solubility limit of Fe^{3+} in 1.0 M KOH [169] and comparable to that expected in high-purity commercial electrolytes that have not been rigorously cleaned of Fe [56] (Figure 76). The latter observation aligns with activation from the uptake of soluble Fe and not from adsorption of FeOOH precipitate or colloids, although these may be relevant at higher Fe concentrations.

In a typical Fe-spiking experiment with electrodeposited NiO_xH_y, Fe adsorbs to nominally surface/edge sites immediately after spiking which increases the OER activity greatly, but the activity only marginally increases with further cycling and further Fe incorporation [173]. The Ni peak position also shifts anodically ~30 mV with 100 cycles in Fe-spiked conditions indicating strong interactions between Fe and the majority of the Ni sites [66, 173]. Using this result from Stevens *et al.*, we would expect an anodic shift of about 4 mV over 14 cycles (30 mV/100 cycles = 0.3 mV $cycle^{-1}$) if the redox-active Ni on LNO

resembles NiO_xH_y. Interestingly, the peak position after spiking indeed shifts ~4 mV (inset of Figure 15a) in total. Rod-shaped $La_2Ni_1O_4$ nanostructures (214-LNO) and epitaxial LNO also exhibit the same general change in OER activity after Fe-spiking (inset of Figures 3b-c). Anodic shift of the redox peaks has been observed for $La_{0.5}Sr_{1.5}Ni_{1-x}Fe_xO_{4+\delta}$ [80] increasing Fe substitution consistent with the growth of a NiFeOOH phase.

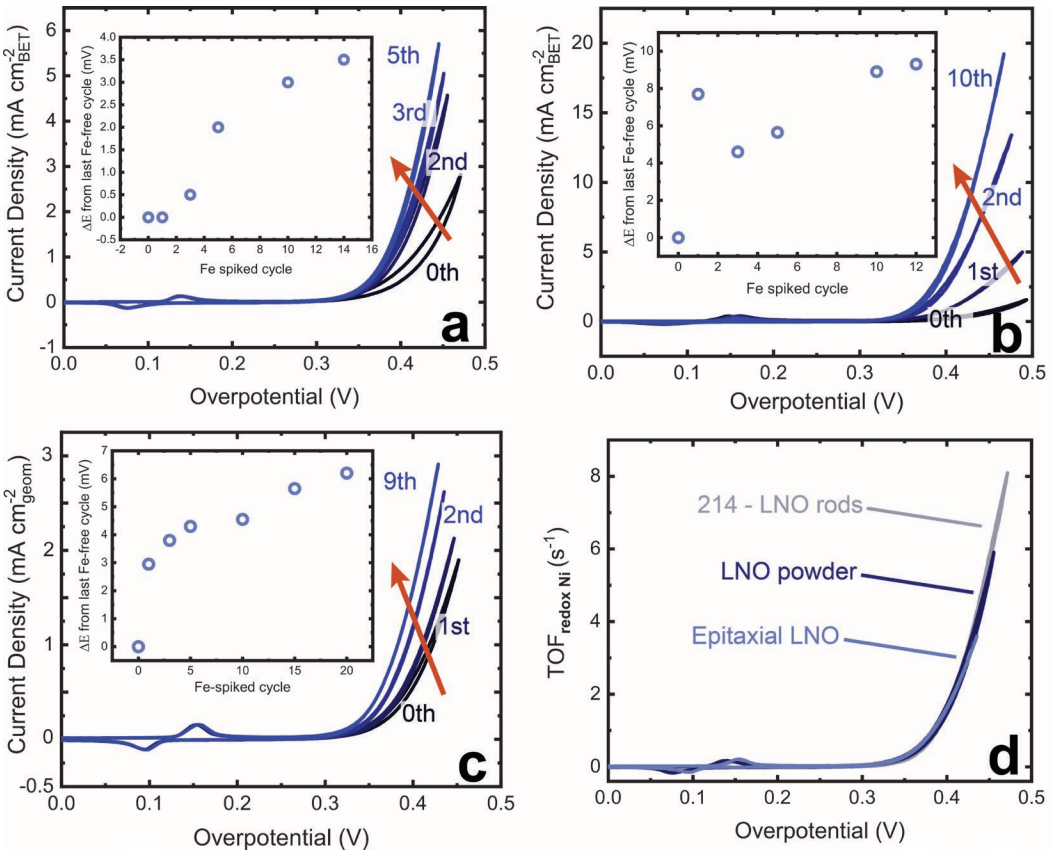

Figure 15. Activation of $LaNiO_3$ and La_2NiO_4 by intentionally introduced Fe.
Comparison of activation of **(a)** particulate $LaNiO_3$, **(b)** La_2NiO_4 nanorods, and **(c)** epitaxial $LaNiO_3$ films upon introduction of 100 ppb $Fe(NO_3)_3$ into Fe-free 1.0 M KOH electrolyte at room temperature. The 0th cycle is the last Fe-free cycle before 100 ppb Fe was spiked into electrolyte. The insets illustrate the change in average redox peak position with cycle number. **(d)** TOF for the cycle corresponding to full activation by Fe (2nd or 3rd depending on the pace of activation) normalized to the redox active Ni from the integrated charge of the anodic redox peak of the 0th cycle. This data suggests that the active surface phases formed are the same on all three of the samples.

In the literature many electronic structure parameters have been suggested to describe such an activity difference between perovskites including position of the O-2*p* orbitals relative to the Fermi level [197] the filling of the antibonding e_g orbital [53, 157], and the charge-transfer energy Δ where smaller Δ is associated with increased Ni-O covalency [230]. We use

the e_g orbital filling for La_2NiO_4 and $LaNiO_3$ as an example. This values has been calculated as ~0.74 and 0.91, for 214-LNO and LNO, respectively [231]. Based on the idea in many works that the best perovskite catalysts are those with near unity filling of e_g antibonding orbital of Ni [53] we would predict that LNO should outperform 214-LNO. In Fe-free conditions this appears to be case, but in Fe-spiked conditions (and therefore in realistic electrolysis conditions) this prediction fails (see the overlay of CVs after activation in Figure 75).

Instead let us suppose the activity is dominated by a $Ni(Fe)O_xH_y$ – like phase formed from the surface Ni and adsorbed Fe. We can then immediately rationalize the higher activity of 214-LNO because at any cycle, it will have a higher areal density of redox active Ni than LNO. It follows that if this $NiFeO_xH_y$ species has a similar intrinsic activity across the materials tested, then normalization of the current to the integrated Ni-related redox-peak area should yield equivalent polarization curves. This idea appears to be justified given the good match between samples once normalized to integrated charge (Figure 15d). Ultimately, these data illustrate that rather than a bulk electronic descriptor, a surface-chemical descriptor, namely, the surface density of redox-active Ni is a more suitable descriptor for activity under realistic conditions.

Because the introduction of Fe is a shared trait among these oxides, it can be used as a convenient indicator to determine whether the materials reconstruct, a strategy that has been highlighted recently in the $Li_xCo_{1-x}O_4$ family of materials [232]. Interestingly, we find that $LaCoO_3$ exhibits no such Fe activation (Figure 67), which suggests its surface is more stable and does not as easily form cobalt-oxyhydroxide-like surface-phases generally consistent with previous literature [233]. Given that these materials are isostructural (rhombohedral, belonging to $R\bar{3}c$ space group) [234], we hypothesize that the enhanced stability with respect to surface-phase reconstruction arises from stronger Co-O bonding compared to Ni-O [130]. This is also consistent with the higher surface-reduction temperature as observed from H_2 temperature-programmed-reduction studies which indicate stronger Co-O bonding in $LaCoO_3$, as compared to Ni-O bonding in $LaNiO_3$ [234].

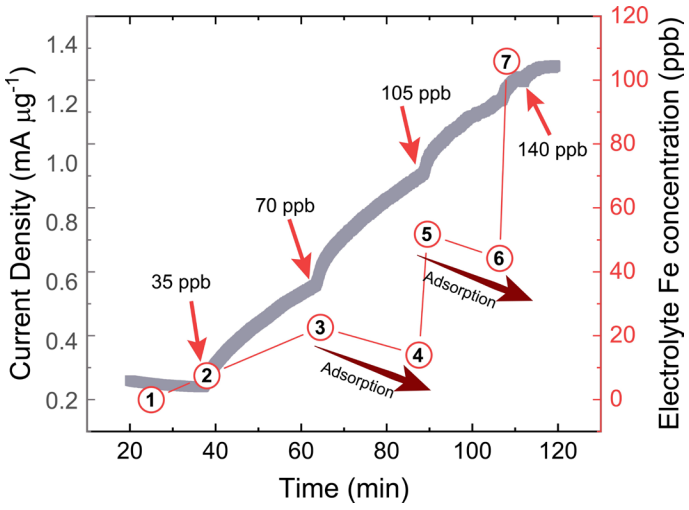

Figure 16. Chronoamperometry with intermittent Fe-spikes
Current is reported as mass activity versus time. Yellow arrows show points where a replicate additional Fe spike was performed. Concentration labels (black text) are the nominal Fe concentration at the time of the spike. Numbered circles indicate actual concentration of Fe (red axis) in the electrolyte measured from ICP-MS. This data shows Fe absorption from the electrolyte to the solid is coupled with increases in OER activity of the catalyst.

Activation of the reconstructed perovskites after spiking a small amount of Fe into 1.0 M KOH was evident in the cyclic voltammograms. Figure 16 shows 2 h of chronoamperometry at 1.7 V vs RHE on a LNO electrode with additions of Fe at regular intervals. The yellow arrows indicate the approximate time and nominal concentration of electrolyte Fe after the spike while the red squares show the actual concentration of Fe in an aliquot of the electrolyte which was later measured by ICP-MS. The concentration of Fe in the electrolyte before the experiment was below the detection limit of ^{57}Fe in our ICP-MS of 3.9 ppb. Points 2, 3, 5, and 7 are aliquots of the electrolyte taken immediately after (~10 s) successive spikes of Fe. Points 4 and 6 are aliquots withdrawn before the corresponding spikes. Note that between the 2nd and 3rd, and 3rd and 4th spikes, the Fe concentration in the electrolyte decreases while the OER activity increases. This observation provides direct evidence that Fe adsorption from the electrolyte onto the electrode correlates with higher OER activity. Moreover, the impact of Fe adsorption on activity is noticeable even without performing any cyclic voltammetry, an observation which emphasizes that Tafel slopes and other activity parameters from chronoamperometric data must be collected in purified electrolyte for these materials to

avoid strong effects of Fe-activation. Figure 16 also shows that pre-cycling the catalysts to generate redox active Ni is not necessary for increased activity in the presence of Fe; Fe enhancement should be expected from the moment the catalyst film adsorbs Fe.

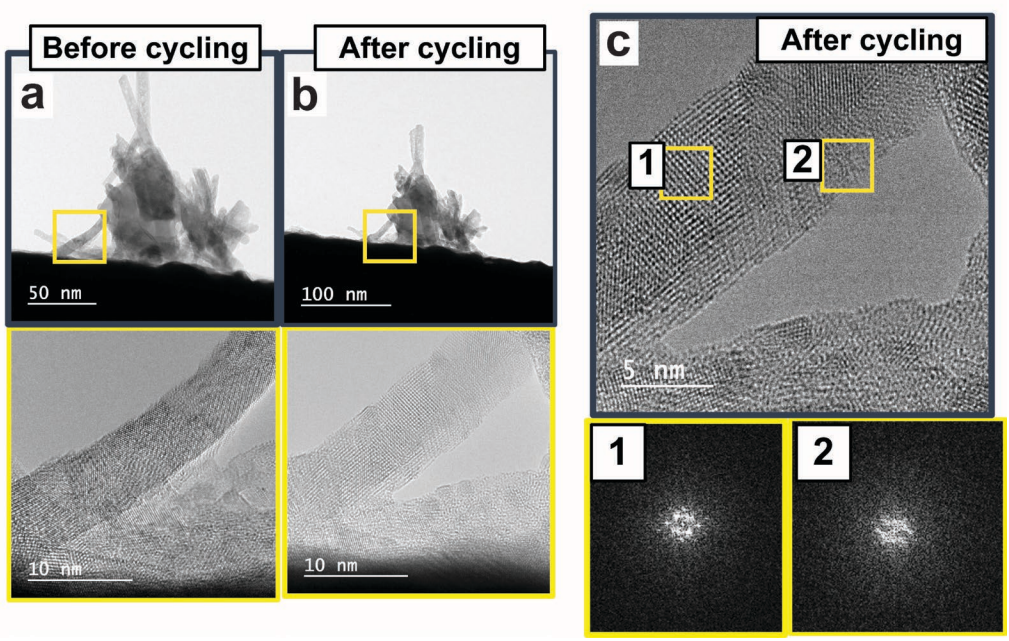

Figure 17. Identical-location TEM of a cluster of 214-LNO particles
Identical-location TEM of a cluster of 214-LNO particles **(a)** before and **(b)** after 300 cycles on a gold TEM grid. Panel **(c)** shows fast Fourier transforms (FFTs) of two regions on the yellow boxed region. Comparing before and after cycling, the identical location appears to show a thicker nanorod. We suspect this is an artefact of non-identical imaging conditions and/or slit rotation of the nanorod during the electrochemical testing.

Identical location TEM (IL-TEM) was conducted on the LNO particulate materials before and after cycling with the aim of observing any obvious signs of structural changes such as amorphization. No clear surface layers were observed, likely because of the near-atomic thinness of any reconstructed layers. The larger per-surface-area growth of redox-active Ni on 214-LNO would increase the likelihood of observing structural changes. Figures 17 shows the near-surface structure of a cluster of 214-LNO nanorods before (Figure 17a) and after (Figure 17b-c) 300 cycles in 1.0 M KOH. The similar appearance of the cluster indicates that the same area and particles were successfully imaged both before and after cycling. We observed regions which apparently lack the crystalline order of neighboring areas after cycling as can be seen by the fast Fourier transform (FFT). This is

a cautious interpretation because TEM studies can be subject to a variety of imaging artefacts, especially at edges, and over-interpretation. The disordered surface hydrated oxyhydroxide layers are thin, would be expected to scatter with low intensity, as they lack long range order, and may be unstable in the electron beam[235]. Selected-area electron-diffraction experiments did not suggest dramatic changes in crystal structure after cycling (Figure 77 and Table 9), consistent with the thinness of the surface-reconstructed layer. The inability to routinely observe reconstructed surfaces with TEM places a premium on careful electrochemical experiments as an alternative.

Finally, we performed post-mortem characterization by atomic force microscopy (AFM) and X-ray photoelectron spectroscopy (XPS) on the cycled, Fe-spiked epitaxial film corresponding to Figure 15c to learn about changes in the surface topology and chemical state. The 30-unit-cell films have a pseudocubic c-lattice parameter of ~3.81 Å [217] and are ~11 nm thick. The AFM scans shown in Figure 18 indicate roughening of the surface of the cycled film (arithmetic average roughness R_a = 4.6 nm) compared to the pristine film R_a = 0.45 nm consistent with previous AFM images of cycled epitaxial nickelate films [216, 217]. The magnitude of the roughness changes are highly suggestive of surface restructuring and formation of secondary phases which could be composed of one or more oxides or hydroxides of La, Ni and Fe. Assuming a component of the surface is NiO_xH_y, the large magnitude of the roughening could be driven by adsorbed Fe impurites by formation of $Ni_zFe_{1-z}O_xH_y$ or FeO_xH_y in a manner observed when Fe is intentionally added to NiO_xH_y nanoplatelets [102, 153].

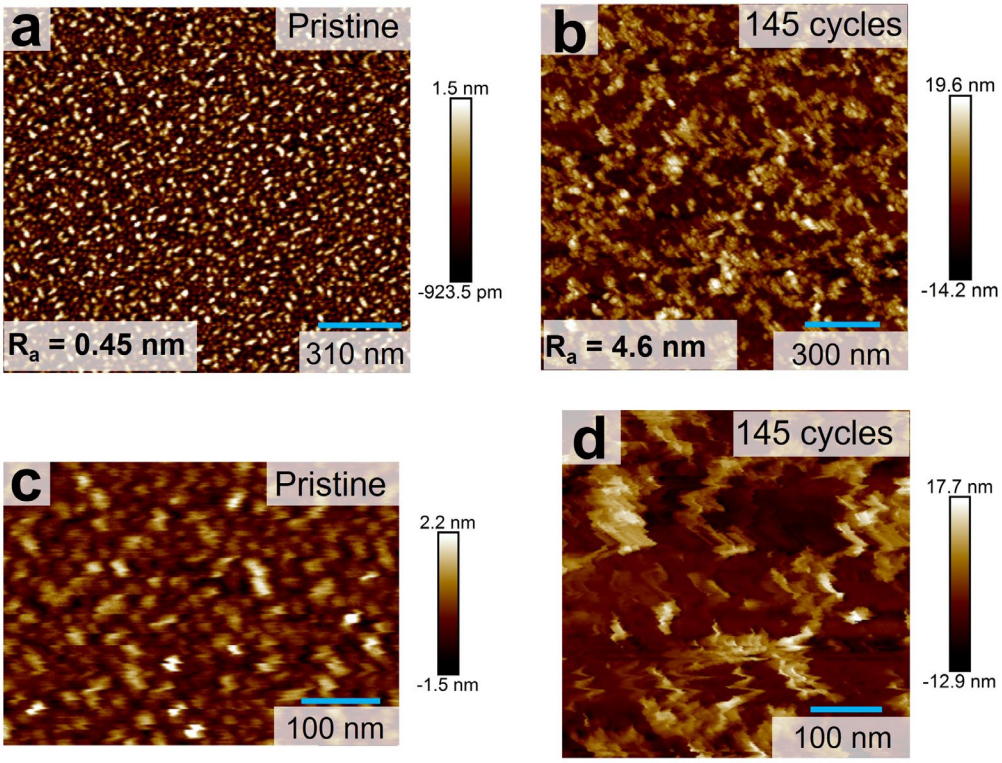

Figure 18. AFM of $LaNiO_3$ epitaxial film before and after cycling
Atomic force microscopy image of the same **(a,c)** pristine epitaxial LNO film (note diffferent scales) and **(b,d)** the same film after cycled 120 times in Fe-free 1 M KOH followed by 25 times in 100 ppb Fe-spiked 1 M KOH. The arithmetic average roughness is given by R_a and indicates that cycling causes topological restructuring.

X-ray photoelectron spectroscopy (XPS) was used to detect the formation of new surface Ni phases on LNO electrodes after extended cycling (Figure 19). Unfortunately, the XPS spectra of the most intense lines – Ni 2*p* and La 3*d* – are difficult to interpret and deconvolute. Both Ni 2*p* and La 3*d* have multiplet structure and accompanying satellites [236-238], which directly interfere with each other. Consequently, little information was obtained from these regions. Therefore, we restrict our interpretation to the O 1*s* region where large, reproducible changes were observed. Figure 19 a, b shows the comparison of O 1*s* XPS for LNO and epitaxial LNO before and after extended cycling. After cycling, a significant decrease in the characteristic lattice oxygen feature located at ~528 eV was observed in the O 1*s* XPS core level spectra for both samples and resembles that of pure $Ni(OH)_2$ [239, 240]. Based on the cycling data in Figure 1, we estimated the depth of redox activity for the epitaxial sample would be about 1.5 nm after 300 cycles. Mild sputtering of the epitaxial film through the reconstructed surface with an argon cluster source caused

the lattice oxygen peak to reemerge. The peak at higher binding energies, associated with weakly adsorbed oxygenated species and oxidized carbon, may also increase due to oxidation of the ionomer binder [241] and/or surface hydroxylation after exposure to alkaline electrolyte. Given the signs of reconstruction in the cyclic voltammetry, EIS, and AFM, the loss of the lattice-oxygen feature is consistent with transformation to NiO_xH_y. The disappearance of the ~528 eV component within the O 1*s* spectra of initially crystalline nickel-based oxides upon electrochemical conditioning is not without precedent and has been shown to correspond to conversion of NiO to $Ni(OH)_2$ [152]. It has also been observed after cycling epitaxial LNO [216], similar to our observations.

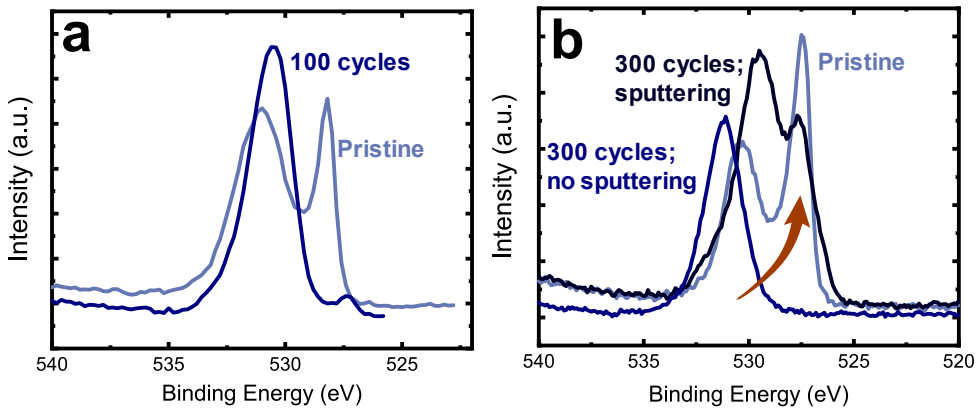

Figure 19. X-ray photoelectron spectroscopy of O - 1*s* region of $LaNiO_3$
O 1*s* spectrum of **(a)** a spin-coated particulate LNO electrode before and after cycling and **(b)** an epitaxial LNO electrode after 300 cycles (dark blue), after mild sputtering with an argon ion source (black) and the pristine epitaxial sample (matte blue).

However, the decrease in intensity in the low binding-energy region might also arise from formation of a layer containing weakly adsorbed species like water, hydroxide, and/or adventitious carbon which could attenuate the signal originating from the underlying crystalline O^{2-}. We tested whether the disappearance of the lattice oxide feature in epitaxial films occurs from immersion in KOH alone. Figure 78 shows that the lattice oxygen feature is largely retained, implicating structural change from electrochemical treatment as the reason for the changes to the O 1*s* spectra. As shown in Figure 19, sputtering can be used to remove the layer of putative reconstructed material.

The broad role of restructuring in electrolysis. The results presented in this study adds a class of materials, perovskite and Ruddlesden-Popper oxide nickelates, to the growing roster of pre-catalysts where Fe impurities, whether introduced intentionally or

not, play an important role in boosting OER activity. The role of Fe has already been well established among pure electrodeposited NiO_xH_y [58, 79, 221], Ni-based chalcogenides [156, 242], and CoO_xH_y [243]. A common theme emerging from these diverse materials is amorphization of A-site doped perovskite oxides, leading to the formation of active Fe-containing surface phases that are the actual agents responsible for catalysis [205, 244] and that these phases are the ones largely influenced by Fe impurities in the electrolyte. The interaction with Fe impurities holds critical implications not just for intrinsic activity studies of perovskite nickelates, *but for any investigation using electrocatalytic materials in alkaline electrolyzers*, which generally do not use highly purified electrolytes and use stainless-steel components. The fact that nickelates with distinct structures, rhombohedral, oxygen-deficient particulate $LaNiO_3$, and tetragonal oxygen super-stoichiometric nanorod La_2NiO_4, are activated by Fe suggests these effects could be a universal phenomenon that has gone relatively unacknowledged. Interestingly, in this work the surface chemistry changes occurred in catalysts with full La-stoichiometry at the A-site while typically some substitution of the La at the A-site with an alkaline earth metal is required to observe instability in Co oxides[204, 205, 245, 246].

Other studies have also reported pH-dependent OER catalytic activity for perovskite oxides in which activity decreases with pH. This observation, coupled with isotopic oxygen labelling and on-line electrochemical mass spectroscopy data showing oxygen exchange, has led to the proposal of a lattice-oxygen-evolution (LOER) mechanism [213, 247]. An alternate proposal is that an oxidizing potential drives the reconstruction of the pristine material, a process which requires oxygen lability and exchange. The new surface species may be sensitive to soluble Fe, especially when the B-site is occupied by Ni or Co. Consequently, the decreasing activity with decreasing pH could be, at least in part, due to the corresponding decrease in soluble Fe by an order of magnitude with each unit decrease in pH, as has been suggested recently for $La_{1-x}Sr_xCoO_3$ [205]. Since lattice-oxygen exchange has been detected for NiO_xH_y [248], it is still not clear whether LOER after reconstruction is from the perovskite or the *in-situ* formed NiO_xH_y.

Conclusions

Both $LaNiO_3$ and La_2NiO_4 exhibit a growth of redox-active Ni species that

increases in quantity as a function of cycling and duration of chronoamperometric conditioning. Fe-spiking experiments demonstrate that high OER activity is achieved upon the introduction of Fe. After Fe introduction, further activity increase with cycle number correlates with the increased quantity of redox-active Ni. Analysis of impedance spectroscopy, XPS and TEM data support the proposal here that generation of redox-active surface species involves a structural transformation leading to increased electrochemically active surface area with cycling, a decrease in nominally surface O^{2-} content compared to -OH, and the nominal amorphization of the catalyst. Normalization of the catalytic current to the integrated charge corresponding to redox-active Ni available during the Fe spike experiments show that the redox-active species share similar OER activity characteristics despite disparate structures of the host $LaNiO_3$ and La_2NiO_4. La_2NiO_4 displays a higher tendency for the growth of redox-active Ni than $LaNiO_3$, indicating the significance of Ni-O termination in the formation of these surface species. Although the analogy between the reconstructed perovskite surface in Fe-spiked conditions and $NiFeO_xH_y$ is strong, the precise surface structure remain under debate and the characterization here is not sufficiently detailed to settle it. Surface-sensitive X-ray absorption fine stucture analysis and *in situ* XRD studies would be extremely valuable for reconciling the electrochemical observations here to the bulk structure of the perovskites.

The data and analyses reported here show that interpretations of intrinsic activity and the correlation of this activity to electronic and structural features of the pristine material necessitate Fe-free conditions and pre- and post-mortem surface analysis. Reports of intrinsic activity of nickelate perovskites and related materials should be made with caution – especially if only a single voltammetry sweep or chronoamperometry is performed in unpurified electrolytes without paying close attention to pre-catalytic redox waves which may become prominent with further cycling. The implications of these results are that in any practical alkaline electrolyzer system (unpurified 30 wt% KOH and with stainless-steel cell components) the activity of a perovskite nickelate catalyst will be controlled by its extent of surface reconstruction and interactions with Fe impurities. Future effort could focus on characterizing and tailoring the catalyst composition, along with the precise electrolye composition, to tune the activity and stability of this surface phase. The formation of these surface phases, their interaction with the underlying substrate, and

catalytic turnover of intermediates, must fundamentally be related to nature of bonding within the material as well as adsorbates, and therefore its electronic structure. The use of descriptors from quantum-mechanical calculations of electronic structure to understand structure-restructuring relationships in the presence of potential, water, and alkali electrolyte would thus be a valuable addition to the field of heterogeneous OER electrocatalysis. Such approaches would complement typical calculations of intermediate binding energies [249].

Methods and Materials

Synthesis. $LaNiO_3$ was prepared using a nitrate precipitation method. 1.95 mmol of nickel (II) nitrate hexahydrate and 2 mmol lanthanum (III) nitrate nonahydrate was weighed out and dissolved in 10 mL 18.2 MΩ nanopure water. A slight under-stoichiometry was chosen for the nickel nitrate to prevent minor NiO species formation. A mixed La/Ni hydroxide was precipitated by rapid addition of a 4 mL + 4 mL mixture of water and semiconductor-grade tetramethylammonium hydroxide. The resulting mixture was stirred for 30 min to ensure complete reaction. The solid was recovered with centrifugation, ground in an agate mortar and pestle for 5 min and calcined in air at 900 °C for 12 h. The solid was ground and refired until phase-pure samples were obtained based on powder X-ray diffraction (PXRD) patterns. La_2NiO_4 rods were prepared using a reverse microemulsion procedure described in prior work [226]. A reverse-microemulsion-based technique was used for the synthesis of rod-shaped La_2NiO_4 (214-LNO) nanostructures [227, 250]. A typical synthesis of 214-LNO involved the reaction between two quaternary phase microemulsions. Both the microemulsions contained equal amounts of cetyltrimethylammonium bromide (CTAB; 11.0 g), hexane (Sigma Aldrich, HPLC grade), and *n*-butanol (Sigma Aldrich >99%). The difference between the two microemulsions was that one of the microemulsions contained stoichiometric amounts of $La(NO_3)_3{\cdot}6H_2O$ (Sigma Aldrich, >99.999%) and $Ni(NO_3)_2{\cdot}6H_2O$ (Sigma Aldrich, >98%) salts (2 mmol equivalent) dissolved in 1.155 mL of deionized (DI) water (>18.2 MΩ). KOH solution was used in the anionic microemulsion to aid in precipitation of the hydroxides. The morphology of the samples can be changed by varying the ratio of water used to dissolve salts and that of CTAB. A water to CTAB ratio of 1.6 was used to obtain rod-shaped 214-

LNO nanostructures. The two microemulsions were mixed and subsequently allowed to react for 4 h to form a sol-gel mixture of metal hydroxides. Subsequently, the formed hydroxides were collected by centrifugation, and washed three times with ethanol and three times with deionized water. The precipitate was dried in an oven in air at 80 °C overnight, followed by calcination in Ar at 835 °C for 2 h (heating rate: 2 °C/min).

Epidtaxial $LaNiO_3$ thin films with the thickness of 20 unit cells (~8 nm) were grown on (001) oriented $LaAlO_3$ substrates by using O_2-plasma–assisted molecular beam epitaxy (OPA-MBE). The growth details have been described elsewhere and films prepared in this manner are expected to yield a surface with a (001) orientation [215]. The substrate temperature was set to 700 °C during growth which is expected to yield primarily La-O termination based on the report by Baeumer, *et al.*[62] although this was not explicitly investigated here.

Electrochemical measurements. Catalyst films were either prepared by spin-coating or by drop-casting onto Pt/Ti-coated (25 nm Pt on 50 nm Ti) glass slides made using electron beam evaporation. Choice of coating technique is indicated for the given data in the text. Spin-coated films were chosen for intrinsic activity measurements so that electron-transport distances were reduced relative to drop-cast films and conductive binder, which oxidizes during OER, could be excluded in ink preparation. Ink for spin-coating was ~5:1 by mass of catalyst to Nafion binder suspended in solvent of 2:1 by volume of isopropanol to nanopure water. Inks were sonicated for at least 1 h before coating. A typical spin-coating procedure involved adding ~80 uL onto the substrate after sonication and spinning at 3000 RPM for 2 min. Nafion was neutralized with a few drops of Fe-free 1.0 M KOH to avoid possible dissolution of the catalyst by reaction with acidic groups. Spin-coated Ti/Pt slide pieces were then assembled into working electrodes as described elsewhere [251]. All electrochemical measurements were performed in Fe/Ni free 1.0 M KOH (prepared from semiconductor-grade KOH using the standard methods from our team [57]) using a Hg|HgO reference electrode calibrated against RHE and Pt coil counter electrode. Plastic cells were used and cleaned with 1.0 M sulfuric acid before experimentation to remove trace Fe from the cell. All electrochemistry was performed using a Biologic SP-300 potentiostat. Impedance spectroscopy was performed from 1 Hz to 7 MHz from the DC voltage of 0.8 V vs Hg|HgO with 10 mV AC amplitude. The impedance data was fit to

the equivalent circuit depicted as an inset in Figure 3b; the circuit includes a solution and cell resistance, R1, in series with a Randles cell element with constant phase element Q2 parallel with faradaic impedance, R2. A constant phase element was chosen because its impedance is similar to that of a pure capacitance, but more closely fit the slightly depressed semicircular shape of the measured impedance. Uncompensated series resistance (R_u) was extracted using impedance spectroscopy at 0 V vs Hg|HgO from 1 Hz to 1 MHz and was estimated from the associated Nyquist plot as the value of the real component of the impedance at high frequencies where the imaginary impedance approaches zero. All electrochemical data is iR_u-corrected unless otherwise indicated.

Characterization. XRD studies were performed using a powder diffractometer (Bruker D2 Phaser) with a Cu Kα source. Scans were obtained between a 2θ of 20-80°. ICP-MS measurements (ThermoFisher iCAP-RQ) were performed in kinetic energy discrimination mode with calibrations of all measured elements having R^2 values > 0.998. All digestions of catalyst films were done with concentrated TraceMetal® grade nitric acid (Fisher Scientific). Laboratory control standards containing known amounts of La, Ni, Fe, and Co were run at intervals between unknown samples to continually verify good performance of hardware and internal standards. XPS studies were done using an ESCALAB 250 (ThermoScientific). Spectra were obtained using an Al Kα monochromated (150 W, 20 eV pass energy, 500μm spot size) X-ray source. All samples were optimally charge-neutralized using an in-lens electron source combined with a low-energy Ar^+ flood source. TEM data was acquired using a FEI 80-300 kV (S)TEM equipped with a spherical aberration image corrector. All data was collected at 300 kV. For IL-TEM experiments, a PELCO gold pinpointer grid (400 mesh, Ted Pella) was dip-coated by repeated rounds of immersion into the catalyst ink until a visible change of the grid color to that of the ink was achieved. Loading was not measured or controlled since only some locations with good contact between grid and catalyst were required for these studies. Powder X-ray diffractograms were obtained with a benchtop Bruker D2 Phaser.

For BET surface area experiments, 50 – 80 mg of samples were loaded into BET sample tubes without the use of solvent, ensuring that sample did not touch the neck of the BET tube. Then, samples were degassed under high vacuum at 170 ºC on a Micromeritics ASAP 2020. Degassing was considered complete when the outgas rate fell below 2.5

μtorr/min. Once the degassing was completed, the samples were subjected to N_2 surface sorption measurements and BET surface area was calculated.

V: SUMMARY AND OUTLOOK ON FUTURE RESEARCH

Chapter I showed that the development and deployment of advanced green technologies is not only necessary but urgent. The timeline for the energy transition is short relative to the staggering scale of the challenge and the consequences of failing will be felt on a global scale by the most vulnerable segments of our population. I offer the following future research directions with this urgency in mind. I take as a guiding assumption in the discussion below that the highest impact research directions are those that bridge the realms of basic and applied water electrolysis science, an assumption based on several years of immersion in the literature and electrolysis science community.

Chapters II and III offers a useful physical picture for engineers of advanced liquid alkaline electrolyzer anodes: the OER activity of transition metal hydroxides is driven by a small fraction of dynamically adsorbed Fe sites the activity of which increases exponentially with temperature. If higher activity is desired by increasing the number of catalytic sites, the total mass loading of the hydroxide is not necessarily the parameter to optimize unless one understands how the number of edge/defect/adsorption sites scales with that total loading. Increasing catalyst loading may yield diminishing returns as a result. Since the controlled formation of surface Fe sites using chronoamperometric Fe-spiking and optimization of ICP-MS Fe detection has been developed only recently, with the completion of this dissertation, the likely complicated nexus between surface Fe site availability, hydroxide loading, synthesis method, structure, and transition metal identity remains virtually unknown.

Understanding Fe-site management in relationship to intrinsic catalyst chemistry is not the only knowledge gap worth pursuing. The effects of high temperature, current density, and electrolyte concentration are also poorly understood at the academic research level, yet are critical to high performance anodes in industrial settings. There is good reason to think these conditions matter for Fe site management. Thermodynamic stability of Fe, Ni and Co species are a function of pH and applied bias.[252] Chapter II is a demonstration of this reality because the experiments therein rely on the knowledge that increasing the potential above ~1.35 V RHE causes a restructuring of $Ni(OH)_2$ to NiOOH and cycling the

potential causes Fe inclusion into bulk sites. Chapter IV shows that the surfaces of $LaNiO_3$ and La_2NiO_4 undergo bias-prompted reconstruction, another demonstration. The maximum potential sampled in those studies was 1.7 V, well below typical electrolyzer cell voltages. OER kinetics of the thermodynamically preferred phase are in turn governed by free energy activation barriers to reactions occurring within an electrochemical double-layer that is a function of bias, electrolyte concentration, and temperature. Thus extension of the methods of Chapter II and III to industrial electrolyzer applications should provide bridging design principles. It should be noted that this discussion is restricted to OER *activity* concerns, but *stability* is at least as, if not more, important for industrial anode development. Bipolar alkaline stacks are especially plagued by instability arising from the formation of reverse currents between adjacent cells[253-256] - another understudied phenomenon that must be considered in the problem of Fe site management.

Based on what I learned in completing Chapter IV, I see a shift in perovskite oxide OER catalyst research away from one-step connection between electronic descriptors and activity and toward two-step connection between descriptors, surface reconstruction, and activity as pivotal for the field. In other words, research that involves structure-restructuring relationships should better predict catalyst activity than the historical norm of structure-activity relationships. Fortunately, electronic descriptors of the bulk apparently correlate with surface properties[197] so this shift need not be a painful one. Indeed, I expect much prior work can be reframed in light of what we now know about surface reconstruction. For example, if surface reconstruction is a function of bond strength at the surface (as it should be based on common chemical intuition) then a descriptor reporting on antibonding character in an oxide[53] should be relevant. An exhaustive reframing of this kind is beyond the scope of this dissertation, but is nonetheless promising for future efforts.

Repurposing old descriptors is one approach to new insight, but generation of new descriptors would also be useful. Chapter IV of this thesis suggests two for lanthanum nickelate: the integrated Ni wave per microscopic surface area (mC cm^{-2}) and the total iron adsorbed to the surface. A simpler version of current electronic descriptors could augment these experimentally accessible ones. I suggest that the electronegativity of the B-site metal cation is a better candidate than popularly-cited ones like the metal-oxygen covalency or

O-2*p* band position relative to the Fermi level. Though intriguing I find these descriptors needlessly far removed from widely understood core chemistry concepts. The viability of this suggestion is explored below. I acknowledge the possibility that there may be some regimes where another descriptor, like d-electron count, could be better suited, and that the below discussion probably only holds when large deviation in bond distances do not occur, but it is my hope that this discussion broadly encourages critical reflection on the utility of electronic descriptors.

My reasoning behind the suggested reliance on B-site electronegativity is founded on three strands of a common thread: complicated does not necessarily equal "better". First, B-site electronegativity sets the degree of mixing between oxygen 2*p* and metal 3*d* states and thus the higher-level descriptors are *consequences* of this core property. Indeed, to explain the physical meaning of the O-2*p* band descriptor in reviews[197, 257] the authors must appeal to how it varies with B-site electronegativity anyway. Why not start from the starting point (electronegativity) rather than the ending point (DFT calculated result)?

Second, electronegativity is a concept that is more accessible to the typical electrochemical practitioner, particularly for chemistry graduate students. By the time one has finished an undergraduate degree in chemistry, the concept of electronegativity has already been used many times to characterize and rank the bonding between metals and non-metals. Since more electronegative metals will more readily accept electrons, an obvious connection can be made to binding energy-related theories of heterogeneous catalysis. Even for an engineer thrust into the role of catalyst design, metal electronegativity is more readily grasped than a property computed using quantum mechanics. Thus electronegativity as a descriptor presents a lower barrier to understanding general trends in perovskite catalysis and does not require the reader to assess density-functional theory methods for which they probably have little prior knowledge.

Thirdly, most perovskite oxide OER studies involve systematic variation of the B-site and subsequent measurement of their catalytic activity in relation to that chemical variation. The X-site ligand rarely if ever varies from oxygen. It then seems more natural to use a property directly related to the dependent variable of the experiment in question to understand these activity changes. Even when the A-site is varied, or the oxygen content

changes this has the effect of changing the cation electronegativity due to the requirement of charge balance. For example, suppose I have two perovskites that are identical, but one is substoichiometric with respect to oxygen. I know that the compound with less oxygen must have a relatively lower average B-site oxidation state and lower electronegativity assuming the A-site occupation is relatively unchanged. I would expect higher covalency therefore in the stoichiometric compound and higher O-2*p* band position as a *consequence* of the electronegativity differences. Electronegativity remains the root cause of expected bond strength.

This dissertation, taken as a whole, has yielded new, fundamental insights into the nature of high OER activity of earth-abundant catalysts for liquid alkaline electrolyzers. It has also clarified that the OER catalysis community must, if it hopes to inform practical advances in economical green hydrogen output, address open questions about catalyst activity and durability in industrially relevant conditions while striving toward adoption of more physically meaningful and easily understood chemical descriptors. Such steps are needed to match the pace of technology transfer from benchtop to plant-scale with that of ambitious energy transition timelines.

APPENDICES

A. CHAPTER II: SUPPLEMENTARY INFORMATION

X-ray absorption spectroscopy measurements and methods.

XAS measurements at the Fe-K edge were carried out at the KMC-3 beamline[258] *using the CryoEXAFS endstation*[259] *at the BESSY II electron storage ring operated by the Helmholtz-Zentrum Berlin für Materialien und Energie.* The spectra were recorded in fluorescence mode using a 13-element Si drift detector from RaySpec. The monochromator was a double-crystal Si (111), and the polarization of the beam was horizontal. To obtain Fe K-edge spectra, a servo system (PID controller) was needed to subtract counts coming from other elements that absorb at the same energy. A home-made 3D printed XAS cell was used. X-rays can enter the cell through a Kapton window (5 mm diameter and 65 µm thick) and an electrolyte flow channel of 250 µm thick between this window and the sample, which was exposed to the electrolyte 5.0 mm in length and 7.0 mm in width. A Hg/HgO reference electrode (ALS Inc.) was placed before the inlet and the counter electrode was a Pt tube placed at the outlet. The 0.1 M KOH electrolyte was flown at 2.00 mL min^{-1} using a Fluigent FlowEZ system and controlled by a flow rate sensor (Flow EZ XL).

The data was collected to $k = 13$ $Å^{-1}$ and the energy was calibrated by assigning the inflection point of a Fe metal foil to 7112 eV.[260] The foil was measured immediately before the samples and re-measured periodically. All spectra were normalized by subtracting a constant obtained by fitting the data before the *K* edge and division by a 2nd polynomial function obtained by fitting the data after the *K* edge for XANES analysis. For EXAFS analysis, the data after the edge was instead fit by a knot-spline with 7-10 knots followed by subtraction of one. The procedure of data extraction is detailed elsewhere[261]. Glitches were removed from the data, for which the deviation of individual scans from the average of all scans was considered. The FT of the EXAFS was calculated between 22 and 244 eV (2.4 – 8.0 $Å^{-1}$) above the Fe-*K* edge (E_0 = 7112 eV). The extracted EXAFS was re-binned to give an equal step size of 0.05 $Å^{-1}$ in k-space. A cosine window covering 10% on the left side and 20% on the right side of the EXAFS spectra was used to suppress the side

lobes in the FTs. Weighing of the intensity by k^2 was chosen to emphasize the oscillations between 2 and 8 $Å^{-1}$.

EXAFS simulations were performed using the software SimXLite (developed by Dr. Petko Chernev). After calculating the phase functions with FEFF8-Lite[262] version 8.5.3, self-consistent field option activated), atomic coordinates of the FEFF input files were generated from the structure of g-FeOOH (lepidocrocite)[263] [data: http://www.crystallography.net/cod/1538421.html]. An amplitude reduction factor (S_0^2) of 0.8 and energy shift DE_0 of 4.0 eV were used. They were determined by fits to g-FeOOH [data https://doi.org/10.48505/nims.2040] in an identical range as used for the samples. The data range used in the simulation was 49.4–231.8 eV (3.6–7.8 $Å^{-1}$) above the Fe-*K* edge (E_0 = 7112 eV) if not stated otherwise. The EXAFS simulations were performed in(unfiltered) k-space and optimized by minimizing the sum of the squared deviations (error sum) between measured and simulated values using a least-squares fit. The fit was performed using the Levenberg–Marquardt algorithm with numerical derivatives. The Fe-O (reduced distance ~1.5 Å) and Fe-Fe (reduced distance ~2.6 Å) peaks in the FT were considered in the fit. The parameter errors were obtained as described in detail in Risch *et al.*[139] The essential steps are: (1) Fourier isolation of the data and fit between 0.00 and 3.2 Å (i.e., the first two peaks in the FT); (2) back transformation to k-space; (3) assumption that the minimized reduced error sum of the Fourier-filtered fit (given by steps 1-2) provides a sound estimate of the measurement error; (4) calculation of the parameter variances from the covariance matrix of the minimized fit parameters; (5) the 1s-standard deviation is obtained from the square root of the diagonal elements of the covariance matrix. The goodness of fit parameter, R_f, was obtained by summing the squared difference between data and fit divided by the squared data for each measured point; we provide it for data Fourier filtered between 0.00 and 3.2 Å (R_f').

Supplementary Discussion on the lack of redox behavior observable for Fe species.

From the Pourbaix diagram for Fe, Fe^{3+} has a wide range of redox stability. The higher valent states can be accessed only in a region of OER current, for example likely leading to the soluble species FeO_4^{2-} (Fe^{6+} formally, this degrades to release O_2 and has much

positive charge on the O ligand compared to formal O^{2-}) and FeO_2^{2-} (formally Fe^{4+}). Hunter and Gray have shown that in non-aqueous electrolytes redox signatures related to the formation of such a species can be seen that are not present in water.[94]

The $Fe^{2/3+}$ couple can be accessed at lower potentials, but this is made difficult to quantify because the entire host Ni- or Co hydroxide is electrically an insulator at these potentials, isolating the Fe sites electronically. In previous work[122] we showed from *in-situ* in-plane conductivity measurements that the onset of conductivity for cobalt and nickel hydroxides is concurrent with the cobalt and nickel redox wave which is much higher potentials than one would expect the $Fe^{2/3+}$ couple to be. Previous work studying thin films of FeOOH have discussed this redox behavior[125].

Supplementary Discussion on the differences in Fe incorporation in NiOOH and CoOOH.

Co oxyhydroxides/hydroxides have stronger bonding than those of Ni. We have shown in AFM studies[102] of NiOOH and CoOOH nanosheets that the former undergoes much more dynamic morphology changes than the latter. Specifically, NiOOH seems to restructure dramatically by dissolution and redeposition which is a process we expect would drive the dissolution of surface adsorbed Fe and then substitution of this dissolved Fe in Ni sites. This is consistent with empirically measured metal-hydroxide bond strengths[129] and metal oxide dissociation energies[130].

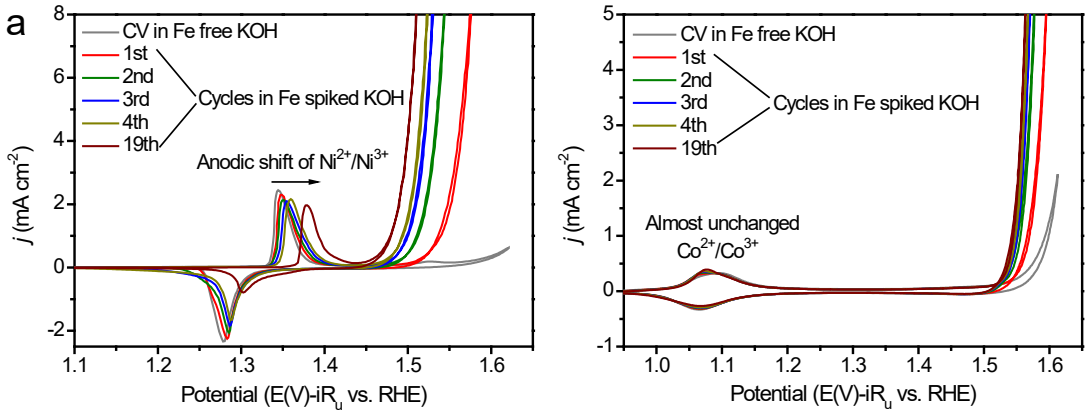

Figure 20. Cyclic voltammetry showing effect of incorporated Fe

Cyclic voltammetry showing the effect of incorporated Fe from the electrolyte on the OER activity and redox profiles of **(a)** NiO_xH_y and **(b)** CoO_xH_y films. For the NiO_xH_y film, the first CV cycle after the addition of 0.1 ppm aq. Fe^{3+} into 1 M KOH resulted in ~87 mV decrease in overpotential (at 0.5 mA cm^{-2}), while the redox peak potentials of Ni^{2+}/Ni^{3+} shifted positive by ~4 mV. After the initial 4 cycles, less-pronounced activity enhancement was observed in the following cycles, while the redox peaks kept shifting anodic and shrinking in integrated peak area. For CoO_xH_y film, most of the activity increase also occurred in the initial 4 cycles, but the Co^{2+}/Co^{3+} redox peak potential and area were almost unaffected by Fe incorporation.

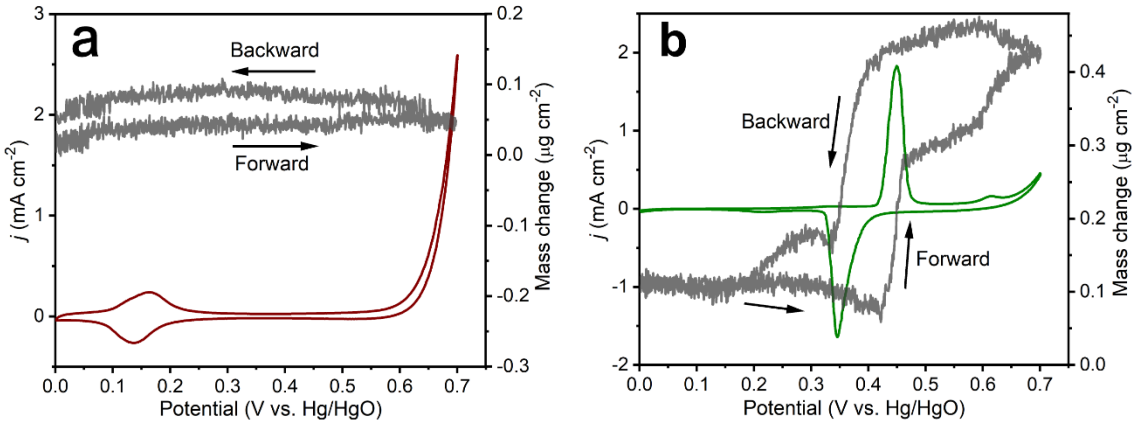

Figure 21. *In-situ* mass change of freshly electrodeposited Ni/CoO_xH_y.

The in-situ mass change of freshly electrodeposited CoO_xH_y (a) and NiO_xH_y (b) films on the electrochemical quartz crystal microbalance substrate during the second voltammetry cycle in purified 1 M KOH solution

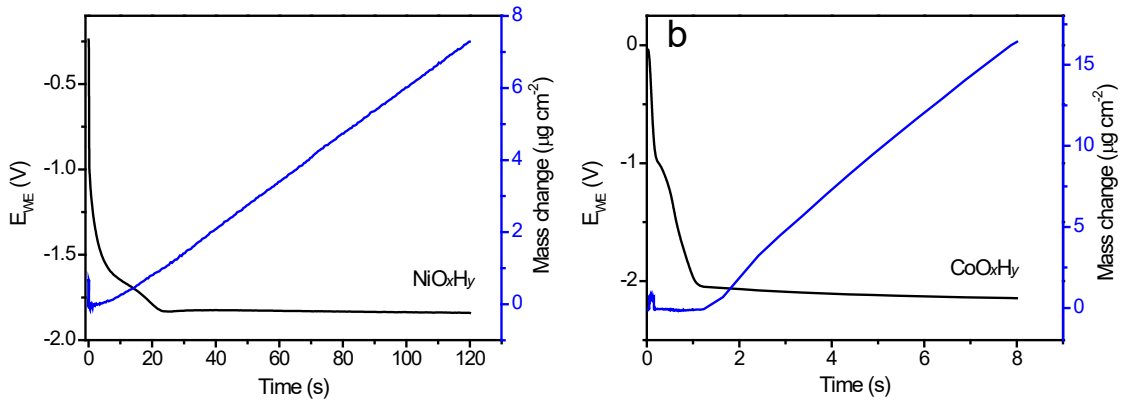

Figure 22. Potential vs time deposition curves
Potential vs. time deposition curves (black) and corresponding mass change profiles (blue) of EQCM electrodes for **(a)** NiO_xH_y film deposited at -0.1 mA cm^{-2} for 120 s, and **(b)** CoO_xH_y film deposited at -2 mA cm^{-2} for 8 s. The typical film mass loading for NiO_xH_y and CoO_xH_y are ~7.3 and 16.5 μg cm^{-2}, respectively.

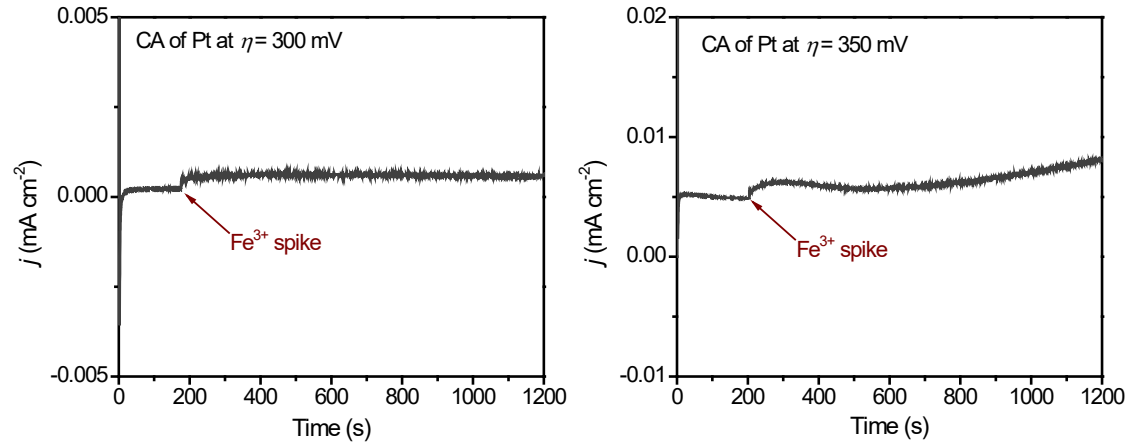

Figure 23. Fe spiking control on Pt substrate
The effect of Fe spiking on the OER activity of a Pt substrate under chronoamperometry measurements at overpotentials of **(a)** 300 mV and **(b)** 350 mV. It was found that the addition of Fe^{3+} (0.1 ppm) into 1 M KOH electrolyte caused negligible OER current increase for the Pt substrate. Thus, the dramatic current increase observed for NiO_xH_y or CoO_xH_y loaded Pt electrode was attributed to the adsorbed Fe species on (oxy)hydroxides rather than on underlying Pt substrate.

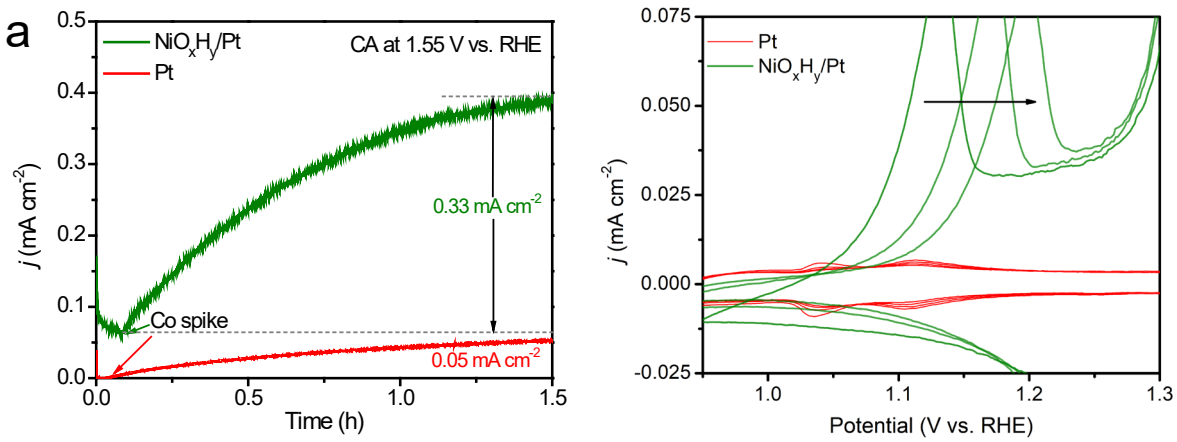

Figure 24. Chronoamperometry of Pt and NiO_xH_y

(a) Chronoamperometry (CA) of bare Pt (red) and NiO_xH_y/Pt (green) electrodes in 0.1 ppm Co^{2+} spiked 1 M KOH solution. In the case of bare Pt substrate, the addition of Co^{2+} into the electrolyte resulted in much smaller current increase compared to NiO_xH_y/Pt. Thus, the current increase of NiO_xH_y/Pt mainly originated from adsorbed Co (oxy)hydroxides on the surface of NiO_xH_y film rather than on the Pt substrate. This could be explained by the substantially larger surface area of the porous NiO_xH_y film relative to the planar Pt substrate. **(b)** Voltammetry cycles after the Co^{2+} spiking CA measurement demonstrating the redox peaks of Co^{2+}/Co^{3+} on bare Pt (red) and NiO_xH_y/Pt (green) electrode. The integrated peak area on the Pt substrate is negligible compared to that on NiO_xH_y/Pt.

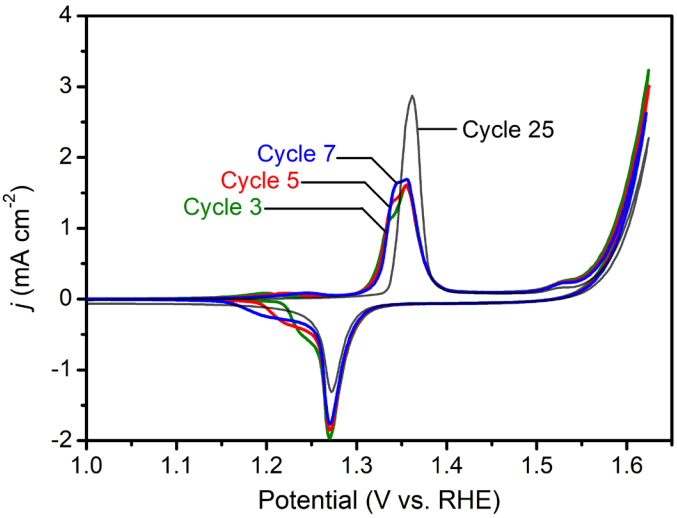

Figure 25. Co^{2+} spiking voltammetry of NiO_xH_y.

Typical voltammetry cycles of NiO_xH_y after Co^{2+} spiking CA measurement. The movement of surface Co species into the bulk structure of NiO_xH_y affects the redox behavior of NiO_xH_y – likely due to electronic interactions between cations. In the initial cycles, Co-incorporated NiO_xH_y exhibited broadened redox peaks, which consist of two distinct oxidation and reduction peaks. This suggested an inhomogeneous local environment within the NiO_xH_y lattice. After 25 cycles, these distinct redox peaks merged into one pair of sharp peaks, which we interpret as associated with a homogeneous distribution of Co sites within the NiO_xH_y.

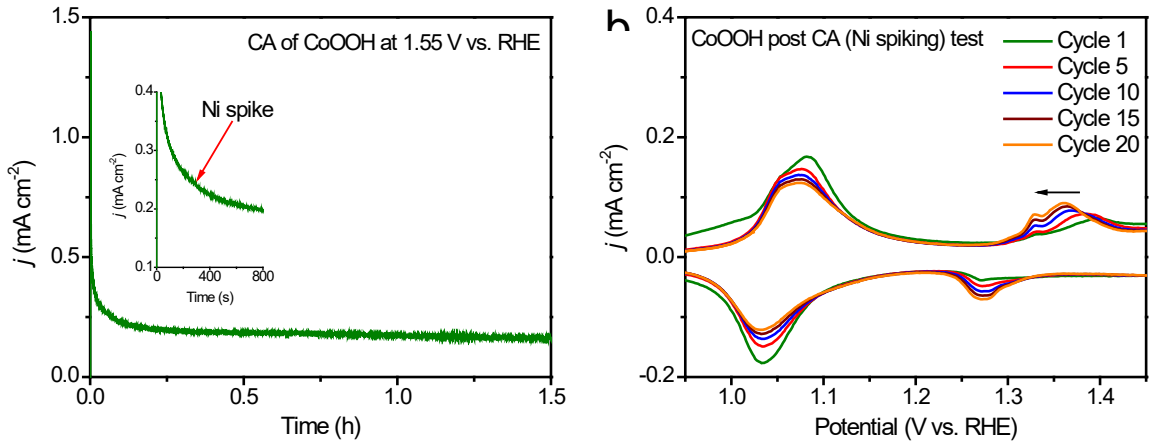

Figure 26. Chronoamperometry of Ni^{2+} spiking of CoOOH
(a) Chronoamperometry (CA) measurements of CoOOH at the potential of 1.55 V vs. RHE in Ni^{2+} spiked 1 M KOH. CoOOH was first measured in purified KOH solution (inset), then $Ni(NO_3)_2$ aqueous solution was added into the electrolyte. The Ni concentration in the electrolyte was 0.1 ppm. **(b)** Voltammetry of CoO_xH_y after Ni^{2+}-spiking CA measurement in Ni^{2+} spiked 1 M KOH.

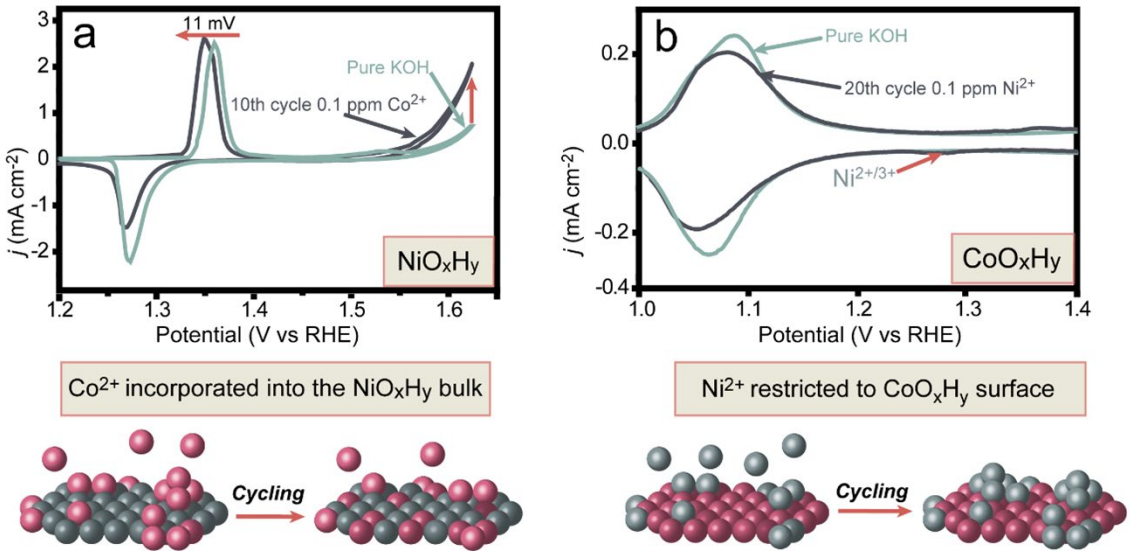

Figure 27 The effect of cyclic voltammetry on foreign-cation incorporation
(a) NiO_xH_y was first cycled at 10 mV/s in purified 1.0 M KOH, then aq. $Co(NO_3)_2$ was added to provide 0.1 ppm Co^{2+} in the electrolyte and a further 10 voltammograms were collected. (b) CoO_xH_y was first cycled in purified 1.0 M KOH, then aq. $Ni(NO_3)_2$ was added to provide 0.1 ppm Ni^{2+} in the electrolyte and a further 20 voltammograms were collected.

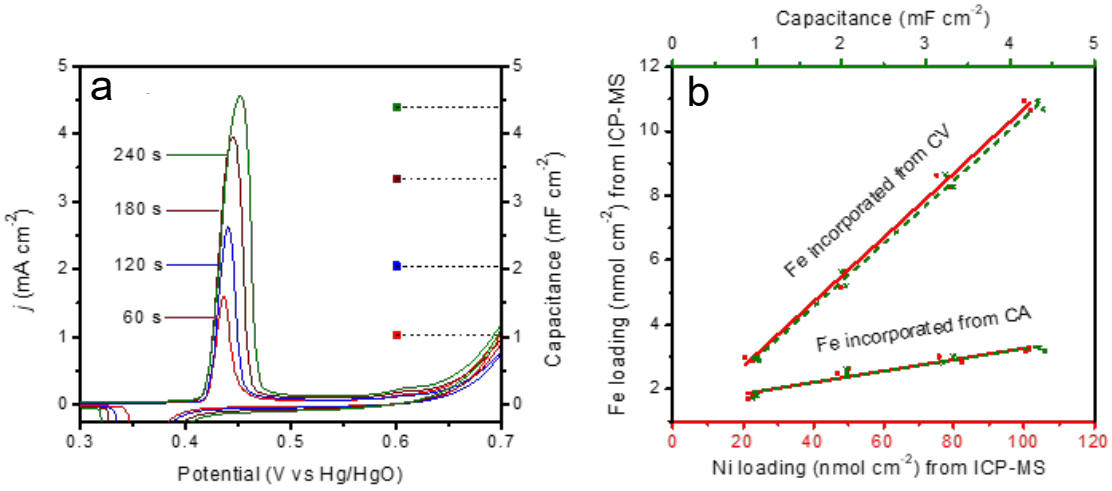

Figure 28. Mass loading of NiO_xH_y and incorporation of Fe.
(a) Typical voltammetry of NiO_xH_y films with different mass loadings controlled by applying different electrodeposition times of 60 s (red), 120 s (blue), 180 s (wine), and 240 s (olive) under the same deposition current of -0.1 mA·cm^{-2}. The corresponding double-layer capacitance (C_{DL}) of each film was determined via AC impedance measurements at a constant potential of 0.6 V vs Hg/HgO. **(b)** Mass of Fe incorporated under CV and CA modes as a function of Ni mass loading (red symbols and solid fitted lines) and double-layer capacitance (olive symbols and dash fitted lines) of NiO_xH_y films per geometric area of substrate. The mass of Ni and Fe in the films was determined by ICP-MS. The voltammetry measurements were performed in Fe-spiked 1 M KOH for 10 cycles. The chronoamperometry measurements were performed in Fe-spiked 1 M KOH until maximum OER current was reached.

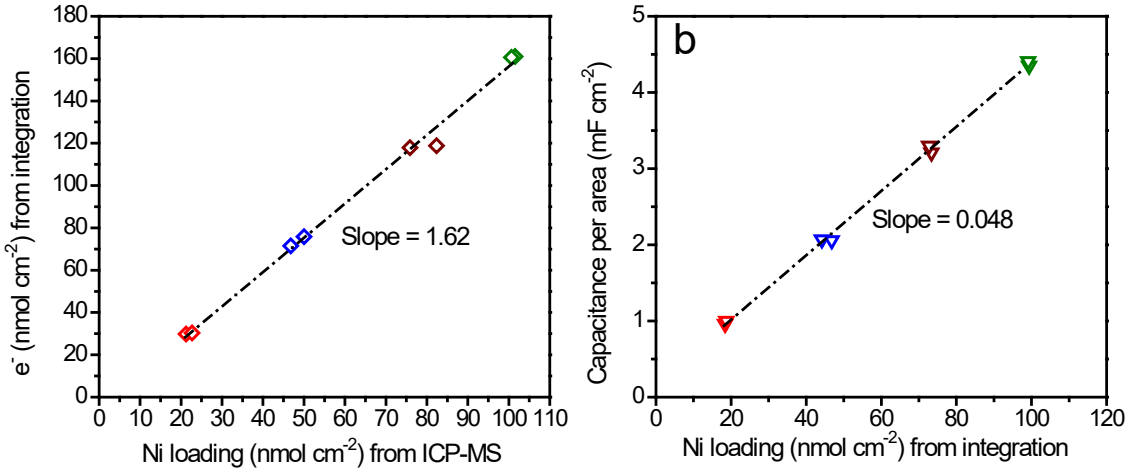

Figure 29. Mole of electrons per Ni loading
(a) Moles of electrons from integration of the anodic peak in the voltammograms as a function of the moles of Ni determined by ICP-MS analysis for NiO_xH_y films with different mass loading. The mass of NiO_xH_y films is controlled by different electrodeposition time of 60 s (red), 120 s (blue), 180s (wine), and 240 s (olive) under the same deposition current of -0.1 mA·cm^{-2}. From the linear fitting, there was ~1.6 e$^-$ transferred per Ni during the redox process, consistent with previous findings. **(b)** The correlation between the double-layer capacitance (C_{DL}) and the mass loading for the NiO_xH_y films. The linear increase of electrons transferred and C_{DL} with the mass of films indicate that the films are electrolyte-permeable and electron-accessible throughout the mass loading range.

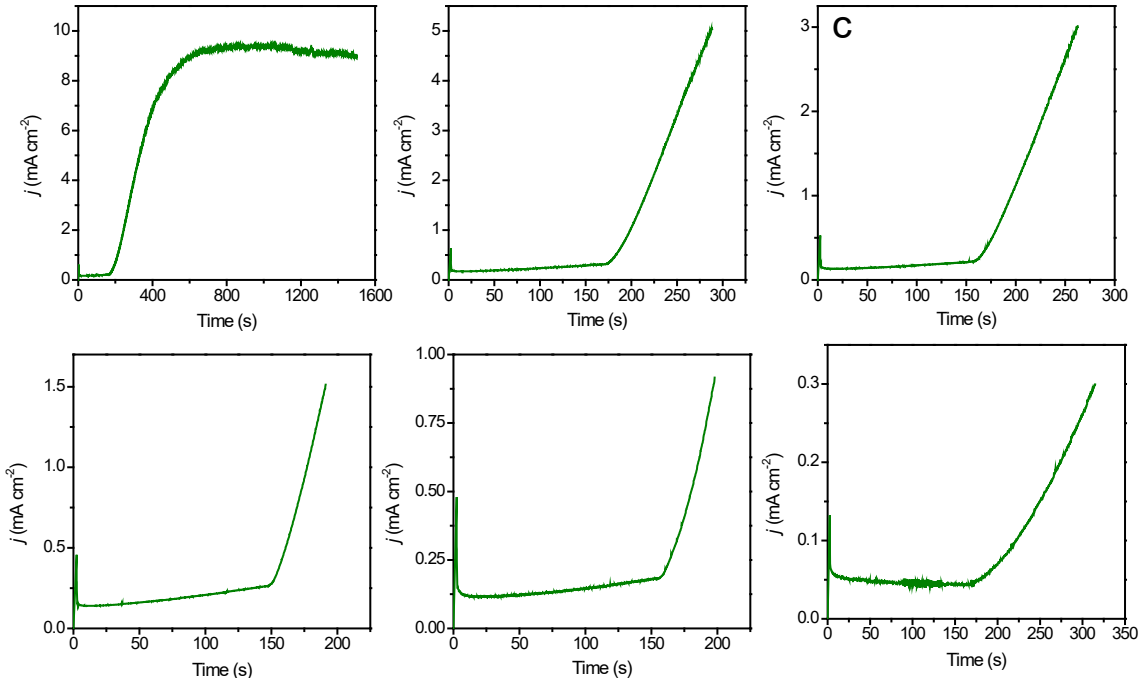

Figure 30. Chronoamperometry of Fe-spiked NiOOH at 300 mV

Representative chronoamperometry (CA) tests of NiOOH at an overpotential of 300 mV in Fe-spiked 1 M KOH solution. $Fe(NO_3)_3$ aqueous solution was added into KOH electrolyte at the initial stage of CA tests. The Fe concentration in the electrolyte was 0.1 ppm. CA tests were stopped after reaching current densities of **(a)** the maximum OER current density, **(b)** 5 mA·cm^{-2}, **(c)** 3 mA·cm^{-2}, **(d)** 1.5 mA·cm^{-2}, **(e)** 0.9 mA·cm^{-2}, **(f)** 0.3 mA·cm^{-2}. The iR_u potential drop was corrected in real time using the manual iR compensation mode. Commercial semiconductor-grade KOH was used for **(a)-(e)**; purified "Fe-free" KOH solution was used for **(f)**

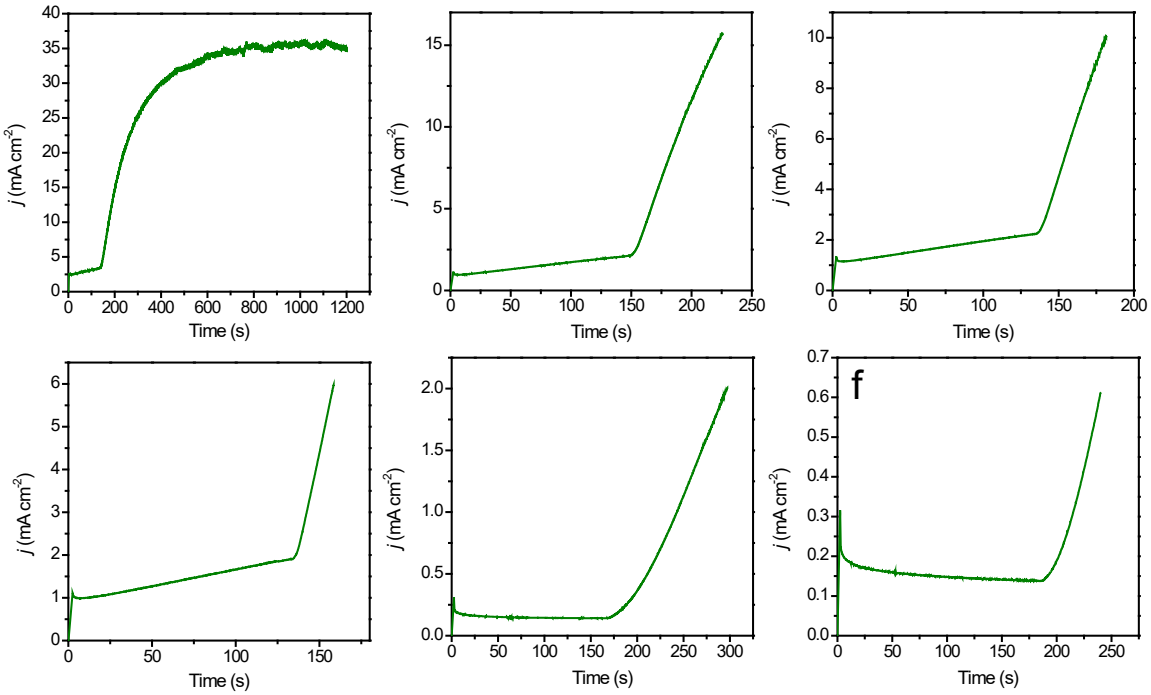

Figure 31. Chronoamperometry of Fe-spiked NiOOH at 350 mV

Representative chronoamperometry (CA) tests of NiOOH at an overpotential of 350 mV in Fe-spiked 1 M KOH solution. $Fe(NO_3)_3$ aqueous solution was added into KOH electrolyte at the initial stage of CA test. The Fe concentration in the electrolyte was 0.1 ppm. CA tests were stopped after reaching current densities of **(a)** the maximum OER current density, **(b)** 16 mA·cm^{-2}, **(c)** 10 mA·cm^{-2}, (d) 6 mA·cm^{-2}, **(e)** 2 mA·cm^{-2}, and **(f)** 0.6 mA·cm^{-2}. The iR_u potential drop was corrected in real time using the manual *iR* compensation mode. Commercial semiconductor grade KOH was used for **(a)-(d)**; Purified "Fe-free" KOH solution was used for **(e)-(f)**.

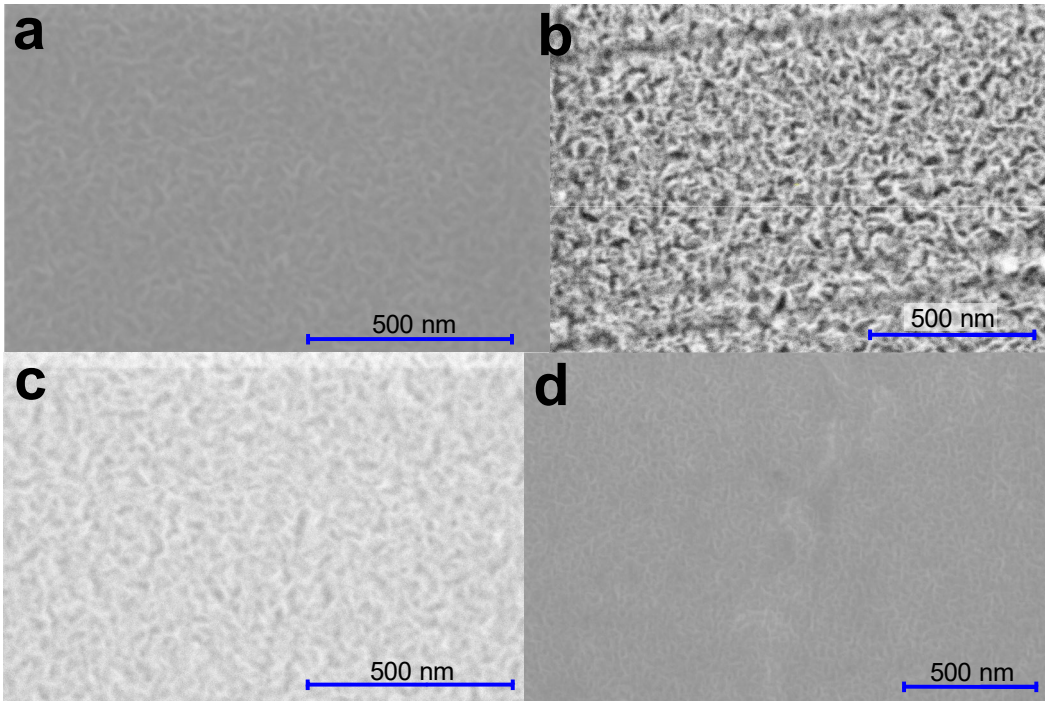

Figure 32. SEM images of the surface of an electrodeposited NiO_xH_y
Films were prepared as described in the Methods section. **(a, c, d)** are all the images of the same spot on a single film, but captured with different detectors. **(b)** shows a different spot on the same film, but shown with high contrast to capture the porosity of the film.

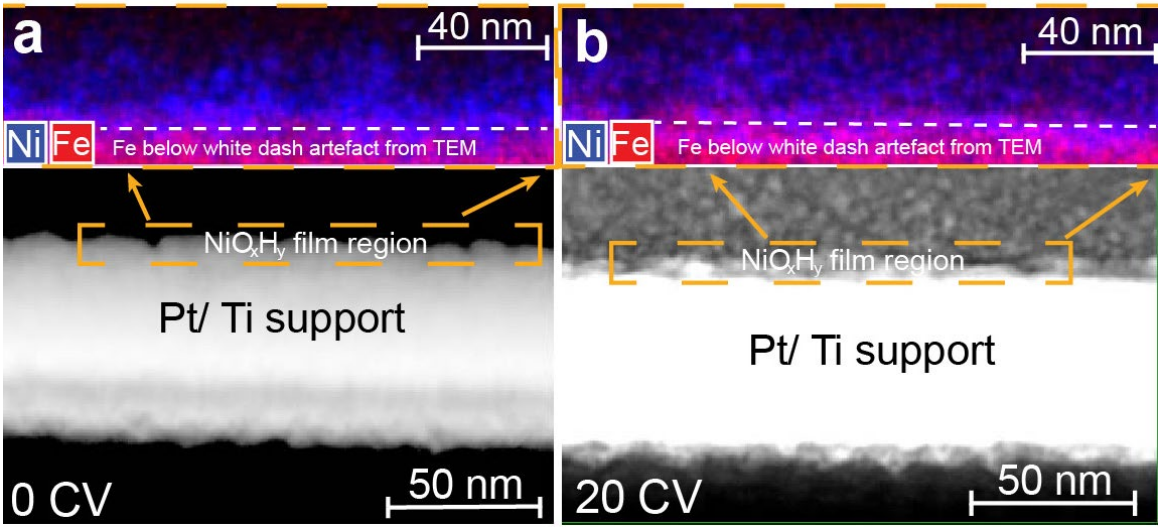

Figure 33. TEM/EDX of cross-sections of a NiO_xH_y film
TEM/EDX of cross-sections of a NiO_xH_y film electrodeposited as described in the methods sections and with Fe incorporated by electrolyte spiking during constant potential polarization at 1.55 V vs RHE. Lamellar cross sections were cut and thinned with a Ga focused ion beam from films of morphology like those shown in SI figure 12. (a) shows a film without further cycling after Fe incorporation and (b) shows a separate but analogous film with 20 cycles

after Fe incorporation. We note that the high Fe concentration toward the bottom of the EDX picture is partially due to system peaks arising from Fe in the lenses of the TEM instrument. This signal scales with the scattering intensity of nearby high mass elements. Because substrate is platinum, Fe appears more intensely in the areas closest to the substrate. Regions below the dashed boxes are all either the Pt substrate, Ti adhesion layer, or the glass slide these are coated on, so their EDX profiles are omitted.

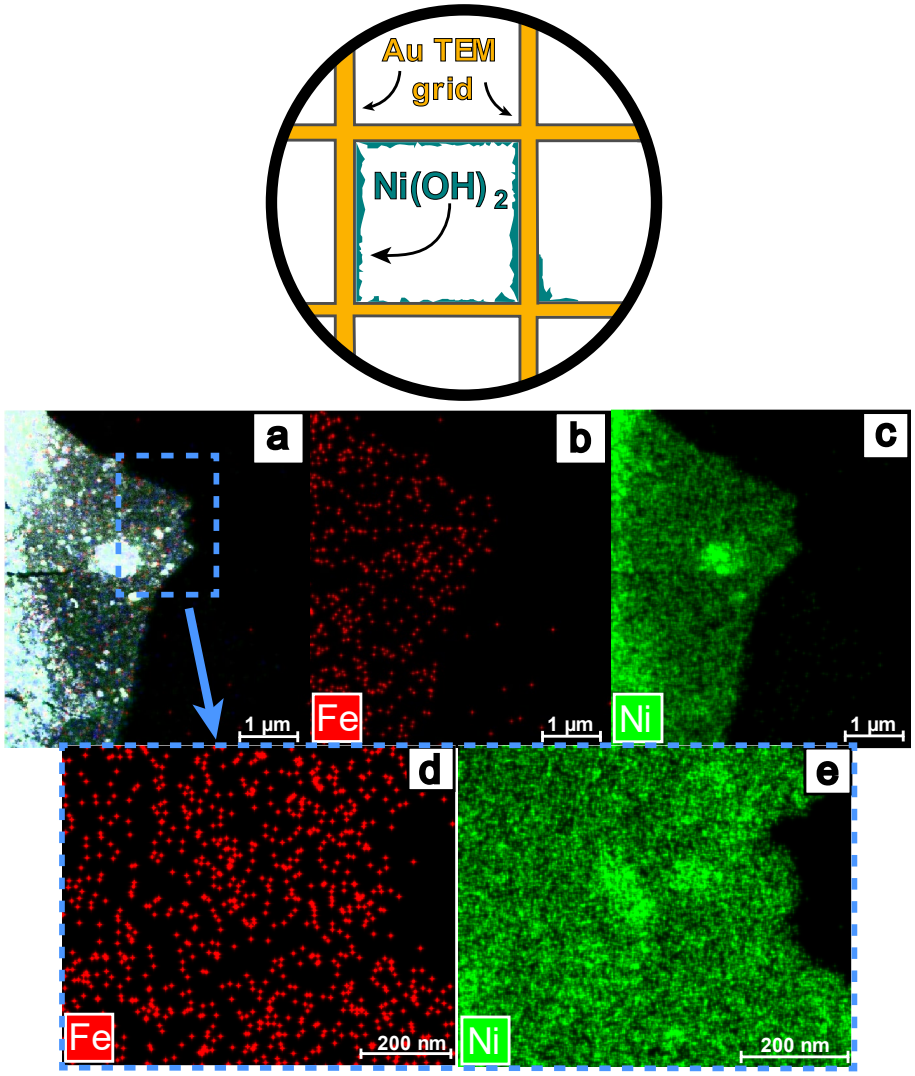

Figure 34. TEM-EDX images of NiO_xH_y electrodeposited directly onto a gold TEM grid.
Fe was then adsorbed during chronoamperometry at 1.55 V vs RHE. The topmost image illustrates qualitatively how $Ni(OH)_2$ flakes (teal) grow directly onto the TEM grid (yellow) and span into the interior grid space. A single flake was selected and used to generate images (a-e) which are representative of other locations sampled on the deposited flakes. Fe is relatively sparsely distributed relative to Ni and appears as separated clusters; however, we cannot discriminate between specific bulk surface position of the iron from these images. Further, the low concentrations of Fe make it difficult to say much definitively about the structure of Fe.

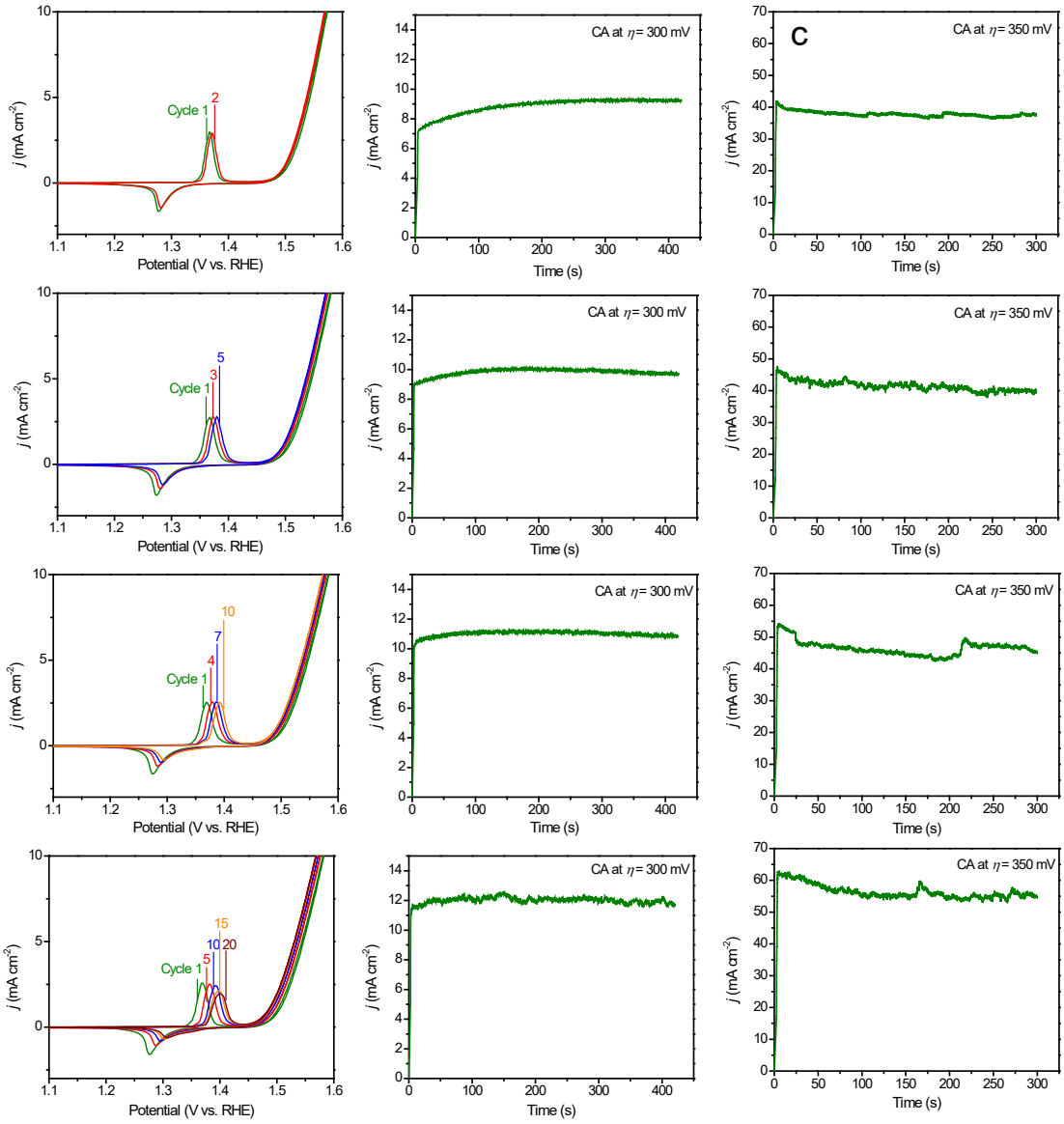

Figure 35. Cycling of surface Fe films

To calculate the TOF_{Fe} of mixed (bulk and surface) Fe species, $Ni(Fe)O_xH_y$ films obtained from initial CA-spiking route were further cycled for **(a)** 2, **(d)** 5, **(f)** 10, and **(i)** 20 cycles. Then CA measurements at overpotentials of **(b)**, **(e)**, **(g)**, **(f)** 300 mV, and **(c)**, **(f)**, **(h)**, **(k)** 350 mV were used to collect the OER currents.

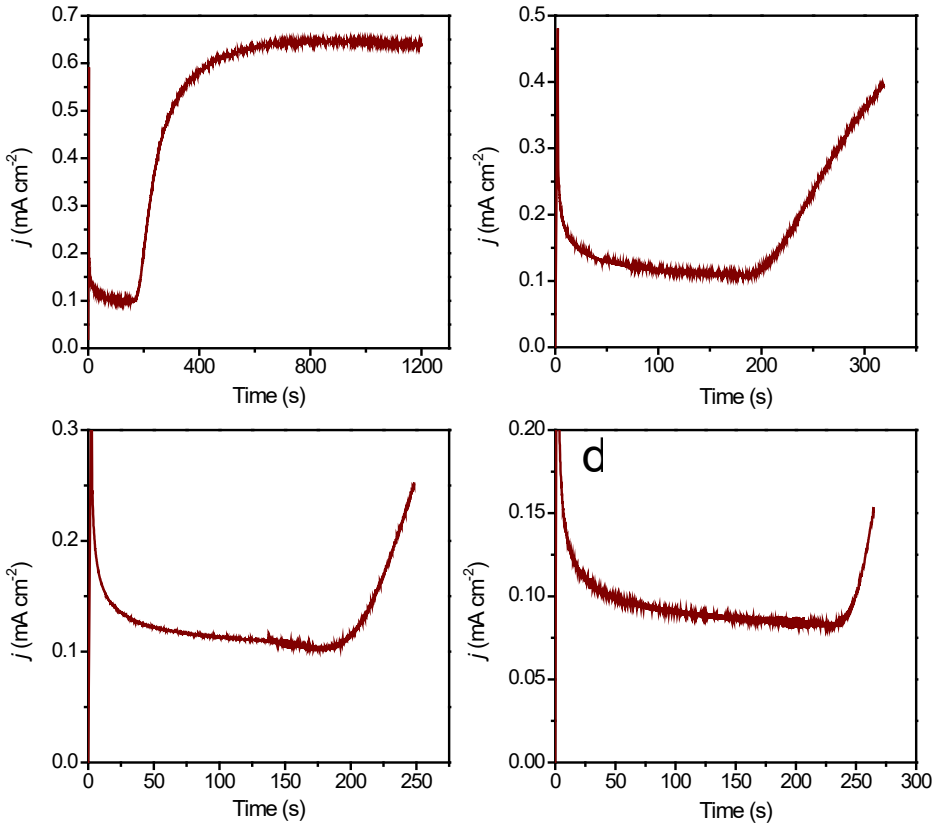

Figure 36. Representative chronoamperometry (CA) tests of CoOOH
Performed in Fe-spiked 1 M KOH solution at 300 mV overpotential. $Fe(NO_3)_3$ aqueous solution was added into KOH electrolyte at the initial stage of CA tests. The Fe concentration in the electrolyte was 0.1 ppm. CA tests were stopped after reaching current densities of **(a)** the maximum OER current density, **(b)** 0.4 mA·cm^{-2}, **(c)** 0.25 mA·cm^{-2}, **(d)** 0.15 mA·cm^{-2}. The iR_u potential drop was corrected in real time using the manual iR compensation mode. Commercial semiconductor grade) KOH was used for **(a)-(c)**; purified "Fe-free" KOH solution was used for **(d).**

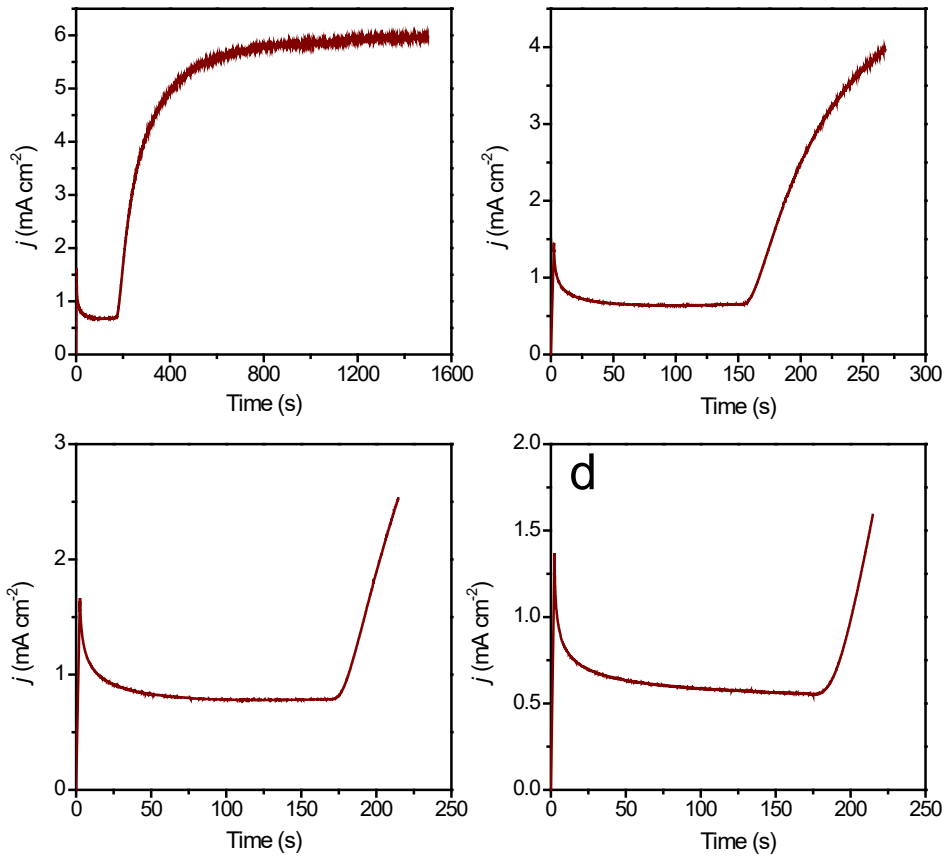

Figure 37. Representative chronoamperometry (CA) tests of CoOOH
Performed in Fe-spiked 1 M KOH solution at 350 mv overpotential. $Fe(NO_3)_3$ aqueous solution was added into KOH electrolyte at the initial stage of CA tests. The Fe concentration in the electrolyte was 0.1 ppm. CA tests were stopped after reaching current densities of **(a)** the maximum OER current density, **(b)** 4 $mA \cdot cm^{-2}$, **(c)** 2.5 $mA \cdot cm^{-2}$, **(d)** 1.5 $mA \cdot cm^{-2}$. The iR_u potential drop was corrected in real time using the manual *iR* compensation mode. Commercial semiconductor grade) KOH was used for **(a)-(c)**; purified "Fe-free" KOH solution was used for **(d).**

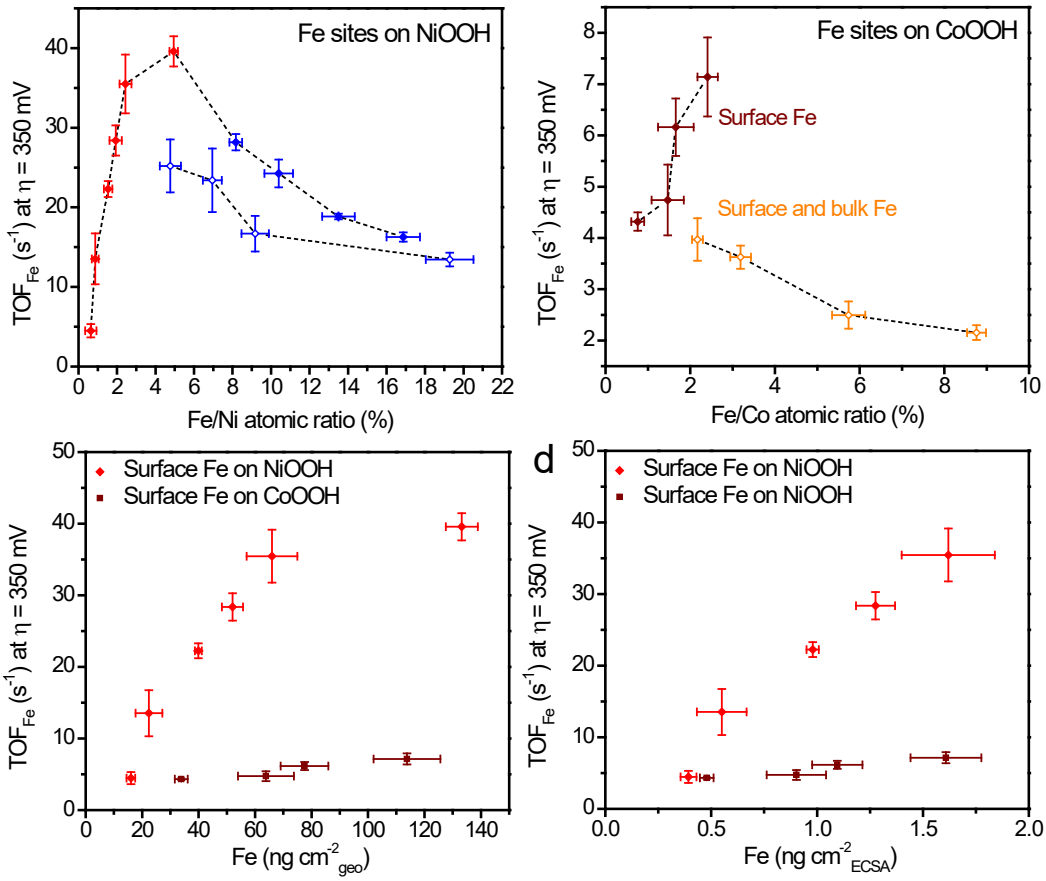

Figure 38. Turnover frequencies of NiOOH and CoOOH

The intrinsic activity comparison of Fe sites reflected by the turnover frequency (TOF_{Fe}) at η = 350 mV (complementing the η = 300 mV data in the main text). The TOF_{Fe} is calculated based on the mass of all Fe sites determined by ICP-MS analysis. **(a)** Correlation between the TOF_{Fe} and Fe/Ni atomic ratio. The closed red symbols are for surface Fe sites obtained from CA-Fe spiking method, and the closed blue symbols stand for mixed (surface and bulk) Fe sites obtained from further voltammetry cycling. The open blue symbols represent co-deposited $Ni_{1-x}Fe_xOOH$. **(b)** Correlation between the TOF_{Fe} and Fe/Co atomic ratio. The closed wine symbols stand for surface Fe sites obtained from CA-Fe spiking method and the open orange symbols stand for Fe sites in co-deposited $Co_{1-x}Fe_xOOH$. **(c)** The correlation between the TOF_{Fe} of surface Fe sites on NiOOH (red symbols) and CoOOH (wine symbols) and the adsorbed Fe mass loading normalized by the geometric area of substrate. **(d)** The correlation between the TOF_{Fe} of surface Fe sites on NiOOH (red symbols) and CoOOH (wine symbols) and the adsorbed Fe mass loading normalized by the electrochemically active surface areas of NiOOH and CoOOH films. Error bars are standard deviations based on samples measured in triplicate.

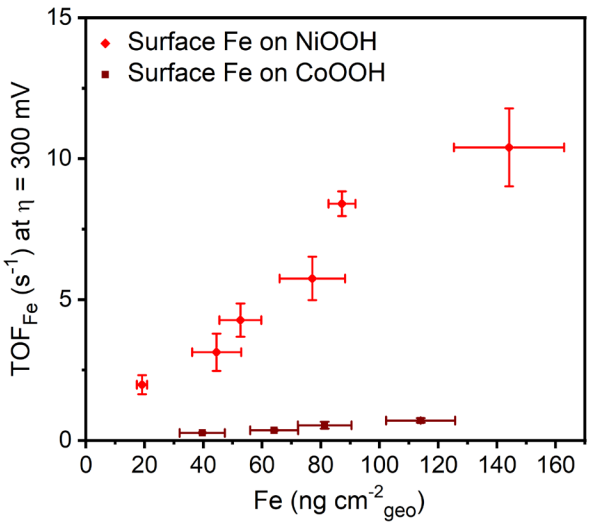

Figure 39. Correlation between TOF_{Fe} and Fe mass loading
The correlation between the TOF_{Fe} (η = 300 mV) of surface Fe sites on NiOOH (red symbols) and CoOOH (wine symbols) and the adsorbed Fe mass loading normalized by the geometric area of substrate. Error bars are one standard deviation from the average of triplicate measurements.

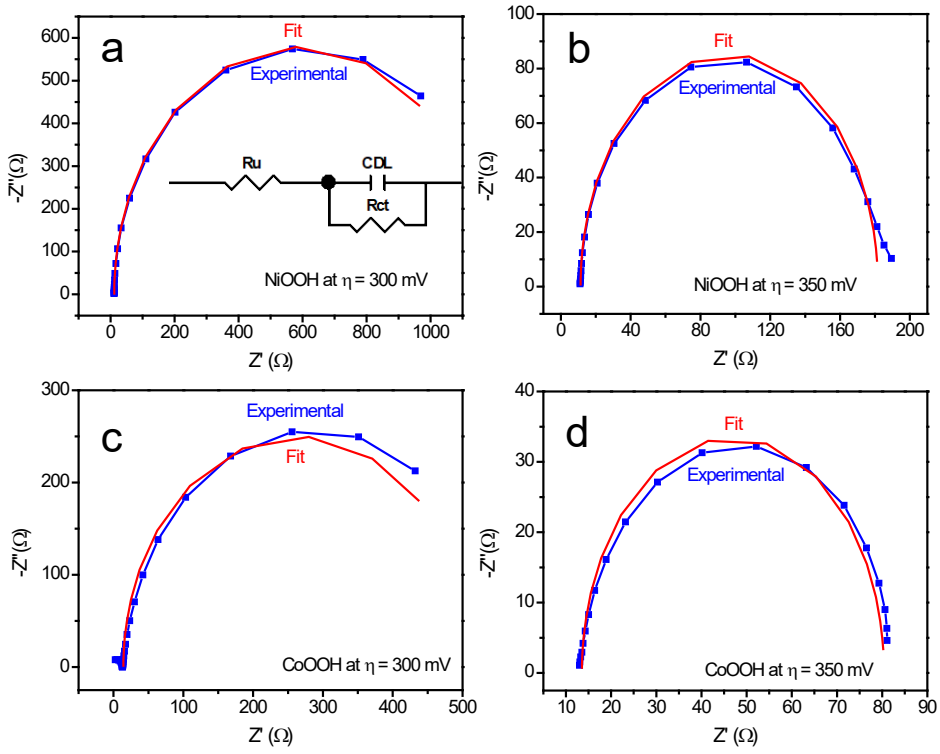

Figure 40. Impedance spectroscopy for NiOOH double-layer capacitance
Potentioelectrochemical impedance spectroscopy (PEIS) measurements used to determine the double-layer capacitance of NiOOH film at the overpotential of **(a)** 300 mV and **(b)** 350 mV, and the CoOOH films at the overpotential of **(c)** 300 mV and **(d)** 350 mV. The equivalent circuit shown in the inset of **(a)** was used to fit the experimental impedance results. Least-squares data fitting was conducted to determine the circuit elements (EC Lab, Biologic).

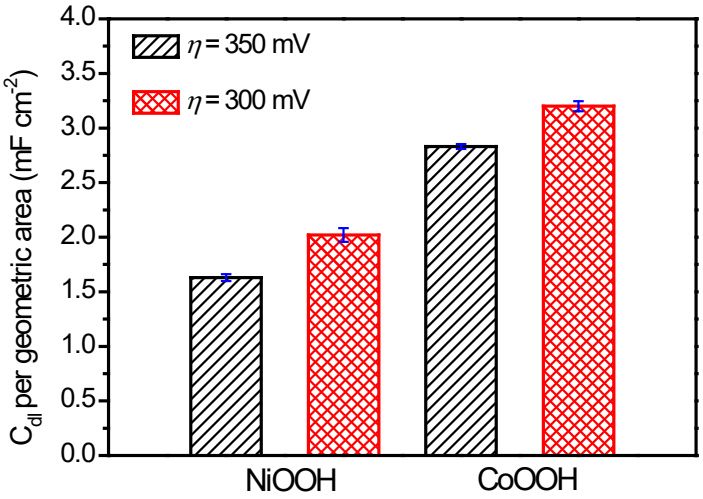

Figure 41. NiOOH and CoOOH double-layer capacitance
Double-layer capacitance (C_{dl}) per geometric area from PEIS equivalent circuit fitting for NiOOH and CoOOH films at the overpotentials of 300 mV and 350 mV. Error bars are one standard deviation from the average of triplicate measurements.

Supplementary Note 1: X-ray absorption measurement discussion

A NiOOH film was electrodeposited on a polycrystalline Pt plate at -0.1 mA cm^{-2} for 120 s from a 0.1 M $Ni(NO_3)_3 \cdot 6H_2O$ solution. Then 0.1 M KOH was filled into the cell. $Fe(NO_3)_3$ was added into the flowing electrolyte reservoir to a final concentration of ~150 ppb. The electrode potential was then immediately stepped and held at 0.68 V vs Hg/HgO and XAS spectra were simultaneously recorded (Fe@0.68V, after 0 CVs). Spectra were next obtained at 0.60 V vs. Hg/HgO (Fe@0.60 V, after 0 CVs). Following a short open-circuit potential step, the sample was cycled 17 times to introduce Fe into the internal sites of the NiO_xH_y structure, and finally held at 0.68 V vs. Hg/HgO (Fe@0.68V, after 17 CVs) for a final set of XAS spectra. We focus on the analysis of the Fe *K*-edge of the film at 0.68 V vs. Hg/HgO before and after cycling. There were no significant changes in the edge position of shape of the XANES (Fig. S24).

The lack of significant changes to the Fe spectra show that in all cases the nominal valence state of the Fe is similar and comparison to hematite (α-Fe_2O_3) indicates a valence of 3+. This is consistent with picture of structural differences between the FeOx surface cluster active sites and internal sites driving activity differences.

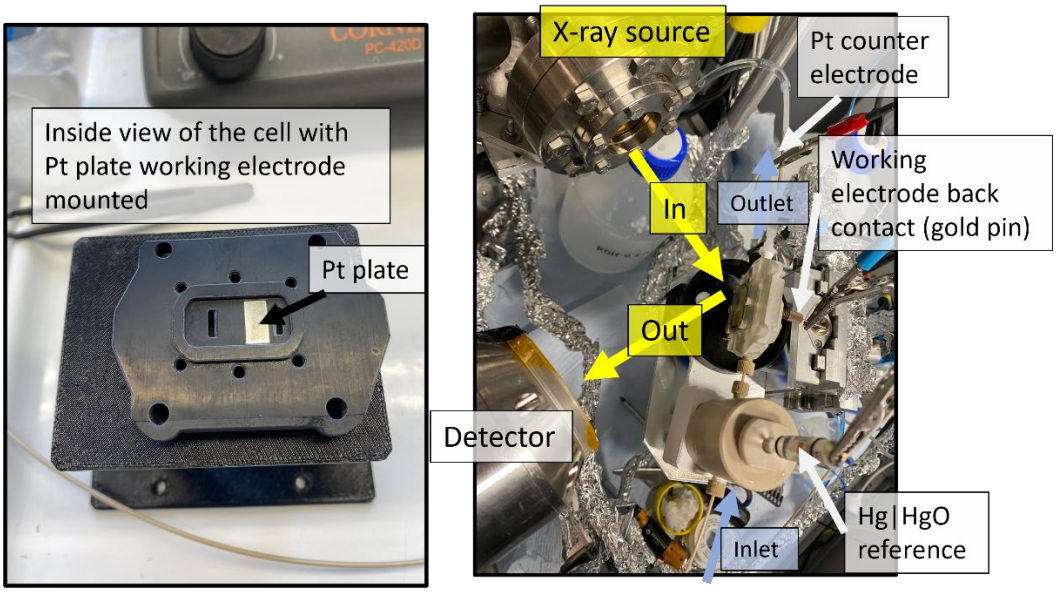

Figure 42: *In-situ* XAS cell
Left panel: inside view of the *in-situ* XAS flow cell with Pt plate working electrode mounted. Electrical contact was made from the back (underneath the plate in left image) using a gold pin. $Ni(OH)_2$ was deposited directly onto the Pt plate in a separate conventional cell according to the method presented in the main text prior to mounting into the flow cell. **Right panel:** Complete experimental set-up with flow cell connected to flowing electrolyte and counter and reference electrodes.

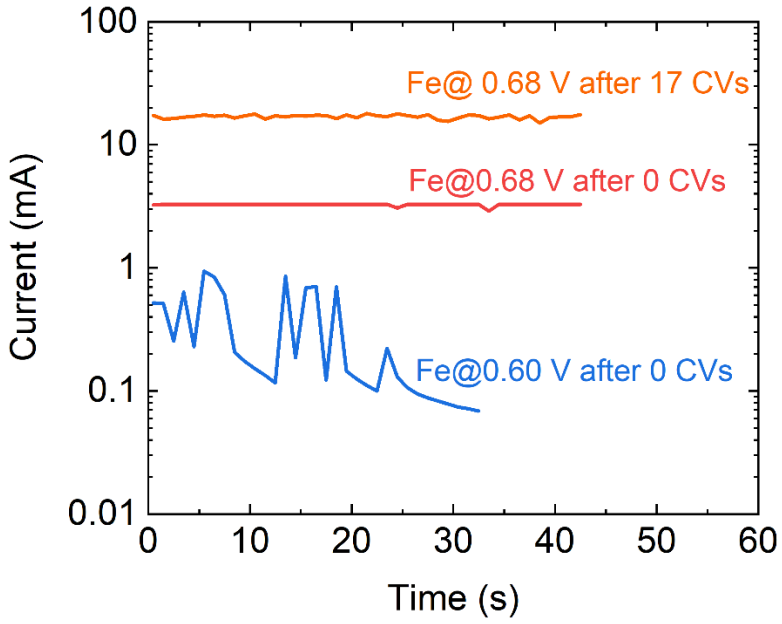

Figure 43. Chronoamperometry in XAS cell
Constant potential data acquired in the *operando* XAS cell immediately after Fe spiking (red – 0.68 V; blue – 0.60 V) and after 17 CVs (orange).

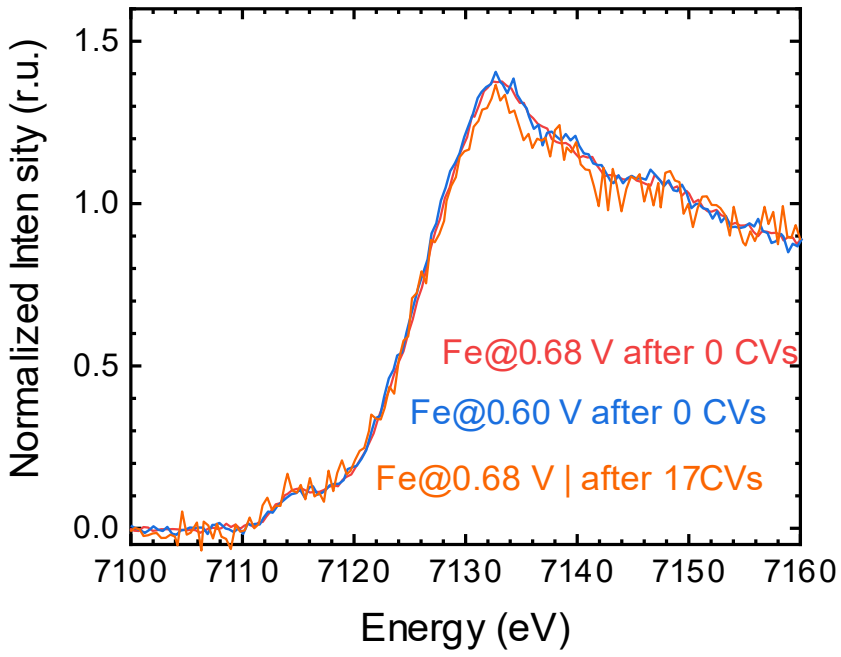

Figure 44. XANES at Fe-K-edge

XANES at the Fe-K edge of NiO_xH_y electrodeposited on a Pt plate with Fe incorporated by spiking ~170 ppb Fe into the electrolyte reservoir during a short (< 2 min) period at open circuit. Fe spiking was done during open circuit because of concerns that the *operando* cell would dry out and over-polarize during CA, thereby destroying the film. After spiking the reservoir, the sample was immediately polarized to 0.68 V vs. Hg/HgO and an XAS spectra was obtained (red) followed by another set of spectra obtained at 0.60 V vs Hg/HgO (blue) with a short (< 90 s) OCV period between this and the 0.68 V spectra. 17 cycles were performed after the 0.60 V scans and another spectrum was obtained at 0.68 V vs Hg/HgO (orange). The lack of significant changes to the Fe spectra show that in all cases the nominal valence state of 3+ of the Fe is unchanged, consistent with our picture of structural differences between the FeOx surface cluster active sites and internal sites driving activity differences.

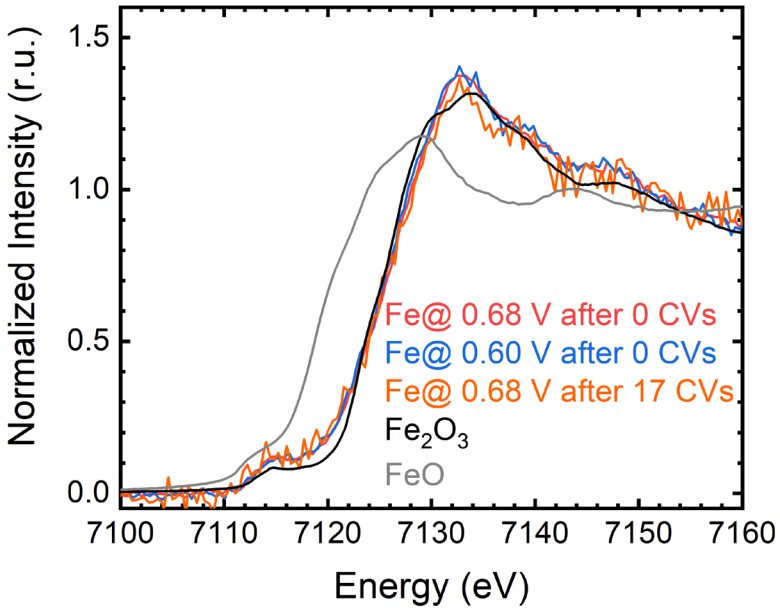

Figure 45. Comparison of Fe *K*-edge to reference spectra
Comparison of experimental data with reference materials Fe_2O_3 and FeO. The similarity in shape and position of the data with Fe_2O_3 confirms that the valence of Fe species incorporated by spiking during CA is 3+.

Table 1. Parameters of the data extraction and fits.

Fit ID	Sample	EXAFS range (eV)	# knots	Fit range ($Å^{-1}$)	Degree of freedom
CA068-B	Fe@0.68, after 0 CVs	10 – 680	10	3.6 – 7.8	7
CA068-A	Fe@0.68, after 0 CVs	10 – 680	10	3.2 – 7.8	9
CA060-A	Fe@0.60, after 0 CVs	15 - 660	10	3.2 – 7.8	7
CV068-A	Fe@0.68, after 17 CVs	20 – 690	7	3.2 – 7.8	7

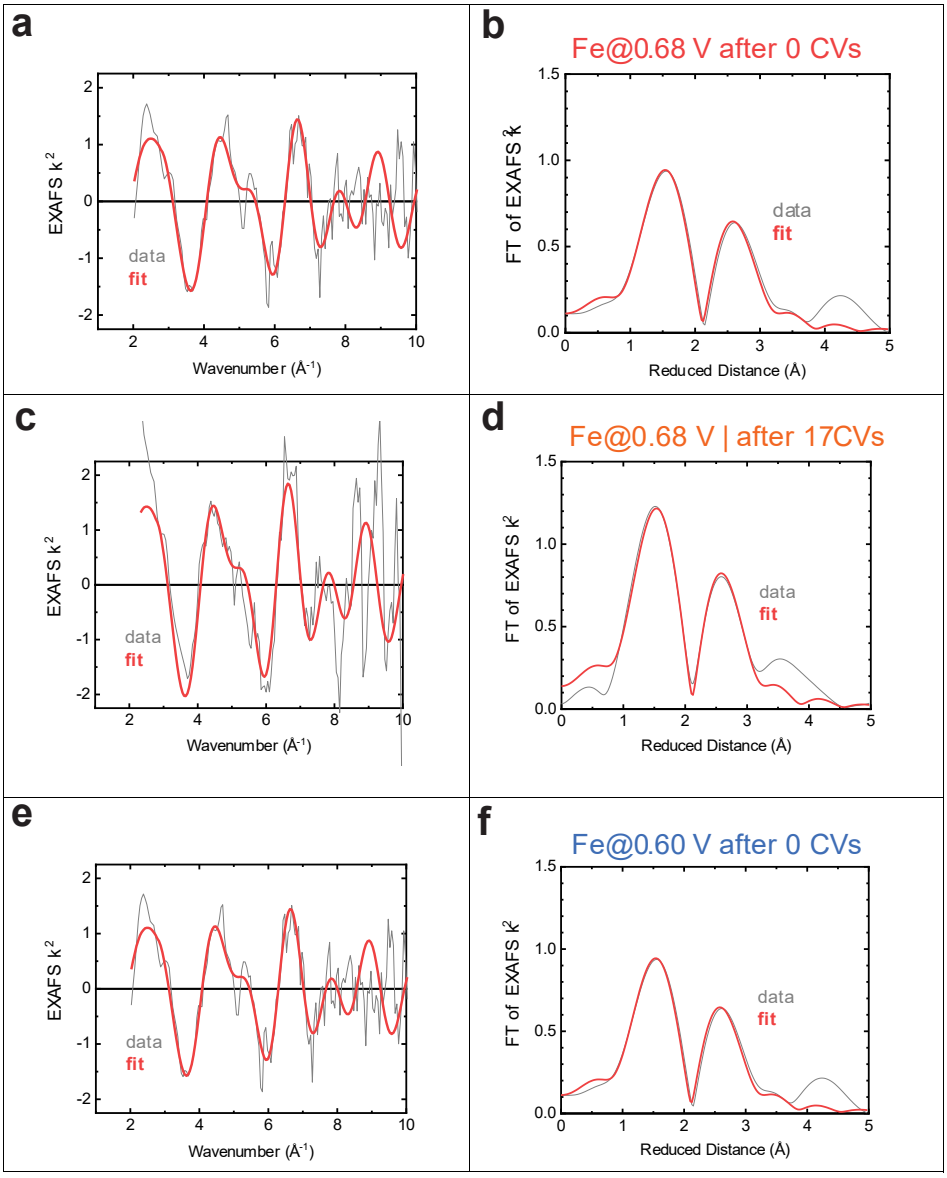

Figure 46. Fits of XAFS signal in *k*-space

Fits in *k*-space and real space of **(a,b)** Fe@0.68 V vs Hg/HgO after 0 cycles – the red curve in SI figure 22 **(c,d)** Fe@0.68 V vs Hg/HgO after 17 cycles, the orange curve in SI figure 22 and **(e,f)** Fe@0.60 V vs Hg/HgO after 0 cycles, the blue curve in SI figure 22. Note that the actual fits were always performed in *k*-space and then Fourier transformed between 22 to 244 eV (2.4 – 8.0 $Å^{-1}$) using a cosine window on the first and last 10% of the data. All data above was transformed identically.

Table 2. EXAFS fit results

		Fe-O*			Fe-M**		
Exp. ID	**Sample History**	**N**	**R (Å)**	**Rf' (%)**	**N**	**R (Å)**	**Rf' (%)**
CA068-A	Spectra collected on NiOOH (sample A) held at 0.68 V vs. Hg/HgO with 150 ppb Fe^{3+} in the electrode	4.26 ± 0.2	1.953 ± 0.004	0.82	5.08 ± 0.3	2.988 ± 0.005	0.82
CA068-B	Same as CA068-A except analysed with different fit range, notice similar fit results	4.09 ± 0.2	1.951 ± 0.005	1.31	5.10 ± 0.3	2.987 ± 0.006	1.31
CA060-A	Sample A was then allowed to rest for 90 s at OCV, and another spectra collected at 0.60 V vs Hg/HgO	4.29 ± 0.1	1.941 ± 0.003	0.49	5.03 ± 0.2	2.975 ± 0.004	0.49
CV068-A	Sample A was then subjected to 17 voltammogram cycles in the same electrolyte with 150 ppb Fe^{3+}	5.56 ± 0.6	1.939 ± 0.011	5.67	6.38 ± 1.1	2.974 ± 0.014	5.67

Fixed parameters: $\Delta E0 = 4$ eV; $S_0^2 = 0.65$; * $2\sigma^2 = 0.05$ Å^2. ** $2\sigma^2 = 0.01$ Å^2. Where $\Delta E0$ is the energy for aligning XAS data to an absolute energy grid for fitting, S_0^2 is the amplitude reduction factor, and $\sigma 2$ is the Debye-Waller factor. Note that EXAFS cannot distinguish Fe (atomic number 24) from Ni (atomic number 26). The information whether Fe is in a NiO_x host or FeO_x host is derived from the bond length, which can be determined more precisely than coordination numbers by EXAFS analysis.

XAS interpretation. The EXAFS was extracted and fit as detailed in the experimental section with parameters in Table 1. The restriction to 7.8 Å^{-1} in the fits was necessary due to noise and/or distortions in some of the samples, in particular for Fe-CV, 0.68 V. Extending the fit range on the lower end yields identical parameters within error (Table 2). The Fe-O bond length at 0.68 V vs. Hg/HgO contracted after cycling, which is consistent with the movement from (primarily) absorbed FeO_x cluster species, to a mixed $NiFeO_xH_y$ where the Fe-O bond is compressed due to integration the $NiFeO_xH_y$ mixed cation phase as discussed in the main text. However, the differences in bond length are within error and the contraction was also found after the open circuit measurement and holding the sample at 0.60 V in some cases. Further work repeating these measurements on the $NiFeO_xH_y$ and the $CoFeO_xH_y$ system with higher signal-to-noise ratio should be done to confirm the statistical significance of the bond contraction upon cycling.

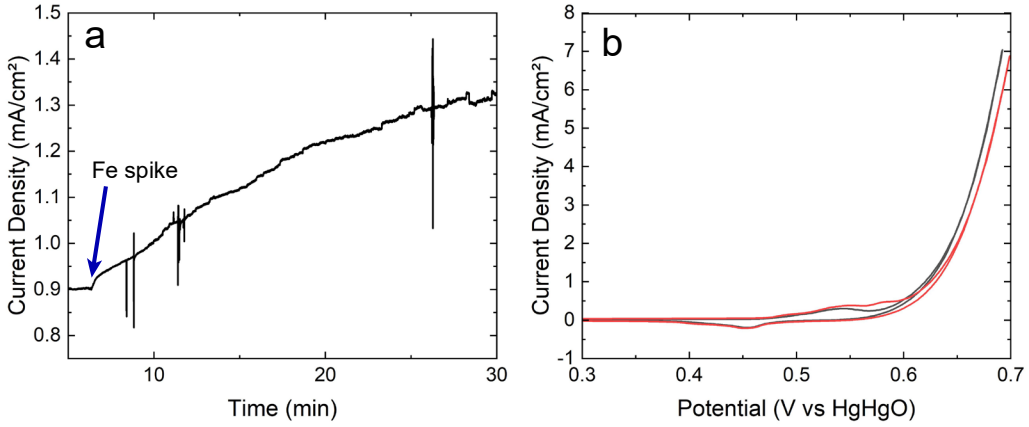

Figure 47. Fe-spiking of $Ni_{0.8}Fe_{0.2}O_xH_y$
(a) Current density of a $Ni_{0.8}Fe_{0.2}O_xH_y$ film after addition of 100 ppb Fe while polarizing at 1.55 V vs RHE as was done with Fe-free films. (b) Cyclic voltammetry of the film immediately after deposition and before the Fe spike (red) and after the Fe-spike (black).

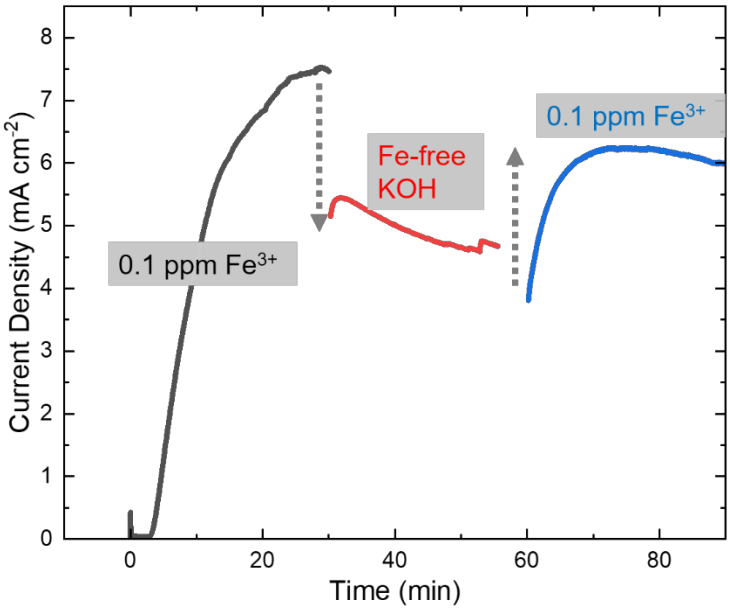

Figure 48. De-activation of Fe:NiO_xH_y in Fe-free KOH
The OER current density increase at 1.55 V vs RHE of a NiO_xH_y film from addition of $Fe(NO_3)_3$ until the electrolyte concentration was nominally 0.1 ppm (black trace). This current density decreases upon placement of the electrode into Fe-free KOH (red trace) and is largely recovered (blue trace) when re-immersed in the original Fe spiked solution.

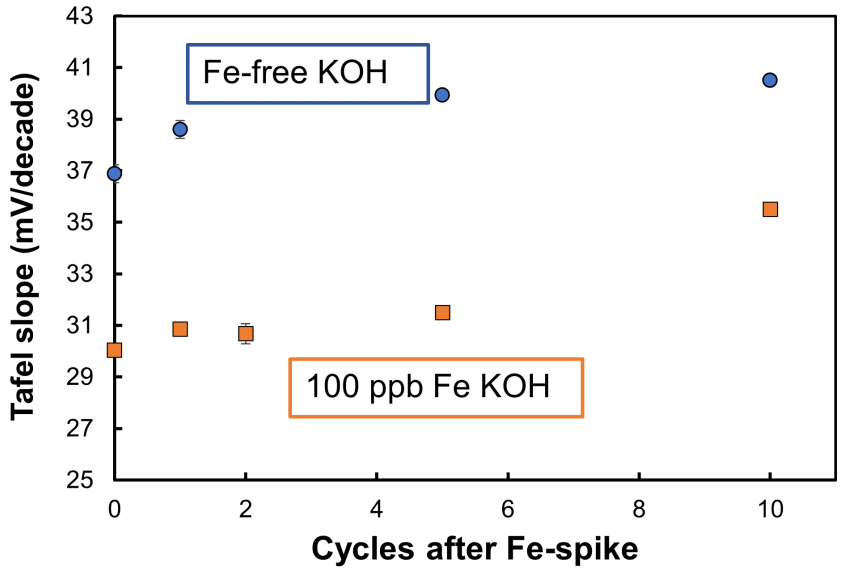

Figure 49. Tafel slopes of CA Fe-spiked NiOOH.
Data in blue was acquired in fresh Fe-free 1 M KOH after the CA Fe-spike while that in orange was kept in the electrolyte with 100 ppb Fe. Error bars are one standard deviation in the average linear fit to the data and are in some cases smaller than the data point and in general were < 1 mV decade^{-1}.

Table 3. ΔG and theoretical reaction overpotential (η_{th}) for OER mechanisms*

Gibbs free energy change (eV)	(0$\bar{1}$5) surface										(001) surface	
	isolated Fe-O		Fe-O-M dimer								Fe-O monomer	Fe-O-Fe dimer
	axial		*axial*		*insertion*		*bridge*		*equatorial*		*axial*	*axial*
	Fe	Ni	Fe	Ni	Fe	Ni	Fe	Ni	Fe	Ni	Fe	Fe
ΔG_1	1.60	1.62	1.73	1.80	1.73	1.80	1.45	1.41	1.16	1.48	1.84	2.01
ΔG_2	2.03	2.03	1.67	2.12	0.93	1.01	1.56	1.78	1.70	1.92	2.56	1.88
ΔG_3	-1.16	1.03	1.23	0.65	1.59	1.53	1.05	0.96	0.52	0.27	-0.14	0.37
ΔG_4	2.19	-0.03	0.22	0.36	0.67	0.58	0.86	0.76	1.47	1.46	0.30	0.47
ΔG_5	0.26	0.27	0.07	0.00	–	–	–	–	0.07	-0.20	0.36	0.18
η_{th} (V)	0.96	0.80	0.50	0.89	0.50	0.57	0.33	0.55	0.47	0.68	1.33	0.78

a

*η_{th} is the theoretical overpotential of the entire reaction, which is defined as the potential needed for all the reactions steps to have negative free energies. "–" indicates that ΔG is absent for that pathway due to different number of intermediates for each mechanism. Columns with "Fe" mean that the dimer has two Fe atoms and columns with "Ni" mean that the dimer has one Fe atom and one Ni atom.

The elementary steps of the above mechanisms are represented as follows:

Axial Mechanism and Equatorial Mechanism

Step 1: $\mathbf{M_{sur\_H_2O} \longrightarrow M_{sur\_OH} + (H^+ + e^-)}$

Step 2: $\mathbf{M_{sur\_OH} \longrightarrow M_{sur\_O} + (H^+ + e^-)}$

Step 3: $\mathbf{M_{sur\_O} + H_2O \longrightarrow M_{sur\_OOH} + (H^+ + e^-)}$

Step 4: $\mathbf{M_{sur\_OOH} \longrightarrow M_{sur\_OO} + (H^+ + e^-)}$

Step 5: $\mathbf{M_{sur\_OO} + H_2O \longrightarrow M_{sur\_H_2O} + O_2}$

Bridge Mechanism

Step 1: $\mathbf{M_{sur\_OH} \longrightarrow M_{sur\_O} + (H^+ + e^-)}$

Step 2: $\mathbf{M_{sur\_O} + H_2O \longrightarrow M_{sur\_OOH} + (H^+ + e^-)}$

Step 3: $\mathbf{M_{sur\_OOH} \longrightarrow M_{sur\_OO} + (H^+ + e^-)}$

Step 4: $\mathbf{M_{sur\_OO} + H_2O \longrightarrow M_{sur\_OH} + O_2 + (H^+ + e^-)}$

Insertion Mechanism

Step 1: $\mathbf{M_{sur\_H_2O} \longrightarrow M_{sur\_OH} + (H^+ + e^-)}$

Step 2: $\mathbf{M_{sur\_OH} + H_2O \longrightarrow M_{sur\_H_2O\_O_p} + (H^+ + e^-)}$

Step 3: $\mathbf{M_{sur\_H_2O\_O_p} \longrightarrow M_{sur\_OH\_O_p} + (H^+ + e^-)}$

Step 4: $\mathbf{M_{sur\_OH\_O_p} + H_2O \longrightarrow M_{sur\_H_2O} + O_2 + (H^+ + e^-)}$

$\mathbf{M_{sur}}$ represents the metal site on the surface where the reaction is taking place

$\mathbf{M_{sur\_X}}$ (x=H_2O, OH, O, OOH, OO) represents the reactive metal site with respective intermediate.

$\mathbf{M_{sur_X_O_p}}$represents the reactive metal site with oxygen penetrated at the bridge position along with the intermediate at the metal site.

Reaction free energies are calculated using the formulae:

$$\Delta G_1 = E^*_{OH} - E^*_{H_2O} + \frac{1}{2}E_{H_2} + \frac{1}{2}(ZPE - T.S)_{H_2}$$

$$\Delta G_2 = E^*_{O} - E^*_{OH} + \frac{1}{2}E_{H_2} + \frac{1}{2}(ZPE - T.S)_{H_2}$$

$$\Delta G_3 = E^*_{OOH} - E^*_{O} + \frac{1}{2}E_{H_2} - E_{H_2O} + \frac{1}{2}(ZPE - T.S)_{H_2} - (ZPE - T.S)_{H_2O}$$

$$\Delta G_4 = E^*_{OO} - E^*_{OOH} + \frac{1}{2}E_{H_2} + \frac{1}{2}(ZPE - T.S)_{H_2}$$

$$\Delta G_5 = E^*_{H_2O} - E^*_{OO} + E_{O_2} - E_{H_2O} + (ZPE - T.S)_{O_2} - (ZPE - T.S)_{H_2O}$$

Where E^*_X is the VASP energy of the intermediates that includes the ZPE corrections, E_x is the energy of the gaseous molecules, ZPE and TS are the respective zero point and entropy correction.

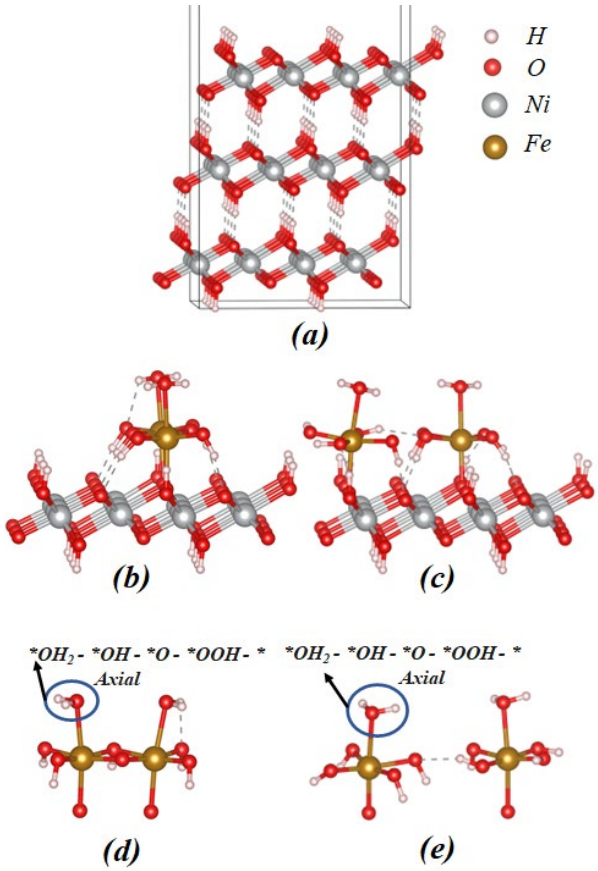

Figure 50. Computational structural model of NiOOH

(a) The structure of bare NiOOH (001) surface. The adsorption model for the **(b)** Fe-O-Fe dimer and **(c) isolated** Fe-O on the NiOOH (001) surface. Reaction sites (circled in blue), Fe-coordination and reaction pathways with intermediates involved in the OER process for the **(d)** Fe-O-Fe dimer and **(e) isolated** Fe-O case. Only the upper part of the (001) surface is shown for clarity.

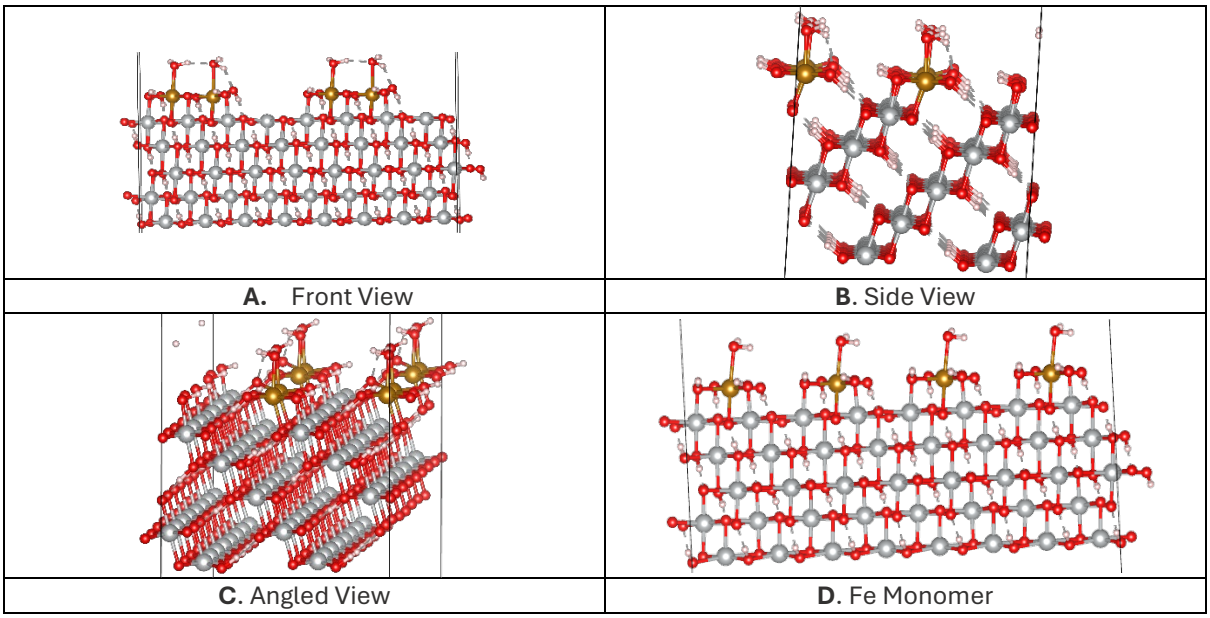

Figure 51. Angular views of adsorption model for Fe-O-Fe dimer clusters
(a) The front view **(b)** side view **(c)** angular view. **(d)** The front view of the adsorption model for the Fe monomer clusters. The Fe dimer cluster on the NiOOH edge/surface is distinct from a Ni vacancy. To test whether an Fe adsorbed dimer cluster facilitates OER, we have considered an Fe cluster where Fe has four OH bonds in plane parallel to the oxygen atoms of the NiOOH (monomer) and for the dimer where two Fe atoms are bonded to the NiOOH slab and to each other via a bridging oxygen and terminated otherwise with 4 OH bonds. The rest of the coordination is satisfied by one water molecule on top. Hence, the adsorbed cluster has a different structure and symmetry from possible vacancies on NiOOH. All Ni atoms on the surface of the dimer model are bonded to -OH if they are not attached to Fe atoms.

Table 4. Supporting numerical data.

Sample Identification	Deposition parameters	Mass Ni[a] (ng cm^{-2})	Mass Co[a] (ng cm^{-2})	Mass Fe[a] (ng cm^{-2})	Fe/Ni at. ratio (%)	Fe/Co at. ratio (%)	TOF_{Fe} (s^{-1}) η = 300 mV	TOF_{Fe} (s^{-1}) η = 350 mV
NiO_xH_y	0.1 M Ni^{2+} -0.1 mA cm^{-2} 120 s	2744 ± 43						
CoO_xH_y	0.1 M Co^{2+} -2 mA cm^{-2} 8 s		4966 ± 213					
Fe incorporated NiO_xH_y from CA Fe-spiking	0.1 M Ni^{2+} -0.1 mA cm^{-2} 120 s	2713 ± 47		19 ± 2	0.7 ± 0.3		1.9 ± 0.3	4.5 ± 0.8
Fe incorporated NiO_xH_y from CA Fe-spiking		2941 ± 58		45 ± 8	1.6 ± 0.3		3.1 ± 0.7	13.5 ± 3.2
Fe incorporated NiO_xH_y from CA Fe-spiking		2737 ± 92		53 ± 7	2.0 ± 0.4		4.3 ± 0.6	22.3 ± 1.0
Fe incorporated NiO_xH_y from CA Fe-spiking		2843 ± 56		77 ± 11	2.9 ± 0.4		5.8 ± 0.8	28.4 ± 1.9

Sample Identification		Mass Ni[a] (ng cm^{-2})	Mass Co[a] (ng cm^{-2})	Mass Fe[a] (ng cm^{-2})	Fe/Ni at. ratio (%)	Fe/Co at. ratio (%)	TOF_{Fe} (s^{-1}) η = 300 mV	TOF_{Fe} (s^{-1}) η = 350 mV
Fe incorporated NiO_xH_y from CA Fe-spiking	0.1 M Ni^{2+} -0.1 mA cm^{-2} 120 s	2956 ±144		87 ± 5	3.1 ± 0.5		8.4 ± 0.4	35.5 ± 3.7
Fe incorporated NiO_xH_y from CA Fe-spiking		2975 ± 122		144 ± 19	5.1 ± 0.5		10.4 ± 1.4	39.6 ± 1.9
Fe incorporated NiO_xH_y from CA-2CV Fe-spiking		2636 ± 22		207 ± 11	8.3 ± 0.4		6.7 ± 0.2	28.2 ± 1.0
Sample Identification		**Mass Ni[a] (ng cm^{-2})**	**Mass Co[a] (ng cm^{-2})**	**Mass Fe[a] (ng cm^{-2})**	**Fe/Ni at. ratio (%)**	**Fe/Co at. ratio (%)**	**TOF_{Fe} (s^{-1}) η = 300 mV**	**TOF_{Fe} (s^{-1}) η = 350 mV**
Fe incorporated NiO_xH_y from CA-5CV Fe-spiking		3033 ± 34		337 ± 16	11.7 ± 0.4		4.3 ± 0.2	24.3 ± 1.7
Fe incorporated NiO_xH_y from CA-10CV Fe-spiking		2853 ± 47		389 ± 31	13.9 ± 1.2		3.7 ± 0.2	18.9 ± 0.4
Fe incorporated NiO_xH_y from CA-20CV Fe-spiking		2790 ± 27		508 ± 16	19.0 ± 0.5		3.5 ± 0.2	16.3 ± 0.6
Co-deposited $Ni_{0.95}Fe_{0.05}O_xH_y$	0.09975 M Ni^{2+} 0.00025 M Fe^{2+} -0.1 mA cm^{-2} 120 s	2929 ± 55		136 ± 17	4.9 ± 0.4		5.2 ± 0.2	25.5 ± 3.3
Co-deposited $Ni_{0.93}Fe_{0.07}O_xH_y$	0.0995 M Ni^{2+} 0.0005 M Fe^{2+} -0.1 mA cm^{-2} 120 s	2868 ± 42		194 ± 13	7.1 ± 0.5		4.4 ± 0.2	23.4 ± 4.0
Co-deposited $Ni_{0.91}Fe_{0.09}O_xH_y$	0.099 M Ni^{2+} 0.001 M Fe^{2+} -0.1 mA cm^{-2} 120 s	2842 ± 153		252 ± 27	9.3 ± 1.2		3.3 ± 0.2	16.7 ± 2.2
Co-deposited $Ni_{0.84}Fe_{0.16}O_xH_y$	0.098 M Ni^{2+} 0.002 M Fe^{2+} -0.1 mA cm^{-2} 120 s	2737 ± 66		500 ± 10	19.2 ± 1.1		3.0 ± 0.1	13.4 ± 0.9
Fe incorporated CoO_xH_y from CA Fe-spiking	0.1 M Co^{2+} -2 mA cm^{-2} 8 s		4859 ± 306	40 ± 8		0.9 ± 0.1	0.27 ± 0.05	4.3 ± 0.2
Fe incorporated CoO_xH_y from CA Fe-spiking			5284 ± 356	64 ± 8		1.3 ± 0.2	0.35 ± 0.05	4.7 ± 0.7
Fe incorporated CoO_xH_y from CA Fe-spiking	0.1 M Co^{2+} -2 mA cm^{-2} 8 s		4988 ± 382	81 ± 9		1.7 ± 0.3	0.54 ± 0.12	6.2 ± 0.6
Fe incorporated CoO_xH_y from CA Fe-spiking			4951 ± 296	114 ± 12		2.4 ± 0.3	0.71 ± 0.08	7.1 ± 0.8
Co-deposited $Co_{0.98}Fe_{0.02}O_xH_y$	0.099 M Co^{2+} 0.001 Fe^{2+} -2 mA cm^{-2} 8 s		4992 ± 119	111 ± 16		2.3 ± 0.3	0.23 ± 0.06	4.0 ± 0.4
Co-deposited $Co_{0.97}Fe_{0.03}O_xH_y$	0.098 M Co^{2+} 0.002 Fe^{2+} -2 mA cm^{-2} 8 s		5108 ± 231	167 ± 13		3.5 ± 0.2	0.23 ± 0.04	3.6 ± 0.2
Co-deposited $Co_{0.94}Fe_{0.06}O_xH_y$	0.096 M Co^{2+} 0.003 Fe^{2+} -2 mA cm^{-2} 8 s		4724 ± 142	264 ± 15		5.9 ± 0.4	0.18 ± 0.02	2.5 ± 0.3

Co-deposited $Co_{0.92}Fe_{0.08}O_xH_y$	0.093 M Co^{2+} 0.007 Fe^{2+} -2 mA cm^{-2} 8 s		4258 ± 83	365 ± 18		9.0 ± 0.4	0.14 ± 0.01	2.2 ± 0.1

[a] Mass of metals was determined by ICP-MS analysis at least in triplicate.

Table 5. Additional activity metric summary of investigated samples.

Sample Identification	*J* @ η = 300 mV (mA cm^{-2})	*J* @ η = 350 mV (mA cm^{-2})	η @ 10 mA cm^{-2} (mV)
Fe-incorporated NiO_xH_y from CA Fe spiking – 1 CV	4.0	11.4	340
Fe-incorporated NiO_xH_y from CA Fe spiking – 10 CV	5.1	12.4	335
Fe-incorporated CoO_xH_y from CA Fe spiking – 1 CV	0.14	1.7	n/a*
Fe-incorporated CoO_xH_y from CA Fe spiking – 10 CV	0.16	2.1	n/a*

*indicates experiments were not performed at or above 10 mA cm^{-2}

Table 6. Oxidation states for Fe-O monomer and Fe-O-Fe dimer.
The respective Ni substitution cases for all are as mentioned in Figure 5 of the manuscript with the mechanisms given above. M represents the magmom value in the output file and O represents the corresponding oxidation state.*

Reaction Name	PDS		Atom Name	Before		After	
				M	O	M	O
Fe-O monomer	OOH	OO	Fe	4.17	3	3.60	4
			Fe	3.75	3	3.72	3
Fe-O monomer (Ni subs)	OH	O	Ni	1.19	3	0.07	4
			Fe	3.06	5	2.41	6
Fe-O-Fe Axial	H_2O	OH	Ni	1.39	3	1.47	2
			Ni	1.39	3	1.73	2
			Fe	4.18	3	3.72	4
			Fe	3.85	3	3.60	4
Fe-O-Fe Insertion	H_2O	OH	Ni	1.39	3	1.47	2
			Ni	1.39	3	1.73	2
			Fe	4.18	3	3.72	4
			Fe	3.85	3	3.60	4
Fe-O-Fe Bridge	OH	O	Ni	1.12	3	0.10	4
			Fe	4.22	3	3.85	4
Fe-O-Fe	OH	O	Ni	1.39	3	0.50	4

Equatorial			Ni	1.31	3	1.42	2
			Fe	3.80	3	3.66	4
			Fe	3.88	3	3.75	4
Fe-O-Ni Axial	OH	O	Fe	3.62	4	2.58	5
Fe-O-Ni Insertion	H_2O	OH	Fe	3.97	3	3.62	4
Fe-O-Ni Bridge	OH	O	Ni	1.40	2	1.36	3
			Ni	1.00	3	0.06	4
			Ni	1.31	3	1.40	2
Fe-O-Ni Equatorial	OH	O	Ni	1.34	3	1.42	2
			Fe	3.63	2	3.65	4
Fe-O monomer (001)	OH	O	Fe	3.62	3	3.62	3
			Fe	3.10	4	2.91	5
Fe-O-Fe Axial (001)	H_2O	OH	Fe	3.66	3	3.17	4
			Fe	3.69	3	3.11	4

*According to previous work[264, 265], the magnetization range 3.75 to 4.3 is assigned to +3 oxidation state and the magnetization range 3.2 to 3.75 is assigned to +4 or +2 oxidation states, depending on the mechanism, while the values ~3.6-3.8 are on the boarder of these two ranges. In cases where there is a change in the magnetization within the range, but the change is significant, we regard this as a change in the oxidation state. Note that in some cases there is a partial change in charge and not a full change in oxidation state as indicated, depending on the magnitude of the magnetic moment change. However, we indicated the best estimate to emphasize that there is a change in atomic charges.

Table 7. Free energies and theoretical overpotentials

From Table 3 plus those calculated for a "core" Fe active site, an Fe that is substituted at a Ni position according to the model below.

Gibbs free energy change	**(0$\bar{1}$5) surface**														
	isolated Fe-O			**Fe-O-M dimer**											
	Axial			*axial*			*insertion*			*bridge*			*equatorial*		
	Fe	Ni	Core	Fe	Ni	Core	Fe	Ni	Core	Fe	Ni	Core	Fe	Ni	Core
ΔG_1	1.60	1.62	1.52	1.73	1.80	2.04	1.73	1.80	2.04	1.45	1.41	1.59	1.16	1.48	1.44
ΔG_2	2.03	2.03	2.34	1.67	2.12	1.82	0.93	1.01	0.74	1.56	1.78	1.95	1.70	1.92	1.74
ΔG_3	-1.16	1.03	-1.12	1.23	0.65	0.68	1.59	1.53	2.12	1.05	0.96	0.71	0.52	0.27	-0.02
ΔG_4	2.19	-0.03	1.85	0.22	0.36	0.44	0.67	0.58	0.03	0.86	0.76	0.67	1.47	1.46	1.49
ΔG_5	0.26	0.27	0.34	0.07	0.00	-0.06	–	–	–	–	–		0.07	-0.20	0.27
η_{th}	0.96	0.80	1.11	0.50	0.89	0.81	0.50	0.57	0.89	0.33	0.55	0.72	0.47	0.68	0.51

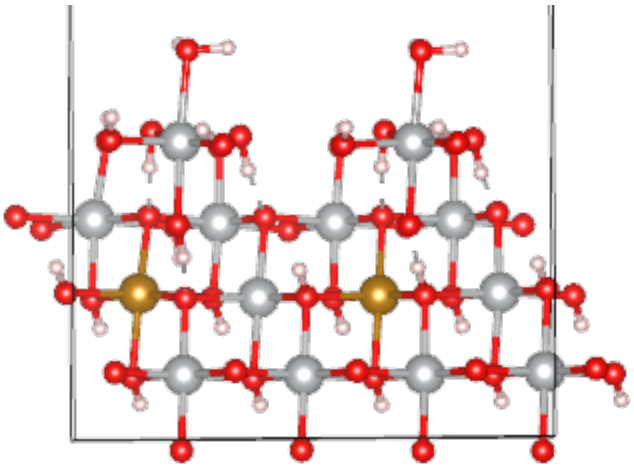

Figure 52. Gibbs free energy calculations slab model
The slab model used to calculate the "core" Fe Gibbs free energies in Table 6 above. Gray spheres are Ni, red spheres are oxygen, and gold spheres are Fe atoms.

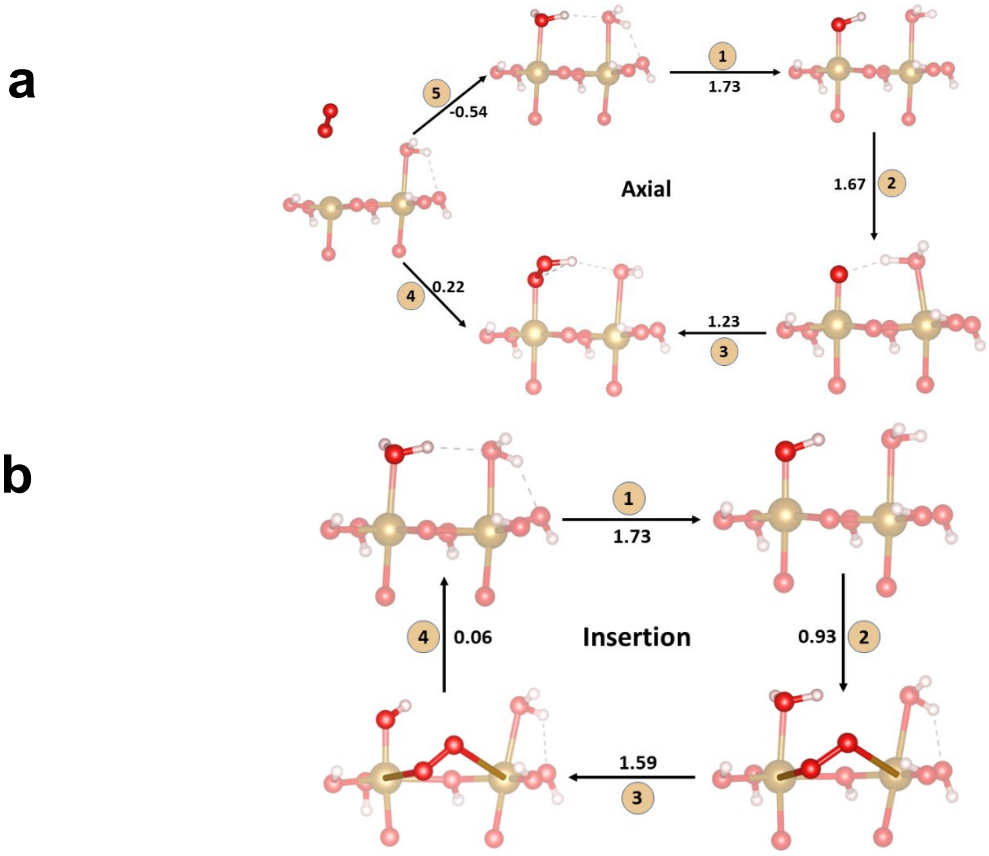

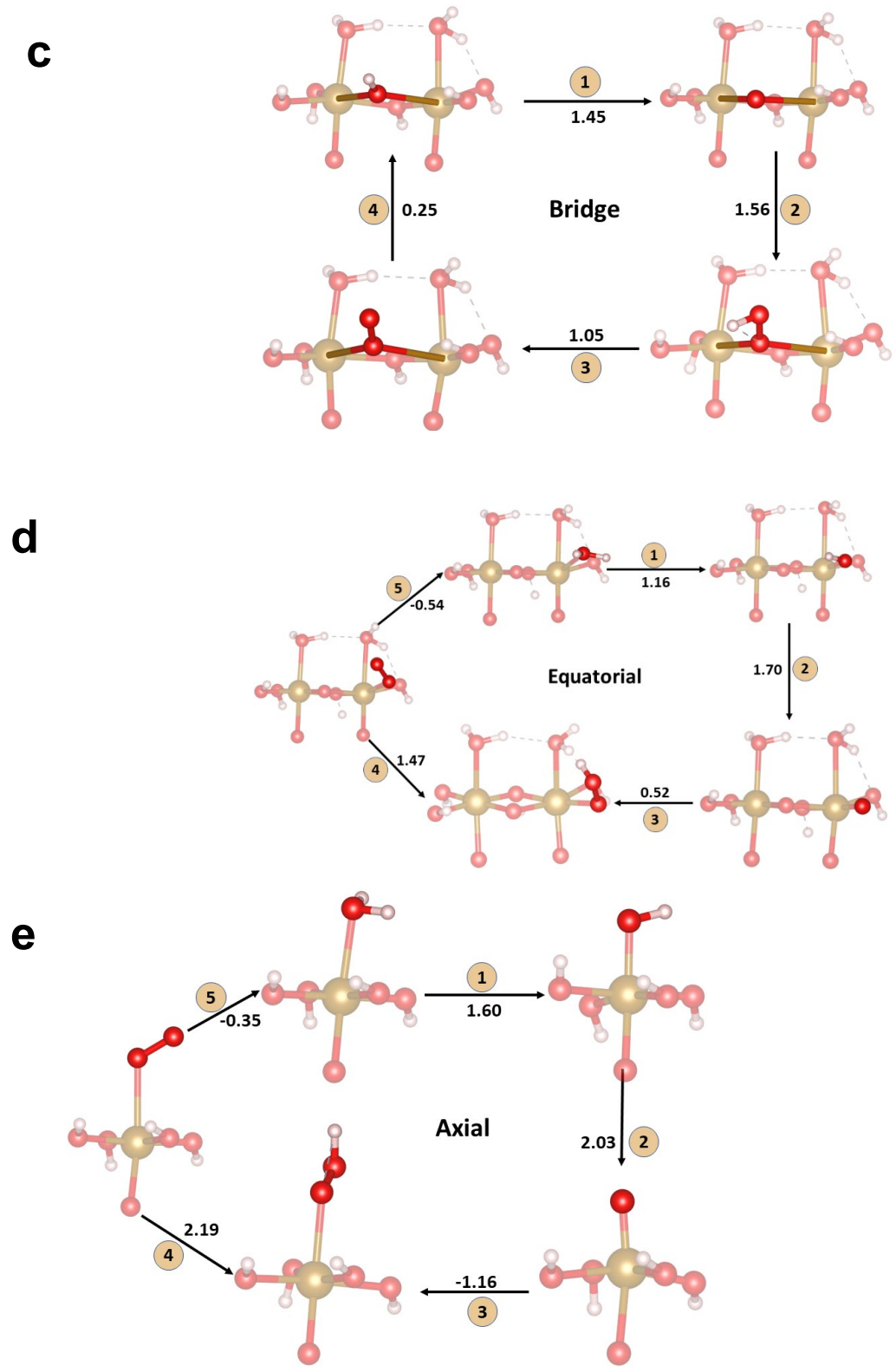

Figure 53. Dimer and monomer reaction pathways
Additional large-scale depictions of dimer and monomer reaction pathways used in DFT calculations: **(a-d)** dimer mechanisms and **(e)** monomer mechanism.

B. CHAPTER III SUPPLEMENTARY INFORMATION

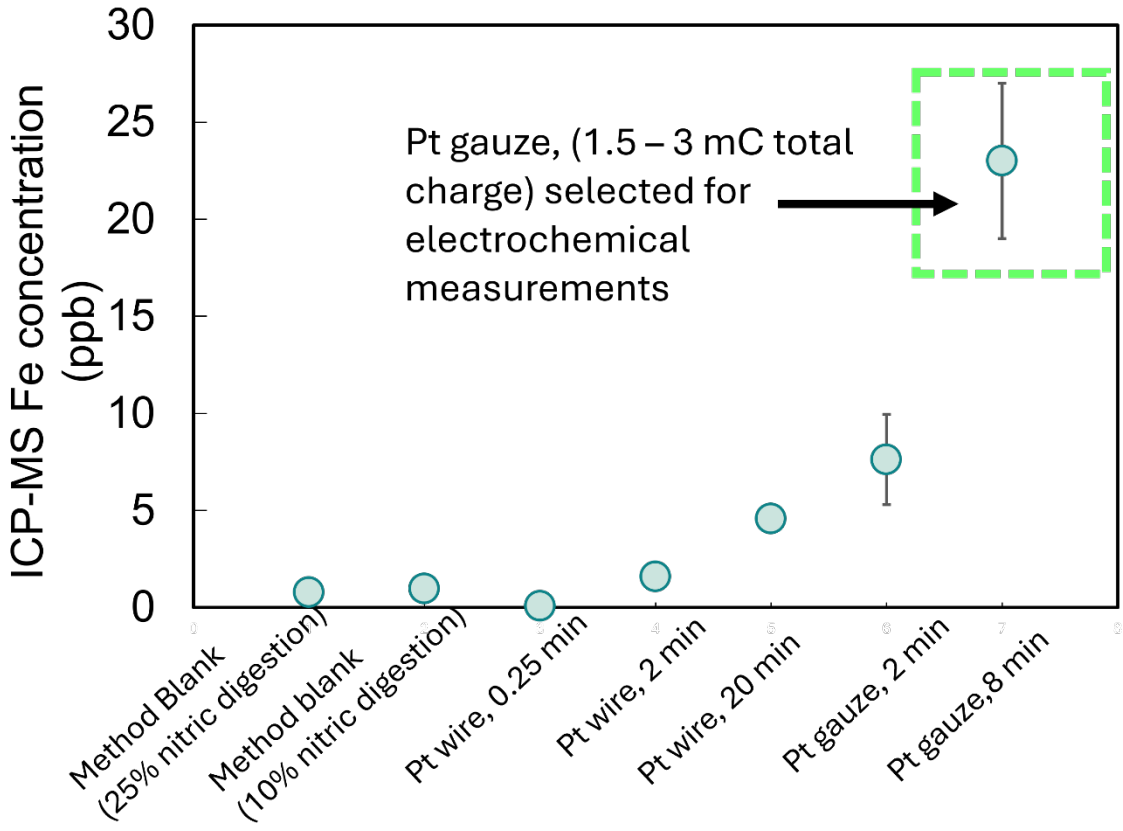

Figure 54. Optimization of ICP-MS Fe detection
ICP-MS concentration of Fe detected in digested films of NiO_xH_y deposited for various deposition times and with different Pt substrates are compared against method blanks. The conditions which led to the value of Fe in the dashed green box were selected for the temperature-dependent study.

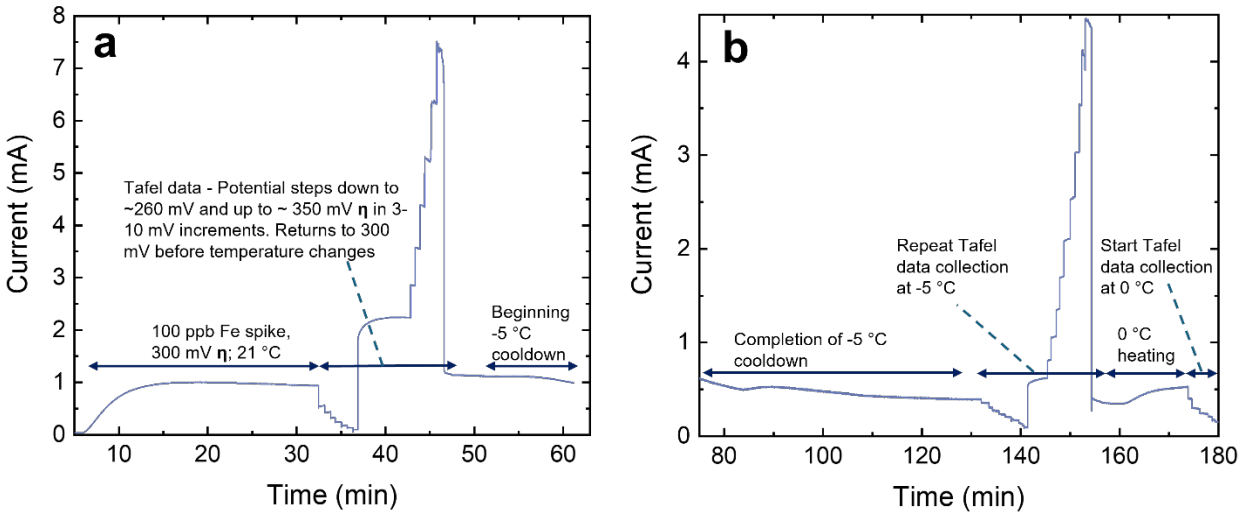

Figure 55. Example of raw temperature-dependent chronoamperometry data
(a) Shows the start of a variable temperature experiment including the Fe-spiking and Tafel data collection at room temperature followed by a typical temperature change and recollection of Tafel data in **(b).**

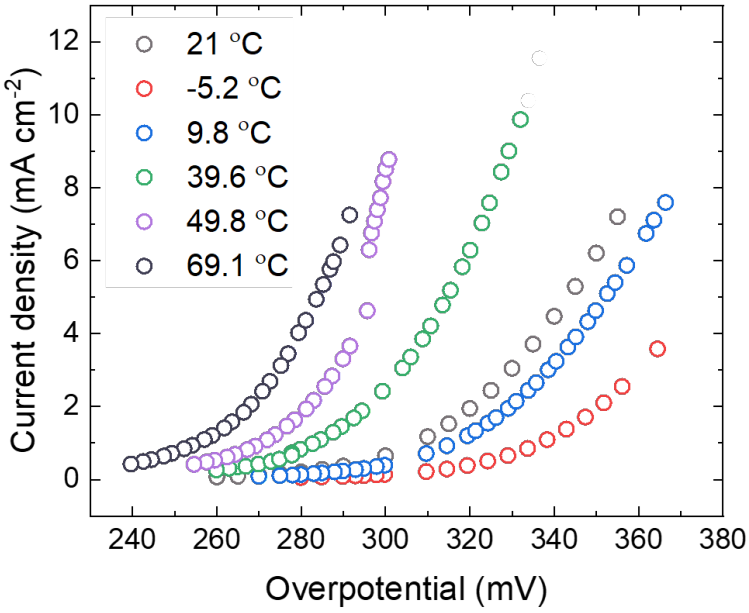

Figure 56. J-V plots of typical variable temperature OER currents.
Each current value is extracted as the average current at each potential step in the Tafel collection windows in Figure 54 and used to reconstruct the J-V curves. The exponential shape suggests an Arrhenius and Tafel analysis is applicable.

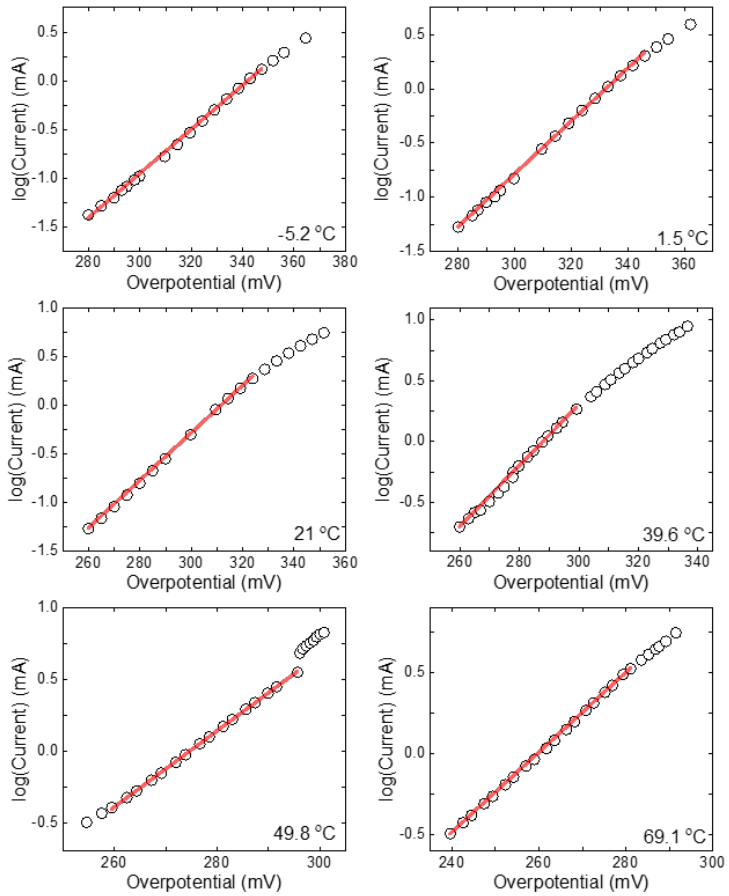

Figure 57. Tafel plots and fits
Tafel plots were constructed by taking the logarithm of the current and plotting it against the overpotential. Fits were done in the linear regions of the data in the lowest ~60 mV of the data.

Table 8. Summary of Tafel data

Temperature (°C)	Tafel slope (mV dec^{-1})	[a]Exchange current, i_0 (x10^{-8} mA)	[b]Exchange current density, j_0 (x10^{-8} mA cm^{-2})	Transfer coefficient, α	Number of measurements, n
-5.2	42 ± 3.3	1.8 ± 0.02	2.3 ± 0.02	1.27 ± 0.10	3
1.5	38 ± 3.7	0.8 ± 0. 01	1.1 ± 0.01	1.43 ± 0.14	3
21	39 ± 1.8	2.6 ± 0.03	3.4 ± 0.04	1.49 ± 0.07	3
39.6	40 ± 0.2	6.6 ± 0.05	8.6 ± 0.06	1.54 ± 0.01	2
49.8	39 ± 1.5	4.8 ± 0.01	6.3 ± 0.02	1.64 ± 0.06	2
69.1	41 ± 0.2	39 ± 0.2	51 ± 0.2	1.67 ± 0.01	1

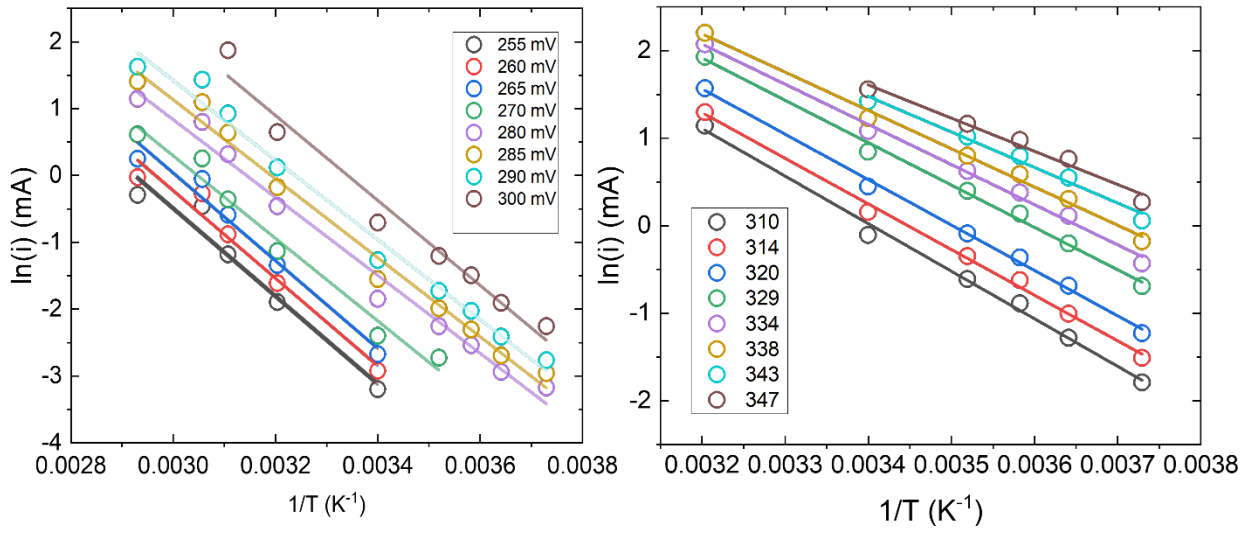

Figure 58. Arrhenius plots
Plots were made by linearization of the Arrhenius equation. Currents were taken from the temperature-dependent Tafel plots in Figure 9.

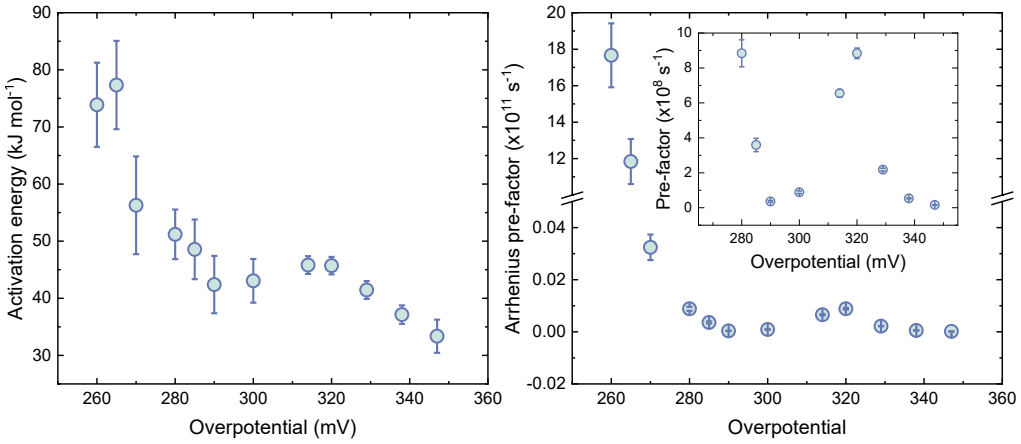

Figure 59. Arrhenius parameters from TOF_{Fe}
Activation energies (left) and pre-exponential factors (right) as a function of overpotential using ln(TOF_{Fe}) instead of ln(current).

Supplementary Calculation 2

Below is a reproduction of Conway's derivation[164] showing how a temperature-dependence of the transfer coefficient is expected when the standard electrochemical entropy of activation is potential dependent. We have included more steps than in the original paper to make it easier to follow for the reader.

Butler-Volmer equation for an oxidation reaction (IUPAC convention) far from equilibrium where good mass transfer ensures surface concentrations are approximately equal to bulk concentrations (see Bard, 2001. Ch. 3, section 3.4.3)[42].

$$i = i_0 e^{-\alpha f \eta} \tag{1}$$

Where $f = F/RT$

Linearizing by taking the natural logarithm and using ln(x) = 2.3*log(x) we obtain

$$2.3\log(i) = 2.3\log(i_0) - \alpha f \eta \tag{2}$$

Differentiation with respect to η yields the reciprocal Tafel slope, b, in (dec V^{-1})

$$2.3\left(\frac{dlog(i)}{d\eta}\right) = 2.3 * \left(\frac{1}{b}\right) = 2.3\left(\frac{dlogi_0}{d\eta}\right) - \alpha f \tag{3}$$

Now recall that i_0 proportional to the rate constant at standard conditions k_0. We group the constants into A' and using the definition of k_0 we may write

$$i_0 = A' e^{-\Delta \bar{G}_0^{\ddagger}/RT} \tag{4}$$

Where $\Delta \bar{G}_0^{\ddagger}$ is the standard electrochemical free energy of activation. Then by the definition

$$\Delta \bar{G}_0^{\ddagger} = \Delta \bar{H}_0^{\ddagger} - T\Delta \bar{S}_0^{\ddagger} \tag{5}$$

substituting (5) for $\Delta \bar{G}_0^{\ddagger}$ in (4) and taking the logarithm we obtain

$$2.3 \log(i_0) = 2.3 \log(A') + \frac{\Delta \bar{S}_0^{\ddagger}}{R} - \frac{\Delta \bar{H}_0^{\ddagger}}{RT} \tag{6}$$

Substituting (6) into (3) we get

$$\frac{2.3}{b} = \frac{d}{d\eta}\left(2.3 \log(A') + \frac{\Delta \bar{S}_0^{\ddagger}}{R} - \frac{\Delta \bar{H}_0^{\ddagger}}{RT}\right) - \alpha f \tag{7}$$

Key assumption: now suppose $\Delta \bar{S}_0^{\ddagger}$ is potential-dependent and that the fractional change in $\Delta \bar{S}_0^{\ddagger}$ can be represented as

$$\Delta \bar{S}_0^{\ddagger} \pm \alpha_S F(E - E^0)$$

Substituting this into (7), completing the differentiation and rearranging yields

$$\frac{2.3RT}{bF} = transfer\ coefficient = \alpha \pm \alpha_S T \tag{8}$$

The problem we see with this approach is in the necessary assumption that $\Delta \bar{S}_0^{\ddagger}$ is dependent on the potential. This quantity is a constant as defined because it follows from the free energy of reactants and products defined for a reference condition, namely, standard conditions. Making this key assumption is tantamount to asking: what is the potential dependence of standard conditions? This seems non-physical as proposed. We suspect another explanation for the temperature-dependence of the transfer coefficient would be more convincing. Perhaps an explanation lies in the fact that k_0 is temperature dependent in the classic sense via modulation of the exponential term

$-\Delta\bar{G}_0^{\ddagger}/RT$ though we have not successfully used this observation to derive an appropriate expression. Alternatively, if A' is potential dependent we would recover an expression similar to (8). This latter approach is similar to that suggested by Chen *et al.* for water-dissociation catalysts in bipolar membrane electrolyzers where *A* was set proportional to the overpotential by a constant labelled as the "proton conductance".

C. CHAPTER IV SUPPLEMENTARY INFORMATION

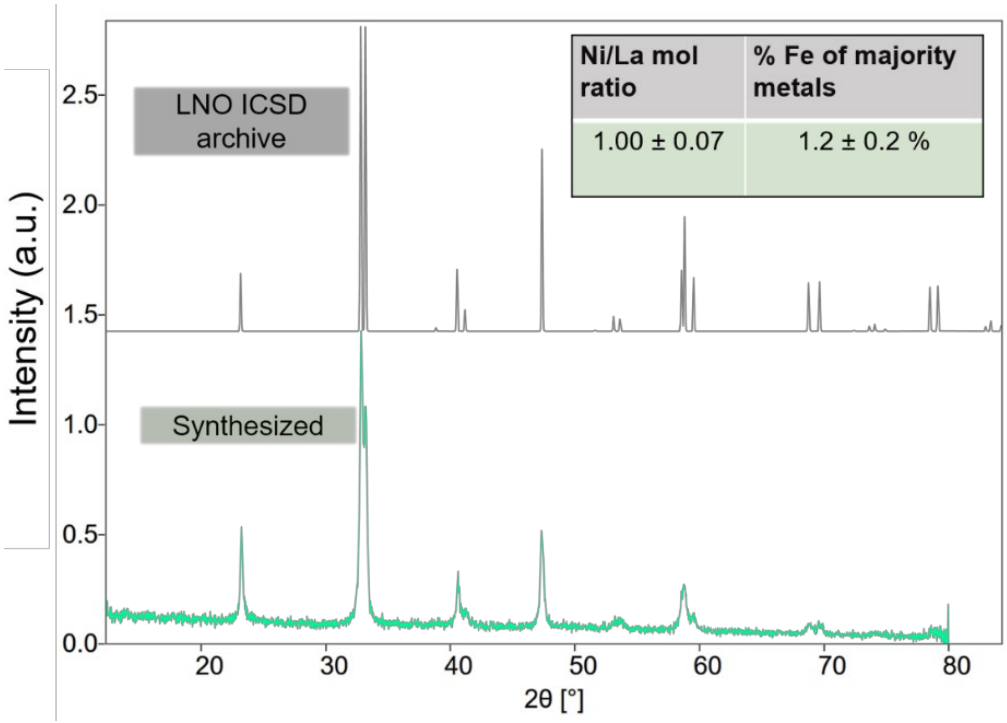

Figure 60. PXRD comparison of literature and synthesized $LaNiO_3$.
Top pattern corresponds to International Crystal Structure Database entry #67714 which is rhombohedral $LaNiO_3$ with space group R-3c. The inset table shows the composition of the synthesized phase from ICP-MS analysis.

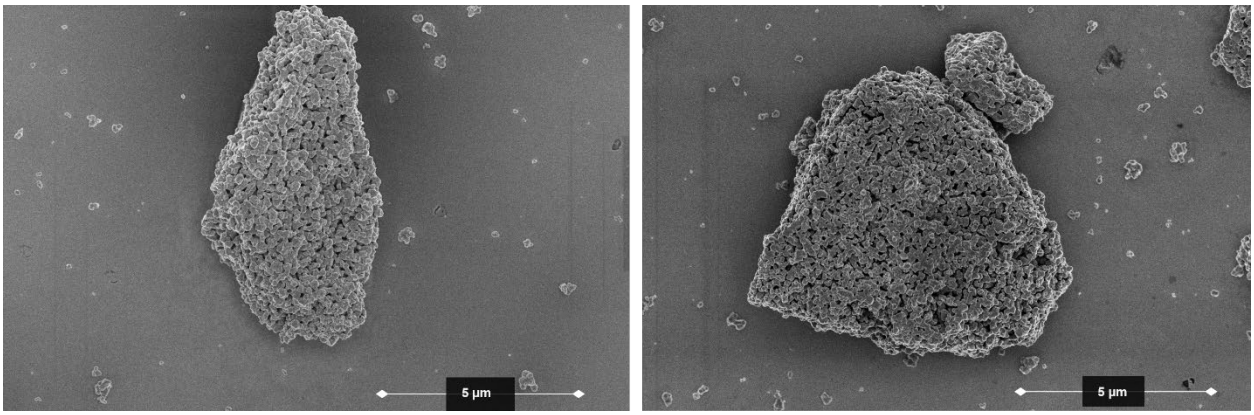

Figure 61. SEM images of particulate $LaNiO_3$.
Particles sizes range from large micrometer scale sintered agglomerates to particles in the 100-nm range.

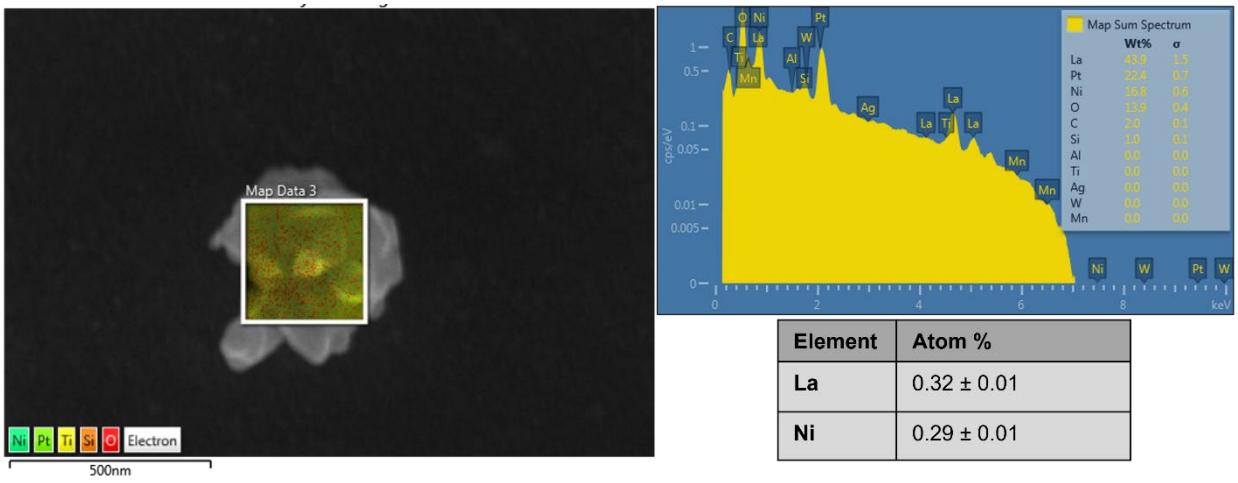

Element	Atom %
La	0.32 ± 0.01
Ni	0.29 ± 0.01

Figure 62. EDX spectrum of $LaNiO_3$
A roughly 300-nm diameter particle showing the 1:1 La:Ni stoichiometry in agreement with ICP-MS

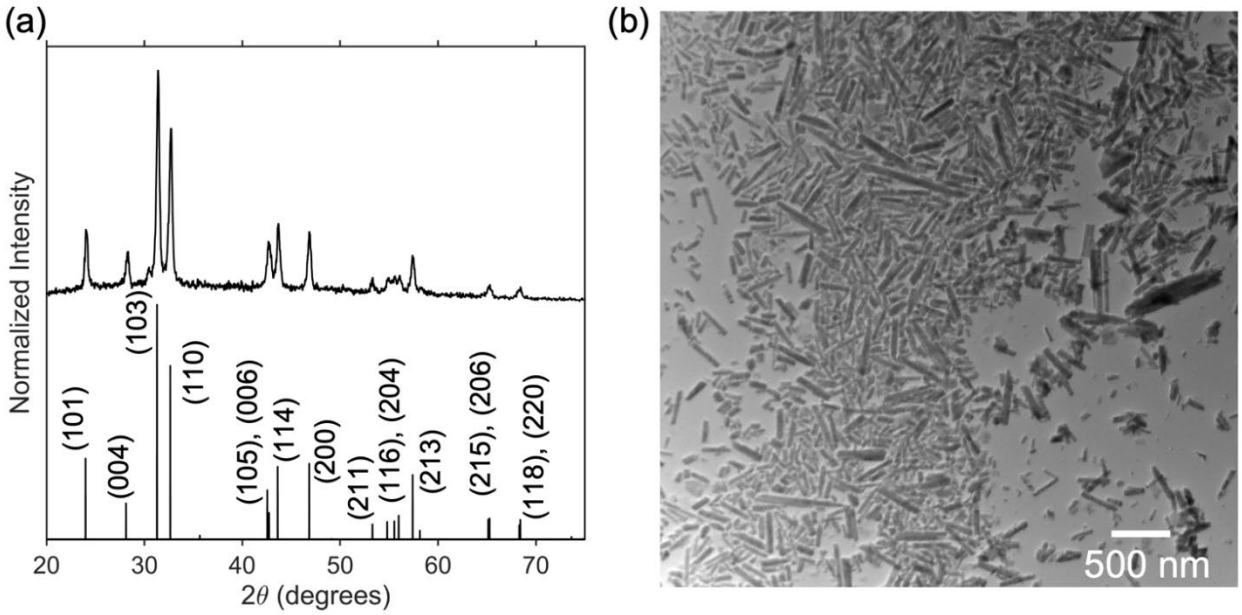

Figure 63. La_2NiO_4 rods PXRD and SEM
(a) PXRD of La_2NiO_4 rods confirming the pure Ruddelsden-Popper tetragonal structure belonging to I4/*mmm* symmetry. (b) SEM micrograph confirming rod-shaped morphology of La_2NiO_4 synthesized using a reverse microemulsion technique.

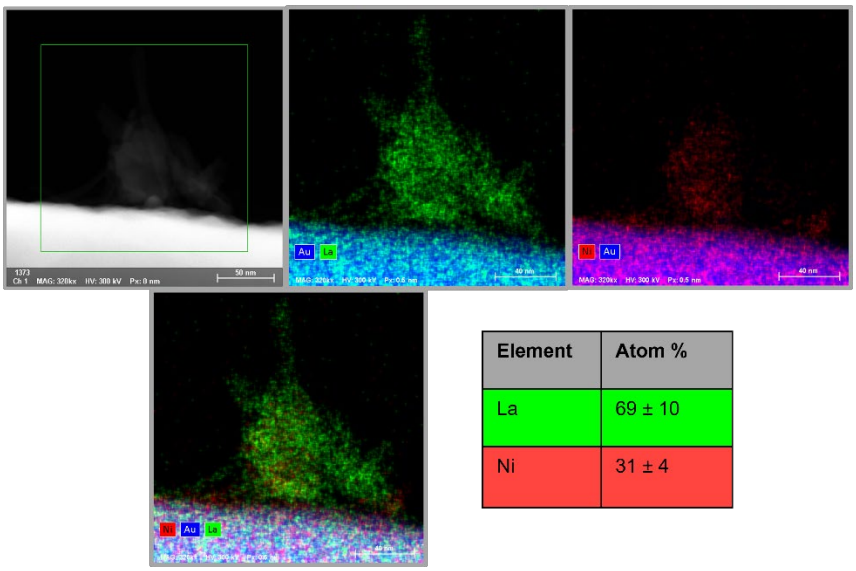

Figure 64. TEM/EDX images of La_2NiO_4 rod bundle
Corresponds to TEM presented in main-text Figure 16. Initial expected stoichiometry of 2:1 La:Ni (66% : 33%) was obtained within error.

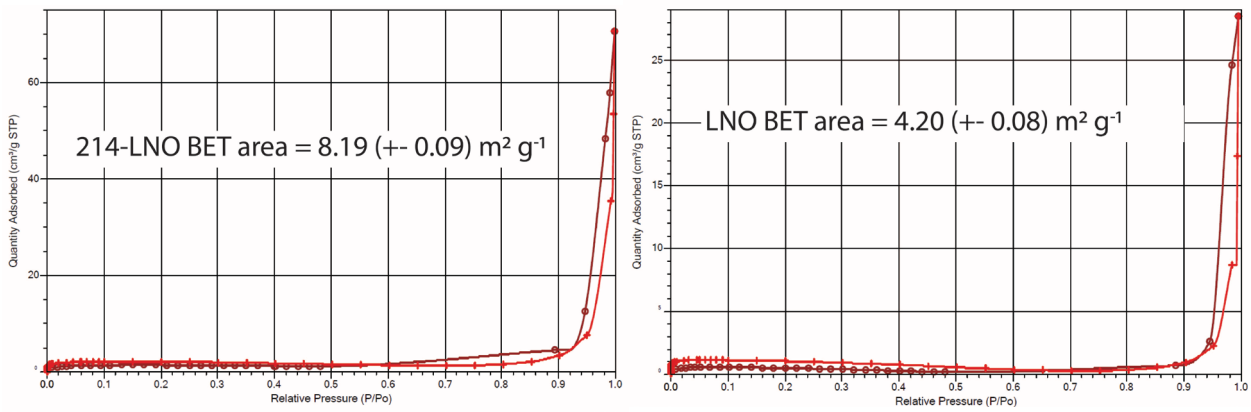

Figure 65. Adsorption isotherms/BET surface areas of 214-LNO and LNO.

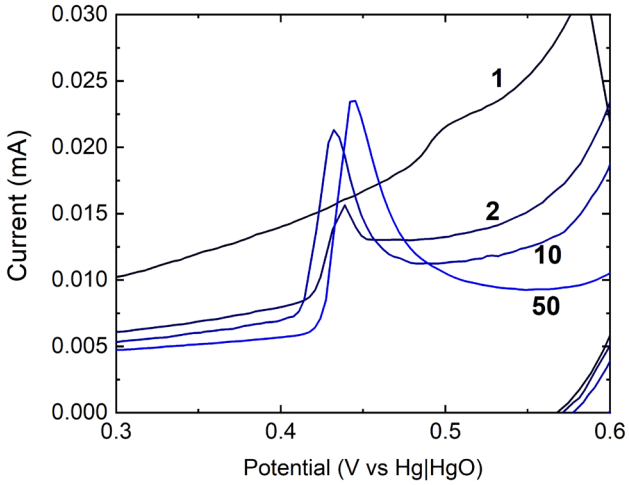

Figure 66. Cyclic voltammetry of $LaNiO_3$ in $Co(OH)_2$ - cleaned 1.0 M KOH
Electrolyte was cleaned using $Co(OH)_2$ as the Fe sorbent. The redox wave is seen and grows analogously to that seen in $Ni(OH)_2$-cleaned KOH showing Ni impurities in the electrolyte are not depositing to form the redox-active surface phases studied herein because deposition of Co impurities would result in a redox wave centered at a more negative potential.

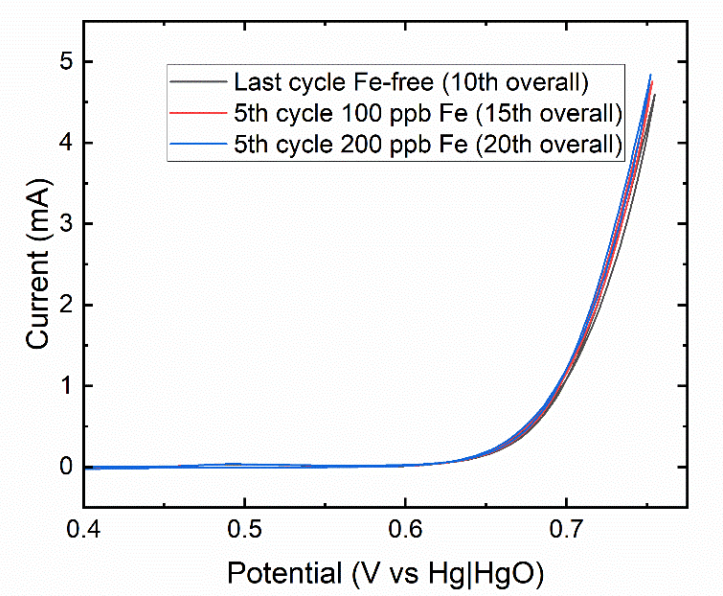

Figure 67. CVs Fe-spiked $LaCoO_3$
Cyclic voltammetry of a drop-cast $LaCoO_3$ electrode with one Fe spike of 100 ppb between the 10^{th} and 11^{th} cycle and another 100 ppb between the 15^{th} and 16^{th} cycle. Slurry used was 5:1:1 $LaCoO_3$:Nafion:acetylene carbon black. Voltage is iR-corrected. No redox waves were evident from zooming in at all precatalytic regions of the CV. Drop casting was chosen instead of spin coating because the Ni redox waves were small and if Co redox waves were present, they would be easier to see at higher mass loading. Note that there are not any Ni redox waves, further confirming that those features do not originate from Ni impurities.

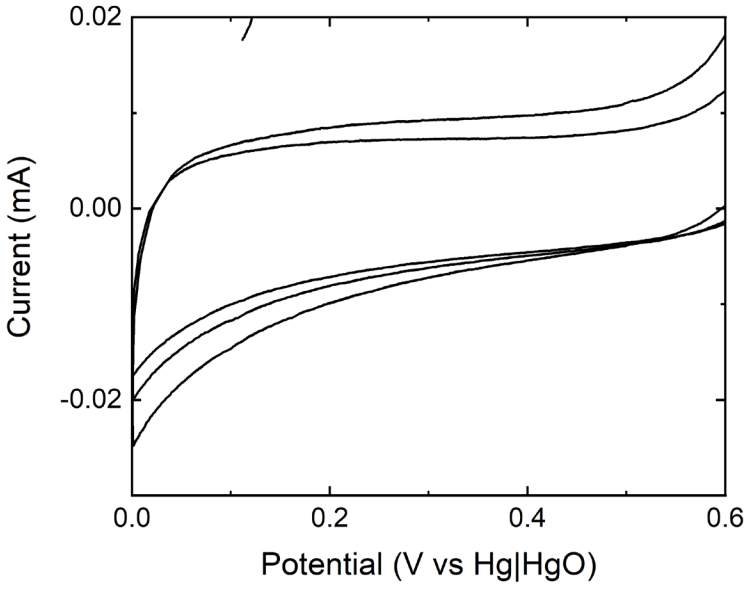

Figure 68. Pt-coil Ni residue test
3 cycles of a high surface area Pt coil electrode in 1 M KOH used for electrochemical experiments. If Ni residues were present and adsorbing to the electrode, small redox waves between 0.2 and 0.45 V would be observed as in Liu *et al.*[57].

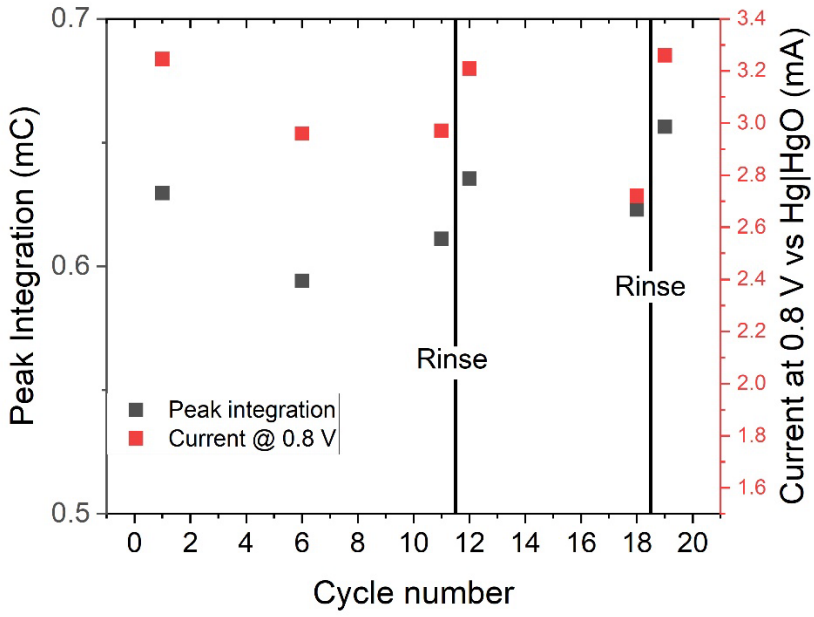

Figure 69. The effect of bubble accumulation
Bubble effects on the electrode during a typical experiment with spin-coated LNO films. Bubble accumulation causes a decrease in peak integration values of ~16% and 8% between cycles 1-6 and 12 – 18, respectively. The current and peak integration values can be recovered by removing the electrode, washing with water, and returning to the cell. The overall trends in current and peak integration are observed (e.g. peak integration increases among bubble-free electrode states) thus the occlusion of the electrode does not change the general conclusions of the main text.

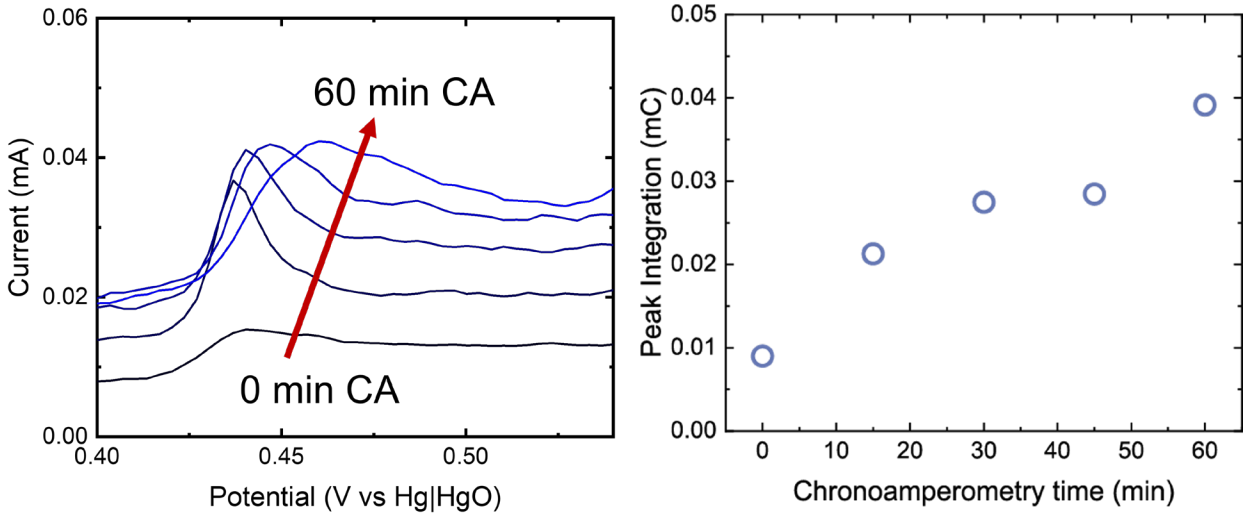

Figure 70. $LaNiO_3$ Ni redox wave after CA
Left panel shows the redox wave evolution after increments of 15 minute constant voltage (0.8 V vs Hg|HgO) polarization and right panel gives the integrated charge of those peaks. This illustrates that cyclic application of voltage is not required to induce redox wave growth.

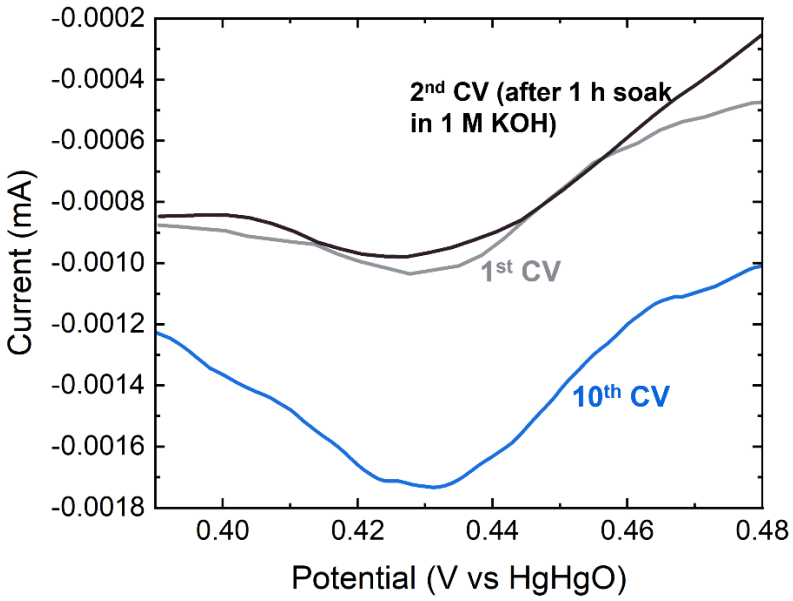

Figure 71. Ni redox wave after electrolyte exposure
Cathodic Ni redox wave for a spin-coated $LaNiO_3$ electrode after soaking in 1.0 M KOH. It was observed that allowing the as-prepared electrode to soak in 1.0 M KOH has little to no effect on the size of the cathodic wave (gray versus black curve), whereas cycling increases the size of the redox feature. This data suggests that Ni reconstruction is an electrochemically driven process.

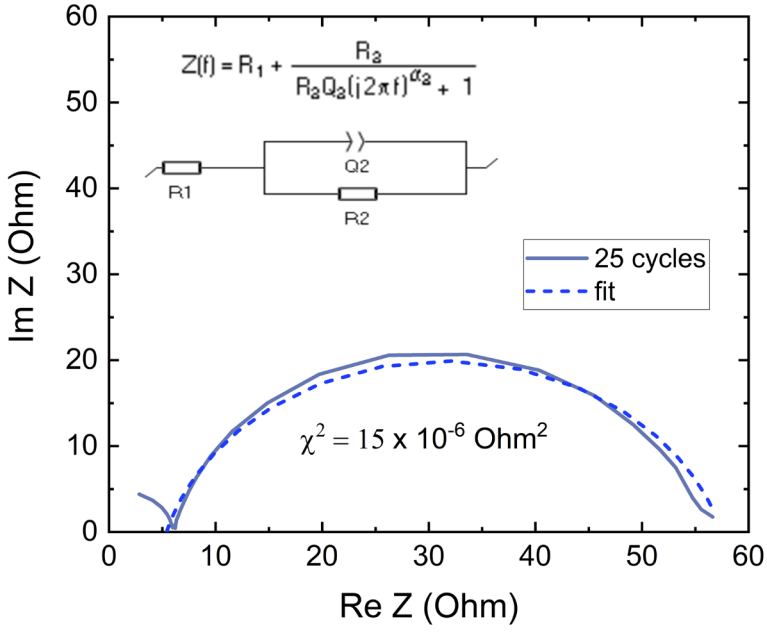

Figure 72. LNO Nyquist plot
Nyquist plot of the LNO electrode at a DC-potential of 0.8 V vs Hg|HgO referenced in Figure 14 of the main text. The fit to the data was made in EC-Lab z-fit software using a resistor for the Ohmic resistance of the cell, R1, in series with a Randles' circuit consisting of a constant phase element, Q2, (to account for the compressed semicircular shape)

in parallel with a charge transfer resistance, R2. The inset equation gives the total impedance expression as a function of frequency for this equivalent circuit model.

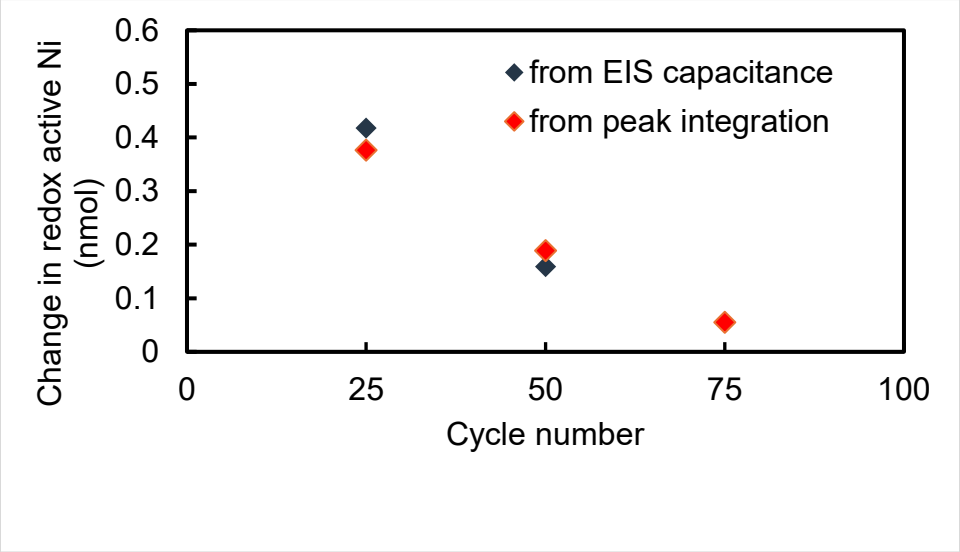

Figure 73. Redox active Ni from EIS
Redox active Ni in a given cycle of $LaNiO_3$ using the extracted double-layer capacitance from EIS data combined with value of intrinsic capacitance of a single $Ni(OH)_2$ nanosheet [225] compared to direct integration of the redox wave. The amount of nmol of Ni from EIS capacitance beyond 75 cycles could not be estimated reliably due to data being obscured by artifacts.

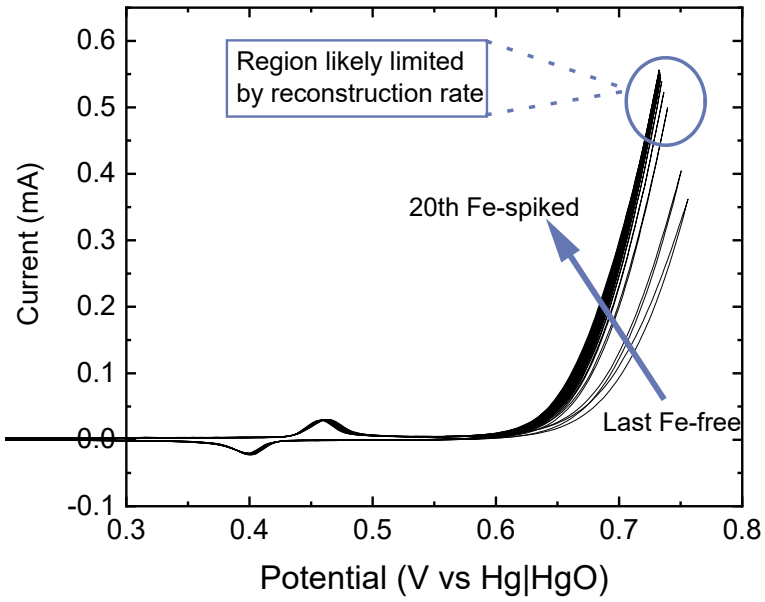

Figure 74. Cyclic voltammogram Fe-spiked epitaxial LNO

Complete cyclic voltammogram for the Fe-spiking of electrolyte for epitaxial LNO. Note that the primary activation occurs rapidly and slows to rate likely bottlenecked by further reconstruction.

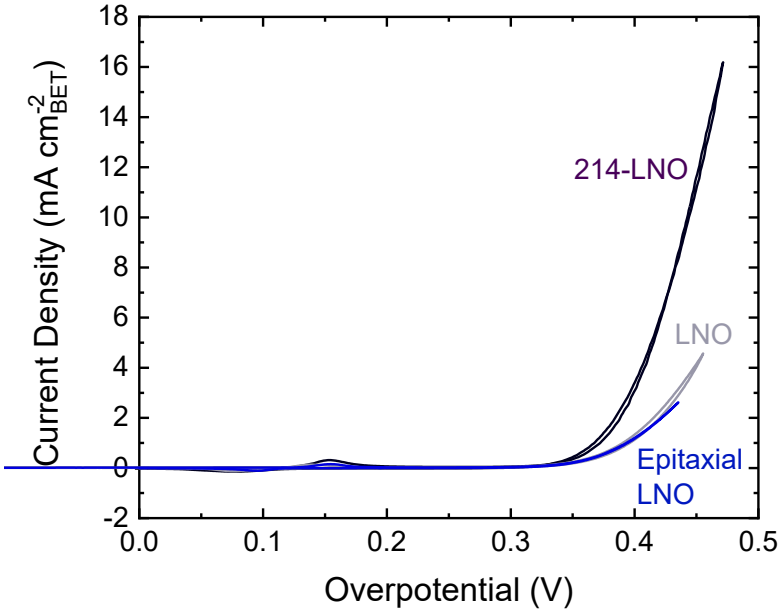

Figure 75. Overlays of Fe-spiked CVs for all catalysts
Overlay of CV corresponding to maximal primary activation of the catalysts after Fe spiking. Note that on a BET surface area basis, 214-LNO has higher intrinsic activity than LNO. The epitaxial LNO current density is normalized to its geometric area.

Supplementary Calculation 2: Monolayer equivalents (MLE) of nickel hydroxide

We use data from the 214-LNO nanorod sample depicted in Figure 1b for the below calculation:

BET surface area = 8.18 $m^2\ g^{-1}$ or 0.0818 $cm^2\ \mu g^{-1}$

From Batchellor *et al.*[225]

1 MLE = 1.7 nmol Ni cm^{-2}.

(this can be readily verified using the lattice parameters of β-$Ni(OH)_2$: a = b = 3.126 Å and 1 Ni atom per unit cell)

From ICP-MS

mass loading of the electrode = 2.06 µg

Then

total catalyst area = 2.06 µg * 0.0818 $cm^2\ \mu g^{-1}$ = 0.168 cm^2

and

Redox peak area of the 40th Fe-free cycle = 0.1045 mC

Areal molar density of redox active Ni on the catalyst (nmol cm^{-2})

(0.1045 mC/1000/96485 C mol^{-1}) / 0.168 cm^2 = 6.45 nmol cm^{-2}

Finally then

MLE = 6.45 nmol cm^{-2} / 1.7 nmol Ni cm^{-2} = **3.79 MLE**

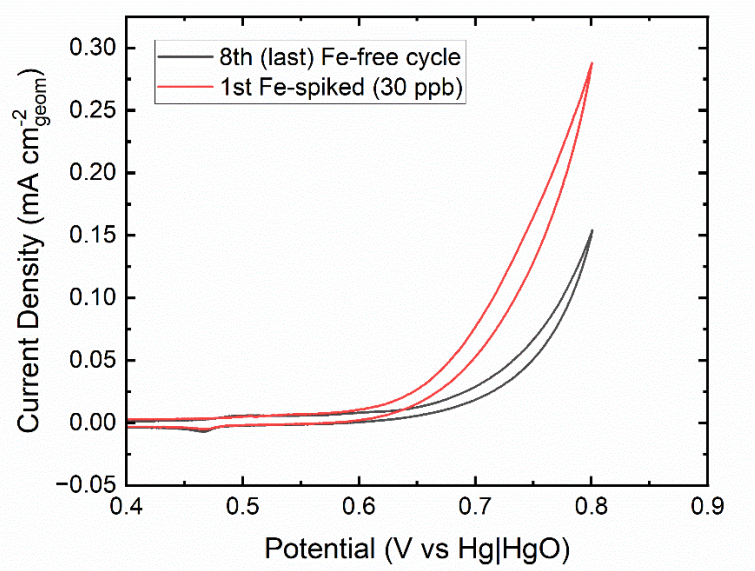

Figure 76. Fe-spiked LNO CV after 8 cycles.
Black curve is 8th Fe-free cycle of an LNO electrode and red curve is the 11th cycle. 30 ppb Fe was added between the two cycles which led to the current enhancement. Note the current density is normalized to the geometric area of the electrode.

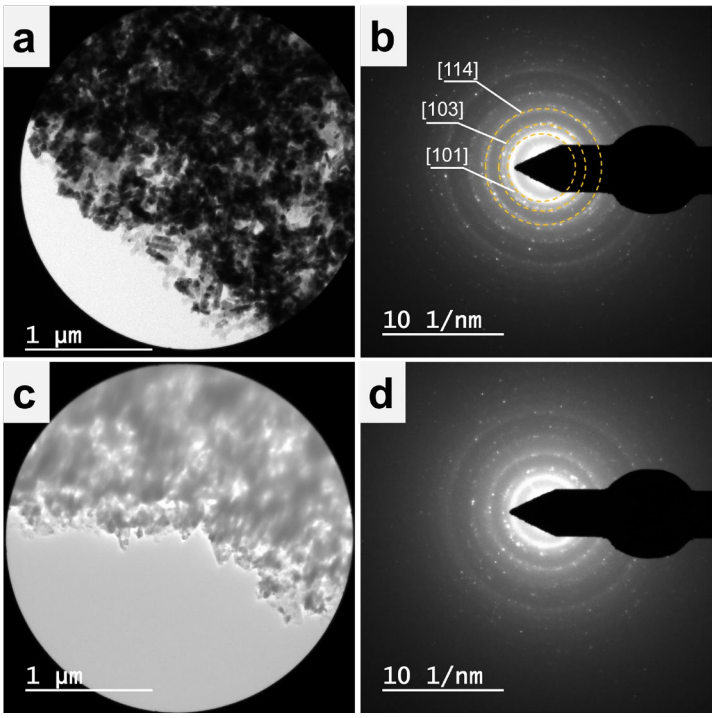

Figure 77. Selected area diffraction patterns for 214-LNO
(a-b) one of three replicate HR-TEM selected area and acquired diffraction pattern for pristine 214-LNO rods. **(c-d)** are after cycling over 100 times.

Table 9. SAED d-spacings

Calculated d-spacings from selected area diffraction experiments on pristine and cycled 214-LNO. Values are given as an average of three sites on the TEM grid for each condition ± one standard deviation. Reflections for pristine 214-LNO were retained despite extended cycling indicating that bulk technique such as this fails to suggest the presence of a reconstructed surface.

	[101] / Å	[103] / Å	[114] / Å
Pristine 214-LNO	3.53 ± 0.04	2.82 ± 0.01	2.06 ± 0.01
Ref I4/*mmm* La_2NiO_4 ICSD Coll. Code 69172	3.70	2.85	2.07
214-LNO cycled > 100x	3.45 ± 0.03	2.84 ± 0.02	2.04 ± 0.03

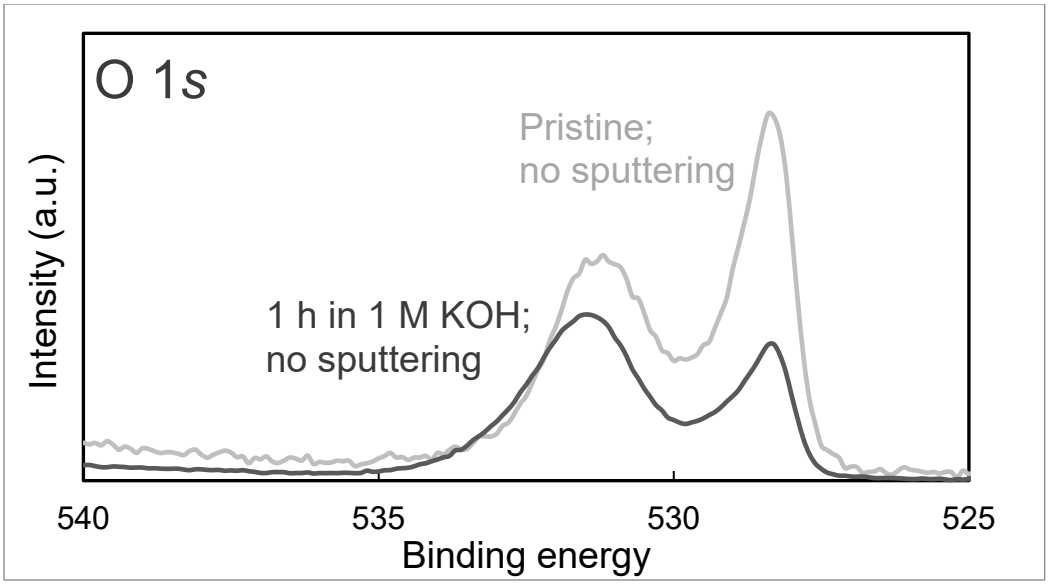

Figure 78. O 1*s* XPS epitaxial LNO after KOH exposure
Effect of 1 h 1 M KOH soak of an epitaxial LNO film. Besides a decrease in intensity, the lattice oxide feature is retained and so any changes in the region after cycling must be due to electrochemical treatment.

Table 10. Post-CVs ICP-MS LNO and 214-LNO
Post-cycling ICP-MS elemental quantities and ratios for replicate analyses of catalysts. LNO electrode were cycled over 100 times and 214-LNO electrodes were cycled 50-60 times. Note that the adsorbed Fe per cm^2 catalyst can be affected by adsorption of Fe by conductive additives, binder, uncoated platinum, and any exposed hot glue on the electrode during ICP-MS digestion.

	Adsorbed Fe post-cycling (ng Fe / cm^2_{BET})	Elemental composition of catalyst films after cycling		
		Ni (nmol)	La (nmol)	La : Ni ratio
LNO (1)	41 ± 6	9.4 ± 0.8	9.6 ± 0.1	1.02 ± 0.08
LNO (2)	137 ± 13	5.2 ± 0.2	5.5 ± 0.1	1.06 ± 0.04
214-LNO (1)	457 ± 5	11.7 ± 0.01	25.5 ± 0.04	2.19 ± 0.04
214-LNO (2)	608 ± 12	4.9 ± 0.01	10.9 ± 0.01	2.24 ± 0.06
214-LNO (3)	412 ± 6	3.4 ± 0.01	7.3 ± 0.02	2.19 ± 0.06

REFERENCES

(1) Ritchie, H.; Rosado, P. Fossil Fuels. Online at OurWorldInData.Org, 2017.

(2) NASA. *GISS Surface Temperature Analysis (v4): Temperature Anomalies over Land and over Ocean*. 2024. https://data.giss.nasa.gov/gistemp/graphs_v4/ (accessed 08/09/2024).

(3) Fourier, J.-B. F. On the temperatures of the terrestrial sphere and interplanetary space. *Memoires de l'Academie Royale des Sciences* **1827**, *7*, 569-604.

(4) Tyndall, J. I. The Bakerian Lecture.—On the absorption and radiation of heat by gases and vapours, and on the physical connexion of radiation, absorption, and conduction. *Philosophical Transactions of the Royal Society of London* **1861**, *151*, 1-36. DOI: 10.1098/rstl.1861.0001.

(5) Arrhenius, S. On the Influence of Carbonic Acid in the Air upon the Temperature of the Ground. *Philosophical Magazine and Journal of Science* **1896**, *41*, 237-276.

(6) Plass, G. N. The influence of the 15μ carbon-dioxide band on the atmospheric infra-red cooling rate. *Quarterly Journal of the Royal Meteorological Society* **1956**, *82* (353), 310-324. DOI: https://doi.org/10.1002/qj.49708235307.

(7) Callendar, G. S. The artificial production of carbon dioxide and its influence on temperature. *Quarterly Journal of the Royal Meteorological Society* **1938**, *64* (275), 223-240. DOI: https://doi.org/10.1002/qj.49706427503.

(8) Manabe, S.; Wetherald, R. T. Thermal Equilibrium of the Atmosphere with a Given Distribution of Relative Humidity. *Journal of Atmospheric Sciences* **1967**, *24* (3), 241-259. DOI: https://doi.org/10.1175/1520-0469(1967)024<0241:TEOTAW>2.0.CO;2.

(9) Sellers, W. D. A Global Climatic Model Based on the Energy Balance of the Earth-Atmosphere System. *Journal of Applied Meteorology and Climatology* **1969**, *8* (3), 392-400. DOI: https://doi.org/10.1175/1520-0450(1969)008<0392:AGCMBO>2.0.CO;2.

(10) Manabe, S.; Wetherald, R. T. The Effects of Doubling the CO2 Concentration on the climate of a General Circulation Model. *Journal of Atmospheric Sciences* **1975**, *32* (1), 3-15. DOI: https://doi.org/10.1175/1520-0469(1975)032<0003:TEODTC>2.0.CO;2.

(11) Hansen, J.; Lacis, A.; Rind, D.; Russell, G.; Stone, P.; Fung, I.; Ruedy, R.; Lerner, J. Climate Sensitivity: Analysis of Feedback Mechanisms. In *Climate Processes and Climate Sensitivity*, Geophysical Monograph Series, 1984; pp 130-163.

(12) Hansen, J.; Nazarenko, L.; Ruedy, R.; Sato, M.; Willis, J.; Del Genio, A.; Koch, D.; Lacis, A.; et al. Earth's Energy Imbalance: Confirmation and Implications. *Science* **2005**, *308* (5727), 1431-1435. DOI: 10.1126/science.1110252.

(13) Revelle, R. *Atmospheric Carbon Dioxide, Appendix Y4 of Restoring the Quality of Our Environment, a Report of the Environmental Pollution Panel*; 1965.

(14) Feldman, D. R.; Collins, W. D.; Gero, P. J.; Torn, M. S.; Mlawer, E. J.; Shippert, T. R. Observational determination of surface radiative forcing by CO2 from 2000 to 2010. *Nature* **2015**, *519* (7543), 339-343. DOI: 10.1038/nature14240.

(15) Andrews, T.; Forster, P. M. Energy budget constraints on historical radiative forcing. *Nature Climate Change* **2020**, *10* (4), 313-316. DOI: 10.1038/s41558-020-0696-1.

(16) IPCC. *Climate Change 2013: The Physical Science Basis. Contribution of Working Group I to the Fifth Assessment Report of the Intergovernmental Panel on Climate Change*; Cambridge, United Kingdom and New York, NY, USA, 2013.

(17) Change, I. P. o. C. Climate Change 2022: Mitigation of Climate Change. Contribution of Working Group III to the Sixth Assessment Report of the Intergovernmental Panel on Climate Change. Cambridge University Press, Cambridge, UK and New York, NY, USA: 2022.

(18) Ritchie, H.; Rosado, P.; Roser, M. *Energy Production and Consumption*. Our World in Data, 2020. https://ourworldindata.org/energy-production-consumption (accessed.

(19) IRENA. *World Energy Transitions Outlook 2023: 1.5 C Pathway*; International Renewable Energy Agency, Abu Dhabi, 2023.

(20) Agency, I. E. *Net Zero by 2050*; Paris, 2021. https://www.iea.org/reports/net-zero-by-2050.

(21) Tesla. *Master Plan Part 3*; 2023. https://www.tesla.com/blog/master-plan-part-3.

(22) IRENA. *Renewable capacity statistics 2024*; International Renewable Energy Agency, 2024.

(23) Budget, U. S. O. o. M. a. *Budget of the U.S. Government: Fiscal year 2024*; Washington, DC, 2024.

(24) Company, M. Ten strategic moves can help the power sector play a pivotal role in reducing carbon emissions. 2021.

(25) Machaj, K.; Kupecki, J.; Malecha, Z.; Morawski, A. W.; Skrzypkiewicz, M.; Stanclik, M.; Chorowski, M. Ammonia as a potential marine fuel: A review. *Energy Strategy Reviews* **2022**, *44*, 100926. DOI: https://doi.org/10.1016/j.esr.2022.100926.

(26) IEA. *International Shipping*. 2023. https://www.iea.org/energy-system/transport/international-shipping (accessed.

(27) Twelve. *How Twelve Makes Jet Fuel From Air*. https://www.twelve.co/post/how-twelve-makes-jet-fuel-without-oil (accessed 2024 August).

(28) Bergero, C.; Gosnell, G.; Gielen, D.; Kang, S.; Bazilian, M.; Davis, S. J. Pathways to net-zero emissions from aviation. *Nature Sustainability* **2023**, *6* (4), 404-414. DOI: 10.1038/s41893-022-01046-9.

(29) IEA. *Aviation*; 2022. https://www.iea.org/reports/aviation.

(30) Agency, I. E. *Iron and Steel Technology Roadmap: Towards more sustainable steelmaking*; 2020. https://www.iea.org/reports/iron-and-steel-technology-roadmap

(31) Agency, I. E. *Ammonia technology roadmap: Toward more sustainable nitrogen fertilizer production*; 2021. https://www.iea.org/reports/ammonia-technology-roadmap.

(32) Monteiro, P. J. M.; Miller, S. A.; Horvath, A. Towards sustainable concrete. *Nat. Mater.* **2017**, *16* (7), 698-699. DOI: 10.1038/nmat4930.

(33) SCHOTT. *SCHOTT developing climate-friendly glass production using hydrogen*. 2022. (accessed.

(34) Springer, C.; Hasanbeigi, A. *Emerging Energy Efficiency and Carbon Dioxide Emissions-Reduction Technologies for the Glass Industry*; Energy Analysis and Environmental Impacts Division Lawrence Berkeley National Laboratory, 2017.

(35) IEA. *Global Hydrogen Review*; International Energy Agency, Paris, 2023. https://www.iea.org/reports/global-hydrogen-review-2023.

(36) Capdevila-Cortada, M. Electrifying the Haber–Bosch. *Nat. Catal.* **2019**, *2* (12), 1055-1055. DOI: 10.1038/s41929-019-0414-4.

(37) Devlin, A.; Kossen, J.; Goldie-Jones, H.; Yang, A. Global green hydrogen-based steel opportunities surrounding high quality renewable energy and iron ore deposits. *Nat. Commun.* **2023**, *14* (1), 2578. DOI: 10.1038/s41467-023-38123-2.

(38) Oliveira, A. M.; Beswick, R. R.; Yan, Y. A green hydrogen economy for a renewable energy society. *Current Opinion in Chemical Engineering* **2021**, *33*, 100701. DOI: https://doi.org/10.1016/j.coche.2021.100701.

(39) Agency, I. E. Global average levelised cost of hydrogen production by energy source and technology, 2019 and 2050. Paris, 2020.

(40) Lazard. *Lazard's Levelized Cost of Hydrogen Analysis*; 2021.

(41) IRENA. *Green Hydrogen Cost Reduction: Scaling up Electrolyzers to Meet the 1.5 C Climate Goal*; International Renewable Energy Agency, Abu Dhabi, 2020.

(42) Bard, A. J.; Faulkner, L. R. *Electrochemical Methods (2nd ed.)*; 2001.

(43) Roger, I.; Shipman, M. A.; Symes, M. D. Earth-abundant catalysts for electrochemical and photoelectrochemical water splitting. *Nat. Rev. Chem.* **2017**, *1* (1), 0003. DOI: 10.1038/s41570-016-0003.

(44) Song, F.; Bai, L.; Moysiadou, A.; Lee, S.; Hu, C.; Liardet, L.; Hu, X. Transition Metal Oxides as Electrocatalysts for the Oxygen Evolution Reaction in Alkaline Solutions: An Application-Inspired Renaissance. *J. Am. Chem. Soc.* **2018**, *140* (25), 7748-7759. DOI: 10.1021/jacs.8b04546.

(45) Xu, Q.; Oener, S. Z.; Lindquist, G.; Jiang, H.; Li, C.; Boettcher, S. W. Integrated Reference Electrodes in Anion-Exchange-Membrane Electrolyzers: Impact of Stainless-Steel Gas-Diffusion Layers and Internal Mechanical Pressure. *ACS Energy Lett.* **2021**, *6* (2), 305-312. DOI: 10.1021/acsenergylett.0c02338.

(46) Huang, M.; Lao, K.; Ma, L.; Tao, J.; Zhuang, X.; Hu, T.; Pan, Y.; Liu, H.; et al. A Solid Electrolyte RHE for Electrode Diagnosis of Proton Exchange Membrane Water Electrolyzers. *ACS Appl. Mater. Interfaces* **2024**, *16* (30), 39408-39417. DOI: 10.1021/acsami.4c07472.

(47) Hansen, K. U.; Cherniack, L. H.; Jiao, F. Voltage Loss Diagnosis in CO2 Electrolyzers Using Five-Electrode Technique. *ACS Energy Lett.* **2022**, *7* (12), 4504-4511. DOI: 10.1021/acsenergylett.2c02096.

(48) Suen, N.-T.; Hung, S.-F.; Quan, Q.; Zhang, N.; Xu, Y.-J.; Chen, H. M. Electrocatalysis for the oxygen evolution reaction: recent development and future perspectives. *Chem. Soc. Rev.* **2017**, *46* (2), 337-365, 10.1039/C6CS00328A. DOI: 10.1039/C6CS00328A.

(49) Burke, M. S.; Zou, S.; Enman, L. J.; Kellon, J.; Gabor, C. A.; Pledger, E.; Boettcher, S. W. Revised oxygen evolution reaction activity trends for first-row transition-metal (oxy)hydroxides in alkaline media. *J. Phys. Chem. Lett.* **2015**, *6* (18), 3737-3742.

(50) Medford, A. J.; Vojvodic, A.; Hummelshøj, J. S.; Voss, J.; Abild-Pedersen, F.; Studt, F.; Bligaard, T.; Nilsson, A.; et al. From the Sabatier principle to a predictive theory of transition-metal heterogeneous catalysis. *J. Catal.* **2015**, *328*, 36-42. DOI: https://doi.org/10.1016/j.jcat.2014.12.033.

(51) Parsons, R. The rate of electrolytic hydrogen evolution and the heat of adsorption of hydrogen. *Transactions of the Faraday Society* **1958**, *54* (0), 1053-1063, 10.1039/TF9585401053. DOI: 10.1039/TF9585401053.

(52) Trasatti, S. Electrocatalysis by oxides — Attempt at a unifying approach. *J. Electroanal. Chem. Interf. Electrochem.* **1980**, *111* (1), 125-131. DOI: https://doi.org/10.1016/S0022-0728(80)80084-2.

(53) Suntivich, J.; May, K. J.; Gasteiger, H. A.; Goodenough, J. B.; Shao-Horn, Y. A perovskite oxide optimized for oxygen evolution catalysis from molecular orbital principles. **2011**, *334*, 1383-1385.

(54) Anantharaj, S.; Kundu, S.; Noda, S. "The Fe Effect": A review unveiling the critical roles of Fe in enhancing OER activity of Ni and Co based catalysts. *Nano Energy* **2021**, *80*, 105514. DOI: https://doi.org/10.1016/j.nanoen.2020.105514.

(55) Chen, J.; Chen, H.; Yu, T.; Li, R.; Wang, Y.; Shao, Z.; Song, S. Recent Advances in the Understanding of the Surface Reconstruction of Oxygen Evolution Electrocatalysts and Materials Development. *Electrochemical Energy Reviews* **2021**, *4* (3), 566-600. DOI: 10.1007/s41918-021-00104-8.

(56) Márquez, R. A.; Kawashima, K.; Son, Y. J.; Castelino, G.; Miller, N.; Smith, L. A.; Chukwuneke, C. E.; Mullins, C. B. Getting the Basics Right: Preparing Alkaline Electrolytes for Electrochemical Applications. *ACS Energy Lett.* **2023**, *8* (2), 1141-1146. DOI: 10.1021/acsenergylett.2c02847.

(57) Liu, L.; Twight, L. P.; Fehrs, J. L.; Ou, Y.; Sun, D.; Boettcher, S. W. Purification of Residual Ni and Co Hydroxides from Fe-Free Alkaline Electrolyte for Electrocatalysis Studies. *ChemElectroChem* **2022**, *9* (15), e202200279. DOI: https://doi.org/10.1002/celc.202200279.

(58) Trotochaud, L.; Young, S. L.; Ranney, J. K.; Boettcher, S. W. Nickel–Iron Oxyhydroxide Oxygen-Evolution Electrocatalysts: The Role of Intentional and Incidental Iron Incorporation. *J. Am. Chem. Soc.* **2014**, *136* (18), 6744-6753. DOI: 10.1021/ja502379c.

(59) Roger, I.; Symes, M. D. Efficient Electrocatalytic Water Oxidation at Neutral and High pH by Adventitious Nickel at Nanomolar Concentrations. *J. Am. Chem. Soc.* **2015**, *137* (43), 13980-13988. DOI: 10.1021/jacs.5b08139.

(60) Reikowski, F.; Maroun, F.; Pacheco, I.; Wiegmann, T.; Allongue, P.; Stettner, J.; Magnussen, O. M. Operando Surface X-ray Diffraction Studies of Structurally Defined Co_3O_4 and CoOOH Thin Films during Oxygen Evolution. *ACS Catal.* **2019**, *9* (5), 3811-3821. DOI: 10.1021/acscatal.8b04823.

(61) Wiegmann, T.; Pacheco, I.; Reikowski, F.; Stettner, J.; Qiu, C.; Bouvier, M.; Bertram, M.; Faisal, F.; et al. Operando Identification of the Reversible Skin Layer on Co_3O_4 as a Three-Dimensional Reaction Zone for Oxygen Evolution. *ACS Catal.* **2022**, *12* (6), 3256-3268. DOI: 10.1021/acscatal.1c05169.

(62) Baeumer, C.; Li, J.; Lu, Q.; Liang, A. Y.-L.; Jin, L.; Martins, H. P.; Duchoň, T.; Glöß, M.; et al. Tuning electrochemically driven surface transformation in atomically flat $LaNiO_3$ thin films for enhanced water electrolysis. *Nat. Mater.* **2021**, *20* (5), 674-682. DOI: 10.1038/s41563-020-00877-1.

(63) Su, H.; Zhou, W.; Zhang, H.; Zhou, W.; Zhao, X.; Li, Y.; Liu, M.; Cheng, W.; et al. Dynamic Evolution of Solid–Liquid Electrochemical Interfaces over Single-Atom Active Sites. *J. Am. Chem. Soc.* **2020**, *142* (28), 12306-12313. DOI: 10.1021/jacs.0c04231.

(64) Mefford, J. T.; Akbashev, A. R.; Kang, M.; Bentley, C. L.; Gent, W. E.; Deng, H. D.; Alsem, D. H.; Yu, Y.-S.; et al. Correlative operando microscopy of oxygen evolution electrocatalysts. *Nature* **2021**, *593* (7857), 67-73. DOI: 10.1038/s41586-021-03454-x.

(65) Zhang, Q.; Song, Z.; Sun, X.; Liu, Y.; Wan, J.; Betzler, S. B.; Zheng, Q.; Shangguan, J.; et al. Atomic dynamics of electrified solid–liquid interfaces in liquid-cell TEM. *Nature* **2024**, *630* (8017), 643-647. DOI: 10.1038/s41586-024-07479-w.

(66) Ou, Y.; Twight, L. P.; Samanta, B.; Liu, L.; Biswas, S.; Fehrs, J. L.; Sagui, N. A.; Villalobos, J.; et al. Cooperative Fe sites on transition metal (oxy)hydroxides drive high oxygen evolution activity in base. *Nat. Commun.* **2023**, *14* (1), 7688. DOI: 10.1038/s41467-023-43305-z.

(67) Grigoriev, S. A.; Fateev, V. N.; Bessarabov, D. G.; Millet, P. Current status, research trends, and challenges in water electrolysis science and technology. *Int. J. Hydrogen Energy* **2020**, *45* (49), 26036-26058. DOI: 10.1016/j.ijhydene.2020.03.109.

(68) Schalenbach, M.; Zeradjanin, A. R.; Kasian, O.; Cherevko, S.; Mayrhofer, K. J. J. A perspective on low-temperature water electrolysis – challenges in alkaline and acidic technology. *Int. J. Electrochem. Sci.* **2018**, *13*, 1173-1226. DOI: 10.20964/2018.02.26.

(69) Lindquist, G. A.; Oener, S. Z.; Krivina, R.; Motz, A. R.; Keane, A.; Capuano, C.; Ayers, K. E.; Boettcher, S. W. Performance and Durability of Pure-Water-Fed Anion Exchange Membrane Electrolyzers Using Baseline Materials and Operation. *ACS Appl. Mater. Interfaces* **2021**, *13* (44), 51917-51924. DOI: 10.1021/acsami.1c06053.

(70) Krivina, R. A.; Ou, Y.; Xu, Q.; Twight, L. P.; Stovall, T. N.; Boettcher, S. W. Oxygen Electrocatalysis on Mixed-Metal Oxides/Oxyhydroxides: From Fundamentals to Membrane Electrolyzer Technology. *Acc. Mater. Res.* **2021**, *2* (7), 548-558. DOI: 10.1021/accountsmr.1c00087.

(71) Corrigan, D. A. The catalysis of the oxygen evolution reaction by iron impurities in thin film nickel oxide electrodes. *J. Electrochem. Soc.* **1987**, *134*, 377. DOI: 10.1149/1.2100463.

(72) Feng, C.; Faheem, M. B.; Fu, J.; Xiao, Y.; Li, C.; Li, Y. Fe-based electrocatalysts for oxygen evolution reaction: progress and perspectives. *ACS Catal.* **2020**, *10* (7), 4019-4047. DOI: 10.1021/acscatal.9b05445.

(73) Burke, M. S.; Enman, L. J.; Batchellor, A. S.; Zou, S.; Boettcher, S. W. Oxygen evolution reaction electrocatalysis on transition metal oxides and (oxy)hydroxides: activity trends and design principles. *Chem. Mater.* **2015**, *27* (22), 7549-7558. DOI: 10.1021/acs.chemmater.5b03148.

(74) Trotochaud, L.; Young, S. L.; Ranney, J. K.; Boettcher, S. W. Nickel-iron oxyhydroxide oxygen-evolution electrocatalysts: the role of intentional and incidental iron incorporation. *J. Am. Chem. Soc.* **2014**, *136* (18), 6744-6753. DOI: 10.1021/ja502379c.

(75) Burke, M. S.; Kast, M. G.; Trotochaud, L.; Smith, A. M.; Boettcher, S. W. Cobalt-iron (oxy)hydroxide oxygen evolution electrocatalysts: the role of structure and composition on activity, stability, and mechanism. *J. Am. Chem. Soc.* **2015**, *137* (10), 3638-3648. DOI: 10.1021/jacs.5b00281.

(76) Farhat, R.; Dhainy, J.; Halaoui, L. I. OER catalysis at activated and codeposited NiFe-oxo/hydroxide thin films is due to postdeposition surface-Fe and is not sustainable without Fe in solution. *ACS Catal.* **2019**, *10* (1), 20-35. DOI: 10.1021/acscatal.9b02580.

(77) Zhang, T.; Nellist, M. R.; Enman, L. J.; Xiang, J.; Boettcher, S. W. Modes of Fe incorporation in Co-Fe (oxy)hydroxide oxygen evolution electrocatalysts. *ChemSusChem* **2019**, *12* (9), 2015-2021. DOI: 10.1002/cssc.201801975.

(78) Bao, F.; Kemppainen, E.; Dorbandt, I.; Xi, F.; Bors, R.; Maticiuc, N.; Wenisch, R.; Bagacki, R.; et al. Host, suppressor, and promoter—the roles of Ni and Fe on oxygen evolution reaction activity and stability of NiFe alloy thin films in alkaline media. *ACS Catal.* **2021**, *11* (16), 10537-10552. DOI: 10.1021/acscatal.1c01190.

(79) Chung, D. Y.; Lopes, P. P.; Farinazzo Bergamo Dias Martins, P.; He, H.; Kawaguchi, T.; Zapol, P.; You, H.; Tripkovic, D.; et al. Dynamic stability of active sites in hydr(oxy)oxides for the oxygen evolution reaction. *Nat. Energy* **2020**, *5* (3), 222-230. DOI: 10.1038/s41560-020-0576-y.

(80) Forslund, R. P.; Hardin, W. G.; Rong, X.; Abakumov, A. M.; Filimonov, D.; Alexander, C. T.; Mefford, J. T.; Iyer, H.; et al. Exceptional electrocatalytic oxygen evolution via tunable charge transfer interactions in $La_{0.5}Sr_{1.5}Ni_{1-x}Fe_xO_{4\pm\delta}$ Ruddlesden-Popper oxides. *Nat. Commun.* **2018**, *9* (1), 3150. DOI: 10.1038/s41467-018-05600-y.

(81) Lopes, P. P.; Chung, D. Y.; Rui, X.; Zheng, H.; He, H.; Farinazzo Bergamo Dias Martins, P.; Strmcnik, D.; Stamenkovic, V. R.; et al. Dynamically stable active sites from surface evolution of perovskite materials during the oxygen evolution reaction. *J. Am. Chem. Soc.* **2021**, *143* (7), 2741-2750. DOI: 10.1021/jacs.0c08959.

(82) Shen, T. H.; Spillane, L.; Vavra, J.; Pham, T. H. M.; Peng, J.; Shao-Horn, Y.; Tileli, V. Oxygen evolution reaction in $Ba_{0.5}Sr_{0.5}Co_{0.8}Fe_{0.2}O_{3-\delta}$ aided by intrinsic Co/Fe spinel-like surface. *J. Am. Chem. Soc.* **2020**, *142* (37), 15876-15883. DOI: 10.1021/jacs.0c06268.

(83) Wygant, B. R.; Kawashima, K.; Mullins, C. B. Catalyst or precatalyst? The effect of oxidation on transition metal carbide, pnictide, and chalcogenide oxygen evolution catalysts. *ACS Energy Lett.* **2018**, *3* (12), 2956-2966. DOI: 10.1021/acsenergylett.8b01774.

(84) Jin, S. Are metal chalcogenides, nitrides, and phosphides oxygen evolution catalysts or bifunctional catalysts? *ACS Energy Lett.* **2017**, *2* (8), 1937-1938. DOI: 10.1021/acsenergylett.7b00679.

(85) Mabayoje, O.; Shoola, A.; Wygant, B. R.; Mullins, C. B. The role of anions in metal chalcogenide oxygen evolution catalysis: electrodeposited thin films of nickel sulfide as "pre-catalysts". *ACS Energy Lett.* **2016**, *1* (1), 195-201. DOI: 10.1021/acsenergylett.6b00084.

(86) Enman, L. J.; Stevens, M. B.; Dahan, M. H.; Nellist, M. R.; Toroker, M. C.; Boettcher, S. W. Operando X-ray absorption spectroscopy shows iron oxidation is concurrent with oxygen evolution in cobalt-iron (oxy)hydroxide electrocatalysts. *Angew. Chem., Int. Ed.* **2018**, *57* (39), 12840-12844. DOI: 10.1002/anie.201808818.

(87) Dionigi, F.; Zeng, Z.; Sinev, I.; Merzdorf, T.; Deshpande, S.; Lopez, M. B.; Kunze, S.; Zegkinoglou, I.; et al. In-situ structure and catalytic mechanism of NiFe and CoFe layered double hydroxides during oxygen evolution. *Nat. Commun.* **2020**, *11* (1), 2522. DOI: 10.1038/s41467-020-16237-1.

(88) Liu, Z.; Ma, R.; Osada, M.; Takada, K.; Sasaki, T. Selective and controlled synthesis of α- and β-cobalt hydroxides in highly developed hexagonal platelets. *J. Am. Chem. Soc.* **2005**, *127* (40), 13869-13874. DOI: 10.1021/ja0523338.

(89) Delahaye-Vidal, A.; Figlarz, M. Textural and structural studies on nickel hydroxide electrodes. II. turbostratic nickel (II) hydroxide submitted to electrochemical redox cycling. *J. Appl. Electrochem.* **1987**, *17* (3), 589-599. DOI: 10.1007/bf01084134.

(90) Ma, R.; Liu, Z.; Takada, K.; Iyi, N.; Bando, Y.; Sasaki, T. Synthesis and exfoliation of Co^{2+}-Fe^{3+} layered double hydroxides: an innovative topochemical approach. *J. Am. Chem. Soc.* **2007**, *129* (16), 5257-5263. DOI: 10.1021/ja0693035.

(91) Friebel, D.; Louie, M. W.; Bajdich, M.; Sanwald, K. E.; Cai, Y.; Wise, A. M.; Cheng, M.-J.; Sokaras, D.; et al. Identification of Highly Active Fe Sites in (Ni,Fe)OOH for Electrocatalytic Water Splitting. *J. Am. Chem. Soc.* **2015**, *137* (3), 1305-1313. DOI: 10.1021/ja511559d.

(92) Gong, L.; Chng, X. Y. E.; Du, Y.; Xi, S.; Yeo, B. S. Enhanced catalysis of the electrochemical oxygen evolution reaction by iron(III) ions adsorbed on amorphous cobalt oxide. *ACS Catal.* **2017**, *8* (2), 807-814. DOI: 10.1021/acscatal.7b03509.

(93) Wang, D.; Zhou, J.; Hu, Y.; Yang, J.; Han, N.; Li, Y.; Sham, T.-K. In situ X-ray absorption near edge structure study of advanced $NiFe(OH)_x$ electrocatalyst on carbon paper for water oxidation. *J. Phys. Chem. C* **2015**, DOI: 10.1021/acs.jpcc.1025b02685. DOI: 10.1021/acs.jpcc.5b02685.

(94) Hunter, B. M.; Thompson, N. B.; Müller, A. M.; Rossman, G. R.; Hill, M. G.; Winkler, J. R.; Gray, H. B. Trapping an Iron(VI) Water-Splitting Intermediate in Nonaqueous Media. *Joule* **2018**, *2* (4), 747-763. DOI: https://doi.org/10.1016/j.joule.2018.01.008.

(95) Gorlin, M.; Chernev, P.; Ferreira de Araujo, J.; Reier, T.; Dresp, S.; Paul, B.; Krahnert, R.; Dau, H.; et al. Oxygen evolution reaction dynamics, faradaic charge efficiency, and the active metal redox states of Ni-Fe oxide water splitting electrocatalysts. *J. Am. Chem. Soc.* **2016**, *138* (17), 5603-5614. DOI: 10.1021/jacs.6b00332.

(96) Chen, J. Y.; Dang, L.; Liang, H.; Bi, W.; Gerken, J. B.; Jin, S.; Alp, E. E.; Stahl, S. S. Operando analysis of NiFe and Fe oxyhydroxide electrocatalysts for water oxidation: detection of Fe^{4+} by Mossbauer spectroscopy. *J. Am. Chem. Soc.* **2015**, *137* (48), 15090-15093. DOI: 10.1021/jacs.5b10699.

(97) Li, N.; Hadt, R. G.; Hayes, D.; Chen, L. X.; Nocera, D. G. Detection of high-valent iron species in alloyed oxidic cobaltates for catalysing the oxygen evolution reaction. *Nat. Commun.* **2021**, *12* (1), 4218. DOI: 10.1038/s41467-021-24453-6.

(98) Stevens, M. B.; Trang, C. D. M.; Enman, L. J.; Deng, J.; Boettcher, S. W. Reactive Fe-sites in Ni/Fe (oxy)hydroxide are responsible for exceptional oxygen electrocatalysis activity. *J. Am. Chem. Soc.* **2017**, *139* (33), 11361-11364. DOI: 10.1021/jacs.7b07117.

(99) Song, F.; Busch, M. M.; Lassalle-Kaiser, B.; Hsu, C. S.; Petkucheva, E.; Bensimon, M.; Chen, H. M.; Corminboeuf, C.; et al. An unconventional iron nickel catalyst for the oxygen evolution reaction. *ACS Cent. Sci.* **2019**, *5* (3), 558-568. DOI: 10.1021/acscentsci.9b00053.

(100) Bai, L.; Lee, S.; Hu, X. Spectroscopic and electrokinetic evidence for a bifunctional mechanism of the oxygen evolution reaction. *Angew. Chem., Int. Ed.* **2021**, *60* (6), 3095-3103. DOI: 10.1002/anie.202011388.

(101) Subbaraman, R.; Tripkovic, D.; Chang, K.-C.; Strmcnik, D.; Paulikas, A. P.; Hirunsit, P.; Chan, M.; Greeley, J.; et al. Trends in activity for the water electrolyser reactions on 3d M(Ni,Co,Fe,Mn) hydr(oxy)oxide catalysts. *Nat. Mater.* **2012**, *11*, 550-557. DOI: 10.1038/nmat3313.

(102) Dette, C.; Hurst, M. R.; Deng, J.; Nellist, M. R.; Boettcher, S. W. Structural Evolution of Metal (Oxy)hydroxide Nanosheets during the Oxygen Evolution Reaction. *ACS Appl. Mater. Interfaces* **2019**, *11* (6), 5590-5594. DOI: 10.1021/acsami.8b02796.

(103) Schalenbach, M.; Kasian, O.; Mayrhofer, K. J. J. An alkaline water electrolyzer with nickel electrodes enables efficient high current density operation. *Int. J. Hydrogen Energy* **2018**, *43* (27), 11932-11938. DOI: https://doi.org/10.1016/j.ijhydene.2018.04.219.

(104) Stevens, M. B.; Enman, L. J.; Batchellor, A. S.; Cosby, M. R.; Vise, A. E.; Trang, C. D. M.; Boettcher, S. W. Measurement techniques for the study of thin film heterogeneous water oxidation electrocatalysts. *Chem. Mater.* **2016**, *29* (1), 120-140. DOI: 10.1021/acs.chemmater.6b02796.

(105) Batchellor, A. S.; Boettcher, S. W. Pulse-electrodeposited Ni–Fe (oxy)hydroxide oxygen evolution electrocatalysts with high geometric and intrinsic activities at large mass loadings. *ACS Catal.* **2015**, *5* (11), 6680-6689. DOI: 10.1021/acscatal.5b01551.

(106) Cornell, R. M.; Schwertmann, U. *The iron oxides: Structure, properties, reactions, occurrences, and uses*; Wiley-VCH, 2003.

(107) Kresse, G.; Furthmüller, J. Efficiency of ab-initio total energy calculations for metals and semiconductors using a plane-wave basis set. *Comput. Mater. Sci.* **1996**, *6* (1), 15-50. DOI: 10.1016/0927-0256(96)00008-0.

(108) Kresse, G.; Hafner, J. Ab initio molecular dynamics for liquid metals. *Phys. Rev. B: Condens. Matter Mater. Phys.* **1993**, *47* (1), 558-561. DOI: 10.1103/physrevb.47.558.

(109) Kresse, G.; Joubert, D. From ultrasoft pseudopotentials to the projector augmented-wave method. *Phys. Rev. B: Condens. Matter Mater. Phys.* **1999**, *59* (3), 1758-1775. DOI: 10.1103/PhysRevB.59.1758.

(110) Dudarev, S. L.; Botton, G. A.; Savrasov, S. Y.; Humphreys, C. J.; Sutton, A. P. Electron-energy-loss spectra and the structural stability of nickel oxide: an LSDA+U study. *Phys. Rev. B: Condens. Matter Mater. Phys.* **1998**, *57* (3), 1505-1509. DOI: 10.1103/PhysRevB.57.1505.

(111) Li, Y. F.; Selloni, A. Mosaic texture and double c-axis periodicity of beta-NiOOH: insights from first-principles and genetic algorithm calculations. *J. Phys. Chem. Lett.* **2014**, *5* (22), 3981-3985. DOI: 10.1021/jz502127g.

(112) Tkalych, A. J.; Yu, K.; Carter, E. A. Structural and electronic features of β-$Ni(OH)_2$ and β-NiOOH from first principles. *J. Phys. Chem. C* **2015**, *119* (43), 24315-24322. DOI: 10.1021/acs.jpcc.5b08481.

(113) Fidelsky, V.; Caspary Toroker, M. Engineering band edge positions of nickel oxyhydroxide through facet selection. *J. Phys. Chem. C* **2016**, *120* (15), 8104-8108. DOI: 10.1021/acs.jpcc.6b00214.

(114) Zaffran, J.; Caspary Toroker, M. Benchmarking density functional theory based methods to model NiOOH material properties: Hubbard and van der Waals corrections vs hybrid functionals. *J. Chem. Theory Comput.* **2016**, *12* (8), 3807-3812. DOI: 10.1021/acs.jctc.6b00657.

(115) Wang, L.; Maxisch, T.; Ceder, G. Oxidation energies of transition metal oxides within the GGA+U framework. *Phys. Rev. B* **2006**, *73* (19). DOI: 10.1103/PhysRevB.73.195107.

(116) Ding, H.; Virkar, A. V.; Liu, M.; Liu, F. Suppression of Sr surface segregation in $La_{1-x}Sr_xCo_{1-y}Fe_yO_{3-\delta}$: a first principles study. *Phys. Chem. Chem. Phys.* **2013**, *15* (2), 489-496. DOI: 10.1039/c2cp43148c.

(117) Perdew, J. P.; Burke, K.; Ernzerhof, M. Generalized gradient approximation made simple. *Phys. Rev. Lett.* **1996**, *77* (18), 3865-3868. DOI: 10.1103/PhysRevLett.77.3865.

(118) Blochl, P. E. Projector augmented-wave method. *Phys. Rev. B: Condens. Matter Mater. Phys.* **1994**, *50* (24), 17953-17979. DOI: 10.1103/physrevb.50.17953.

(119) Methfessel, M.; Paxton, A. T. High-precision sampling for Brillouin-zone integration in metals. *Phys. Rev. B* **1989**, *40* (6), 3616-3621. DOI: 10.1103/PhysRevB.40.3616.

(120) Press, W. H.; Flannery, B. P.; Teukolsky, S. A.; Vetterling, W. T. *Numerical Recipes*; Cambridge University Press, 1986.

(121) Rossmeisl, J.; Qu, Z.-W.; Zhu, H.; Kroes, G.-J.; Nørskov, J. K. Electrolysis of water on oxide surfaces. J. Electroanal. Chem.: 2007; Vol. 607, pp 83-89.

(122) Burke, M. S.; Zou, S.; Enman, L. J.; Kellon, J. E.; Gabor, C. A.; Pledger, E.; Boettcher, S. W. Revised Oxygen Evolution Reaction Activity Trends for First-Row Transition-Metal (Oxy)hydroxides in Alkaline Media. *J. Phys. Chem. Lett.* **2015**, *6* (18), 3737-3742. DOI: 10.1021/acs.jpclett.5b01650.

(123) Enman, L. J.; Burke, M. S.; Batchellor, A. S.; Boettcher, S. W. Effects of Intentionally Incorporated Metal Cations on the Oxygen Evolution Electrocatalytic Activity of Nickel (Oxy)hydroxide in Alkaline Media. *ACS Catal.* **2016**, *6* (4), 2416-2423. DOI: 10.1021/acscatal.5b02924.

(124) Enman, L. J.; Vise, A. E.; Burke Stevens, M.; Boettcher, S. W. Effects of metal electrode support on the catalytic activity of Fe(oxy)hydroxide for the oxygen evolution reaction in alkaline media. *ChemPhysChem* **2019**, *20* (22), 3089-3095. DOI: 10.1002/cphc.201900511.

(125) Zou, S.; Burke, M. S.; Kast, M. G.; Fan, J.; Danilovic, N.; Boettcher, S. W. Fe (oxy)hydroxide oxygen evolution reaction electrocatalysis: Intrinsic activity and the roles of electrical conductivity, substrate, and dissolution. *Chem. Mater.* **2015**, *27*, 8011-8020.

(126) Corrigan, D. A.; Bendert, R. M. Effect of coprecipitated metal ions on the electrochemistry of nickel hydroxide thin films: cyclic voltammetry in 1 M KOH *J. Electrochem. Soc.* **1989**, *136* (3), 723-728. DOI: 10.1149/1.2096717.

(127) Zhang, Y. Oxygen evolution reaction on Ni hydroxide film electrode containing various content of Co. *Int. J. Hydrogen Energy* **1999**, *24* (6), 529-536. DOI: 10.1016/s0360-3199(98)00086-x.

(128) Dette, C.; Hurst, M. R.; Deng, J.; Nellist, M. R.; Boettcher, S. W. Structural Evolution of Metal (Oxy)hydroxide Nanosheets during the Oxygen Evolution Reaction. *ACS Appl. Mater. Interfaces* **2018**, *11* (6), 5590-5594. DOI: 10.1021/acsami.8b02796.

(129) Subbaraman, R.; Tripkovic, D.; Chang, K.-C.; Strmcnik, D.; Paulikas, A. P.; Hirunsit, P.; Chan, M.; Greeley, J.; et al. Trends in activity for the water electrolyser reactions on 3d M(Ni,Co,Fe,Mn) hydr(oxy)oxide catalysts. *Nat. Mater.* **2012**, *11* (6), 550-557. DOI: 10.1038/nmat3313.

(130) Rumble, J. R.; Rumble, J. C. H. o. C. a. P., 98th Edition; Physics, C. H. o. C. a.; CRC Press LLC. *CRC Handbook of Chemistry and Physics, 103rd Edition*; CRC Press LLC, 2021.

(131) Wu, T.-H.; Scivetti, I.; Chen, J.-C.; Wang, J.-A.; Teobaldi, G.; Hu, C.-C.; Hardwick, L. J. Quantitative resolution of complex stoichiometric changes during electrochemical cycling by density functional theory-assisted electrochemical quartz crystal microbalance. *ACS Appl. Energy Mater.* **2020**, *3* (4), 3347-3357. DOI: 10.1021/acsaem.9b02386.

(132) Kim, M. S.; Kim, K. B. A study on the phase transformation of electrochemically precipitated nickel hydroxides using an electrochemical quartz crystal microbalance. *J. Electrochem. Soc.* **1998**, *145* (2), 507-511. DOI: 10.1149/1.1838294.

(133) Dionigi, F.; Zeng, Z.; Sinev, I.; Merzdorf, T.; Deshpande, S.; Lopez, M. B.; Kunze, S.; Zegkinoglou, I.; et al. In-situ structure and catalytic mechanism of NiFe and CoFe layered double hydroxides during oxygen evolution. *Nat. Commun.* **2020**, *11* (1), 2522. DOI: 10.1038/s41467-020-16237-1.

(134) Deng, J.; Nellist, M. R.; Stevens, M. B.; Dette, C.; Wang, Y.; Boettcher, S. W. Morphology dynamics of single-layered $Ni(OH)_2$/NiOOH nanosheets and subsequent Fe incorporation studied by in situ electrochemical atomic force microscopy. *Nano Lett.* **2017**, *17* (11), 6922-6926. DOI: 10.1021/acs.nanolett.7b03313.

(135) Lee, S.; Bai, L.; Hu, X. Deciphering iron-dependent activity in oxygen evolution catalyzed by nickel-iron layered double hydroxide. *Angew. Chem., Int. Ed.* **2020**, *59* (21), 8072-8077. DOI: 10.1002/anie.201915803.

(136) Martirez, J. M. P.; Carter, E. A. Unraveling oxygen evolution on iron-doped β-nickel oxyhydroxide: the key role of highly active molecular-like sites. *J. Am. Chem. Soc.* **2019**, *141* (1), 693-705. DOI: 10.1021/jacs.8b12386.

(137) Hao, Y.; Li, Y.; Wu, J.; Meng, L.; Wang, J.; Jia, C.; Liu, T.; Yang, X.; et al. Recognition of surface oxygen intermediates on NiFe oxyhydroxide oxygen-evolving catalysts by homogeneous oxidation reactivity. *J. Am. Chem. Soc.* **2021**, *143* (3), 1493-1502. DOI: 10.1021/jacs.0c11307.

(138) Roy, C.; Sebok, B.; Scott, S. B.; Fiordaliso, E. M.; Sørensen, J. E.; Bodin, A.; Trimarco, D. B.; Damsgaard, C. D.; et al. Impact of nanoparticle size and lattice oxygen on water oxidation on NiFeOxHy. *Nat. Catal.* **2018**, *1* (11), 820-829. DOI: 10.1038/s41929-018-0162-x.

(139) Risch, M.; Klingan, K.; Ringleb, F.; Chernev, P.; Zaharieva, I.; Fischer, A.; Dau, H. Water Oxidation by Electrodeposited Cobalt Oxides—Role of Anions and Redox-Inert Cations in Structure and Function of the Amorphous Catalyst. *ChemSusChem* **2012**, *5* (3), 542-549, https://doi.org/10.1002/cssc.201100574. DOI: https://doi.org/10.1002/cssc.201100574.

(140) Valden, M.; Lai, X.; Goodman, D. W. Onset of Catalytic Activity of Gold Clusters on Titania with the Appearance of Nonmetallic Properties. *Science* **1998**, *281* (5383), 1647-1650. DOI: 10.1126/science.281.5383.1647.

(141) Xu, Z.; Xiao, F. S.; Purnell, S. K.; Alexeev, O.; Kawi, S.; Deutsch, S. E.; Gates, B. C. Size-dependent catalytic activity of supported metal clusters. *Nature* **1994**, *372* (6504), 346-348. DOI: 10.1038/372346a0.

(142) Song, F.; Busch, M. M.; Lassalle-Kaiser, B.; Hsu, C.-S.; Petkucheva, E.; Bensimon, M.; Chen, H. M.; Corminboeuf, C.; et al. An Unconventional Iron Nickel Catalyst for the Oxygen Evolution Reaction. *ACS Cent. Sci.* **2019**, *5* (3), 558-568. DOI: 10.1021/acscentsci.9b00053.

(143) Zhang, J.; Tao, H. B.; Kuang, M.; Yang, H. B.; Cai, W.; Yan, Q.; Mao, Q.; Liu, B. Advances in Thermodynamic-Kinetic Model for Analyzing the Oxygen Evolution Reaction. *ACS Catal.* **2020**, *10* (15), 8597-8610. DOI: 10.1021/acscatal.0c01906.

(144) Batchellor, A. S.; Kwon, G.; Laskowski, F. A. L.; Tiede, D. M.; Boettcher, S. W. Domain Structures of Ni and NiFe (Oxy)Hydroxide Oxygen-Evolution Catalysts from X-ray Pair Distribution Function Analysis. *J. Phys. Chem. C* **2017**, *121* (45), 25421-25429. DOI: 10.1021/acs.jpcc.7b10306.

(145) Li, Y.-F.; Selloni, A. Mechanism and activity of water oxidation on selected surfaces of pure and Fe-doped NiO_x. *ACS Catal.* **2014**, *4*, 1148-1153. DOI: 10.1021/cs401245q.

(146) Casas-Cabanas, M.; Canales-Vazquez, J.; Rodriguez-Carvajal, J.; Palacin, M. R. Deciphering the structural transformations during nickel oxyhydroxide electrode operation. *J. Am. Chem. Soc.* **2007**, *129* (18), 5840-5842. DOI: 10.1021/ja068433a.

(147) Oliva, P.; Leonardi, J.; Laurent, J. F.; Delmas, C.; Braconnier, J. J.; Figlarz, M.; Fievet, F.; Guibert, A. d. Review of the structure and the electrochemistry of nickel hydroxides and oxy-hydroxides. *J. Power Sources* **1982**, *8*, 229-255. DOI: 10.1016/0378-7753(82)80057-8.

(148) Delaplane, R. G.; Ibers, J. A.; Ferraro, J. R.; Rush, J. J. Diffraction and spectroscopic studies of the cobaltic acid system $HCoC_2$–$DCoO_2$. *The Journal of Chemical Physics* **1969**, *50* (5), 1920-1927. DOI: https://doi.org/10.1063/1.1671307.

(149) Chen, J.; Selloni, A. First principles study of cobalt (hydr)oxides under electrochemical conditions. *J. Phys. Chem. C* **2013**, *117* (39), 20002-20006. DOI: 10.1021/jp406331h.

(150) Zhou, Y.; López, N. The role of Fe species on NiOOH in oxygen evolution reactions. *ACS Catal.* **2020**, *10* (11), 6254-6261. DOI: 10.1021/acscatal.0c00304.

(151) Stevens, M. B.; Enman, L. J.; Korkus, E. H.; Zaffran, J.; Trang, C. D. M.; Asbury, J.; Kast, M. G.; Toroker, M. C.; et al. Ternary Ni-Co-Fe oxyhydroxide oxygen evolution catalysts: Intrinsic activity trends, electrical conductivity, and electronic band structure. *Nano Research* **2019**, *12* (9), 2288-2295. DOI: 10.1007/s12274-019-2391-y.

(152) Trotochaud, L.; Ranney, J. K.; Williams, K. N.; Boettcher, S. W. Solution-Cast Metal Oxide Thin Film Electrocatalysts for Oxygen Evolution. *J. Am. Chem. Soc.* **2012**, *134* (41), 17253-17261. DOI: 10.1021/ja307507a.

(153) Deng, J.; Nellist, M. R. N.; Stevens, M. B.; Dette, C.; Wang, Y.; Boettcher, S. W. Morphology dynamics of single-layered $Ni(OH)_2$/NiOOH nanosheets and subsequent Fe incorporation studied by *in situ* electrochemical atomic force microscopy. *Nanoletters* **2017**, *17*, 6922-6926.

(154) Twight, L.; Tonsberg, A.; Samira, S.; Velinkar, K.; Dumpert, K.; Ou, Y.; Wang, L.; Nikolla, E.; et al. Trace Fe activates perovskite nickelate OER catalysts in alkaline media via redox-active surface Ni species formed during electrocatalysis. *J. Catal.* **2024**, *432*, 115443. DOI: https://doi.org/10.1016/j.jcat.2024.115443.

(155) Gutiérrez-Martín, D.; Asserghine, A.; Torres-Pardo, A.; Varela, Á.; Rodríguez-López, J.; González-Calbet, J. M.; Parras, M. Evaluating the impact of iron impurities in KOH on OER performance of BaNiO3 single crystals using scanning electrochemical cell microscopy. *Electrochim. Acta* **2024**, *499*, 144705. DOI: https://doi.org/10.1016/j.electacta.2024.144705.

(156) Wygant, B. R.; Kawashima, K.; Mullins, C. B. Catalyst or Precatalyst? The Effect of Oxidation on Transition Metal Carbide, Pnictide, and Chalcogenide Oxygen Evolution Catalysts. *ACS Energy Lett.* **2018**, *3* (12), 2956-2966. DOI: 10.1021/acsenergylett.8b01774.

(157) Wang, L.; Stoerzinger, K. A.; Chang, L.; Yin, X.; Li, Y.; Tang, C. S.; Jia, E.; Bowden, M. E.; et al. Strain Effect on Oxygen Evolution Reaction Activity of Epitaxial $NdNiO_3$ Thin Films. *ACS Appl. Mater. Interfaces* **2019**, *11* (13), 12941-12947. DOI: 10.1021/acsami.8b21301.

(158) Laidler, K. J.; King, M. C. Development of transition-state theory. *J. Phys. Chem.* **1983**, *87* (15), 2657-2664. DOI: 10.1021/j100238a002.

(159) He, Z.-D.; Chen, Y.-X.; Santos, E.; Schmickler, W. The Pre-exponential Factor in Electrochemistry. *Angew. Chem., Int. Ed.* **2018**, *57* (27), 7948-7956. DOI: https://doi.org/10.1002/anie.201800130.

(160) Swierk, J. R.; Klaus, S.; Trotochaud, L.; Bell, A. T.; Tilley, T. D. Electrochemical Study of the Energetics of the Oxygen Evolution Reaction at Nickel Iron (Oxy)Hydroxide Catalysts. *J. Phys. Chem. C* **2015**, *119* (33), 19022-19029. DOI: 10.1021/acs.jpcc.5b05861.

(161) Chen, L.; Xu, Q.; Boettcher, S. W. Kinetics and mechanism of heterogeneous voltage-driven water-dissociation catalysis. *Joule* **2023**, *7* (8), 1867-1886. DOI: https://doi.org/10.1016/j.joule.2023.06.011.

(162) Emam, A. S.; Hamdan, M. O.; Abu-Nabah, B. A.; Elnajjar, E. A review on recent trends, challenges, and innovations in alkaline water electrolysis. *Int. J. Hydrogen Energy* **2024**, *64*, 599-625. DOI: https://doi.org/10.1016/j.ijhydene.2024.03.238.

(163) Schmickler, W.; Santos, E. *Interfacial Electrochemistry (2nd Ed.)*; Oxford University Press, 2010.

(164) Conway, B. E.; MacKinnon, D. J.; Tilak, B. V. Significance of electrochemical Brønsted factors. Kinetic studies over a wide range of temperatures. *Transactions of the Faraday Society* **1970**, *66* (0), 1203-1226, 10.1039/TF9706601203. DOI: 10.1039/TF9706601203.

(165) Conway, B. E.; Tessier, D. F.; Wilkinson, D. P. Experimental evidence for the potential-dependence of entropy of activation in electrochemical reactions in relations to the temperature-dependence of tafel slopes. *J. Electroanal. Chem. Interf. Electrochem.* **1986**, *199* (2), 249-269. DOI: https://doi.org/10.1016/0022-0728(86)80002-X.

(166) Conway, B. E.; Wilkinson, D. P. Comparison of entropic and enthalpic components of the barrier symmetry factor, β, for proton discharge at liquid and solid Hg in relation to the variation of Tafel slopes and β with temperature. *Journal of the Chemical Society, Faraday Transactions 1: Physical Chemistry in Condensed Phases* **1989**, *85* (8), 2355-2367, 10.1039/F19898502355. DOI: 10.1039/F19898502355.

(167) Hall, D. S.; Lockwood, D. J.; Bock, C.; MacDougall, B. R. Nickel hydroxides and related materials: a review of their structures, synthesis and properties. *Proceedings of the Royal Society A: Mathematical, Physical and Engineering Sciences* **2015**, *471* (2174), 20140792. DOI: 10.1098/rspa.2014.0792.

(168) Schweitzer, G. K.; Pesterfield, L. L. *The Aqueous Chemistry of the Elements*; Oxford University Press, 2010.

(169) Cornell, R. M.; Schwertmann, U. *The Iron Oxides: Structure, Properties, Reactions, Occurrences, and Uses, 2nd Edition*; Wiley-VCH, 2003.

(170) Campo Schneider, L. P.; Dhrioua, M.; Ullmer, D.; Egert, F.; Wiggenhauser, H. J.; Ghotia, K.; Kawerau, N.; Grilli, D.; et al. Advancements in Hydrogen Production using Alkaline Electrolysis Systems: A Short Review on Experimental and Simulation Studies. *Curr. Opin. Electrochem.* **2024**, 101552. DOI: https://doi.org/10.1016/j.coelec.2024.101552.

(171) de Groot, M. T. Alkaline water electrolysis: with or without iron in the electrolyte? *Current Opinion in Chemical Engineering* **2023**, *42*, 100981. DOI: https://doi.org/10.1016/j.coche.2023.100981.

(172) Zankowski, S. P.; Vereecken, P. M. Electrochemical Determination of Porosity and Surface Area of Thin Films of Interconnected Nickel Nanowires. *J. Electrochem. Soc.* **2019**, *166* (6), D227. DOI: 10.1149/2.0311906jes.

(173) Stevens, M. B.; Trang, C. D. M.; Enman, L. J.; Deng, J.; Boettcher, S. W. Reactive Fe-Sites in Ni/Fe (Oxy)hydroxide Are Responsible for Exceptional Oxygen Electrocatalysis Activity. *J. Am. Chem. Soc.* **2017**, *139* (33), 11361-11364. DOI: 10.1021/jacs.7b07117.

(174) Guidelli, R.; Compton, R. G.; Feliu, J. M.; Gileadi, E.; Lipkowski, J.; Schmickler, W.; Trasatti, S. Defining the transfer coefficient in electrochemistry: An assessment (IUPAC Technical Report). **2014**, *86* (2), 245-258. DOI: doi:10.1515/pac-2014-5026.

(175) Nong, H. N.; Falling, L. J.; Bergmann, A.; Klingenhof, M.; Tran, H. P.; Spöri, C.; Mom, R.; Timoshenko, J.; et al. Key role of chemistry versus bias in electrocatalytic oxygen evolution. *Nature* **2020**, *587* (7834), 408-413. DOI: 10.1038/s41586-020-2908-2.

(176) Laidler, K. J.; Glasstone, S.; Eyring, H. Application of the Theory of Absolute Reaction Rates to Heterogeneous Processes II. Chemical Reactions on Surfaces. *J. Chem. Phys.* **1940**, *8* (9), 667-676. DOI: 10.1063/1.1750737.

(177) Moss, B.; Svane, K. L.; Nieto-Castro, D.; Rao, R. R.; Scott, S. B.; Tseng, C.; Sachs, M.; Pennathur, A.; et al. Cooperative Effects Drive Water Oxidation Catalysis in Cobalt Electrocatalysts through the Destabilization of Intermediates. *J. Am. Chem. Soc.* **2024**, *146* (13), 8915-8927. DOI: 10.1021/jacs.3c11651.

(178) Damjanovic, A. Temperature dependence of symmetry factors and the significance of experimental activation energies. *J. Electroanal. Chem.* **1993**, *355* (1), 57-77. DOI: https://doi.org/10.1016/0022-0728(93)80354-K.

(179) Parsons, R. The effect of specific adsorption on the rate of an electrode process. *J. Electroanal. Chem. Interf. Electrochem.* **1969**, *21* (1), 35-43. DOI: https://doi.org/10.1016/S0022-0728(69)80024-0.

(180) Eyring, H. The Activated Complex in Chemical Reactions. *J. Chem. Phys.* **1935**, *3* (2), 107-115. DOI: 10.1063/1.1749604.

(181) Rodellar, C. G.; Gisbert-Gonzalez, J. M.; Sarabia, F.; Roldan Cuenya, B.; Oener, S. Z. Ion solvation kinetics in bipolar membranes and at electrolyte–metal interfaces. *Nat. Energy* **2024**, *9* (5), 548-558. DOI: 10.1038/s41560-024-01484-z.

(182) Sarabia, F.; Gomez Rodellar, C.; Roldan Cuenya, B.; Oener, S. Z. Exploring dynamic solvation kinetics at electrocatalyst surfaces. *Nat. Commun.* **2024**, *15* (1), 8204. DOI: 10.1038/s41467-024-52499-9.

(183) Acharya, P.; Hong, J.; Manso, R.; Hoffman, A. S.; Kekedy-Nagy, L.; Chen, J.; Bare, S. R.; Greenlee, L. F. Temporal Ni K-Edge X-ray Absorption Spectroscopy Study Reveals the Kinetics of the Ni Redox Behavior of the Iron-Nickel Oxide Bimetallic OER Catalyst. *J. Phys. Chem. C* **2023**. DOI: 10.1021/acs.jpcc.3c03480.

(184) Marx, D.; Tuckerman, M. E.; Hutter, J.; Parrinello, M. The nature of the hydrated excess proton in water. *Nature* **1999**, *397* (6720), 601-604. DOI: 10.1038/17579.

(185) Lapid, H.; Agmon, N.; Petersen, M. K.; Voth, G. A. A bond-order analysis of the mechanism for hydrated proton mobility in liquid water. *J. Chem. Phys.* **2004**, *122* (1), 014506. DOI: 10.1063/1.1814973.

(186) Fournier, J. A.; Carpenter, W. B.; Lewis, N. H. C.; Tokmakoff, A. Broadband 2D IR spectroscopy reveals dominant asymmetric H5O2+ proton hydration structures in acid solutions. *Nat. Chem.* **2018**, *10* (9), 932-937. DOI: 10.1038/s41557-018-0091-y.

(187) Carpenter, W. B.; Lewis, N. H. C.; Fournier, J. A.; Tokmakoff, A. Entropic barriers in the kinetics of aqueous proton transfer. *J. Chem. Phys.* **2019**, *151* (3), 034501. DOI: 10.1063/1.5108907.

(188) Xu, P.; von Rueden, A. D.; Schimmenti, R.; Mavrikakis, M.; Suntivich, J. Optical method for quantifying the potential of zero charge at the platinum–water electrochemical interface. *Nat. Mater.* **2023**, *22* (4), 503-510. DOI: 10.1038/s41563-023-01474-8.

(189) Li, C.-Y.; Le, J.-B.; Wang, Y.-H.; Chen, S.; Yang, Z.-L.; Li, J.-F.; Cheng, J.; Tian, Z.-Q. In situ probing electrified interfacial water structures at atomically flat surfaces. *Nat. Mater.* **2019**, *18* (7), 697-701. DOI: 10.1038/s41563-019-0356-x.

(190) Liu, L.; Guo, Q.-X. Isokinetic Relationship, Isoequilibrium Relationship, and Enthalpy−Entropy Compensation. *Chem. Rev.* **2001**, *101* (3), 673-696. DOI: 10.1021/cr990416z.

(191) Bligaard, T.; Honkala, K.; Logadottir, A.; Nørskov, J. K.; Dahl, S.; Jacobsen, C. J. H. On the Compensation Effect in Heterogeneous Catalysis. *J. Phys. Chem. B* **2003**, *107* (35), 9325-9331. DOI: 10.1021/jp034447g.

(192) Teschner, D.; Novell-Leruth, G.; Farra, R.; Knop-Gericke, A.; Schlögl, R.; Szentmiklósi, L.; Hevia, M. G.; Soerijanto, H.; et al. In situ surface coverage analysis of RuO2-catalysed HCl oxidation reveals the entropic origin of compensation in heterogeneous catalysis. *Nat. Chem.* **2012**, *4* (9), 739-745. DOI: 10.1038/nchem.1411.

(193) Piontek, S. M.; Naujoks, D.; Tabassum, T.; DelloStritto, M. J.; Jaugstetter, M.; Hosseini, P.; Corva, M.; Ludwig, A.; et al. Probing the Gold/Water Interface with Surface-Specific Spectroscopy. *ACS Physical Chemistry Au* **2023**, *3* (1), 119-129. DOI: 10.1021/acsphyschemau.2c00044.

(194) Fabbri, E.; Schmidt, T. J. Oxygen Evolution Reaction—The Enigma in Water Electrolysis. *ACS Catal.* **2018**, *8* (10), 9765-9774. DOI: 10.1021/acscatal.8b02712.

(195) Bockris, J. O. M.; Otagawa, T. Mechanism of oxygen evolution on perovskites. *J. Phys. Chem.* **1983**, *87* (15), 2960-2971. DOI: 10.1021/j100238a048.

(196) Song, J.; Jin, X.; Zhang, S.; Jiang, X.; Yang, J.; Li, Z.; Zhou, J.; Zhang, H.; et al. Synergistic Role of Eg Filling and Anion–Cation Hybridization in Enhancing the Oxygen Evolution Reaction Activity in Nickelates. *ACS Appl. Energy Mater.* **2021**, *4* (11), 12535-12542. DOI: 10.1021/acsaem.1c02335.

(197) Giordano, L.; Akkiraju, K.; Jacobs, R.; Vivona, D.; Morgan, D.; Shao-Horn, Y. Electronic Structure-Based Descriptors for Oxide Properties and Functions. *Acc. Chem. Res.* **2022**, *55* (3), 298-308. DOI: 10.1021/acs.accounts.1c00509.

(198) Hammer, B.; Nørskov, J. K. Electronic factors determining the reactivity of metal surfaces. *Surf. Sci.* **1995**, *343* (3), 211-220. DOI: https://doi.org/10.1016/0039-6028(96)80007-0.

(199) Hammer, B.; Norskov, J. K. Why gold is the noblest of all the metals. *Nature* **1995**, *376* (6537), 238-240. DOI: 10.1038/376238a0.

(200) Hammer, B.; Nørskov, J. K. Theoretical surface science and catalysis—calculations and concepts. In *Advances in Catalysis*, Vol. 45; Academic Press, 2000; pp 71-129.

(201) Calle-Vallejo, F.; Díaz-Morales, O. A.; Kolb, M. J.; Koper, M. T. M. K. Why is bulk thermochemistry a good descriptor for the electroctalytic activity of transition metal oxides? ACS Catal.: 2014; Vol. 5, pp 869-873.

(202) Fabbri, E.; Nachtegaal, M.; Binninger, T.; Cheng, X.; Kim, B.-J.; Durst, J.; Bozza, F.; Graule, T.; et al. Dynamic surface self-reconstruction is the key of highly active perovskite nano-electrocatalysts for water splitting. *Nat. Mater.* **2017**, *16* (9), 925-931. DOI: 10.1038/nmat4938.

(203) Burke, M. S.; Kast, M. G.; Trotochaud, L.; Smith, A. M.; Boettcher, S. W. Cobalt–Iron (Oxy)hydroxide Oxygen Evolution Electrocatalysts: The Role of Structure and Composition on Activity, Stability, and Mechanism. *J. Am. Chem. Soc.* **2015**, *137* (10), 3638-3648. DOI: 10.1021/jacs.5b00281.

(204) Shen, T.-H.; Spillane, L.; Vavra, J.; Pham, T. H. M.; Peng, J.; Shao-Horn, Y.; Tileli, V. Oxygen Evolution Reaction in $Ba_{0.5}Sr_{0.5}Co_{0.8}Fe_{0.2}O_{3-\delta}$ Aided by Intrinsic Co/Fe Spinel-Like Surface. *J. Am. Chem. Soc.* **2020**, *142* (37), 15876-15883. DOI: 10.1021/jacs.0c06268.

(205) Lopes, P. P.; Chung, D. Y.; Rui, X.; Zheng, H.; He, H.; Farinazzo Bergamo Dias Martins, P.; Strmcnik, D.; Stamenkovic, V. R.; et al. Dynamically Stable Active Sites from Surface Evolution of Perovskite Materials during the Oxygen Evolution Reaction. *J. Am. Chem. Soc.* **2021**, *143* (7), 2741-2750. DOI: 10.1021/jacs.0c08959.

(206) Boucly, A.; Artiglia, L.; Fabbri, E.; Palagin, D.; Aegerter, D.; Pergolesi, D.; Novotny, Z.; Comini, N.; et al. Direct evidence of cobalt oxyhydroxide formation on a $La_{0.2}Sr_{0.8}CoO_3$ perovskite water splitting catalyst. *J. Mater. Chem. A* **2022**, *10* (5), 2434-2444, 10.1039/D1TA04957G. DOI: 10.1039/D1TA04957G.

(207) Boucly, A.; Fabbri, E.; Artiglia, L.; Cheng, X.; Pergolesi, D.; Ammann, M.; Schmidt, T. J. Surface Segregation Acts as Surface Engineering for the Oxygen Evolution Reaction on

Perovskite Oxides in Alkaline Media. *Chem. Mater.* **2020**, *32* (12), 5256-5263. DOI: 10.1021/acs.chemmater.0c01396.

(208) Zhang, T.; Nellist, M. R.; Enman, L. J.; Xiang, J.; Boettcher, S. W. Modes of Fe Incorporation in Co–Fe (Oxy)hydroxide Oxygen Evolution Electrocatalysts. *ChemSusChem* **2019**, *12* (9), 2015-2021, https://doi.org/10.1002/cssc.201801975. DOI: https://doi.org/10.1002/cssc.201801975.

(209) Oliveira, F. S.; Pimentel, P. M.; Oliveira, R. M. P. B.; Melo, D. M. A.; Melo, M. A. F. Effect of lanthanum replacement by strontium in lanthanum nickelate crystals synthetized using gelatin as organic precursor. *Mater. Lett.* **2010**, *64* (24), 2700-2703. DOI: https://doi.org/10.1016/j.matlet.2010.08.059.

(210) Sankannavar, R.; Sandeep, K. C.; Kamath, S.; Suresh, A. K.; Sarkar, A. Impact of Strontium-Substitution on Oxygen Evolution Reaction of Lanthanum Nickelates in Alkaline Solution. *J. Electrochem. Soc.* **2018**, *165* (15), J3236. DOI: 10.1149/2.0301815jes.

(211) Sun, Y.; Wu, C.-R.; Ding, T.-Y.; Gu, J.; Yan, J.-W.; Cheng, J.; Zhang, K. H. L. Direct observation of the dynamic reconstructed active phase of perovskite $LaNiO_3$ for the oxygen-evolution reaction. *Chem. Sci.* **2023**, *14* (22), 5906-5911, 10.1039/D2SC07034K. DOI: 10.1039/D2SC07034K.

(212) Füngerlings, A.; Wohlgemuth, M.; Antipin, D.; van der Minne, E.; Kiens, E. M.; Villalobos, J.; Risch, M.; Gunkel, F.; et al. Crystal-facet-dependent surface transformation dictates the oxygen evolution reaction activity in lanthanum nickelate. *Nat. Commun.* **2023**, *14* (1), 8284. DOI: 10.1038/s41467-023-43901-z.

(213) Liu, J.; Jia, E.; Stoerzinger, K. A.; Wang, L.; Wang, Y.; Yang, Z.; Shen, D.; Engelhard, M. H.; et al. Dynamic Lattice Oxygen Participation on Perovskite $LaNiO_3$ during Oxygen Evolution Reaction. *J. Phys. Chem. C* **2020**, *124* (28), 15386-15390. DOI: 10.1021/acs.jpcc.0c04808.

(214) Wang, L.; Stoerzinger, K. A.; Chang, L.; Zhao, J.; Li, Y.; Tang, C. S.; Yin, X.; Bowden, M. E.; et al. Tuning Bifunctional Oxygen Electrocatalysts by Changing the A-Site Rare-Earth Element in Perovskite Nickelates. *Adv. Funct. Mater.* **2018**, *28* (39), 1803712, https://doi.org/10.1002/adfm.201803712. DOI: https://doi.org/10.1002/adfm.201803712.

(215) Liu, J.; Jia, E.; Wang, L.; Stoerzinger, K. A.; Zhou, H.; Tang, C. S.; Yin, X.; He, X.; et al. Tuning the Electronic Structure of $LaNiO_3$ through Alloying with Strontium to Enhance Oxygen Evolution Activity. *Adv. Sci.* **2019**, *6* (19), 1901073, https://doi.org/10.1002/advs.201901073. DOI: https://doi.org/10.1002/advs.201901073.

(216) Adiga, P.; Wang, L.; Wong, C.; Matthews, B. E.; Bowden, M. E.; Spurgeon, S. R.; Sterbinsky, G. E.; Blum, M.; et al. Correlation between oxygen evolution reaction activity and

surface compositional evolution in epitaxial $La_{0.5}Sr_{0.5}Ni_{1-x}Fe_xO_{3-\delta}$ thin films. *Nanoscale* **2023**, *15* (3), 1119-1127, 10.1039/D2NR05373J. DOI: 10.1039/D2NR05373J.

(217) Wang, L.; Adiga, P.; Zhao, J.; Samarakoon, W. S.; Stoerzinger, K. A.; Spurgeon, S. R.; Matthews, B. E.; Bowden, M. E.; et al. Understanding the Electronic Structure Evolution of Epitaxial $LaNi_{1-x}Fe_xO_3$ Thin Films for Water Oxidation. *Nano Lett.* **2021**, *21* (19), 8324-8331. DOI: 10.1021/acs.nanolett.1c02901.

(218) Binninger, T.; Mohamed, R.; Waltar, K.; Fabbri, E.; Levecque, P.; Kötz, R.; Schmidt, T. J. Thermodynamic explanation of the universal correlation between oxygen evolution activity and corrosion of oxide catalysts. *Scientific Reports* **2015**, *5* (1), 12167. DOI: 10.1038/srep12167.

(219) Jackson, M. N.; Jung, O.; Lamotte, H. C.; Surendranath, Y. Donor-dependent promotion of interfacial proton-coupled electron transfer in aqueous electrocatalysis. *ACS Catal.* **2019**, *9* (4), 3737-3743.

(220) Jackson, M. N.; Surendranath, Y. Molecular Control of Heterogeneous Electrocatalysis through Graphite Conjugation. *Acc. Chem. Res.* **2019**, *52* (12), 3432-3441. DOI: 10.1021/acs.accounts.9b00439.

(221) Corrigan, D. A. The Catalysis of the Oxygen Evolution Reaction by Iron Impurities in Thin Film Nickel Oxide Electrodes. *J. Electrochem. Soc.* **1987**, *134* (2), 377-384. DOI: 10.1149/1.2100463.

(222) Petrie, J. R.; Cooper, V. R.; Freeland, J. W.; Meyer, T. L.; Zhang, Z.; Lutterman, D. A.; Lee, H. N. Enhanced Bifunctional Oxygen Catalysis in Strained $LaNiO_3$ Perovskites. *J. Am. Chem. Soc.* **2016**, *138* (8), 2488-2491. DOI: 10.1021/jacs.5b11713.

(223) Corrigan, D. A.; Bendert, R. M. Effect of Coprecipitated Metal Ions on the Electrochemistry of Nickel Hydroxide Thin Films: Cyclic Voltammetry in 1M KOH. *J. Electrochem. Soc.* **1989**, *136* (3), 723. DOI: 10.1149/1.2096717.

(224) Heymann, L.; Weber, M. L.; Wohlgemuth, M.; Risch, M.; Dittmann, R.; Baeumer, C.; Gunkel, F. Separating the Effects of Band Bending and Covalency in Hybrid Perovskite Oxide Electrocatalyst Bilayers for Water Electrolysis. *ACS Appl. Mater. Interfaces* **2022**, *14* (12), 14129-14136. DOI: 10.1021/acsami.1c20337.

(225) Batchellor, A. S.; Boettcher, S. W. Pulse-electrodeposited Ni-Fe (oxy)hydroxide oxygen evolution electrocatalysts with high geometric and intrinsic activities at large mass loadings. *ACS Catal.* **2015**, *5* (11), 6680-6689.

(226) Ma, X.; Wang, B.; Xhafa, E.; Sun, K.; Nikolla, E. Synthesis of shape-controlled $La_2NiO_{4+\delta}$ nanostructures and their anisotropic properties for oxygen diffusion. *Chem. Commun.* **2015**, *51* (1), 137-140, 10.1039/C4CC07364A. DOI: 10.1039/C4CC07364A.

(227) Gu, X.-K.; Carneiro, J. S. A.; Samira, S.; Das, A.; Ariyasingha, N. M.; Nikolla, E. Efficient Oxygen Electrocatalysis by Nanostructured Mixed-Metal Oxides. *J. Am. Chem. Soc.* **2018**, *140* (26), 8128-8137. DOI: 10.1021/jacs.7b11138.

(228) Ma, X.; Carneiro, J. S. A.; Gu, X.-K.; Qin, H.; Xin, H.; Sun, K.; Nikolla, E. Engineering Complex, Layered Metal Oxides: High-Performance Nickelate Oxide Nanostructures for Oxygen Exchange and Reduction. *ACS Catal.* **2015**, *5* (7), 4013-4019. DOI: 10.1021/acscatal.5b00756.

(229) Bhavaraju, S.; DiCarlo, J. F.; Scarfe, D. P.; Jacobson, A. J.; Buttrey, D. J. Electrochemical oxygen intercalation in $La_2NiO_{4+\delta}$ crystals. *Solid State Ion.* **1996**, *86-88*, 825-831. DOI: https://doi.org/10.1016/0167-2738(96)00191-9.

(230) Hong, W. T.; Stoerzinger, K. A.; Lee, Y.-L.; Giordano, L.; Grimaud, A.; Johnson, A. M.; Hwang, J.; Crumlin, E. J.; et al. Charge-transfer-energy-dependent oxygen evolution reaction mechanisms for perovskite oxides. *Energy Environ. Sci.* **2017**, *10* (10), 2190-2200, 10.1039/C7EE02052J. DOI: 10.1039/C7EE02052J.

(231) Suntivich, J.; Gasteiger, H. A.; Yabuuchi, N.; Nakanishi, H.; Goodenough, J. B.; Shao-Horn, Y. Design principles for oxygen-reduction activity on perovskite oxide catalysts for fuel cells and metal–air batteries. *Nat. Chem.* **2011**, *3* (7), 546-550. DOI: 10.1038/nchem.1069.

(232) Sun, Y.; Wang, J.; Xi, S.; Shen, J.; Luo, S.; Ge, J.; Sun, S.; Chen, Y.; et al. Navigating surface reconstruction of spinel oxides for electrochemical water oxidation. *Nat. Commun.* **2023**, *14* (1), 2467. DOI: 10.1038/s41467-023-38017-3.

(233) Grimaud, A.; Diaz-Morales, O.; Han, B.; Hong, W. T.; Lee, Y.-L.; Giordano, L.; Stoerzinger, K. A.; Koper, M. T. M.; et al. Activating lattice oxygen redox reactions in metal oxides to catalyse oxygen evolution. *Nat. Chem.* **2017**, *9* (5), 457-465. DOI: 10.1038/nchem.2695.

(234) Samira, S.; Gu, X.-K.; Nikolla, E. Design Strategies for Efficient Nonstoichiometric Mixed Metal Oxide Electrocatalysts: Correlating Measurable Oxide Properties to Electrocatalytic Performance. *ACS Catal.* **2019**, *9* (11), 10575-10586. DOI: 10.1021/acscatal.9b02505.

(235) Zhou, W.; Greer, H. F. What Can Electron Microscopy Tell Us Beyond Crystal Structures? *Eur. J. Inorg. Chem.* **2016**, *2016* (7), 941-950. DOI: https://doi.org/10.1002/ejic.201501342.

(236) Sunding, M. F.; Hadidi, K.; Diplas, S.; Løvvik, O. M.; Norby, T. E.; Gunnæs, A. E. XPS characterisation of in situ treated lanthanum oxide and hydroxide using tailored charge

referencing and peak fitting procedures. *J. Electron Spectrosc. Relat. Phenom.* **2011**, *184* (7), 399-409. DOI: https://doi.org/10.1016/j.elspec.2011.04.002.

(237) Biesinger, M. C.; Payne, B. P.; Grosvenor, A. P.; Lau, L. W. M.; Gerson, A. R.; Smart, R. S. C. Resolving surface chemical states in XPS analysis of first row transition metals, oxides and hydroxides: Cr, Mn, Fe, Co and Ni. *Appl. Surf. Sci.* **2011**, *257* (7), 2717-2730. DOI: https://doi.org/10.1016/j.apsusc.2010.10.051.

(238) San Choi, J.; Ahn, C. W.; Bae, J.-S.; Kim, T. H. Identifying a perovskite phase in rare-earth nickelates using X-ray photoelectron spectroscopy. *Curr. Appl. Phys.* **2020**, *20* (1), 102-105. DOI: https://doi.org/10.1016/j.cap.2019.10.013.

(239) Payne, B. P.; Biesinger, M. C.; McIntyre, N. S. Use of oxygen/nickel ratios in the XPS characterisation of oxide phases on nickel metal and nickel alloy surfaces. *J. Electron Spectrosc. Relat. Phenom.* **2012**, *185* (5), 159-166. DOI: https://doi.org/10.1016/j.elspec.2012.06.008.

(240) Biesinger, M. C.; Payne, B. P.; Lau, L. W. M.; Gerson, A.; Smart, R. S. C. X-ray photoelectron spectroscopic chemical state quantification of mixed nickel metal, oxide and hydroxide systems. *Surf. Interface Anal.* **2009**, *41* (4), 324-332. DOI: https://doi.org/10.1002/sia.3026.

(241) Krivina, R. A.; Lindquist, G. A.; Yang, M. C.; Cook, A. K.; Hendon, C. H.; Motz, A. R.; Capuano, C.; Ayers, K. E.; et al. Three-Electrode Study of Electrochemical Ionomer Degradation Relevant to Anion-Exchange-Membrane Water Electrolyzers. *ACS Appl. Mater. Interfaces* **2022**, *14* (16), 18261-18274. DOI: 10.1021/acsami.1c22472.

(242) Son, Y. J.; Kim, S.; Leung, V.; Kawashima, K.; Noh, J.; Kim, K.; Marquez, R. A.; Carrasco-Jaim, O. A.; et al. Effects of Electrochemical Conditioning on Nickel-Based Oxygen Evolution Electrocatalysts. *ACS Catal.* **2022**, *12* (16), 10384-10399. DOI: 10.1021/acscatal.2c01001.

(243) Gong, L.; Chng, X. Y. E.; Du, Y.; Xi, S.; Yeo, B. S. Enhanced Catalysis of the Electrochemical Oxygen Evolution Reaction by Iron(III) Ions Adsorbed on Amorphous Cobalt Oxide. *ACS Catal.* **2018**, *8* (2), 807-814. DOI: 10.1021/acscatal.7b03509.

(244) Yagi, S.; Yamada, I.; Tsukasaki, H.; Seno, A.; Murakami, M.; Fujii, H.; Chen, H.; Umezawa, N.; et al. Covalency-reinforced oxygen evolution reaction catalyst. *Nat. Commun.* **2015**, *6* (1), 8249. DOI: 10.1038/ncomms9249.

(245) May, K. J.; Carlton, C. E.; Stoerzinger, K. A.; Risch, M.; Suntivich, J.; Lee, Y.-L.; Grimaud, A.; Shao-Horn, Y. Influence of Oxygen Evolution during Water Oxidation on the Surface of Perovskite Oxide Catalysts. *J. Phys. Chem. Lett.* **2012**, *3* (22), 3264-3270. DOI: 10.1021/jz301414z.

(246) Risch, M.; Grimaud, A.; May, K. J.; Stoerzinger, K. A.; Chen, T. J.; Mansour, A. N.; Shao-Horn, Y. Structural Changes of Cobalt-Based Perovskites upon Water Oxidation Investigated by EXAFS. *J. Phys. Chem. C* **2013**, *117* (17), 8628-8635. DOI: 10.1021/jp3126768.

(247) Grimaud, A.; May, K. J.; Carlton, C. E.; Lee, Y.-L.; Risch, M.; Hong, W. T.; Zhou, J.; Shao-Horn, Y. Double perovskites as a family of highly active catalysts for oxygen evolution in alkaline solution. *Nat. Commun.* **2013**, *4* (1), 2439. DOI: 10.1038/ncomms3439.

(248) He, Z.; Zhang, J.; Gong, Z.; Lei, H.; Zhou, D.; Zhang, N.; Mai, W.; Zhao, S.; et al. Activating lattice oxygen in NiFe-based (oxy)hydroxide for water electrolysis. *Nat. Commun.* **2022**, *13* (1), 2191. DOI: 10.1038/s41467-022-29875-4.

(249) Man, I. C.; Su, H.-Y.; Calle-Vallejo, F.; Hansen, H. A.; Martínez, J. I.; Inoglu, N. G.; Kitchin, J.; Jaramillo, T. F.; et al. Universality in Oxygen Evolution Electrocatalysis on Oxide Surfaces. *ChemCatChem* **2011**, *3* (7), 1159-1165. DOI: https://doi.org/10.1002/cctc.201000397.

(250) Carneiro, J. S. A.; Williams, J.; Gryko, A.; Herrera, L. P.; Nikolla, E. Embracing the Complexity of Catalytic Structures: A Viewpoint on the Synthesis of Nonstoichiometric Mixed Metal Oxides for Catalysis. *ACS Catal.* **2020**, *10* (1), 516-527. DOI: 10.1021/acscatal.9b04226.

(251) Stevens, M. B.; Enman, L. J.; Batchellor, A. S.; Cosby, M. R.; Vise, A. E.; Trang, C. D. M.; Boettcher, S. W. Measurement Techniques for the Study of Thin Film Heterogeneous Water Oxidation Electrocatalysts. *Chem. Mater.* **2017**, *29* (1), 120-140. DOI: 10.1021/acs.chemmater.6b02796.

(252) Pourbaix, M. *Atlas of electrochemical equilibria in aqueous solutions*; 1966.

(253) Abdel Haleem, A.; Huyan, J.; Nagasawa, K.; Kuroda, Y.; Nishiki, Y.; Kato, A.; Nakai, T.; Araki, T.; et al. Effects of operation and shutdown parameters and electrode materials on the reverse current phenomenon in alkaline water analyzers. *J. Power Sources* **2022**, *535*, 231454. DOI: https://doi.org/10.1016/j.jpowsour.2022.231454.

(254) Guruprasad, N.; van der Schaaf, J.; de Groot, M. T. Unraveling the impact of reverse currents on electrode stability in anion exchange membrane water electrolysis. *J. Power Sources* **2024**, *613*, 234877. DOI: https://doi.org/10.1016/j.jpowsour.2024.234877.

(255) Kim, Y.; Jung, S.-M.; Kim, K.-S.; Kim, H.-Y.; Kwon, J.; Lee, J.; Cho, H.-S.; Kim, Y.-T. Cathodic Protection System against a Reverse-Current after Shut-Down in Zero-Gap Alkaline Water Electrolysis. *JACS Au* **2022**, *2* (11), 2491-2500. DOI: 10.1021/jacsau.2c00314.

(256) Uchino, Y.; Kobayashi, T.; Hasegawa, S.; Nagashima, I.; Sunada, Y.; Manabe, A.; Nishiki, Y.; Mitsushima, S. Dependence of the Reverse Current on the Surface of Electrode Placed on a

Bipolar Plate in an Alkaline Water Electrolyzer. *Electrochemistry* **2018**, *86* (3), 138-144. DOI: 10.5796/electrochemistry.17-00102.

(257) Hwang, J.; Rao, R. R.; Giordano, L.; Katayama, Y.; Yu, Y.; Shao-Horn, Y. Perovskites in catalysis and electrocatalysis. *Science* **2017**, *358* (6364), 751-756. DOI: 10.1126/science.aam7092.

(258) Zizak, I. The KMC-3 XPP beamline at BESSY II. J. large-scale res. fac.: 2017; Vol. 3.

(259) Schuck, G.; Zisak, I. CryoEXAFS: X-ray absorption spectroscopy station with cryogenic or in-beam operando electrochemistry sample conditions at BESSY II. *J. large-scale res. fac.* **2020**, *6*.

(260) Bearden, J. A.; Burr, A. F. Reevaluation of X-Ray Atomic Energy Levels. *Rev. Mod. Phys.* **1967**, *39* (1), 125-142. DOI: 10.1103/RevModPhys.39.125.

(261) Villalobos, J.; Golnak, R.; Xi, L.; Schuck, G.; Risch, M. Reversible and irreversible processes during cyclic voltammetry of an electrodeposited manganese oxide as catalyst for the oxygen evolution reaction. *Journal of Physics: Energy* **2020**, *2* (3), 034009. DOI: 10.1088/2515-7655/ab9fe2.

(262) Ankudinov, A. L.; Ravel, B.; Rehr, J. J.; Conradson, S. D. Real-space multiple-scattering calculation and interpretation of x-ray-absorption near-edge structure. *Phys. Rev. B* **1998**, *58* (12), 7565-7576. DOI: 10.1103/PhysRevB.58.7565.

(263) Oleś, A.; Szytuła, A.; Wanic, A. Neutron Diffraction Study of γ-FeOOH. *physica status solidi (b)* **1970**, *41* (1), 173-177, https://doi.org/10.1002/pssb.19700410119. DOI: https://doi.org/10.1002/pssb.19700410119.

(264) Zaffran, J.; Burke-Stevens, M.; Trang, C. D. M.; Nagli, M.; Shehadeh, M.; Boettcher, S. W.; Toroker, M. C. Influence of electrolyte cations on Ni(Fe)OOH Catalyzed Oxygen Evolution Reaction. **2017**, *29*, 4761-4767.

(265) Fidelsky, V.; Toroker, M. C. The secret behind the success of doping nickel oxyhydroxide with iron. *Phys. Chem. Chem. Phys.* **2017**, *19* (11), 7491-7497, 10.1039/C6CP08590C. DOI: 10.1039/C6CP08590C.